The impact of stellar activity evolution on atmospheric mass loss of young exoplanets

Laura Ketzer

Dissertation
zur Erlangung des akademischen Grades

doctor rerum naturalium
(Dr. rer. nat.)

in der Wissenschaftsdisziplin
Astrophysik

eingereicht an der
Mathematisch-Naturwissenschaftlichen Fakultät
Institut für Physik und Astronomie
der Universität Potsdam

Potsdam, den 29.8.2023

Hauptgutachterin

Prof. Dr. Katja Poppenhäger
Leibniz-Institut für Astrophysik Potsdam, Universität Potsdam

Gutachter

Dr. habil. Axel Schwope
Leibniz-Institut für Astrophysik Potsdam

Prof. Dr. Peter Wheatley
University of Warwick

Abstract

The increasing number of known exoplanets raises questions about their demographics and the mechanisms that shape planets into how we observe them today. Young planets in close-in orbits are exposed to harsh environments due to the host star being magnetically highly active, which results in high X-ray and extreme UV fluxes impinging on the planet. Prolonged exposure to this intense photoionizing radiation can cause planetary atmospheres to heat up, expand and escape into space via a hydrodynamic escape process known as photoevaporation. For super-Earth and sub-Neptune-type planets, this can even lead to the complete erosion of their primordial gaseous atmospheres. A factor of interest for this particular mass-loss process is the activity evolution of the host star. Stellar rotation, which drives the dynamo and with it the magnetic activity of a star, changes significantly over the stellar lifetime. This strongly affects the amount of high-energy radiation received by a planet as stars age. At a young age, planets still host warm and extended envelopes, making them particularly susceptible to atmospheric evaporation. Especially in the first gigayear, when X-ray and UV levels can be $100 - 10,000$ times higher than for the present-day sun, the characteristics of the host star and the detailed evolution of its high-energy emission are of importance.

In this thesis, I study the impact of stellar activity evolution on the high-energy-induced atmospheric mass loss of young exoplanets. The PLATYPOS code was developed as part of this thesis to calculate photoevaporative mass-loss rates over time. The code, which couples parameterized planetary mass-radius relations with an analytical hydrodynamic escape model, was used, together with Chandra and eROSITA X-ray observations, to investigate the future mass loss of the two young multiplanet systems V1298 Tau and K2-198. Further, in a numerical ensemble study, the effect of a realistic spread of activity tracks on the small-planet radius gap was investigated for the first time. The works in this thesis show that for individual systems, in particular if planetary masses are unconstrained, the difference between a young host star following a low-activity track vs. a high-activity one can have major implications: the exact shape of the activity evolution can determine whether a planet can hold on to some of its atmosphere, or completely loses its envelope, leaving only the bare rocky core behind. For an ensemble of simulated planets, an observationally-motivated distribution of activity tracks does not substantially change the final radius

distribution at ages of several gigayears. My simulations indicate that the overall shape and slope of the resulting small-planet radius gap is not significantly affected by the spread in stellar activity tracks. However, it can account for a certain scattering or fuzziness observed in and around the radius gap of the observed exoplanet population.

Zusammenfassung

Die steigende Anzahl bekannter Exoplaneten wirft Fragen zu ihrer Demografie und den Mechanismen auf, die Planeten in ihre heutige beobachtete Form bringen. Junge Planeten, die sehr nah um ihren Wirtsstern kreisen, sind extremen Umgebungen ausgesetzt, da der Stern eine hohe magnetische Aktivität aufweist. Das führt wiederum dazu, dass der Planet einer enormen Röntgen- und Extrem-UV-Strahlung ausgesetzt ist. Ist der Planet über einen längeren Zeitraum dieser intensiven photoionisierenden Strahlung ausgesetzt, kann dies dazu führen, dass Planetenatmosphären sich aufheizen, ausdehnen und durch einen hydrodynamischen Entweichungsprozess namens Photoevaporation ins All entweichen, sozusagen verdampfen. Bei Planeten, in der Größenordnung von Super-Erden und Sub-Neptunen, kann dies sogar zur vollständigen Erosion ihrer Ur-Atmosphären führen. Ein interessanter Faktor, der für diesen Massenverlustprozess eine Rolle spielt, ist die Aktivitätsentwicklung des Wirtssterns. Die Rotation eines Sterns, die den Dynamo und damit die magnetische Aktivität antreibt, ändert sich im Laufe der Lebensdauer eines Sterns erheblich. Dies hat einen starken Einfluss auf die Menge der hochenergetischen Strahlung, den ein Planet mit zunehmendem Alter des Sterns empfängt. In jungen Jahren besitzen Planeten noch warme und ausgedehnte Hüllen, was sie besonders anfällig für atmosphärische Verdunstung macht. Insbesondere in den ersten Gigajahren, wenn die Röntgen- und UV-Strahlung 100 – 10,000 Mal höher sein kann als bei der heutigen Sonne, sind die Eigenschaften des Wirtssterns und die detaillierte Entwicklung seiner hochenergetischen Emission von Bedeutung.

In dieser Arbeit untersuche ich die Auswirkungen der Entwicklung der stellaren Aktivität auf den durch hochenergetische Strahlung verursachten atmosphärischen Massenverlust junger Exoplaneten. Der PLATYPOS-Code wurde im Rahmen dieser Arbeit entwickelt, um die photoevaporativen Massenverlustraten für verschiedene stellare Alter zu berechnen. Der Code verknüpft parametrisierte Planetenmasse-Radius-Beziehungen mit einem analytischen Modell für den hydrodynamischen Massenverlust. Er wurde zusammen mit Chandra- und eROSITA-Röntgenbeobachtungen dazu verwendet, den zukünftigen Massenverlust der beiden jungen Mehrplanetensysteme V1298 Tau und K2-198 zu untersuchen. Darüber hinaus wurde in einer numerischen Ensemblestudie erstmals der Effekt einer realistischen Verteilung von stellaren Aktivitäts-Tracks auf das sogenannte Radius-Tal bei kleinen Planeten untersucht. Die Arbeiten

in dieser Dissertation zeigen, dass für einzelne Systeme, insbesondere wenn die Planetenmassen unbestimmt sind, der Unterschied zwischen einem jungen Wirtsstern, der einem Track mit niedriger Aktivität gegenüber einem solchen mit hoher Aktivität folgt, gravierende Auswirkungen haben kann: Die genaue Form der Aktivitätsentwicklung kann darüber entscheiden, ob ein Planet einen Teil seiner Atmosphäre behält oder seine Hülle vollständig verliert und nur den nackten Gesteinskern behält. Für ein Ensemble von simulierten Planeten ändert eine durch Beobachtungen motivierte Verteilung von Aktivitäts-Tracks die endgültige Radiusverteilung der Planeten nach mehreren Gigajahren nicht wesentlich. Meine Simulationen deuten darauf hin, dass die Form und Steigung des sich ergebenden Radius-Tals bei Kleinplaneten nicht wesentlich von der Streuung der stellaren Aktivitäts-Tracks beeinflusst wird. Eine gewisse Streuung oder Unschärfe im Radius-Tal der beobachteten Exoplanetenpopulation kann damit allerdings durchaus erklärt werden.

Contents

1   Thesis overview and list of included manuscripts

This thesis is divided into two parts: Part I serves as an introduction, and Part II contains four chapters – one for each publication in a peer-reviewed journal, in order of publication date. The four research papers, published in or submitted to Monthly Notices of the Royal Astronomical Society and Astronomische Nachrichten, form the core of this thesis.

Part I gives the reader background information on the three main topics of this thesis: (i) exoplanet demographics and the radius–gap feature seen in the observed population of small exoplanets (Ch. 2), (ii) the formation and evolution of planetary atmospheres, with particular focus on the photoevaporative mass-loss process (Ch. 3), and (iii) the importance of understanding the host star, its current X-ray emission as well as its activity evolution (past and future) in determining the fate of planets and their primordial planetary atmospheres (Ch. 4).

Part II contains four independent chapters, which, however, all share a common motive: to study the role of the host star activity evolution on the high-energy-induced atmospheric mass loss of exoplanet atmospheres, with focus on young and X-ray bright star–planet systems. Chapters 5 and 8 explore two individual, young multi-planet systems, V1298 Tau and K2-198, and the expected mass-loss histories of their planets. For both systems, X-ray observations with Chandra and eROSITA lay the foundation for subsequent numerical simulations of the atmospheric mass loss. Chapter 6 describes the code PLATYPOS, which was developed to conduct all mass-loss simulations contained within this thesis, and Ch. 7 is a purely numerical ensemble study to investigate how a realistic spread of stellar activity tracks influences the mass loss of a simulated population of small exoplanets and the observable properties of the radius gap. Lastly, Ch. 9 presents some concluding remarks. It highlights the contribution of the findings made in this thesis for the field, and discusses future perspectives.

All four manuscripts and the contributions of L. Ketzer to each paper are listed below.

1. X-ray irradiation and evaporation of the four young planets around V1298 Tau

Poppenhaeger, K.; Ketzer, L.; Mallonn, M.
Monthly Notices of the Royal Astronomical Society. Volume 500, Issue 4, Pages 4560–4572 (2021).
DOI: 10.1093/mnras/staa1462

Contribution: For this first publication, I am the second author, but with large contributions to the final work. While the X-ray and optical data were analyzed and interpreted by K. Poppenhaeger and M. Mallonn, the second half of the paper is my contribution. I used the measured X-ray luminosity of the host star as input to perform mass-loss calculations for the four planets around V1298 Tau. All calculations and plots in the discussion have been produced by me, as well as the majority of the associated text. This work is based on an early version of the publicly available python code PLATYPOS, which I started to develop as part of this project, and expanded upon later in subsequent works.

2. Estimating photoevaporative mass loss of exoplanets with PLATYPOS

Ketzer, L.; Poppenhaeger, K.
Astronomische Nachrichten. Volume 343, Issue 4, e210105 (2022).
DOI: 10.1002/asna.20210105

Contribution: For this paper, I am the lead author. The paper explains the building blocks of the atmospheric mass-loss code PLATYPOS (which was developed by me), and all the extensions made to the code since its first usage in the V1298 Tau publication. I wrote the initial draft for the publication and gathered feedback from my co-author, K. Poppenhaeger.

3. The influence of host star activity evolution on the population of super–Earths and mini–Neptunes

Ketzer, L.; Poppenhaeger, K.
Monthly Notices of the Royal Astronomical Society. Volume 518, Issue 2, Pages 1683–1706 (2023).
DOI: 10.1093/mnras/stac2643

Contribution: I am the lead author of this study, which investigated, for the first time, the effect of a spread of stellar activity tracks on the exoplanet radius gap. In the paper, we use the code PLATYPOS to conduct en ensemble study of an observationally-motivated planet population, evolving the planetary sample across a range of different stellar activity tracks from infant age to several Gyr. I conducted all numerical simulations, as well as the subsequent analysis and scientific exploration of the resulting data. While I wrote the majority of the initial draft, my co-author K. Poppenhaeger gave me scientific advice throughout the different stages of the project and contributed to parts of the text in the discussion section.

4. Three young planets around the young K–dwarf K2–198: High–energy environment, evaporation history and expected future

Ketzer, L.; Poppenhaeger, K.; Baratella, M.; Ilin, E.
Submitted to Monthly Notices of the Royal Astronomical Society on May 15, 2023; referee report received on July 2, 2023. Revised version to be resubmitted.

Contribution: I am the lead author of this study. For this paper, we use all available literature data, as well as updated eROSITA X-ray measurements, to determine the age of the star–planet system. I performed the photometric analysis of the light curve using Kepler and TESS archival data to determine the rotation period of the star, E. Ilin used her code AltaiPony to investigate flares and their frequency in the lightcurve. M. Baratella performed an analysis of the spectroscopic data to determine the stellar lithium abundance, and K. Poppenhaeger contributed the updated X-ray flux measurements of the host star. I conducted the remaining analysis and interpretation of the data, and performed the mass-loss calculations with the previously developed PLATYPOS code. K. Poppenhaeger, E. Ilin and M. Baratella contributed to the text in the context of their respective contributions and gave feedback. K. Poppenhaeger also gave input on the discussion.

Part I

Introduction

2   Exoplanet discovery and demographics

The discovery of planets orbiting stars other than the Sun (so-called exoplanets) is considered one of the most thrilling astronomical findings of recent decades. Crowned with a Nobel Prize in 2019, the first unambiguous detection of an exoplanet around a solar-like star, 51 Pegasi b, by Mayor & Queloz in 1995, has opened the door to an ever-growing field of exoplanetary science. Since then, more than 5,000 new exoplanets have been discovered, in particular thanks to dedicated space-borne observing missions (Borucki et al., 2010; Howell et al., 2014; Ricker et al., 2015). An interesting fact about the newly-discovered distant worlds is that no star–planet system discovered so far resembles our own home – the solar system. This, however, is not surprising, because the methods used to detect and confirm planets around stars other than our own are biased towards certain types of planets that can be more easily detected than others. The first puzzling example was indeed 51 Pegasi b, which shows no resemblance to any planet known in the solar system. The planet, which has a size similar to the cold gas-giant Jupiter (the largest planet in the solar system, orbiting the Sun in 11.2 years), revolves around its host star with a remarkable speed, namely in 4.23 days (much closer than Mercury's orbit). Today, such close-in giant planets are known as 'Hot Jupiters'. In addition to this new and peculiar class of exoplanets, a plethora of diverse star–planet systems outside our solar system have been discovered, challenging our conventional understanding of the formation and evolution of star–planet systems. Studying these unique systems can not only give new insights into the origin and destiny of distant worlds, but also our own.

2.1   Detection methods

Over the last few decades, numerous fascinating and unusual exoplanets have been discovered. The first detection was achieved by measuring periodic radial velocity variations in the stellar light with ground-based spectrographs (Mayor & Queloz, 1995). This method exploits the fact that a planet's gravitational pull on the star causes a wobbling of the star along the line-of-sight to the observer, which results in measurable blue- and redshifts in the stellar spectrum (see Fig. 2.1). As of today, however, the transit method stands out as the most successful detection method for planets beyond our solar system. Thanks to

dedicated space-based photometric missions like Kepler (Borucki et al., 2010; Howell et al., 2014) and TESS (Ricker et al., 2015), several (hundred) thousand stars (e.g. 150,000 stars for Kepler) can be continuously monitored over the period of weeks to years. The time-series data is then vetted for periodic dips in the stellar brightness caused by a planet transiting the stellar disc in the line-of-sight to the observer and blocking out up to a few percent of the total light of a star. For Sun-like stars, this fraction is usually only at most 1%, but for later spectral types, i.e. stars with smaller stellar radii, this fraction can be of the order of a few percent for large, Jupiter-sized planets.

Other successful methods, but with a significantly lower detection rate, include microlensing, direct imaging or astrometry. Microlensing is a technique that detects exoplanets by observing the magnification of light from a distant star due to the gravitational lensing effect caused by a foreground exoplanet (Griest & Safizadeh, 1998), direct imaging captures images of exoplanets directly, separate from their host stars, using a coronograph to block out the stellar light which usually outshines the planet (Lagrange et al., 2010), and astrometry exploits the fact that exoplanets induce tiny changes in a star's position caused by the gravitational pull of an orbiting planet (Sozzetti, 2010).

Due to different detection methods exhibiting different biases, e.g. the transit method being favorable for large planets in close orbits around small, low-mass stars, or the radial velocity method favoring more massive planets close in, it is crucial to account for these detection biases as well as any other observational limitations due to astrophysical sources like stellar activity, or any instrumental effects. It is the inherent distribution of exoplanets that theories of planet formation and evolution must reproduce (Cumming et al., 2008; Winn & Fabrycky, 2015).

Figure 2.2 shows the demographics of exoplanets discovered so far, color-coded by their detection method. Only exoplanets which either have measured masses or upper limits are shown, which is why the number of planets in the plot, around 3,000, is lower than the total number of detected exoplanets, which is currently around 5,000.

2.2 Exoplanet demographics and the small-planet radius gap

The main objective in the field of exoplanet demographics is to determine the occurrence rate or frequency distribution of planets, as well as possible
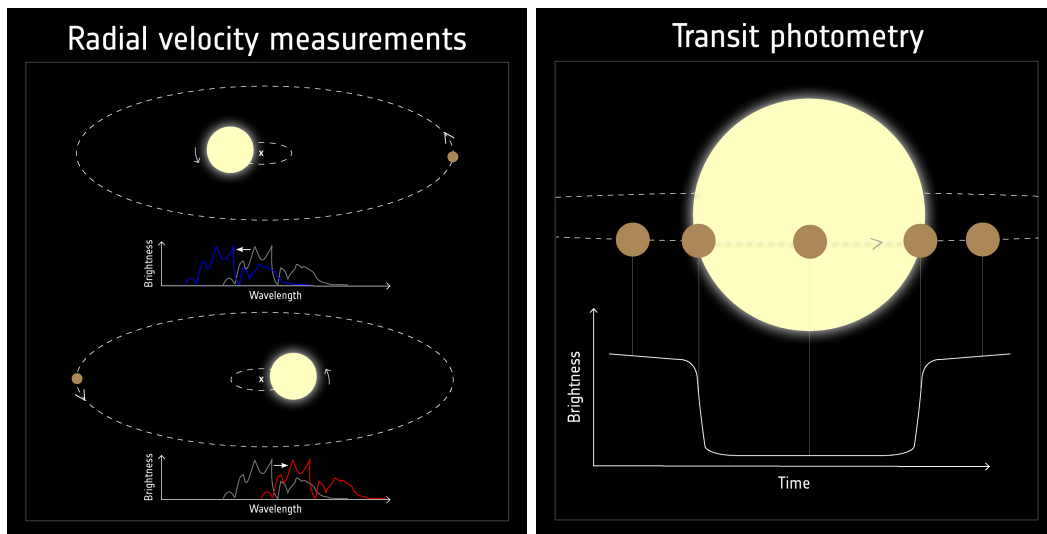
Figure 2.1: Illustrations of the two most successful exoplanet detection methods. The radial velocity method (left) detects exoplanets by measuring a star's subtle motion caused by an orbiting planet's gravity. This planet-induced stellar "wobble" can be observed in blue- and redshift of the stellar light. The transit method (right) observes the slight dimming of a star's brightness when an exoplanet passes in front of it. Both methods have been successful in discovering and characterizing numerous exoplanets. Figure credit: The European Space Agency.

patterns in this distribution, as a function of various physical parameters that could impact their formation and evolution, across a wide spectrum of such parameters (Gaudi et al., 2021). This, for example, includes properties related to the planet itself, like radius, mass and orbital properties (semi-major axis, orbital period, eccentricity), as well as host star-properties like stellar mass, radius, luminosity, effective temperature, activity level or age. Finally, any environmental characteristics of the star–planet system, such as the presence of multiple planets (multi-planet systems), or the conditions during its formation (birth environment) are of interest.

The over 5,000 confirmed exoplanets can be categorized into different groups based on their planetary parameters. Figure 2.2 shows the observed present-day exoplanet distribution in mass vs. semi-major axis space. Planets can be grouped into four main classes:

i) *Hot Jupiters* have orbital periods less than 7 days and masses above 100 Earth masses ($M_\oplus$) (or ≥0.3 Jupiter masses (M_{jup})). They are readily detectable, but represent, with an occurrence rate of <0.5–1% among nearby Sun-like main-
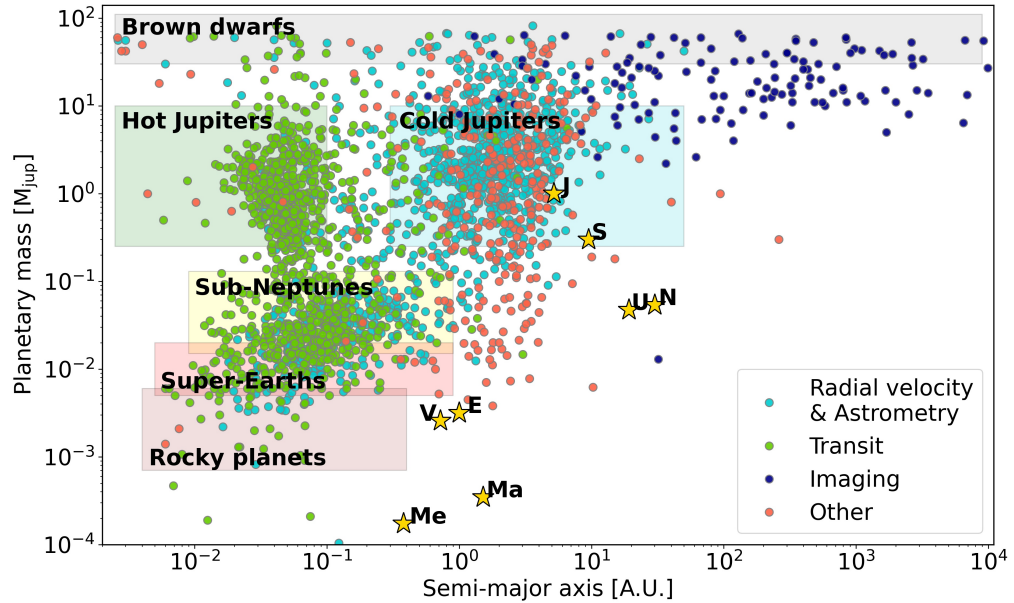
Figure 2.2: Distribution of the almost 3000 confirmed exoplanets with mass constraints (measured masses or upper limits). Shown here is planetary mass against semi-major axis, with the different planetary detection methods color coded. For reference, around 50% of planets in the sample come with a mass estimate, while roughly 30% have a mass measurement with upper and lower limits, and of those, 50% have an error of less than 15%. Solar-system planets are marked with yellow stars, and the shaded squares label the different classes of observed exoplanets. While some features seen in this diagram are authentic, many of them are due to selection effects. For instance, the paucity of planets in the lower-right corner of the plot arises due to the lack of sensitivity of transit, radial velocity and direct imaging methods to planets in this parameter space. In contrast, the nearly equal number of hot Jupiters and cold Jupiters results from ground-based surveys being primarily sensitive to close-in, large and massive hot Jupiters, which leads to their over-representation. The data shown here has been taken from NASA's Exoplanet Archive (https://exoplanetarchive.ipac.caltech.edu/, accessed on 18. May 2023).

sequence stars, only a tiny fraction of the overall planet population (e.g. Batalha et al., 2013).

ii) *Cold Jupiters* or *longer-period giant planets* are classified by having orbital periods in the range of hundreds to thousands of days, masses similar to or greater than Jupiter, and often times found to have substantial eccentricities (Perryman, 2018, see Ch. 65 for a review). These planets tend to be more similar to the classical gas giants in our solar system. Roughly 5-10% of the FGK[1] main-sequence dwarfs in the local galactic neighborhood host a planet in this cold gas giant regime, implying that such planets are almost ten times more abundant than hot Jupiters (Winn & Fabrycky, 2015).

iii) *Sub-* or *mini-Neptunes* are, similar to hot Jupiters, a rather surprising class of planets, having no analog in the solar system. With radii between roughly 1.8-4.5 Earth radii ($R_\oplus$), they are of the order or smaller than Neptune or Uranus in our own solar system (for reference, Neptune has a radius of about $4\,R_\oplus$ and a mass of almost $17\,M_\oplus$). Most sub-Neptunes have been found in close orbits with periods less than 100 days (for reference, Mercury has an orbital period of 88 days). They show a broad range of compositions, ranging from rocky Earth-like cores beneath gaseous envelopes of various sizes to water worlds or planets containing significant ice fractions. Regardless of the exact composition, their observed low densities indicate that they must contain significant fractions of volatile material and typically have hydrogen- and helium-dominated atmospheres to explain their large observed radii (Rogers, 2015).

iv) *Rocky planets* and *super-Earths* are planets with radii smaller than approximately $1.8\,R_\oplus$. As the name suggests, they are rocky and made up of a mixture of iron and silicates. Planets in this terrestrial regime might also host secondary atmospheres, for example, from out gassing due to volcanic activity (Kite & Barnett, 2020; Tian & Heng, 2023).

A surprising discovery is that these small, low-mass ($\leq 20\,M_\oplus$) planets, with orbital periods less than 100 days, and radii between Earth and Neptune, are very abundant. They show a ubiquity almost on the order of unity: about half of Sun-like stars host a planet of super-Earth or sub-Neptune class (Mullally et al., 2015; Winn & Fabrycky, 2015) (later type K and M stars even host roughly 2 planets per star (Dressing & Charbonneau, 2015)), making them

---

[1]FGK refers to the classification of stars based on their spectral characteristics. The term FGK represents the spectral types of stars, with F being hotter, G being similar to our Sun, and K being slightly cooler. FGK stars are relatively common and include stars like our Sun, with temperatures ranging from approximately 5,500 to 7,500 K.

the most common type of known exoplanets. This abundance contradicted the predictions of traditional planet-formation theories, according to which close-in super-Earth or sub-Neptune planets were expected to be rare (e.g. Ida & Lin, 2010). However, the unexpectedly high number of such planets prompted the development of new theories suggesting that small planets can form directly in short-period orbits, rather than forming farther from the star and migrating inward (e.g. Hansen & Murray, 2012; Chiang & Laughlin, 2013).

Figure 2.3 shows the observed exoplanet population in a different way – namely in mass vs. radius space, together with the empirical mass-radius relationships for exoplanets around older stars (Chen & Kipping, 2017a; Otegi et al., 2020a). Regarding the general pattern observed in the planetary mass-radius relationship, it is evident that low-mass planets exhibit compact sizes due to their composition: they are primarily mad-up of solid materials. On the other hand, planets with higher masses exhibit larger sizes as they are primarily composed of gaseous elements. In addition to this general trend, the mass–radius plot reveals different regimes, starting from rocky planets up to about $2\,R_\oplus$ in radius on the lower mass end, and extending into a regime of larger mass and radius, where planets host significant fractions of volatile and gaseous material in their envelope. Scatter increases in the volatile-rich regime, where observed masses for a given planetary radius can vary due to differences in core versus envelope fractions. Planets in the gas-giant regime, extending all the way to brown dwarfs, also follow their own mass–radius relation. For completeness, brown dwarfs are also shown in Fig. 2.2 and 2.3. They gap the bridge between the most massive planets and lowest-mass stars, and are distinguished from planets as they are massive enough to fuse deuterium.

The small–period radius gap

The identification of a significant population of planets with masses and radii intermediate between those of terrestrial planets and gas giants found within our own solar system has been one of the most remarkable recent findings in the field of planetary science. Among this ever-growing number of different exoplanets, the ones with orbital periods less than 100 days and radii in the super-Earth and sub-Neptune regimes are of particular relevance for this thesis.

With the thousands of newly discovered planets by the Kepler space telescope (Borucki et al., 2010; Howell et al., 2014), two striking features in the distribution of exoplanet radii were revealed. One is a paucity of short-period sub-Neptune-sized planets (Lundkvist et al., 2016; Berger et al., 2018), also known as the Neptune desert, and the second is a relatively clean gap in planetary radii around 1.8-2 $R_\oplus$ (Fulton et al., 2017a; Owen & Lai, 2018; Van Eylen et al., 2018a;
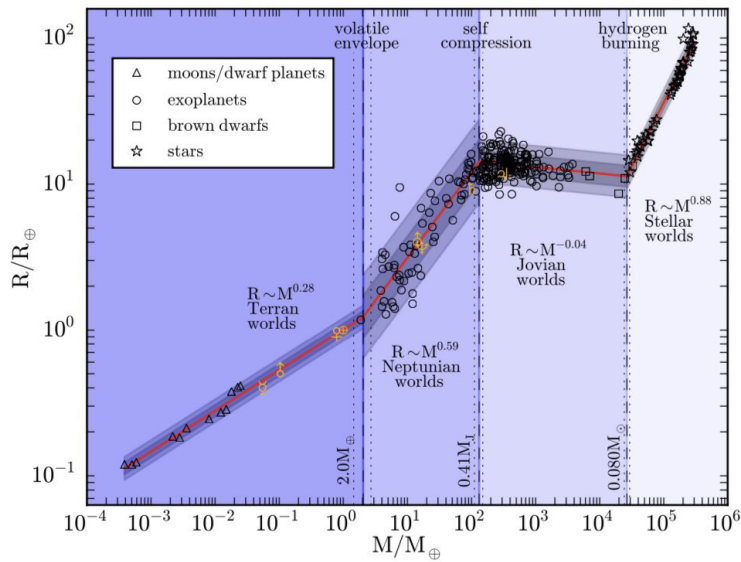
Figure 2.3: Mass–radius relation of mature exoplanets. Four different regimes are recognizable, starting with the rocky, terran worlds, followed by a Neptunian regime, where planets host significant volatile envelopes. At even larger masses and radii, Jovian worlds make up the class of the largest exoplanets. Brown dwarfs and the lowest mass stellar population is also included at the very right end of this plot. It is easily noticeable that, compared to the rocky regime, the scatter in the volatile regime is much larger, indicating a broader range of possible planetary configurations within this mass and radius regime. The red lines represent the power-law fits to the four different regimes, i.e. the corresponding mass–radius relations. Figure from Chen & Kipping (2017b).

Hardegree-Ullman et al., 2020). This feature was first noticed in the histogram of planetary radii, which shows a clear bimodality with a deficit around $1.8\,R_\oplus$. Since it could not be attributed to any observational limitations (planetary detection methods are equally sensitive in detecting planets with radii below and above $1.8\,R_\oplus$), it has to be of physical origin. With increasing precision on stellar and thus exoplanet radii (Petigura et al., 2017), this feature also emerged in radius–period space. As can be seen in Fig. 2.4 (zoom-in), there is a thin, almost empty band in the exoplanet population – the so-called 'radius valley' or small-planet radius gap – which has been demonstrated to correlate with the planetary orbital period or irradiation, with a slight decrease in gap radius towards larger periods. This supports the hypothesis that atmospheric mass loss plays a significant role in shaping the observed substructure. Theoretical studies had previously predicted this phenomenon (Owen & Wu, 2013; Lopez & Fortney, 2013a), before it was later confirmed by observations.

An increasing number of planetary mass measurements using radial velocity follow-up and transit timing variations (TTVs) (Marcy et al., 2014; Hadden & Lithwick, 2017) have revealed another interesting correlation. Planets with radii smaller than approximately $1.8\text{-}2\,R_\oplus$ exhibit densities consistent with a rocky composition similar to Earth, while those with larger radii have lower densities indicating the presence of gaseous envelopes(Rogers, 2015). The radius gap seems to form a narrow transition region between a population of predominantly rocky super-Earths below the gap, and more volatile-rich, sub-Neptune type planets residing above the gap. These gaseous envelopes, primarily composed of hydrogen and helium (short: H/He), are susceptible to mass loss, especially the ones of lower-mass planets. In this mass-loss scenario, a planet can either hold on to some of its atmosphere and remain above the gap with somewhat larger radii due to the remaining gaseous envelope, or, if the mass loss is too extreme, drop below the gap as a bare rocky core. While giant impacts (e.g. Liu et al., 2015; Wyatt et al., 2020) can account for some mass loss, the two dominant physical processes that have been proposed for explaining the radius gap are photoevaporation and core-powered mass loss.

Photoevaporation is an externally induced mass-loss mechanism that occurs when the high-energy radiation (X-rays and extreme UV) from the host star heats the upper planetary atmosphere and launches a hydrodynamic outflow. This mechanism has been studied extensively (e.g. Watson et al., 1981a; Güdel, 2007; Owen & Jackson, 2012a; Lopez et al., 2012), and can explain the hot Neptunian desert at very short orbital periods (≤ 3 days), where irradiation levels and thus mass-loss rates are extreme, as well as the radius gap. Additionally, core-powered mass loss, driven by the internal luminosity of the cooling
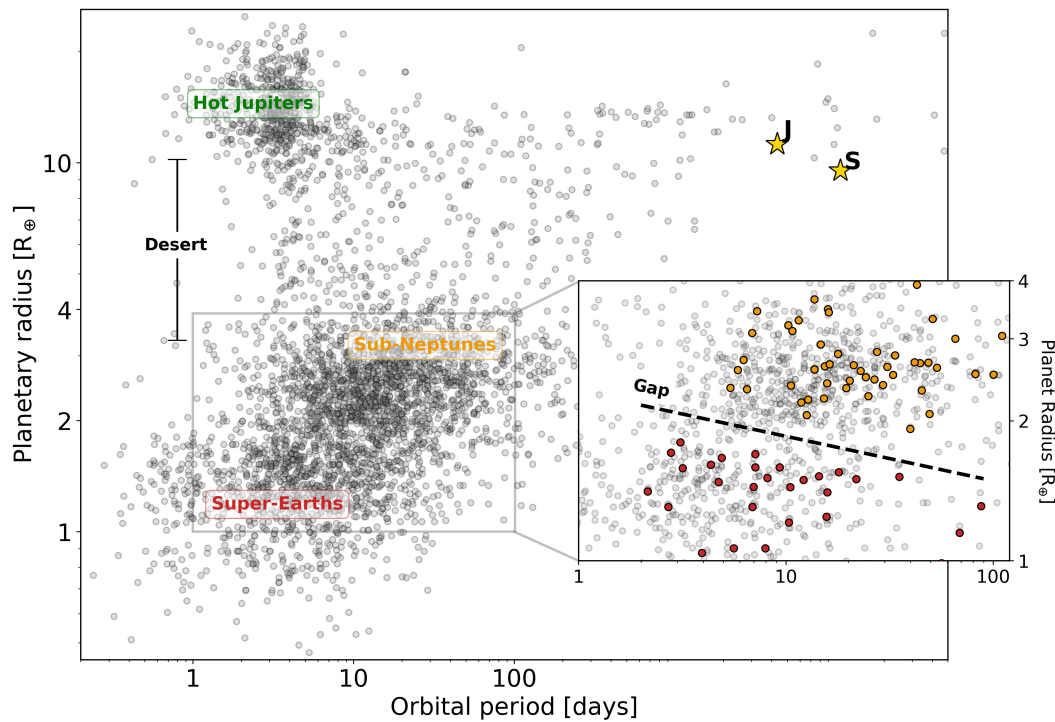
Figure 2.4: Distribution of planetary radius vs. orbital period of roughly 4,000 exoplanets with measured radii. Hot Jupiters conglomerate at the top left of the plot, having the largest radii at orbital periods of less than a few days. Close-in, low mass planets, i.e. sub-Neptunes and super-Earths, are dominant in numbers, and populate the lower left corner of the plot. The Neptune desert, a region at intermediate radii and very short orbital periods, is labeled, together with the locations of Jupiter and Saturn (stars) for reference. The zoom-in shows a subsample of planets with a radius precision better than 10% in gray, together with small astroseismic sample with highly accurate stellar parameters determined from asteroseismology (Van Eylen et al., 2018b) in red and orange. The red data points represent planets which have been identified to belong to the rocky super-Earth population below the radius gap, whereas the planets in gold belong to the volatile-rich sub-Neptune class above the radius gap. The approximate location of the small-planet radius gap or valley is indicated by the black dashed line. The data shown in gray has been taken from NASA's Exoplanet Archive (https://exoplanetarchive.ipac.caltech.edu/, accessed on 13. June 2023).

planetary core, is a mostly internally-driven mechanism to explain observed exoplanet population (e.g. Ginzburg et al., 2018; Gupta & Schlichting, 2019). In contrast to photoevaporation, this mechanism acts on much longer Gyr timescales. Recently, gas accretion during the gas-poor phase of disk evolution (Lee et al., 2022), and the existence of water- and ice-worlds (e.g. Zeng et al., 2019; Venturini et al., 2020) have also been put forth as mechanisms to explain the radius dichotomy of close-in exoplanets.

The combination of gaseous envelopes around lower-mass planets (and thus a much smaller gravitational pull than Jupiter-mass planets), makes them prone to escaping. This has led to the detection of planetary tails composed of escaping gas, primarily through the hydrogen Lyman-alpha line (e.g Ehrenreich et al., 2015; Bourrier et al., 2018; Zhang et al., 2022), and more recently through helium absorption (Spake et al., 2018; Mansfield et al., 2018; Damasso et al., 2023). The method used to detect material escaping from the planetary atmosphere is called transmission spectroscopy, and is based on detecting the distinct absorption features present in the stellar light as it passes through the planetary atmosphere just when the planet transits in front of its host star. It enables the investigation of the atmospheric conditions of exoplanets, detect outflow signatures and constrain the chemical composition of the atmospheres of transiting exoplanets. Studying outflows in young planetary systems is particularly intriguing, as it can provide insights into planetary evolution models and help distinguish between different mass-loss processes. Although detecting and characterizing young planets is challenging due to the high activity levels of their host stars, dedicated campaigns have increased the number of known young planets, offering valuable insights into the role of photoevaporation in early exoplanet evolution. Noteworthy systems with detected outflow signatures include GJ 436b, which shows an extended egress absorption of a few tens of percent, indicating the probable existence of a comet-like tail trailing the exoplanet (Kulow et al., 2014; Ehrenreich et al., 2015), and K2-100b, a highly irradiated planet at the border of the hot Neptunian desert, estimated to be around 750 million years young. Ongoing evaporation is causing a significant reduction in the size of this planet over the next few billion years (Barragán et al., 2019a; Gaidos et al., 2020). Atmospheric escape has also been detected in four young (less than 1 billion years) mini-Neptunes. The measurements indicate the loss of the remaining hydrogen-rich atmospheres for all the planets (Zhang et al., 2022, 2023). All these findings suggest that photoevaporation is an efficient mechanism for stripping primordial gaseous atmospheres of planets orbiting Sun-like stars, transforming planets from gas-rich mini-Neptunes above

the radius gap into rocky super-Earths below the gap. Details on exoplanet mass-loss mechanisms and photoevaporation will be given in Sec. 3.2.

3 Formation and evolution of planetary atmospheres

To investigate the origin and evolution of exoplanetary atmospheres, it is important to have some comprehension of the initial stages of exoplanet formation. Young planets are still warm from their formation, and their atmospheres might not have cooled and settled yet. This makes them vulnerable to internal and external factors like atmospheric mass loss, which can influence individual systems and shape the exoplanet population we observe today. After highlighting some basic planet formation details in the first part of this chapter, the second part addresses different mechanisms for loosing material from the planetary atmosphere to space. The main focus is on hydrodynamic escape, a mass-loss process driven by the high-energy irradiation from the host star, and of particular importance for young, close-in exoplanets around active stars.

3.1 Young planets and their primordial planetary atmospheres

Depending on the formation location and conditions in the protoplanetary disk, there are different channels for planet formation. The scenario of interest for this thesis is the accretion of nebula-based hydrogen/helium-rich gas envelopes. For planets within roughly 0.3 au around Sun-like stars, this is the favored formation scenario (e.g. Rafikov, 2006; Ikoma & Hori, 2012). Starting with the coagulation of dust grains, followed by the accretion of planetesimals, a rocky planetary core, often assumed to be of Earth-like, iron-silicate composition, grows in size and mass (see e.g. Venturini et al., 2020, for the accretion of super-Earth cores). In this core-accretion model, such a core, if below a critical mass, is not massive enough for runaway gas accretion and thus the formation of a gas-giant-like planet. Instead, the accreting protoplanetary core can capture some amount of nebula gases (from a few % up to a few 10% of the total planetary mass), forming a hydrogen-rich proto-atmosphere around the rocky core. Numerical studies suggest that the accretion of planetesimals with a mass just over $\sim 0.1\,M_\oplus$ is enough to capture large amounts of nearby nebular gas from the protoplanetary disk, forming a dense and optically thick hydrogen/helium-rich atmosphere (e.g. Ikoma et al., 2000). Early terrestrial solar system planets, including Earth and Venus, are also thought to have accumulated a thick layer

of hydrogen gas from the planetary nebula during their formation phase, and to later have lost their initial, or also called primordial atmosphere due to various escape processes (further discussed in Sec. 3.2).

In current simulations of planetary formation and evolution, the first ~100 Myr of planetary evolution are influenced by the assumed initial conditions. In particular, the initial entropy (a measure of the thermodynamic state of the planet's interior) at the end of the accretion phase governs, for a given mass, the subsequent evolution of a planet's luminosity and radius. Simulations (such as those presented in Mordasini et al. (2012a)) indicate that during the age range of 10 to 50 million years, planets tend to move from a wide distribution of radii at a given mass towards a more uniform mass–radius relationship (like the ones shown in Fig. 2.3), and continue their gradual cooling and subsequent contraction afterward.

Planets which are formed under the so-called 'cold start' scenario ('start' referring to the beginning of the cooling, i.e. the end of the accretion phase), meaning with low initial entropy, are not expected to undergo significant radius changes as they age. For example, the young-ish planet K2-100b already follows the mass–radius relationship of older planets, despite its moderately young age of approximately 700 Myr (Barragán et al., 2019b). Only recently, it was discovered that the ~20 Myr-old Saturn- to Jupiter-sized infant planet V1298 Tau b has a density comparable to that of the gas giant planets in our solar system and other known giant exoplanets that are considerably older. This might suggest that at least some giant planets contract and evolve even more rapidly than anticipated, which poses a challenge to current models of planetary evolution (Barragán et al., 2019c).

In contrast, infant planets with ages of a few 10s of Myr, which formed under the so-called 'hot start' scenario, where accretion energy is not dissipated efficiently, end up with higher envelope entropy and effective temperature once accretion stops (Fortney et al., 2007; Baraffe et al., 2008). As a consequence, these planets possess enlarged, inflated radii and low densities due to their unsettled nature and leftover heat from the accretion process. Their warm and puffy gaseous atmospheres then cool and contract under gravity, leading to a gradual decrease in the planetary radius over several hundred million years. An example is the ~20 Myr-old massive Jupiter-type planet β Pic b, which shows indications of having been formed under 'hot start' conditions (Snellen & Brown, 2018a). For lower-mass planets, structural evolution models predict that due to the short cooling timescale at infant ages, enlarged, low-mass planets undergo a rapid cooling and subsequent contraction phase, which erases any differences resulting from the choice of initial entropy by ~10-100 Myr (Marley et al., 2007;

Lopez & Fortney, 2014a; Howe & Burrows, 2015). These low-mass planets, however, still host extended envelopes after the initial contraction phase, which then cool and thermally contract over the next Gyr. This means that planets are largest when they are young, and thus have a larger cross-section to interact with the stellar environment, for example through the absorption of high-energy radiation (for more details see Sec. 3.2.1).

It is commonly assumed that planets form around the time the star is born, and thus planet and host star age hand-in-hand. A lot is happening to a planet in its early stages, where enlarged and puffy atmospheres might be particularly vulnerable to external forces. This makes young planets highly intriguing – they can provide insights into the processes that lead to the formation of mature planetary systems like our own. For reference, in this thesis context, young planetary systems have ages less than a Gyr, with infant systems having an age younger than $100\,\mathrm{Myr}$.

3.2 Escape of planetary atmospheres

It has been recognized decades ago that atmospheric escape plays a crucial role in the evolution of terrestrial planets within our own solar system (for a review see Tian, 2015). After the loss of their primordial atmospheres, which were captured from the nebula during formation, solar system terrestrial planets underwent different evolutionary paths. Venus, for example, due to its proximity to the Sun, has likely undergone thermal atmospheric escape and lost its oceans rapidly. A wet middle atmosphere, i.e. the presence of water vapor in the thermosphere, is ideal for the dissociation of water though UV photons and the subsequent escape of the light hydrogen, possibly even dragging heavier species like oxygen along (Kasting & Pollack, 1983; Kumar et al., 1983; Chassefière, 1997). Mars, with its low gravity, most likely never built up a dense atmosphere during the first few $100\,\mathrm{Myr}$ after its formation, and probably experienced gradual erosion due to the cumulative effect of numerous small impact events (Melosh & Vickery, 1989). Even today, the thin atmosphere of Mars still suffers measurable atmospheric mass loss though Jeans escape (see Sec. 3.2.1 for details on this process). For the Earth, hydrodynamic escape models suggest that the early atmospheric hydrogen concentration could have been of the order of a few percent or greater (e.g. Tian et al., 2005), before having been eroded via hydrodynamic escape processes driven by the young and active Sun. These examples illustrate that different atmospheric escape processes have shaped the terrestrial planets in the solar system over the course of their lives.

Specifically, non-thermal escape processes have played a role in the evolution of the atmospheres for Venus, Earth and Mars, and still are in action today. These processes became more important after the first few 100 Myr, where the Sun was no longer saturated in X-ray and extreme ultraviolet (EUV) and planetary irradiation levels became comparable to the present-day solar values.

For exoplanets, of which many are in even closer orbits (P < 100 days) around their host stars, the presence of gas-rich envelopes has posed the question about the stability of their atmospheres (e.g. Koskinen et al., 2007a). The observation of extended hydrogen clouds around transiting planets, like the hot Jupiter HD209458b (Vidal-Madjar et al., 2003), have led to the development of models to understand the hydrodynamic escape from hot Jupiters (Yelle, 2004; Tian et al., 2005; García Muñoz, 2007; Murray-Clay et al., 2009a), and later from lower-mass hot and warm sub-Neptunes (Lopez et al., 2012; Lopez & Fortney, 2013a; Owen & Wu, 2013; Jin et al., 2014). In these close-in planets, the intense X-ray and EUV (together: XUV) radiation from the central star impinging on the upper planetary atmosphere dissociates the hydrogen present in molecular form and leads to the ionization of the remaining atomic hydrogen (e.g. Yelle, 2004). The thermosphere is heated to several thousand degree Kelvin, causing the upper atmosphere to expand significantly, and thus making it only weakly gravitationally bound. As a consequence, the gas can escape rapidly from the planet's gravitational well in the form of a hydrodynamic outflow.

While non-thermal escape processes, like the interaction of the atmosphere with charged particles in the solar/stellar wind, can have a significant impact on the erosion of planetary atmospheres at later ages (like it is the case for solar system bodies today (e.g. Lammer et al., 2008; Tian, 2015)), thermal escape mechanisms, in particular hydrodynamic escape or (photo-)evaporation, are expected to dominate the atmospheric mass loss early on (when stars emit the highest XUV fluxes), and/or for close-in planets (under intense stellar XUV irradiation). Thermal escape processes are discussed in more detail in the following Sec. 3.2.1, and a brief overview over non-thermal escape processes is given in Sec. 3.2.2.

3.2.1 Thermally driven mass loss

Thermal escape processes are in action when the planetary atmosphere undergoes significant heating from the host star. This is especially true for close-in planets in harsh irradiation environments, and/or planets around young stars, which are particularly active and emit large amounts of high-energy photons. A widely used parameter with regard to thermal atmospheric escape is the Jeans

parameter. It is given by the ratio of the gravitational binding energy of a gas particle over the thermal energy of the gas (see e.g. Chamberlain & Hunten, 1987; Fossati et al., 2017):

$$\lambda = \frac{GM_{\mathrm{pl}}\mu m_{\mathrm{H}}}{k_{\mathrm{B}}TR_{\mathrm{pl}}} \tag{3.1}$$

where G is the gravitational constant, k_{B} the Stefan-Boltzmann constant, M_{pl} and R_{pl} the mass and radius of the exoplanet, respectively, and μ the mean particle mass in units of the mass of a hydrogen atom (m_{H}). The temperature T is not the planetary equilibrium temperature, but rather the temperature at the exobase, which is much higher due to the upper atmosphere being heated by high-energy photons. The exobase is a narrow transition region from a collision-dominated to a basically collisionless atmosphere, assuming conditions of hydrostatic equilibrium. The collision-dominated region below the exobase, where the bulk of ionization and dissociation of molecules takes place, is known as the thermosphere, and the collisionless region above the exobase is called the exosphere (García Muñoz, 2007; Koskinen et al., 2007b).

For large λ, the gas layer is tightly bound and thermally driven escape happens on a molecule-by-molecule basis, better known as Jeans escape. With decreasing λ, thermally driven escape starts to occur in the form of an organized, radial outflow, referred to as hydrodynamic escape. For $\lambda \leq 1.5$, the internal energy of the gas molecules is close to or starts to exceed their gravitational binding energy, and the gas simply flows away from the planet in a hydrodynamic blow-off state.

Jeans escape

Jeans escape is an atmospheric mass-loss process that is governed by the thermal motions of gas particles in the upper planetary atmosphere and occurs when λ is large, gas particles are tightly bound to the planet, and/or have relatively small thermal energies, i.e. low thermal speeds, compared to their gravitational potential energy. If one assumes a collisional, isothermal gas layer in hydrostatic equilibrium, the temperature determines the average velocity of each gas particle and the particles will follow a Maxwell velocity distribution. If the thermal energy, i.e. temperature, in the upper atmosphere is high enough, a small fraction of individual gas particles in the high-velocity tail of the velocity distribution will achieve speeds greater than the escape velocity at the exobase, and are able to break free from the gravitational pull of the planet and escape into space (Jeans, 1925). Light gases, such as hydrogen and helium, which

have low molecular masses, are particularly susceptible to this kind of mass loss. Jeans escape is a process that leads to a gradual loss of atmospheric gases over long periods of time, especially in cases where the exoplanet is exposed to intense stellar radiation or other heating mechanisms that elevate the temperature of the upper atmosphere.

Hydrodynamic escape or photoevaporation

As opposed to Jeans escape, where the upper atmosphere is in hydrostatic equilibrium, a second regime of thermally driven atmospheric escape can be reached. If temperatures are high and the bulk of particles below the exobase have energies exceeding their gravitational potential energy, a hydrodynamic wind is launched, and the atmosphere can reach a blow-off state (Parker, 1958; Öpik, 1963; Lammer et al., 2003). As high stellar X-ray and EUV (XUV) fluxes ionize particles and deposit energy in the upper atmosphere, the gas is heated and starts to expand. When light gas particles, like hydrogen and helium, move upwards and are further accelerated, they can reach escape velocities. This scenario occurs if the bulk of the gas below the exobase moves fast enough to reach supersonic speeds. As the gas streams upwards and radially outwards, it drags the remaining atmosphere along, launching an outflowing wind. Hydrodynamic escape can be a very efficient mass-loss mechanism because the whole exosphere evaporates: as long as the heating continues, the upper atmosphere will be refilled by the upwards flowing gas of the dynamically expanding region below the exobase, and will be subsequently lost to space. To sustain such substantial hydrodynamic escape, a significant energy source at a specific altitude is necessary. While this energy can be supplied by X-rays (~10 – 100Å), especially in the case of young active stars (Owen & Jackson, 2012a), it is primarily the stellar extreme ultraviolet emission (~100 – 912 Å) that provides the radiation power necessary for dissociating and ionizing hydrogen (912Å is the Lyman limit, i.e. the wavelength threshold below which photons absorbed by neutral hydrogen will ionize hydrogen in the ground state) in planetary atmospheres (Murray-Clay et al., 2009a; Sanz-Forcada et al., 2011a; Wang & Dai, 2018a). The overall atmospheric mass loss is influenced by the combined input of both X-rays and EUVs (<912 Å), since they both contribute to the heating of the upper atmosphere and consequently drive the escaping wind.

In 1981, Watson et al. (1981a) proposed that based on the basic principle of conservation of energy, the outflowing mass-flux should be "energy-limited", meaning that the upstream conductive heat flux must be balanced by the
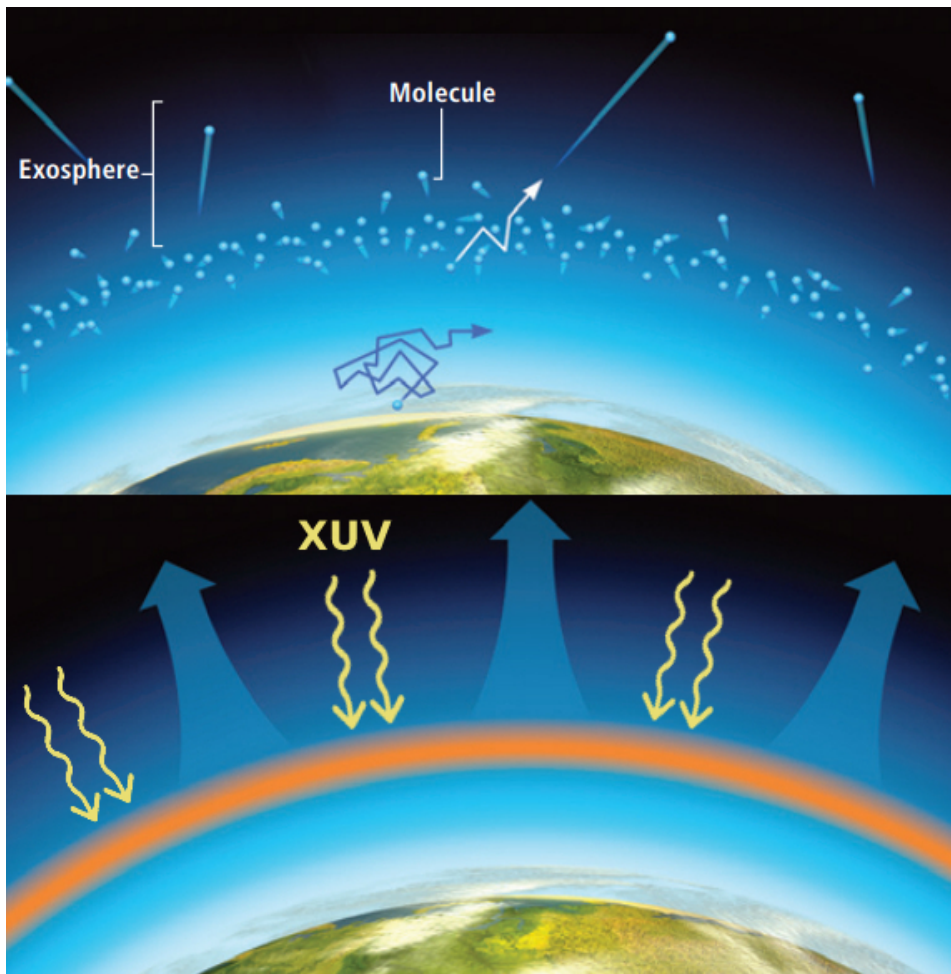
Figure 3.1: Illustration of the thermal escape processes. Jeans escape, where the fastest moving atoms and molecules escape one by one from the uppermost layer of the atmosphere, is shown on at the top, hydrodynamic escape at the bottom. In this process, which is also known as photoevaporation, the stellar high-energy photons impinging on the upper atmosphere cause significant heating (shown in yellow and orange). As a result, the gas expands, reaches escape velocities and escapes from the planet in the form of a hydrodynamic wind. Figure adopted from Catling & Zahnle (2009).

adiabatic cooling of the expanding gas. If one assumes that a planet absorbs a significant fraction of the incoming XUV photons at a thin layer at some radius, R_{XUV}, which is roughly where the optical depth of high-energy photons is equal to unity, then, in the absence of additional sources of heating or cooling, the incoming high-energy flux must be counterbalanced by the expansion work on the atmosphere, which ultimately lifts the material out of the planet's gravitational well. If during this process minimal energy is lost through cooling radiation and internal energy changes (Murray-Clay et al., 2009a), the mass loss is said to be in the energy-limited regime, and the mass-loss rate ($\dot{M}_{\text{Elim}}$) is then constrained by the deposition of stellar radiative energy and scales linearly with the incident flux of high-energy radiation (e.g. Lammer et al., 2003; Lecavelier Des Etangs, 2007):

$$\dot{M}_{\text{Elim}} = -\epsilon \frac{(\pi R_{\text{XUV}}^2) F_{\text{XUV}}}{KGM_{\text{pl}}/R_{\text{pl}}} = -\epsilon \frac{3\beta^2 F_{\text{XUV}}}{4GK\rho_{\text{pl}}}, \qquad (3.2)$$

where M_{pl} is the mass, ρ_{pl} the density, F_{XUV} the high-energy flux (X-rays and EUVs combined) received by the planet, and K a factor to take into account that the gravitational boundary of the planet is modified by the nearby host star. The efficiency of the heating is given by ϵ, and usually is estimated to take on values around 10 to 30% (e.g Owen & Wu, 2013; Salz et al., 2016a) for planets in the mass regime of sub-Neptunes. This factor takes into account that not 100% of the incoming high-energy radiation is converted directly into kinetic energy of the outflowing gas particles, but some energy is used for chemical reactions or stored in the form of thermal energy. Observations of a planetary X-ray transit (Poppenhaeger et al., 2013a) and hydrodynamic mass-loss simulations (e.g. Salz et al., 2016b) show that planetary atmospheres, when heated and expanded, make a planet appear much larger in size when observed in X-ray or EUV wavelengths compared to the optical. This increased absorption cross-section at high-energies is comprised in the β-parameter, which is defined as $\beta = R_{\text{XUV}}/R_{\text{pl}}$, where R_{pl} and R_{XUV} the planetary radii at optical and XUV wavelengths, respectively.

For close-in planets, another effect has to be taken into account. The host star modifies the planetary gravitational potential, making it a bit easier for the gas to escape compared to the absence of a nearby host star. The factor K encompasses the impact of Roche lobe overflow (Erkaev et al., 2007), i.e. that the gas does not need to escape to infinity, but merely to the Roche lobe of the planet. It can take on values of 1 for no Roche lobe influence and < 1 for planets filling significant fractions of their Roche lobes.

Theoretical studies have identified multiple sub-regimes of hydrodynamic escape in atmospheres dominated by hydrogen. These include the energy-limited regime described above, the radiation-recombination limited regime, and the photon-limited regime (e.g. Lammer et al., 2003; Murray-Clay et al., 2009a; Owen & Jackson, 2012a; Owen & Alvarez, 2016; Kubyshkina et al., 2018a). In case radiative losses dominate the energy budget as opposed to adiabatic cooling due to the expansion of the gas, as is the case for high EUV fluxes, Murray-Clay et al. (2009a) showed that there is a different scaling behavior for the mass-loss rates. In this so-called radiation-recombination-limited regime, where radiative recombination of hydrogen cools the gas efficiently, the mass-loss rate scales roughly with the square-root of the incident high-energy flux. In the photon-limited regime, the mass-loss rate is purely limited by the incoming flux of ionizing photons; this can happen for planets with very shallow gravitational potentials.

Recent observational evidence suggests that giant planets exhibit all three different regimes (Lampón et al., 2021). Each regime involves distinct physics related to the production and loss of neutral hydrogen, as well as the conversion of absorbed stellar radiation into work, which ultimately drives the evaporation and outflow process. Complex hydrodynamic upper atmosphere models are required to calculate the exact temperature and pressure structure of the atmosphere to determine in which hydrodynamic mass-loss regime the planet falls in. These models generally not only solve the system of hydrodynamic equations for mass, energy and momentum conservation, they also try to incorporate radiative transfer, thermodynamics, and photochemistry to account, for example, for photoionization, dissociation, recombination, and hydrogen-Lyα-cooling. While sophisticated models provide better estimates of hydrodynamic escape (e.g. Yelle, 2004; Kubyshkina et al., 2018b), they are complex and computationally expensive. For this reason, the parametrized versions of hydrodynamic mass loss are still used for first-order estimates or studies involving a large number of planets (e.g. Owen & Wu, 2013, 2017; Mordasini, 2020; Kubyshkina et al., 2018a).

The influence of a planetary magnetic field on the hydrodynamic wind is not fully understood, but studies suggest that the highly ionized outflow is coupled to the planetary magnetic field, if present. In simulations by Owen & Adams (2014); Arakcheev et al. (2017), a dipolar magnetic field suppressed the strength of the mass loss in hot Jupiters by an order of magnitude. In these simulations, only the magnetic field lines near the poles are open and allow outflow to occur. Further, interactions with the broader interplanetary environment should be taken into account, too. On larger scales, it is the

magnetized stellar wind that can interact with any planetary magnetic field and the outflowing ionized particles. An increasing number of these state-of-the-art simulations will further enhance our understanding of atmospheric mass-loss processes in action and the complex environment that close-in exoplanets are embedded in (see e.g. Harbach et al., 2021; Alvarado-Gómez et al., 2022).

3.2.2 Non-thermally driven mass loss

Non-thermal escape processes are well studied in the solar system (for a review see Tian et al., 2013; Tian, 2015). They come into play when the velocity of escaping particles does not depend on the temperature of the exobase, and are often related to the presence of ions and their interactions with electric and magnetic fields. An example is ion pick up, a mechanism in which neutral atoms and molecules in the exosphere, get ionized via photoionization, electron impacts or charge exchange with the ions (mostly protons) in the solar/stellar wind. If the planet is not protected by a strong magnetic field, or the upper atmosphere is dynamically extended beyond the magnetopause of the planet (e.g. in the early stages of a planet's life), the ions can be dragged along by the magnetized solar/stellar wind and potentially escape the planet's gravitational pull. Alternatively, neutral atoms can directly escape through a process known as atmospheric sputtering. Collisions between energetic neutral particles in the exosphere and solar/stellar-wind protons can induce a cascade of energy and momentum transfer events, which leads to particles being ejected through collisions or particles reaching velocities greater than the escape velocity and becoming unbound. The magnetic field of a planet, which is usually not known for exoplanets, plays an important role in the strength of different escape process, in particular those which involve interactions between charged particles. It can either enable or suppress escape processes (e.g. Terada et al., 2009). Iron pick up, for example, is efficient for planets like Mars or Venus, which are not protected by a strong magnetic field, and sputtering is mostly relevant for lower gravity planets like Mars with weak or absent magnetic fields. Photochemistry can also drive atmospheric escape processes. High-energy photons from the host star interact readily with molecules in the upper atmosphere, causing photodissociation and photoionization. The ionized particles can then undergo dissociative recombination, which produces suprathermal or "hot" atoms with high kinetic energies, which can escape the upper atmosphere. Such photo-chemical escape processes are most relevant to low-mass planets such as Mars (e.g. Lammer & Bauer, 1991).

3.2.3 Significance and effectiveness of atmospheric escape processes over time

In general, stellar XUV fluxes, as well as the strength of the plasma outflow from the host star (which includes the magnetized stellar wind, coronal mass ejections or the stellar energetic particle flow) control the efficiency of the various thermal and non-thermal atmospheric escape processes. Since the magnetic dynamo weakens as stars age and spin down, the efficiency of different escape processes is strong function of age and changes throughout a planet's life (Lammer, 2013). The evolutionary relevance and efficiency of different processes can be summarized in three phases. The first phase, which is also the most efficient mass-loss period, happens in the first few 100 Myr of a planets' life, when the host star is young and very active. A planet like the early Earth, for example, easily loses light elements like hydrogen and helium to hydrodynamic escape, which is powered by the high XUV irradiation levels. The fate of a planet in this formative stage depends on the XUV evolution of the host star (and main topic of this thesis), the orbital distance and gravity of the planet, as well as the constituents of its atmosphere. By the time planets are a bit more settled and stars have started their spin down and thus activity decrease, Jeans escape becomes more important. In this second phase, the upper atmosphere might still be expanded, but the outflowing gas does not reach escape velocity and thus there is no bulk mass loss anymore. The extended upper atmosphere can also interact with the stellar wind, and ion pick up processes can lead to some amount of mass loss. For low mass planets without strong magnetic fields, sputtering and suprathermal electrons from photochemical escape processes become relevant, too. Even magnetic fields sometimes cannot shield the planet from the eroding stellar wind, in particular in the early stages if the upper atmosphere is expanded and extends beyond the planetary magnetosphere. Then, the wind plasma flow from the central star drives non-thermal atmospheric mass loss. By the age of a few Gyr, a planet, like the Earth, enters the third and last phase. The XUV fluxes have decreased to moderate to low fluxes, similar to the present day Sun, making thermal escape processes much less efficient. All processes in principle work, but in moderate or negligible fashion compared to the period when the star was young and active. Planets considered in this thesis orbit their host star much closer than Earth, which means they receive high XUV fluxes not just at the infant stages, but up to a few Gyr. This makes hydrodynamic escape the dominant escape mechanism considered in all works included in this thesis.

4   Host star activity evolution

Planets and their atmospheres evolve hand in hand with their respective host star. They are influenced by the stellar environment they are embedded in, in particular, by the high-energy photons emitted from the stellar chromosphere and corona, which can ionize the hydrogen in a planet's upper atmosphere. This leads to a heating of the gas up to a few thousand Kelvin and the subsequent launch of a planetary wind that continuously ablates mass from the planetary atmosphere (see Ch. 3). Specifically, close-in, young planets, which orbit active host stars, are bombarded with huge amounts of X-ray and extreme ultraviolet radiation (e.g. Ribas et al., 2005a; Sanz-Forcada et al., 2010a; Jackson et al., 2012a). Young stars rotate more rapidly, which leads to increased magnetic activity and larger amounts of XUV emission, as compared to older stars. For example, a star like the sun emitted over 100-10,000 times more XUV photons at an age of 100 Myr than it does today. As discussed in Sec. 3.1, young planets host extended atmospheres and therefore absorb a more significant fraction of this high-energy flux, resulting in increased mass-loss rates (see Sec. 3.2 for details). To more accurately describe the mass loss that planets undergo early on, it is crucial to understand and properly model the evolution of the host-star activity, and with it the XUV emission, as stars and planets age.

Given the complexity of stellar activity and its evolution, this chapter aims to examine its main components individually, starting with a short introduction to the stellar magnetic dynamo (Sec. 4.1) – the driving force behind all stellar activity phenomena (like the high-energy emission). Since the magnetic dynamo is closely linked to the rotation of a star, the basic description of the stellar rotational evolution (Sec. 4.2) is given, before diving into how stellar activity manifests itself (Sec. 4.3). After tying rotation and activity together in the form of the rotation–activity relation (Sec. 4.4), the last section focuses on the details and complexity of stellar spin-down, including the branching of stellar rotation at young ages, which can have important implications for the erosion of planetary atmospheres (Sec. 4.5).

4.1 The stellar magnetic dynamo

Magnetic fields have a crucial impact on numerous physical processes important for the formation and evolution of stars and planets. They influence the collapse

of molecular birth clouds and their subsequent fragmentation into individual stars and planetary systems, and further play a role in the protostellar cloud, where magnetic fields influence the initial cloud's angular-momentum evolution, as well as the creation of winds, outflows, and jets. Even past this early, active formation phase, the stellar magnetic field, which is produced and maintained by the stellar dynamo, impacts a star's angular momentum evolution throughout its lifespan (see Sec. 4.2 for more details).

A star's magnetic field originates from complex dynamo processes arising in the stellar interior. It is believed that for stars similar to our Sun (or cool stars with outer convective envelopes in general), dynamo processes, resulting from the interaction of rotation and convection, give rise to the stellar magnetic field. It is the interplay between differential rotation and convection (inducing cyclonic turbulences and rotational shearing (Parker, 1955)) in the conducting plasma of the stellar convective envelope, which lead to the production, amplification, and maintenance of a steady magnetic field, continuously converting the kinetic energy of the plasma motion into magnetic energy. By current understanding, these mechanisms are in action at the interface layer between the radiative and the convection zone, the so-called tachocline, a transition region, where a star like our Sun changes from having a solidly rotating, radiative interior to having a differentially rotating, convective envelope (Landstreet, 1992; Covas et al., 2005; Donati & Landstreet, 2009). These processes, which lead to the creation and transformation of the magnetic field, are known as the $\alpha - \Omega$ tachoclinal dynamo (Steenbeck & Krause, 1969). Stellar rotation (in conjunction with convection) plays a key role in the dynamo process, with slower rotation resulting in weaker magnetic fields and vice versa.

4.2 Stellar angular momentum loss and rotational evolution

The stellar dynamo is powered by the rotation of a star, while the magnetic field, which it produces, is in turn responsible for the rotational evolution of a star. As a result of the interaction between a star's magnetic field and its magnetized stellar wind, angular momentum is removed. It is the braking torque of the stellar wind, which is magnetically coupled to the stellar surface, that leads to a slowing down of the rotation of most cool stars once they have reached the main sequence. In simple terms, it is the outwards flowing plasma that carries away angular momentum, causing the star to rotate slower and

slower over time (Parker, 1958; Schatzman, 1962; Weber & Davis, 1967; Mestel, 1999). This aligns with our qualitative understanding that the majority of cool stars, including the Sun, exhibit slow rotation rates. There are, however, two exceptions to this pattern: close binary systems, where spin angular momentum is continuously replenished from the orbital reservoir through tidal coupling, and young stars – of particular interest for this thesis – which have not yet dissipated their initial angular momentum.

During their early stages of evolution, stars undergo a complex history of rotational changes (Bouvier, 2007). Young stars, which form within a collapsing molecular cloud, inherit large amounts of angular momentum during their formation process. In the first million years of the pre-main sequence phase, a star is very efficient at expelling angular momentum, mainly due to processes related to magnetic star-disk interaction like disk-locking or accretion-driven winds (see Bouvier et al., 2014, and references therein). Together with some amount of "classical" magnetic braking due to the stellar wind, this partly counteracts the spin-up of the star to due to the rapid contraction on the PMS, preventing it from reaching break-up velocities as would be expected from conservation of angular momentum alone (e.g. Hartmann et al., 1986; Rebull et al., 2004). The process of spin-up in young stars concludes once the star is eventually released from its disk (after roughly ten million years) and settles onto the zero-age main sequence. At this age, stars show a wide range of rotation periods spanning approximately 0.1 to 10 days (Rebull et al., 2016). Beyond this age, magnetized solar-type winds are thought to be the only source of angular momentum loss.

Skumanich (1972) was the first to observe that the average magnetic surface flux and the rotation rate of main-sequence (MS) stars were correlated. Based on his findings, he proposed a connection between the stellar activity level and the rotation rate, as a result of the interior dynamo mechanisms. He found that main-sequence stars decline in rotation period approximately by the inverse square root of their age ($P \propto t^{1/2}$, where P is the rotation period and t the stellar age), and that rotation and activity are related as $L_X \propto [v \times \sin(i)]^{1.9}$, where L_X is the stellar X-ray luminosity and a measure of the star's activity level, and $\sin(i)$ a proxy for the stellar rotation rate (i being the inclination axis of the star). This stresses that a star's magnetic field and its rotation continue to be interconnected: the presence of the magnetic field in combination with the magnetized stellar wind slow down rotation, but rotation is a key ingredient for fueling dynamo processes. Thus, magnetic activity and rotation decrease hand-in-hand as stars age. An example of the rotational evolution from the pre- to the main-sequence of a solar-type star, and the corresponding X-ray

emission (as a proxy of stellar activity), is shown in Fig. 4.1. Further details and complexities of the spin-down are discussed in Sec. 4.5.

4.3 Stellar activity as a manifestation of the stellar magnetic field

The stellar magnetic field is not only responsible for the angular momentum loss of a star, but also for the wealth of different activity phenomena present on the stellar surface and the whole upper stellar atmosphere. The phrase "stellar activity" serves as an inclusive term for all events linked to the existence of magnetic fields in cool stars, and encompasses phenomena that are more energetic, luminous, time-variable (with timescales ranging from minutes to years), or somehow distinguishable from a star's normal behavior (Schrijver & Zwaan, 2000). This includes, for example, dark and bright spots present at the stellar surface (Solanki, 2003; Berdyugina, 2005), prominences (Donati et al., 2000), stellar flares, coronal mass ejections, coronae and stellar winds (e.g. Davenport et al., 2019; Hazra et al., 2022; Alvarado-Gómez et al., 2022).

It is now well known that X-rays and EUV photons are produced in cool stars, including our sun. The first direct detection of solar X-rays was achieved in the course of a rocket flight in 1949 (Burnight, 1949), and since 1990, space-based missions like ROSAT, XMM-Newton, Chandra and eROSITA, have detected around 30,000 X-ray-bright sources of stellar origin (Freund et al., 2022). The need for space-based observations stems from the fact that the Earth's atmosphere is very efficient at absorbing in this short-wavelength regime, making the stellar high-energy emission inaccessible from the ground.

Above the stellar photosphere, the chromosphere and corona make up the outermost layers of the atmospheres of cool stars. The low-density plasma surrounding these stars reaches temperatures well above a million Kelvin in the corona – conditions in which the hot, highly ionized plasma can emit at high energies, mostly (soft) X-rays and extreme-ultraviolet photons of thermal nature (Güdel, 2004). Solar X-ray observations show that the structure and dynamics of the solar corona is dominated by the magnetic field and the magneto-convective energy present at the underlying photosphere (Testa, 2009).

Most of the X-ray luminosity of a star is emitted by the hot corona, of which the heating is believed to be closely connected to stellar magnetic activity phenomena (e.g. Erdélyi & Ballai, 2007), specifically a system of coronal loops. These semicircular coronal fields, as shown in Fig. 4.2, are the basic structures of
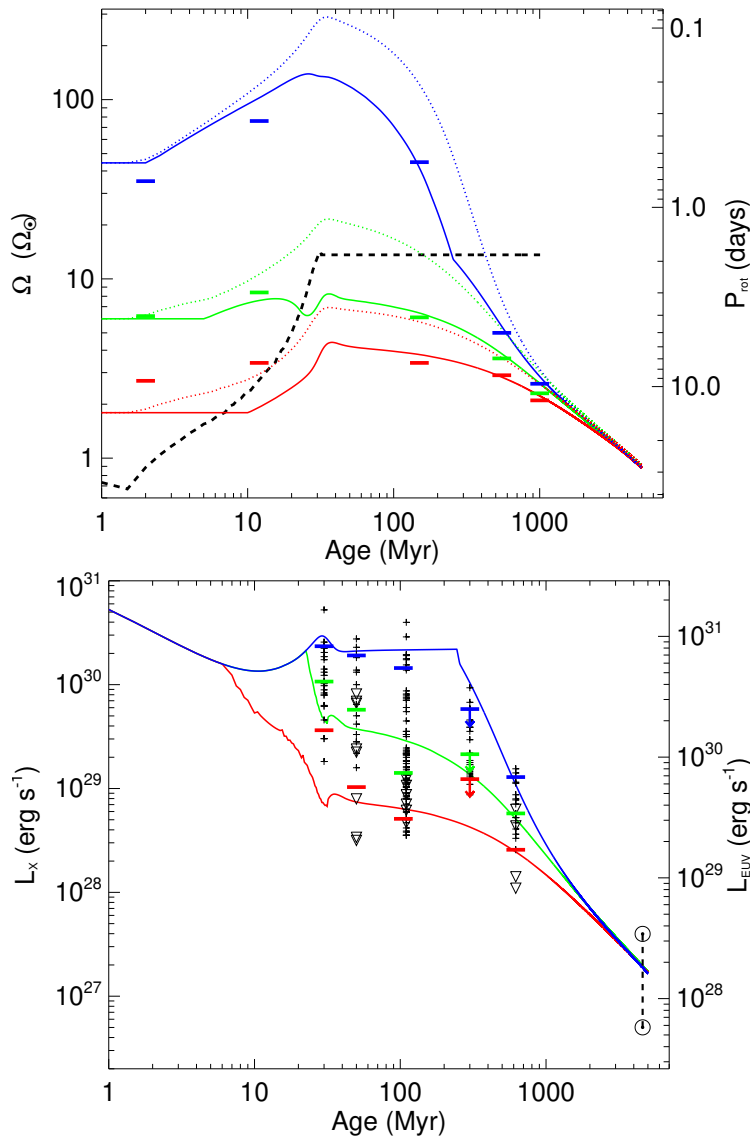
Figure 4.1: *Top*: Model tracks for the rotational evolution of a solar-mass star at the 10th (red), 50th (green), and 90th (blue) percentiles of the observed rotational distribution of young stars in open clusters. Shown here is the star's rotation rate, Ω, as a function of time. The spin-up on the pre-MS as well as spin-down on the MS can be seen. The difference between the red, green and blue tracks is the assumed initial rotation rate of the star. The models show that an initially faster rotating star (blue) will take longer for a significant spin-down to occur, causing it to stay in the saturated regime with a high activity level (i.e. X-ray emission) longer compared to an initially slower rotator (green and red).

Bottom: Predicted X-ray emission along each rotation track, together with observed X-ray measurements for single stars in several young open clusters. The solid horizontal lines represent the 10th, 50th, and 90th percentiles of the observed X-ray luminosity (L_X) distributions at each age. The two solar symbols at 4.5 Gyr represent the range of L_X for the Sun during the solar cycle. Plot is taken from Tu et al. (2015a), and will be discussed in more detail in Sec. 4.5.
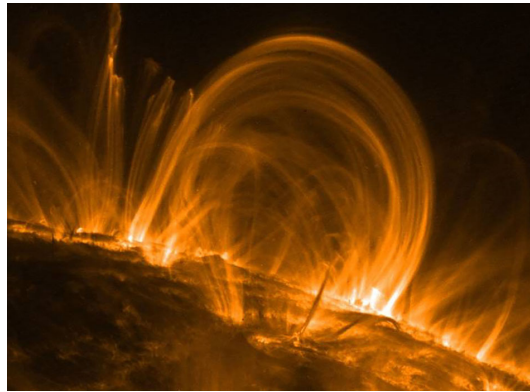
Figure 4.2: Coronal loops as observed by NASA's Transition Region And Coronal Explorer (TRACE) spacecraft. Credit: NASA/TRACE.

the magnetic solar corona, and usually emerge from concentrations of magnetic flux near active regions. The loops fill with and then trap the hot plasma, and thus are highly radiative sources (Engvold et al., 2019). The movement and shuffling of the photospheric foot-points of the coronal magnetic field lines by the convective motions beneath the photosphere are thought to contribute to the heating of the atmospheric layers above. The specific processes, however, which are responsible for heating the stellar corona to temperatures exceeding one million Kelvin via the magnetic field, remain a topic of ongoing debate. Two possible heating mechanisms are: (1) the Alfvén wave model, in which magnetohydrodynamic waves get produced and then transported and dissipated in the corona (e.g. Osterbrock, 1961; van Ballegooijen et al., 2011; Cranmer & Woolsey, 2015), and (2) the 'nanoflare' or field-line braiding model, in which magnetic stresses can build sheets of currents, which then dissipate via magnetic reconnection events (e.g. Parker, 1988). Regardless of the exact heating mechanism, observations demonstrate a distinct correlation between X-ray emissions and the surface magnetic field, both for specific structures on the Sun and for stars in general (Zhuleku et al., 2020).

While stellar X-ray luminosities and their distribution along the main sequence are now commonly accepted as the effect of different magnetic coronal heating mechanisms, stars that possess similar characteristics exhibit significant variations in their X-ray emissions when their rotation periods differ. Late-type stars can show intrinsic, and sometimes cyclic, X-ray variability, with X-ray emission levels covering more than four orders of magnitude (e.g. Coffaro et al., 2022).

4.4 The stellar rotation – activity connection

Since the first observational evidence in 1972, numerous studies have examined the relationship between stellar activity and X-ray emission, both manifestations of the stellar magnetic field, and the stellar rotation (e.g. Pallavicini et al., 1981; Randich et al., 1996; Patten & Simon, 1996; Pizzolato et al., 2003; Preibisch & Feigelson, 2005a; Penz et al., 2008; Wright et al., 2011a; Jackson et al., 2012a; Reiners et al., 2014). It is now known that stars follow the relatively well-constrained rotation–activity relation shown in Fig. 4.3, with faster rotation implying higher activity. Instead of rotation period, P, the Rossby number, Ro, is often used as the key parameter for quantifying the efficiency of the magnetic field generation. It is defined as the ratio of the rotation period of the star to the mass-dependent convective turnover time. It is basically a measure for how strong rotation and convection drive the magnetic field, taking into account the stellar structure via the convective turnover time. Observations have shown that activity correlates better with Ro than rotation period alone (e.g. Noyes et al., 1984; Kiraga & Stepien, 2007), or in other words, that cooler stars are relatively more active at a given rotation rate. This observation aligns closely with the theoretical prediction that convective turnover times are longer for stars with decreasing stellar luminosities.

Figure 4.3 (left) illustrates that stellar activity, as represented by $L_X/L_{\rm bol}$, can be divided into two regimes: (1) a horizontal regime at low Rossby numbers (or fast rotation periods below ∼10 days) on the left, and (2) a regime beyond the breakpoint around Ro ∼0.1, where stars follow a trend with smaller activity for larger Rossby numbers (in close connection to longer rotation periods). These two regimes are better known as the saturated and the unsaturated regime, respectively. Similar trends are observed for other activity indicators like Ca II H & K (e.g. Mamajek & Hillenbrand, 2008), other photospheric and chromospheric activity indicators (e.g. Fritzewski et al., 2020, 2021a), as well as the magnetic field strength, which plays a fundamental role in driving these phenomena (See et al., 2019). The exact cause of stars saturating in activity level below some critical Rossby number is not fully understood. Possible explanations are the saturation of the filling factor of active regions on the surface (Vilhu, 1984), a saturation of the dynamo itself (Blackman & Thomas, 2015), a centrifugal stripping of the corona at high rotation rates (Jardine & Unruh, 1999), or a transition from a convective dynamo to an interface dynamo (see Barnes, 2003a,b, for more details).

As stars age, they spin down and the Rossby number increases. Initially fast rotators (i.e. very active stars) desaturate, and eventually stars move into
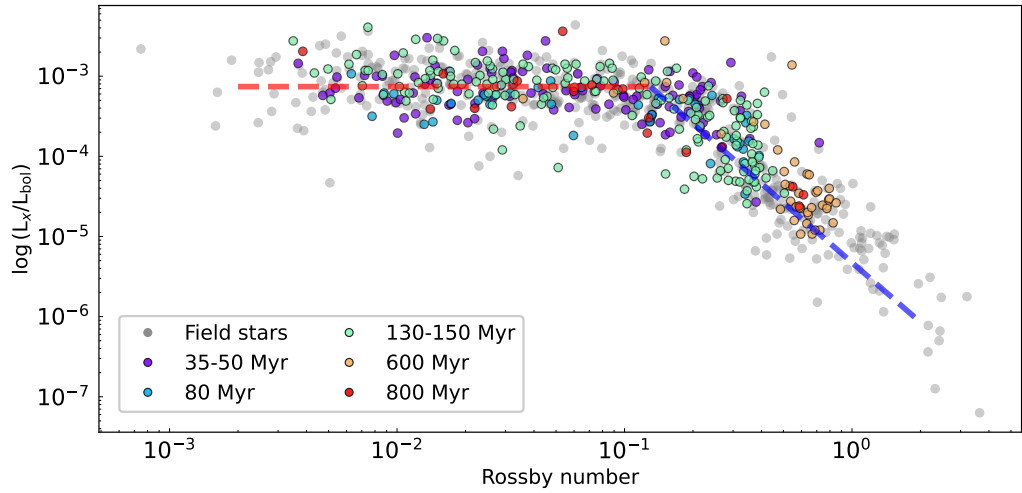
Figure 4.3: Rotation-activity diagram of mostly F, G and K stars illustrating the correlation between stellar activity and rotation. In the flat, saturated regime, L_X/L_{bol} is almost independent of the Rossby number Ro. Beyond the breakpoint around $Ro \approx 0.1$, L_X/L_{bol} – a proxy for stellar activity – is correlated with Rossby number, and decreases for slower rotators with larger Ro. The saturated and unsaturated regime and their corresponding fits are indicated in red and blue, respectively. In addition, young stars with ages below 1 Gyr are color-coded to highlight that there is an age-dependence in the rotation–activity relation. As stars age, they eventually spin down and undergo a decrease in activity, moving them out of the saturated regime. The data and the fits are taken from Wright et al. (2011b).

the unsaturated regime. The exact spin-down and activity evolution from the saturated to the unsaturated regime (and all the factors affecting it) is not fully understood yet, however, it is known that young stars of F, G and K spectral type drop out of the saturated regime within the first few hundred million years of their life. Details on the spin-down and its implications for the irradiation environment of exoplanets will be discussed in the next section.

4.5 Details of the stellar spin-down and why it matters for exoplanets

Observations have revealed that the spin-down of solar-like stars younger than 0.5-1 Gyr does not follow the simple $t^{1/2}$ Skumanich law. Instead, stars with similar mass (or spectral type) in the same open cluster show not only a wide distribution of rotation periods despite their common age (see Fig. 4.4), but also activity indicators (like L_X) which follow this trend (e.g. Wright et al., 2011b; Tu et al., 2015b; Gondoin, 2018). Stars in this young-age regime tend to align either on the fast or slow rotational branch, and the limited number of stars with intermediate rotation periods in young open clusters implies that once a star begins its spin-down process, it occurs relatively swiftly (Barnes, 2003c; Garraffo et al., 2018; Fritzewski et al., 2021b). When the classical magnetic braking eventually takes over, the wide range of initial rotation periods and L_X values observed in the first several 100 Myr converge into uniform rotation and activity levels by $\sim 1\,\mathrm{Gyr}$ (for solar-mass stars), and continue to decay hand-in-hand following a Skumanich-like law.

Models of stellar rotation evolution propose a relatively rapid decline in rotation at various ages or saturation times and can reproduce the observed scatter in rotation periods and X-ray luminosities below 0.5-1 Gyr (e.g. Soderblom et al., 1993; Stauffer et al., 1994) (see Fig. 4.1). In these models, long-term rotational changes are primarily influenced by stellar mass and initial rotation rate at birth (Matt et al., 2015; Tu et al., 2015b; Gondoin, 2018; Johnstone et al., 2021). Stellar mass influences the saturation time, with stars of earlier spectral types (and lower masses) remaining in the saturated regime for longer durations compared to stars of later spectral types (and higher masses). This behavior can be seen in Fig. 4.4, where the highest mass stars (in the bottom left corner) have all spun down significantly and settled on the slow-rotator sequence in the 300 Myr old cluster, whereas stars of similar mass are still on the fast rotational branch in the 150 Myr old cluster. This behavior is supported
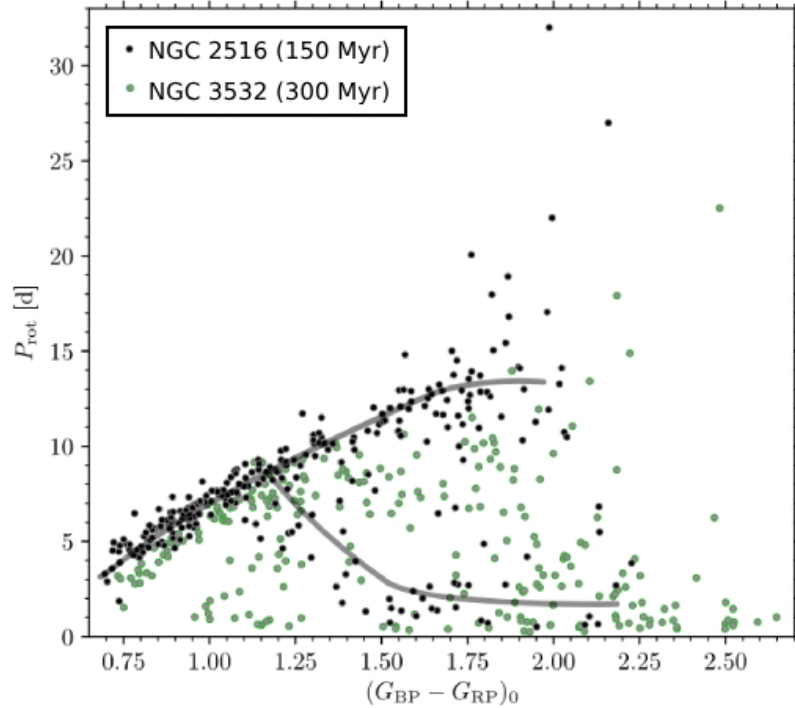
Figure 4.4: Color-period diagram, i.e. rotational period $P_{\rm rot}$ vs. color index (a measure for the stellar temperature), for two young clusters of different age. NGC 2516 (green) has an age of 150 Myr, and NGC 3532 (black) is slightly older with 300 Myr. The slow and fast rotator branch or sequence for NGC 3532 is illustrated by the gray lines. It is evident that the slow rotator sequence of NGC 3532 is shifted upwards compared to NGC 2516. The older cluster stars have had more time to spin-down and thus have longer rotation periods. In addition, there are still more fast rotators at higher stellar masses (in the lower left corner) in the younger cluster, which have not undergone their early rapid spin-down. In NGC 3532, late-G- and early K-type stars currently undergo a transition from their initial fast rotation to a transitional stage, whereas more massive, earlier-type stars have already evolved onto the slow rotator branch. The figure was adjusted from Fritzewski et al. (2021b).

by an increasing number of observations across F, G, K and M spectral types (e.g. Jackson et al., 2012a; Magaudda et al., 2020).

Rotational evolution models further predict that stars with similar mass exhibit a non-uniform spin-down, with some maintaining high activity levels for extended periods while others initiate spin-down and experience a decrease in activity already around the time of disk dissipation. Figure 4.1 shows three example spin-down histories, with different saturation timescales ranging from a few Myr to a few 100 Myr, for a star with the same mass, but different initial rotation period. In this particular model, it is the initial rotation period at birth that determines t_{sat}, with initially fast rotators staying active for longer periods of time as compared to initially slow rotators. An additional factor which has been suggested to contribute to the spin-down and its onset is the complexity of the magnetic field (Garraffo et al., 2018). Zeeman-Doppler imaging maps of young stars show complex magnetic morphologies that simplify into more nearly dipolar configurations as stars age, which supports the idea that a switch to a more simple magnetic field configuration could also initiate the onset of the spin-down. Further magneto-hydrodynamics (MHD) simulations indicate that the angular momentum loss of a star is much smaller for complex magnetic geometries than for simple dipole geometries (Garraffo et al., 2015). In stars with initially high rotation rates and active dynamos, this could stall the spin-down, and explain the diversity in the observed rotation periods for stars with similar mass and age until about 1 Gyr for solar-type stars.

To simplify the intricate activity history in the first few 100 Myr, the evolution of the X-ray luminosity is often assumed to follow a two-piece power law. Up to a certain saturation age, the X-ray luminosity is roughly a constant fraction of the star's bolometric luminosity and considered to be 'saturated' at a value L_{sat}, which, to first order, depends on stellar mass (Güdel, 2004). The saturation phase is then followed by a power-law decay phase with an exponent α on the order of -1/2 (Jackson et al., 2012a; Tu et al., 2015b). It is typically parametrized as:

$$\frac{L_{LH}}{L_{bol}} = \begin{cases} L_{sat} & \text{for } t \leq t_{sat} \\ L_{sat}(\frac{t}{t_{sat}})^{\alpha} & \text{for } t > t_{sat} \end{cases} \tag{4.1}$$

where L_{LH} represents the high-energy emission at time t, and t_{sat} the saturation or spin-down time, i.e. the age until which a star emits intense XUV flux at constant level before decaying (Owen, 2019). For solar-mass stars, this value is assumed to be around 100 Myr (e.g. Jackson et al., 2012a; Johnstone et al., 2021).

High-energy emission in this context represents both X-rays and EUVs, of which the latter has to be estimated based on scaling relations (Chadney et al., 2015; Johnstone et al., 2021). The reason for this is that, although X-ray observations are readily accessible using current space-based telescopes like XMM Newton, Chandra and eROSITA, no space-based telescopes for observing the part of the EUV spectrum ($\leq 400\,\text{Å}$), which is not absorbed by the interstellar medium, are currently in operation. The EUV component of the total stellar high-energy output is, however, very important, because EUV radiation can have a significant impact on a planet's mass-loss history. Since the stellar EUV flux declines slower compared to X-rays, their contribution matters, especially after the initial the X-ray-dominated saturation phase (King & Wheatley, 2021; Ketzer & Poppenhaeger, 2023).

Importance of non-uniform spin-down for exoplanet mass-loss studies

The complex behavior in the rotational and thus activity evolution in the first few 100 Myrs, as discussed at the beginning of this section, makes the parametrization given by Eq. 4.1, and used in many exoplanet mass-loss studies (e.g. Owen & Wu, 2017; Lopez, 2017; Rogers & Owen, 2021), an oversimplification. The onset of the activity decay can span from a few million years to several hundred million years for slow and fast rotators, respectively. Consequently, there exists a range of activity levels for young stars with similar mass, spanning up to two orders of magnitude. This spread can be seen in the bottom panel of Fig 4.1, where the X-ray measurements of different open cluster stars are marked in black. Due to the significant impact of high-energy radiation on the evolution of planetary atmospheres in this early age range, relying on a single radiation decay law is inadequate (e.g. Johnstone et al., 2015a; Kubyshkina et al., 2019a; Kubyshkina & Vidotto, 2021). As such, when estimating the future evolution of planetary mass and radius in young systems over time, it is crucial to consider the wide distribution and long-term evolution of the stellar activity within the first few hundred million years. All publications included in this thesis incorporate the mostly unknown spin-down and thus activity history of a star, and use a broad range of potential spin-down and stellar activity evolutionary tracks to model the high-energy irradiation of an exoplanet and its evolution with time.

Part II

The fate of young planets

5   X–ray irradiation and evaporation of the four young planets around V1298 Tau

K. Poppenhaeger, L. Ketzer, M. Mallonn

Abstract

Planets around young stars are thought to undergo atmospheric evaporation due to the high magnetic activity of the host stars. Here we report on X-ray observations of V1298 Tau, a young star with four transiting exoplanets. We use X-ray observations of the host star with Chandra and ROSAT to measure the current high-energy irradiation level of the planets, and employ a model for the stellar activity evolution together with exoplanetary mass loss to estimate the possible evolution of the planets. We find that V1298 Tau is X-ray bright with $\log L_X \, [\mathrm{erg\,s^{-1}}] = 30.1$ and has a mean coronal temperature of ≈ 9 MK. This places the star amongst the more X-ray luminous ones at this stellar age. We estimate the radiation-driven mass loss of the exoplanets, and find that it depends sensitively on the possible evolutionary spin-down tracks of the star as well as on the current planetary densities. Assuming the planets are of low density due to their youth, we find that the innermost two planets can lose significant parts of their gaseous envelopes, and could be evaporated down to their rocky cores depending on the stellar spin evolution. However, if the planets are heavier and follow the mass-radius relation of older planets, then even in the highest XUV irradiation scenario none of the planets is expected to cross the radius gap into the rocky regime until the system reaches an age of 5 Gyr.

5.1 Introduction

Exoplanets are very common around cool stars, with roughly one expected exoplanet per star (Dressing & Charbonneau, 2013). How exoplanets evolve over time is a key question to understand the range of exoplanet properties we observe today, and to determine how stable exoplanetary atmospheres can be over long time scales.

Making use of the ever growing numbers of known transiting exoplanets, Fulton et al. (2017b) detected a statistically significant gap in the regime of small exoplanets, manifesting as a valley or gap in the radius distribution at about 1.8 Earth radii. Using asteroseismic stellar parameters to refine the planetary radii, Van Eylen et al. (2018b) showed that this gap has a dependence on the orbital period of the planet; this supports an interpretation that many of the small exoplanets are indeed evaporated cores of former larger planets with gaseous envelopes. While some migration in orbital distance can also be expected for exoplanets, especially when the protoplanetary disk has not fully dissolved yet, the presence and slope of the gap suggests that evaporation may be the main driver for its existence. However, other mass-loss scenarios like core-powered mass loss could in theory also lead to the observed gap in the radius distribution (Loyd et al., 2020).

The main driver for atmospheric mass loss of exoplanets is thought to be the X-ray and extreme UV (together, XUV) irradiation the planet receives from its host star (Watson et al., 1981b; Lammer et al., 2003; Lecavelier des Etangs et al., 2004). This stellar emission is driven by the magnetic dynamo, which transforms the stellar rotation into the stellar magnetic field (see for example the review by Brun & Browning 2017). The magnetism manifests itself as a variety of directly observable phenomena called activity, such as coronal and chromospheric emission, flares, and starspots. It is well-studied that the magnetic activity decreases over time as the star spins down through the process of magnetic braking mediated by the stellar wind (see review by Güdel 2007)). By the time the star reaches solar age, its XUV emission has typically decreased by about three orders of magnitude.

This means that by the time we observe the majority of small exoplanets – typically around old main-sequence stars due to the better planet detectability when stars are inactive – the atmospheric evaporation which forms the radius gap is mostly finished. However, in recent years, the number of detected exoplanets in close orbits around young stars has grown rapidly. Such discoveries of small transiting exoplanets in young stellar clusters make it possible to study the XUV environment of exoplanets which are still at relevant ages for significant

atmospheric mass loss. Mainly fueled by the K2 and TESS missions, a growing number of young exoplanets have been discovered by now (David et al., 2016; Mann et al., 2016; Obermeier et al., 2016; Gaidos et al., 2017; Mann et al., 2017; Pepper et al., 2017; Livingston et al., 2018; Rizzuto et al., 2018; Newton et al., 2019a). The fact that their host stars have been identified as members of young stellar clusters gives an age tag to the star-exoplanet systems.

A particularly intriguing system is the four-planet system around the star V1298 Tau. This star is a member of Group 29, an association in the foreground of the Taurus-Auriga association, with a likely age of 23 Myr (David et al., 2019b). It hosts four transiting planets (David et al., 2019a) in orbits between 8 and 60 days with radii between 5.6 and 10.3 $R_\oplus$ (see table 5.1 for the system properties). The youth of this systems means that the stellar X-ray activity is high and can be measured precisely with present-day X-ray telescopes.

In this work, we report on spectrally resolved X-ray observations of the host star V1298 Tau and extrapolate the extreme UV and X-ray (XUV) irradiation received by the exoplanets in the system. We estimate the current mass-loss rates as well as the expected mass-loss evolution of the planets over time scales of Gigayears, using an energy-limited evaporation model that takes into account the possible stellar activity evolution tracks.

5.2 Observations and data analysis

The system was observed in X-rays by the ROSAT and Chandra space telescopes.

5.2.1 ROSAT data

The star V1298 Tau was observed with the ROSAT satellite in its ROSAT All-Sky Survey (RASS). ROSAT is an X-ray space telescope that was in operation from 1990 to 1994 (Trümper, 1982; Aschenbach, 1988), and performed the RASS for seven months during 1990 and 1991 in an energy band of 0.1-2.4 keV. The RASS consists of several scans of each part of the sky, with the individual visits of any given position being typically short, on the order of about 15–30 seconds, and accumulated exposure times of a few hundred seconds. V1298 Tau was observed in the RASS with PSPC-C detector.

We downloaded the archival X-ray data from the ROSAT archive[1]. We used the *xselect* software, which is part of NASA's HEASARC software package, to

---

[1]https://heasarc.gsfc.nasa.gov/FTP/rosat/data/pspc/processed_data/

Table 5.1: Properties of the V1298 Tau system as provided by David et al. (2019b,a).

Parameter	Value
Star:	
Spectral type	K0-K1.5
Stellar age [Myr]	23 ± 4
$M_\star$ $[M_\odot]$	$1.101^{+0.049}_{-0.051}$
$R_\star$ $[R_\odot]$	$1.345^{+0.056}_{-0.051}$
$P_{\rm rot}$ [d]	2.870 ± 0.022
Distance [pc]	108.5 ± 0.7
Planet c:	
P [d]	8.24958 ± 0.00072
R_P $[R_\oplus]$	$5.59^{+0.36}_{-0.32}$
a [AU]	0.0825 ± 0.0013
Planet d:	
P [d]	12.4032 ± 0.0015
R_P $[R_\oplus]$	$6.41^{+0.45}_{-0.40}$
a [AU]	0.1083 ± 0.0017
Planet b:	
P [d]	24.1396 ± 0.0018
R_P $[R_\oplus]$	$10.27^{+0.58}_{-0.53}$
a [AU]	0.1688 ± 0.0026
Planet e:	
P [days]	60^{+60}_{-18}
R_P $[R_\oplus]$	$8.74^{+0.84}_{-0.72}$
a [AU]	$0.308^{+0.182}_{-0.066}$
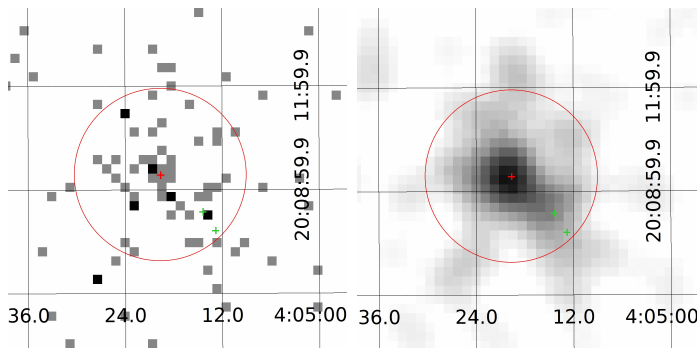
Figure 5.1: ROSAT PSPC X-ray image of V1298 Tau, taken in 1991. The position of V1298 Tau is marked with a red cross, the positions of the two nearby young stars are marked as green crosses. The PSF extraction region with a radius of 150″ is shown as a red circle. *Left:* X-ray image with linear brightness scaling, binned spatially to a bin size of 16″. *Middle:* Same, but smoothed by a Gaussian with a size of 4 bins. *Right:* Fitted 2-D Gaussians to the positions of the three stars; the emission is dominated by X-rays stemming from the position of V1298 Tau.
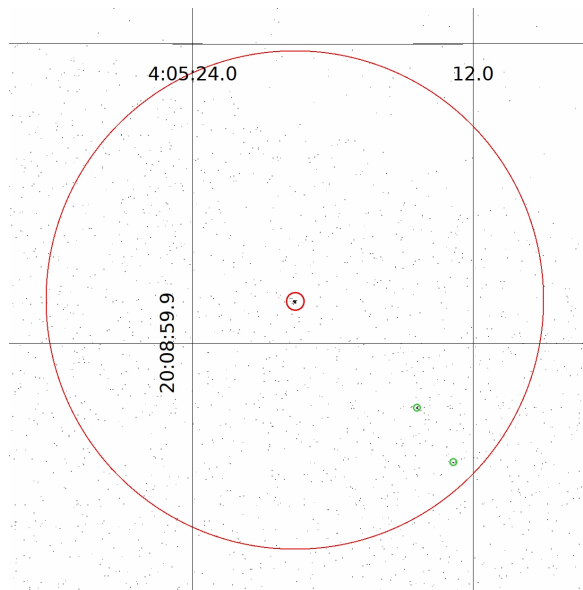
Figure 5.2: Chandra ACIS-S X-ray image of V1298 Tau, taken in 2019. The position of V1298 Tau is marked with a small red circle, the positions of the two nearby young stars are marked with green circles, and the size of the ROSAT PSF is shown as a large red circle.

analyze the data. Specifically, we used the associated exposure map to determine the accumulated exposure time collected at the position of V1298 Tau, which was 297 seconds. We then defined a circular source region at the nominal position of the star with an on-sky radius of 150″. This is motivated by the size of ROSAT's point-spread function (PSF), which varies considerably in width over the field of view; for accumulated RASS observations, a circular region of radius 150″ contains about 90% of the source flux (Boese, 2000). We also selected a background region free of obvious X-ray sources with similar exposure time and in the vicinity of the star. We opted for a background radius of 800″ to obtain a more accurate determination of the background count rate to be expected in the source region.

We proceeded by extracting the source and background region photon event lists and CCD spectra again for the source and background region using NASA's *xselect* data analysis software. The spectra were grouped to bins of at least five counts to avoid empty energy bins; the Cash statistic (Cash, 1979) was used for spectral fitting with the *Xspec* software.

5.2.2 Chandra data

Chandra (Weisskopf et al., 2000) carries as one of its instruments the Advanced CCD Imaging Spectrometer (ACIS). It provides high spatial resolution with a PSF FWHM of 0.42″ at boresight, i.e. much higher than the spatial resolution of ROSAT. Its nominal energy range is 0.245 to 10 keV.

We obtained Chandra data for V1298 Tau using the ACIS-S detector in non-grating mode with an exposure time of 1.04 ks on Nov. 17, 2019 (ObsID 22913). The image of the target was placed on one of the back-illuminated chips of ACIS-S, which provide slightly better energy resolution (approximately 70 eV FWHM for photon energies up to 2 keV) than the front-illuminated chips. ACIS-S provides a nominal energy sensitivity between 0.245 and 10 keV, but the sensitivity to X-ray photons below 0.8 keV has become very low over the life of the telescope.

We used the CIAO software version 4.11 to reduce the Chandra data, employing the standard data analysis steps outlined in the CIAO user guide. We extracted light curves and CCD spectra for V1298 Tau, as well as for two other stars in V1298 Tau's vicinity. We chose a source extraction radius of 2″ radius and a background region of 60″ radius. Again, spectra were grouped to bins of at least five counts.
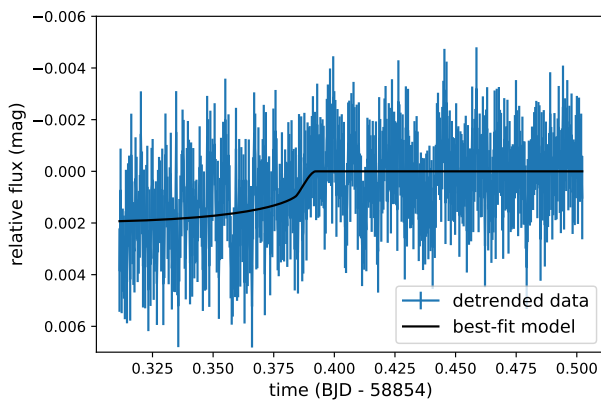
Figure 5.3: Optical light curve of V1298 Tau during the transit of its innermost planet c. The data show the STELLA/WiFSIP observation after removal of the detrending function. The solid black line shows the best-fit transit model, indicating a transit time earlier than predicted by about 3.5 hours.

5.2.3 Updated planetary ephemerides

While the transit depths of the four planets are small and are not expected to significantly alter the X-ray flux of the star during transits, we still report here the timing of the observations with respect to the orbital phases of the planets. As the system was observed with Kepler-K2 in 2015 (David et al., 2019b), the uncertainties in the orbital parameters have grown considerably since then. Typical transit midpoint uncertainties have increased to between three and five hours for observations in late 2019 (i.e. the epoch of the Chandra observation) for the innermost three planets. The outermost planets has an uncertain period measurement, so that its current ephemeris is unknown.

We have performed ground-based transit observations with the STELLA telescope (Strassmeier et al., 2004) and its wide-field imager WiFSIP (Weber et al., 2012) during the night of January 5, 2020 in order to cover a transit of the innermost planet *c*. The data were reduced following standard procedures employing a customised pipeline described in detail in Mallonn et al. (2015). In brief, we used the publicly available software SExtractor for aperture photometry, and selected the aperture size that minimied the scatter in the light curve. The same criterion was applied to chose the ensemble of comparison stars for differential photometry. The light curve was analyzed with the transit modeling tool JKTEBOP (Southworth et al., 2004), keeping all relevant transit parameters fixed to the values derived by David et al. (2019a). The parameters

free-to-fit were the transit mid time and the three coefficients of a second order polynomial over time for light curve detrending. We found that the transit occurred earlier than expected from the David et al. (2019a) ephemeris by about 3.5 hours. Therefore, our optical transit observation started only at about transit mid time and lacks the transit ingress (Fig. 5.3).

We calculate that the start time of the Chandra observation occurred about 5.5 hours after the updated transit egress of planet c. With respect to planets d and b, the Chandra observation also took place well outside of those transits, even taking into account the current midpoint uncertainty of up to 5 hours for these planets. The uncertainty of planet e's mid-transit time is so large that we cannot determine whether the Chandra observation overlapped with it or not.

The transit midpoint uncertainties for the three inner planets are of the order of one day for the ROSAT observing epoch. The accumulated ROSAT data covers a time period of almost 2 days, which may contain short exposures that were collected during a transit of one of the planets. We do not expect a significant influence of a potential planetary transit on the ROSAT or Chandra data, since the transit depths are small with less than 0.5% in the optical.

5.3 Results

5.3.1 X-ray detection of V1298 Tau

The ROSAT All-Sky source catalog lists a detected X-ray source near the nominal position of V1298 Tau (corrected for the known proper motion of the star to match the ROSAT observing epoch), with a spatial offset of $16.1''$ from its nominal position. This offset is not unusual given ROSAT's broad PSF. The detected count rate is 0.16 cps (Voges et al., 1999), and a cursory calculation using V1298 Tau's distance of 108.2 ± 0.7 pc (Gaia Collaboration et al., 2018; Bailer-Jones et al., 2018) and a counts-to-flux conversion factor of 9.423×10^{-12} erg/cm^2/count[2] yields an estimate of $L_X = 2 \times 10^{30}$ erg s^{-1}. This is close to the highest levels of X-ray luminosities observed for cool stars in general, and typical for very young stars like V1298 Tau (Preibisch & Feigelson, 2005b).

We queried the Gaia DR2 archive for nearby stars brighter than $G = 15$ mag within a search radius of $150''$ around V1298 Tau's position. Most of the returned targets are located at distances much farther away than our target, by

---

[2]Conversion factor derived according to Schmitt et al. (1995) using the hardness ratio of $HR_1 = 0.21$ from the ROSAT catalogue.

a factor of three or more; since field stars are intrinsically X-ray fainter than young stars, it is unlikely that those targets are origins for the detected ROSAT X-ray emission.

There are two other stars that have a similar distance as V1298 Tau, located at separations of $\approx 100''$ and $130''$ from our target. These stars are HD 284154 (Gaia DR2 51884824140205824) and Gaia DR2 51884824140206720, which we will abbreviate as GDR2-5188 in the remainder of this publication. The former was previously identified as a candidate member of the same young moving group as V1298 Tau (Oh et al., 2017). The latter is optically fainter and was not included in that candidate list, but has very similar distance and proper motion, so that all three stars may be members of the same young moving group, and as such intrinsically X-ray bright. We show an X-ray image of V1298 Tau's position taken with ROSAT in Fig. 5.1, indicating the position of all three stars.

We also show the Chandra X-ray image of the same position in Fig. 5.2, where the identification of the three stars is trivial due to Chandra's high spatial resolution. We find that V1298 Tau is clearly detected as the X-ray brightest source out of the three young stars, with a detected count number of 70 vs. 20 and 13 for HD 284154 and GDR2-5188, respectively. As a cursory check, we assume a hot coronal plasma temperature of about $10\,\mathrm{MK}$ as appropriate for young stars and estimate an X-ray luminosity of $1.1 \times 10^{30}\ \mathrm{erg\,s^{-1}}$ for V1298 Tau from the detected number of counts and the exposure time using HEASARC's WebPIMMS tool[3]; we will refine this estimate in the next section through spectral fitting. We can also confirm that there are no other X-ray sources detected with Chandra within the ROSAT PSF around V1298 Tau's position.

We can compare the X-ray brightness ratios between the three stars in the Chandra and ROSAT observations. For Chandra, this follows directly from the individually detected source counts. For the ROSAT data, we extracted an X-ray image with a spatial binning factor of 32; to guide the eye, we also extracted an image smoothed by a factor of four bins (see Fig. 5.1). We approximated the ROSAT PSF as a 2-dimensional symmetric Gaussian with standard deviation of $90''$, appropriate for the RASS PSF width, and fitted three Gaussians with free amplitude and centroids fixed to the positions of the three stars to the (unsmoothed) ROSAT image. The fit yielded that $\approx 90\%$ of the X-ray photons come from the PSF centered on V1298 Tau's position, 10% come from GDR2-5188, and the X-ray flux from the third star is compatible with zero.

---

[3]https://heasarc.gsfc.nasa.gov/cgi-bin/Tools/w3pimms/w3pimms.pl
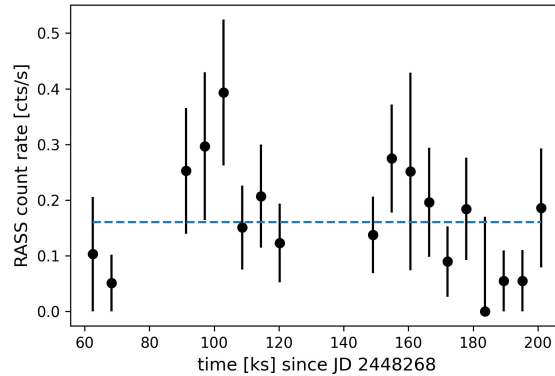
Figure 5.4: ROSAT X-ray light curve of V1298 Tau in 1991, typical exposure time is around 20 seconds. The blue dashed line represents the mean count rate.

The ROSAT brightness ratio between the stars of 90% / 10% / 0% in terms of the added X-ray brightness of all three stars is roughly comparable to the X-ray brightness ratios in the Chandra data, namely 68% / 19% / 13%, when one takes into account that the covered energy bands of the two telescopes are overlapping, but not the same, and the stars may display some intrinsic variability.

5.3.2 Temporal variability

ROSAT scanned the position of V1298 Tau repeatedly over about two days, with individual exposure times of a few tens of seconds. As Fig. 5.4 shows, the X-ray count rate in these individual exposures varies only mildly. No large excursions from the mean count rate, for example from flares, are observed.

Within the Chandra observation, again no large flares are observed for V1298 Tau or any of the two other young stars, see Fig. 5.5. The variability between time bins is consistent with uncertainties due to counting statistics.

The absence of large flares in either of the observations means that the overall X-ray brightness ratios of the stars should indeed be similar, except for differences due to the covered energy range of the telescopes.
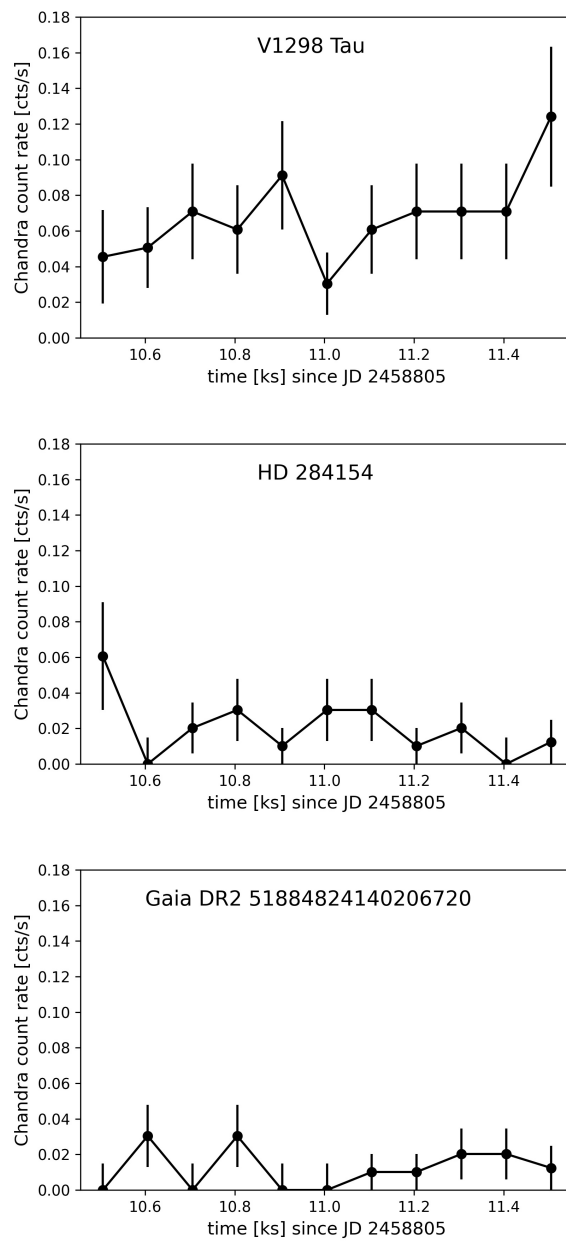
Figure 5.5: Chandra X-ray light curves of V1298 Tau and the two nearby young stars in 2019 with a time binning of 100 seconds.
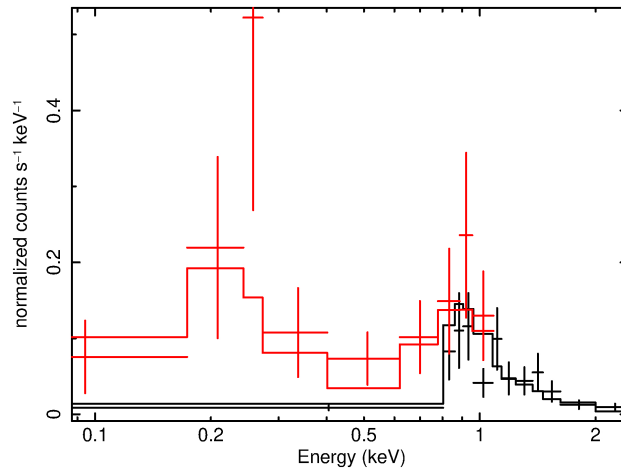
Figure 5.6: ROSAT (red) and Chandra (black) X-ray spectra of V1298 Tau. The data points are shown as crosses with 1σ vertical error bars per energy bin. The best spectral fit is shown as a red and black line for the data sets from the two telescopes, respectively.

5.3.3 Spectral fit and X-ray luminosity

V1298 Tau

To determine an accurate value for V1298 Tau's X-ray luminosity, we extracted CCD spectra from ROSAT and Chandra at V1298 Tau's position. The two data sets cover overlapping, but different energy ranges. ROSAT's low-energy boundary is 0.1 keV. While Chandra's low-energy sensitivity nominally extends down to 0.245 keV, in practice the effective area below 0.8 keV has become very low over the lifetime of the telescope. This means that any emission measure at low coronal temperatures and therefore softer photon energies than 0.8 keV are effectively not probed by the Chandra data. Conversely, ROSAT's high-energy sensitivity ends at 2.4 keV, while Chandra's extends to 10 keV. For our source it turns out that there are almost no photons detected above 2.4 keV even in the Chandra data.

We show both the ROSAT and Chandra X-ray spectrum of V1298 Tau in Fig. 5.6. The different sensitivities of the two instruments become apparent immediately.

We fitted the X-ray spectra with HEASRAC's Xspec software, using the APEC model appropriate for a coronal plasma (Foster et al., 2012) and solar-like abundances from Grevesse & Sauval (1998). The extinction towards V1298

Tau is low with $E(B - V) = 0.024$, translating to a low gas column density N_H of $\approx 1.6 \times 10^{20}\,\mathrm{cm}^{-2}$, which means that X-ray absorption by the interstellar medium is negligible for our target. We grouped the spectra to a minimum of five counts per bin and used the Cash statistic in Xspec's fitting process.

In fitting the two spectra individually, we found that the fitted flux in the energy range where both instruments have decent effective area (0.8-2.4 keV) is similar for both observations with $5.3 \times 10^{-13}\,\mathrm{erg\,s}^{-1}\,\mathrm{cm}^{-2}$ for ROSAT and $4.5 \times 10^{-13}\,\mathrm{erg\,s}^{-1}\,\mathrm{cm}^{-2}$ for Chandra. We therefore decided to fit both spectra simultaneously with the same model to gain better energy coverage for V1298 Tau.

The result of the combined spectral fit is listed in Table 5.2. The fitted coronal temperature is moderately high with a value of $kT = 0.78\,\mathrm{keV}$, corresponding to about 9 MK. The X-ray flux derived from the spectral fit is $9.2 \times 10^{-13}\,\mathrm{erg\,s}^{-1}\,\mathrm{cm}^{-2}$ for the native ROSAT energy band of 0.1-2.4 keV. The uncertainty in this flux was estimated with Xspec to be $\pm 1.0 \times 10^{-13}\,\mathrm{erg\,s}^{-1}\,\mathrm{cm}^{-2}$ i.e. about 11% of the flux (given is the 68% confidence interval). We extrapolated this to two other commonly used energy bands of 0.2-2 keV and 0.2-10 keV, yielding fluxes of $8.0 \times 10^{-13}\,\mathrm{erg\,s}^{-1}\,\mathrm{cm}^{-2}$ and $8.4 \times 10^{-13}\,\mathrm{erg\,s}^{-1}\,\mathrm{cm}^{-2}$, respectively. This places V1298 Tau's X-ray luminosity at $1.3 \times 10^{30}\,\mathrm{erg\,s}^{-1}$ for the 0.1-2.4 keV band (equalling $1.1 \times 10^{30}\,\mathrm{erg\,s}^{-1}$ and $1.2 \times 10^{30}\,\mathrm{erg\,s}^{-1}$ for the 0.2-2.0 keV and 0.2-10 keV bands, respectively).

Using the scaling laws between X-ray and extreme UV (EUV) emission of stars derived by Sanz-Forcada et al. (2010b) and the ROSAT energy band as the input X-ray band, we estimate the combined XUV (X-ray and EUV) luminosity of V1298 Tau to be $L_{\mathrm{XUV}} = 6.3 \times 10^{30}\,\mathrm{erg\,s}^{-1}$ for an EUV energy band of 0.01-2.4 keV.

The two young stars HD 284154 and GDR2-5188

The two nearby young stars do not have sufficient source counts in the Chandra observation to perform an adequate spectral fit for them. However, we can assess their hardness ratios and compare them to the hardness ratio of V1298 Tau. Specifically, we calculate the hardness ratio $HR = \frac{H-S}{H+S}$ with a soft band S of [0.5–1.5) keV and a hard band H of [1.5–5.0] keV.

V1298 Tau, HD 284154 and GDR2-5188 then display hardness ratios of -0.5 ± 0.1, $-0.8^{+0.3}_{-0.2}$, and -0.2 ± 0.3, respectively. These are consistent with each other within their uncertainties, indicating roughly similar spectral shapes. We therefore estimate the X-ray luminosities of the two fainter stars by scaling

Table 5.2: Spectral fitting results for V1298 Tau from the combined Chandra and ROSAT data.

Parameter	Value
kT [keV]	0.78 ± 0.07
EM $[\mathrm{cm}^{-3}]$[4]	$(4.5 \pm 0.4) \times 10^{52}$
$F_{\mathrm{X},\,0.1-2.4\,\mathrm{keV}}\ \left[\mathrm{erg\,s}^{-1}\,\mathrm{cm}^{-2}\right]$	$(9.2 \pm 1.0) \times 10^{-13}$
$F_{\mathrm{X},\,0.2-2\,\mathrm{keV}}\ \ \left[\mathrm{erg\,s}^{-1}\,\mathrm{cm}^{-2}\right]$	$(8.0 \pm 0.9) \times 10^{-13}$
$F_{\mathrm{X},\,0.2-10\,\mathrm{keV}}\ \left[\mathrm{erg\,s}^{-1}\,\mathrm{cm}^{-2}\right]$	$(8.4 \pm 0.9) \times 10^{-13}$
$L_{\mathrm{X},\,0.1-2.4\,\mathrm{keV}}\ \left[\mathrm{erg\,s}^{-1}\right]$	$(1.3 \pm 0.1) \times 10^{30}$
$L_{\mathrm{X},\,0.2-2\,\mathrm{keV}}\ \ \left[\mathrm{erg\,s}^{-1}\right]$	$(1.1 \pm 0.1) \times 10^{30}$
$L_{\mathrm{X},\,0.2-10\,\mathrm{keV}}\ \left[\mathrm{erg\,s}^{-1}\right]$	$(1.2 \pm 0.1) \times 10^{30}$
$L_{\mathrm{XUV},\,0.01-2.4\,\mathrm{keV}}\ \left[\mathrm{erg\,s}^{-1}\right]$	$(6.3 \pm 0.1) \times 10^{30}$

V1298 Tau's X-ray luminosity down by a factor given by the X-ray count ratios between V1298 Tau and the respective other star.

In this manner, we estimate HD 284154's and GDR2-5188's X-ray luminosity to be 0.29 and 0.19 times the X-ray luminosity of V1298 Tau, respectively. In absolute numbers, we estimate the X-ray luminosities of HD 284154 and GDR2-5188 in the 0.1-2.4 keV energy band to be 3.8×10^{29} erg s^{-1} and 2.5×10^{29} erg s^{-1}, respectively.

5.4 Discussion

5.4.1 V1298 Tau's activity evolution in the context of young stars

We can place the X-ray emission level of V1298 Tau, as well as for the other two young stars, into the context of cluster stars of a similar age. The cluster NGC 2547 has a similar age of about 30 Myr and has been studied in X-rays with both ROSAT and XMM-Newton data (Jeffries et al., 2006). A comparison of the fractional X-ray luminosity L_X/L_{bol} versus photometric stellar

---

[4]Emission measure; corresponding to a fitted "norm" parameter in the APEC model of $(3.2 \pm 0.3) \times 10^{-4}$.
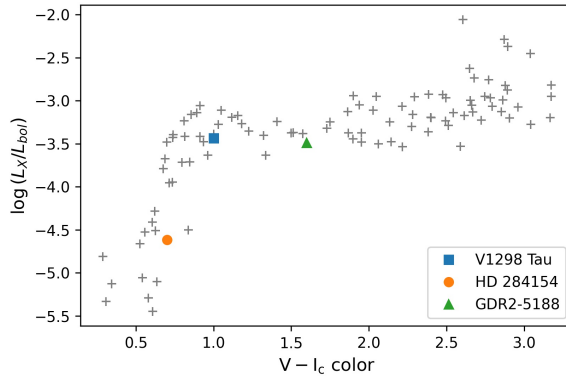
Figure 5.7: Fractional X-ray luminosity (L_X/L_{bol}) of V1298 Tau and the other two young stars as a function of their $V - I_c$ color, together with fractional X-ray luminosities of member stars of the 30 Myr old cluster NGC 2547 (cluster data from Jeffries et al. (2006)).

colours is particularly instructive, because it displays the lower activity state of higher-mass stars compared to lower-mass ones at a fixed given age.

We calculated the fractional X-ray luminosity and photometric colours of the three stars studied here as follows: We queried the Gaia DR2 archive for the approximated bolometric luminosities of the stars, which are given as 0.9, 4.0, and 0.2 for V1298 Tau, HD 284154, and GDR2-5188, respectively. We transformed the stellar $B_P - R_P$ colors from Gaia into $V - I_c$ colors according to the Gaia Data Release 2 Documentation release 1.2[5], which yielded $V - I_c =$ 1.0, 0.7, and 1.6 mag, respectively.

The placement of the three stars studied here in context with the cluster NGC 2547 are shown in Fig. 5.7. All three stars fall within the range of typically observed fractional X-ray luminosities for stars of a similar age. This means that neither of the stars is particularly active or inactive for their age.

5.4.2 Evaporation of the four planets

We investigate the possible future evolution of the four young planets around V1298 Tau with respect to their atmospheric mass loss induced by the stellar X-ray and extreme UV irradiance. The goal of the following calculations is to show the breadth of possible planetary masses and radii at a mature system

---

[5]https://gea.esac.esa.int/archive/documentation/GDR2/

age. We will demonstrate that both the present-day masses of the four planets, which are currently still unknown, and the specific stellar activity evolution in the next few hundred million years have a strong influence on how the planets in the system evolve. We have made the python code for these calculations publicly available[6].

We start by adopting the commonly used energy-limited hydrodynamic escape model (see e.g. Owen & Jackson, 2012b; Lopez et al., 2012):

$$\dot{M} = \epsilon \frac{(\pi R_{XUV}^2) F_{\mathrm{XUV}}}{K G M_{pl}/R_{pl}} = \epsilon \frac{3\beta^2 F_{\mathrm{XUV}}}{4 G K \rho_{pl}}, \tag{5.1}$$

where F_{XUV} is the flux impinging on the planet, R_{pl} and R_{XUV} are the planetary radii at optical and XUV wavelengths, respectively; we use $\beta = R_{XUV}/R_{pl}$ as a shorthand in the following. M_{pl} is the mass and ρ_{pl} the density of the planet, ϵ is the efficiency of the atmospheric escape with a value between 0 and 1, and K is a factor representing the impact of Roche lobe overflow (Erkaev et al., 2007), which can take on values of 1 for no Roche lobe influence and < 1 for planets filling significant fractions of their Roche lobes. For the present-day V1298 Tau system the K factor takes on values of about 0.8 to 0.9 from the innermost to the outermost planet, with a slight dependence on the assumed masses of the planets which have not been measured yet.

Planetary mass estimates

Measuring masses of planets around highly active stars like V1298 Tau is challenging, as stellar activity can mask and distort the radial velocity signatures of planets. No masses for the V1298 Tau planets have been published so far. We therefore estimate their masses based on two different assumptions.

It is possible that the V1298 Tau planets follow the empirical mass-radius relationships observed for planets around older stars (Chen & Kipping, 2017b; Otegi et al., 2020b). These relationships show two regimes, one for small rocky planets up to radii of about $2 R_\oplus$ and one for larger planets with volatile-rich envelopes. The scatter is low in the rocky planet regime and larger in the gaseous planet regime: as core vs. envelope fractions may vary, there is a broader range of observed masses at a given planetary radius for those larger planets. It is noteworthy that the young planet K2-100b, which has an age of ≈ 700 Myr based on the cluster membership of its host star (Mann et al., 2017),

---

[6]https://github.com/lketzer/platypos/

falls into the volatile envelope regime and follows the mass-radius relationship seen for older planets.

If this is correct also for the younger V1298 Tau planets, we can estimate their masses from the mass-radius relationship presented by Otegi et al. (2020b); the relationship by (Chen & Kipping, 2017b) yields essentially the same results. The present-day planetary masses then span a range of approximately 26 to 69 $M_\oplus$. We refer to this assumption as the "high-density scenario" in the following. We note here that we consider this "high-density scenario" as somewhat less likely than the "fluffy planet scenario" described further below. This is due to considerations about the mutual Hill separations of the planets as reported by David et al. (2019a) in their section 3.1, where they show that if the V1298 Tau system follows the typically observed Hill separations in other multi-planet systems, then the combined mass of the two innermost planets should be 7^{+21}_{-5} $M_\oplus$. The "high-density scenario" would yield a combined mass of approximately 59 $M_\oplus$ instead.

In contrast to the mass-radius relation of mature planets, very young planets may display enlarged radii as they are not dynamically settled yet. Simulations of planet formation and evolution (see for example Mordasini et al. 2012b) show that in the age range of 10 to 50 Myr planets evolve from a wide range of possible radii at a given mass towards a more unified mass-radius relationship. If planets are formed under the so-called cold start scenario, i.e. with low initial entropy, their radii may not shrink very much as the planets age. However, if planets are formed according to the hot start scenario, i.e. with a high initial entropy, their radii may be considerably larger at young ages compared to older ages. The planet β Pic b shows indications of having been formed under hot start conditions (Snellen & Brown, 2018b).

If this is also the case for the V1298 Tau planets, their current masses could be much lower than estimated by a mass-radius relationship valid for older planets. We approximate this scenario by using models of planets with a hydrogen/helium envelope on top of a 5 and 10 $M_\oplus$ core, using the tabulated models of Lopez & Fortney (2014b). They calculate radii for low-mass planets with hydrogen-helium envelopes on top of Earth-like rocky cores, taking into account the cooling and thermal contraction of the atmospheres of such planets over time. Their simulations extend to young planetary ages, at which planets are expected to still be warm and possibly inflated. Lopez & Fortney (2014b) provide simple analytical fits to their simulation results, which we use to trace the thermal and photoevaporative evolution of the planetary radius over time. We refer to this as the "fluffy planet scenario" in the following.

Evaporation parameters

Different values for the efficiency parameter ϵ have been suggested in the literature, ranging from 0.4 (Lalitha et al., 2018) down to 0.01 and even lower for high-mass planets like CoRoT-2b (Salz et al., 2016a). In contrast, the V1298 Tau planets are well below Jupiter size and can be expected to have moderately low masses (see above). Salz et al. (2016a) used hydrodynamic simulations of exoplanets in close orbits to estimate ϵ. For planets of relatively low mass (and therefore low gravitational potential energy) and high irradiation level, they reported efficiency values between 0.1 and 0.3. In our work, we choose a ϵ value of 0.1 for all of our mass-loss rate calculations; we refer the reader to section 5.4.3 for a discussion of limitations of the model.

The XUV radii of exoplanets have in some cases been found to be significantly larger than their optical radii from observations at UV and X-ray wavelengths (Poppenhaeger et al., 2013b). We use here again an approximation by Salz et al. (2016a), who derived a scaling law for the planetary XUV radius as a function of planetary gravitational potential and their XUV irradiation. Assuming planetary masses follow a mass-radius relationship also valid for older planets (Otegi et al., 2020b), we find XUV radii for the four planets that are approximately 1.5 to 1.7 times larger than their respective optical radii. If the planets are fluffy, their gravitational potential is lower by half an order of magnitude than the sample simulated by Salz et al. (2016a); if we extrapolate their relationship for XUV radii to this regime, we find that the planetary XUV radii can be enlarged by factors of about 1.5 to 2.3 compared to the optical radius for the individual planets. This significant radius enhancement increases the calculated mass-loss rates by a factor of about 2 to up to 5 compared to an XUV radius that is the same as the optical radius.

Present-day mass-loss rates of the planets

The expected present-day mass-loss rates of the planets depend sensitively on the assumed masses of the planets. We report the mass-loss rates for the high density scenario and for the fluffy planet scenario, the latter one using two different potential core masses of 5 and 10 $M_{\oplus}$. We take into account the measured stellar X-ray luminosity and its extrapolation to the XUV wavelength band, as well as the Roche-lobe overflow factor K (Erkaev et al., 2007) and the planetary XUV radius as simulated by Salz et al. (2016a).

The XUV irradiation in the energy range of 0.01-2.4 keV at the planetary orbital distances is high compared to more mature exoplanet systems; we

find $F_{\text{XUV, orbit}} = 32.9, 19.1, 7.9, 2.4 \times 10^5 \text{ erg s}^{-1} \text{ cm}^{-2}$ from the innermost to the outermost planet (i.e. planets *c*, *d*, *b*, and *e*).

The typical difference in expected mass-loss rates differs by about an order of magnitude between assuming the high-density scenario and the fluffy planets scenario with a core mass of $5\,M_\oplus$ for the planets. The innermost planet *c* yields an expected present-day mass loss of $2.5 \times 10^{13} \text{ g s}^{-1}$ for the fluffy $5\,M_\oplus$ core mass scenario, $8.7 \times 10^{12} \text{ g s}^{-1}$ for the fluffy $10\,M_\oplus$ core mass scenario, and $2.4 \times 10^{12} \text{ g s}^{-1}$ for the high-density scenario. The derived expected mass-loss rates for all planets and considered scenarios are listed in Table 5.3.

Stellar activity evolution

In order to investigate the atmospheric erosion that the four planets might undergo in the future, it is crucial to take into account the change in XUV flux received by the planets over time. Many studies of exoplanet evaporation approximate the stellar XUV evolution by using the average activity level of stars in a specific mass bin for well-studied clusters of different ages. This can be represented as a power law decrease in activity which sets in after some time scale during which the stellar activity stays constant at a saturation level (Ribas et al., 2005b; Jackson et al., 2012b).

However, the rotational and therefore activity evolution of stars with similar mass in young clusters shows a strong spread, which manifests itself as the so-called slow and fast rotational sequences (Barnes, 2003d). It is possible that a star spins down early and follows a low-activity track, or that it maintains its high rotation rate and activity for a longer time and spins down later. Specifically, the observed rotational evolution of stars in clusters has been interpreted as the stellar transition from fast to slow rotation happening quickly for individual stars, but at different stellar ages in the same cluster (Garraffo et al., 2016). In the context of exoplanet irradiation, this was explored in simulations by Tu et al. (2015a); Johnstone et al. (2015b). Their studies show that the saturation timescales may range from ~ 10 to $\sim 300\,\text{Myr}$ for stars of the same mass. Whether a star follows a high- or low-activity track can make a significant difference for the evaporation of its exoplanets.

Inspired by Tu et al. (2015a), we use a simplified broken power-law model to approximate the solar-mass stellar activity evolution, which we show in Fig. 5.8. Specifically, we define a high-activity track, where the star stays very active for a long time, and a low-activity track, where the spin-down and therefore the activity decrease happens early in the life of the star. For comparison with studies using an average activity evolution, we also define an average activity
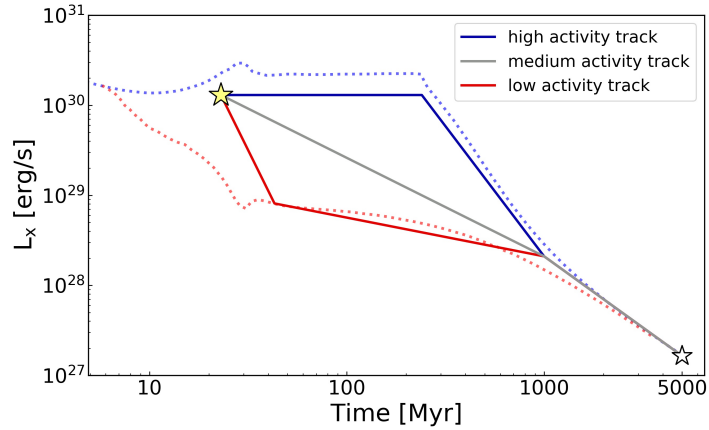
Figure 5.8: High, low and medium activity tracks (blue, grey and red, respectively) showing the future L_X evolution of V1298 Tau assumed in our calculations. The yellow star indicates the current X-ray luminosity of the system, while the white star marks the X-ray luminosity at the end of our calculation at 5 Gyr. The blue and red dotted model tracks (shown for comparison) are taken from (Tu et al., 2015a) and represent the X-ray evolution for an initially fast and slowly rotating solar-like star.

track. We let our high-activity track start at the current activity level of V1298 Tau; it is possible that other stars of the same age and mass may have an even higher activity level.

Mass-loss evolution of the planets

We calculate the evaporation of the four planets for a variety of scenarios. We take into account the possible high-density and fluffy planet scenarios, as explained above, and further divide these cases into different stellar activity evolution scenarios.

   In our calculations, we compute the momentary mass-loss rate of each planet according to equation 5.1, having calculated R_{XUV} and K for the fluffy and the high-density planet scenario, respectively. We adjust the gaseous envelope mass of the planet and calculate its new radius, again using either the fluffy or high-density planet assumption.

   To model the four young planets in the "fluffy planet scenario", we make use of the simulation results from Lopez & Fortney (2014a) and assume core masses of either 5 or 10 $M_\oplus$ for all planets in the system. Coupled with the mass-loss formalism introduced above (see equation 5.1), we allow for the atmospheric

photoevaporative mass loss of the envelope and take into account the thermal contraction of the planets in the model by Lopez & Fortney (2014a). For the fluffy planet scenario, we stop the simulation and assume the complete gaseous envelope has been evaporated once the planetary radius matches the core radius.

In the "high-density scenario" we assume that the planetary radii change according to the mass-radius relation for the more evolved, volatile-rich planet population, considering the decrease in planetary masses as a result of the XUV induced mass loss. If the planetary size reaches $2R_\oplus$, which we assume to be the upper end of possible core sizes based on the location of the exoplanet radius gap, we stop the simulation and assume the complete gaseous envelope has been evaporated.

We perform these calculations for all three stellar activity evolution tracks (see Fig. 5.8). We tested different time step sizes and found that a step size of 1 Myr yields practically the same results for the "high density scenario" planets as for smaller time steps. Due to the much faster radius evolution for planets in the "fluffy-planet scenario", we chose a smaller step size of 0.1 Myr. The planetary mass and radius evolution for the two innermost planets c and d are shown in Figures 5.9 and 5.10.

Our calculations show that the high-energy evolution of the star has a significant effect on the planetary mass loss. The effect is particularly strong for "fluffy" scenario of close-in planets c and d, as they have extended atmospheres and are exposed to much higher XUV fluxes, see Fig. 5.9 and 5.10. In the stellar high activity scenario, those two planets can lose all of their modelled gaseous envelope, which corresponds to a lost mass fraction of around 10%.

If we assume that the host star follows the evolutionary track for a slowly rotating star (low activity track), and will spend no more time in the saturation regime, the photoevaporative mass loss is, especially for the two outer planets, less severe. A summary of the possible radius changes and the remaining envelope mass fractions is given in Table 5.3.

For the planets in the "high density scenario" our calculations show that such high-mass planets would undergo little mass and radius evolution even for high activity track, owing to the larger planetary gravitational potential and the resulting lower mass loss rates. Planets in the low activity scenario undergo negligible mass and radius evolution.

To put these numbers in context with the observed radius gap in the exoplanet population, we show the initial planetary radii and those at a system age of 5 Gyr in Fig. 5.11. The figure only shows the evolution of the two "fluffy planet" scenarios with different core masses, as the "high density" scenario shows very
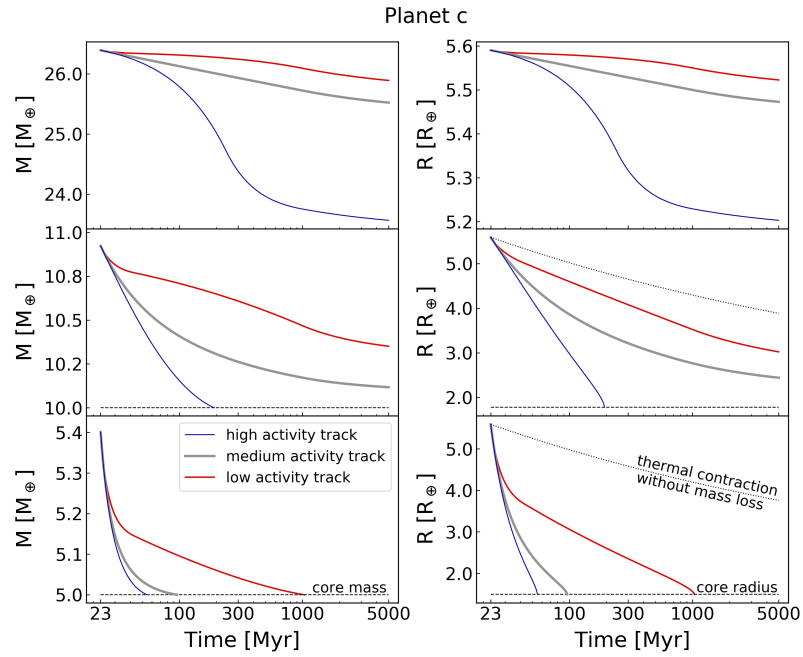
Figure 5.9: Results of our calculations showing the possible future mass and radius evolution of the inner most planet c. The three panels on the left show the mass evolution for our "high-density case" planet (top) and the two "fluffy planet cases" with 10 and 5 Earth-mass cores (middle and bottom, respectively). The panels on the right show the corresponding radius evolutions. The red, grey and blue lines represent the planetary evolution considering a high, medium or low stellar activity evolution for V1298 Tau.
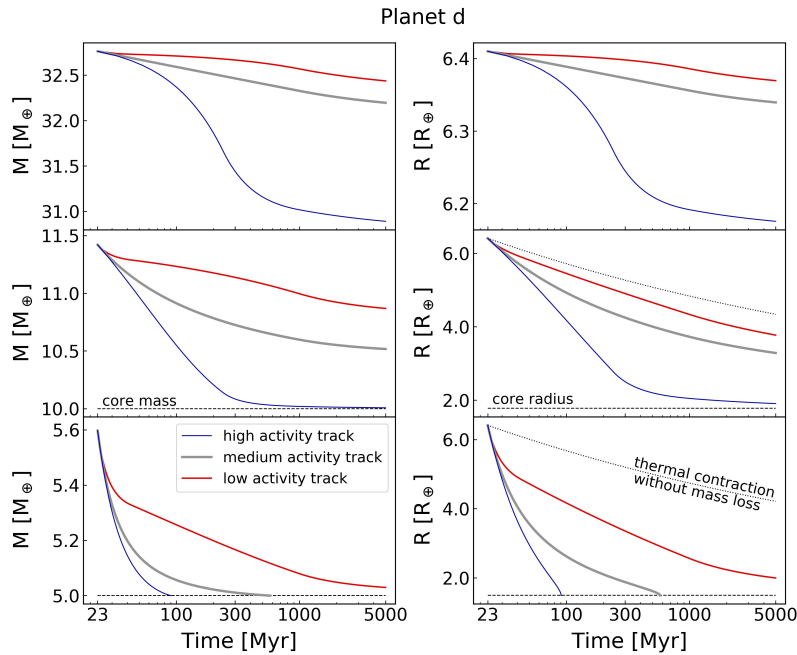
Figure 5.10: Same as Fig. 5.9, but for planet d.

little radius evolution. The combined impact of the stellar activity evolution and the planetary core mass can be seen particularly well for planets d and b, as their evolution on the period-radius diagram shows them either crossing or not crossing the photoevaporation valley around 2 $R_\oplus$ depending on whether V1298 Tau will follow the high, medium or low activity track.

5.4.3 Uncertainties and model limitations

Some uncertainties are introduced into our modelling from observed or assumed parameters, others from the underlying assumptions of the model. We discuss the influence of these uncertainties here briefly.

The measured X-ray flux has an uncertainty of the order of 10%, which makes very little difference in our modelling of the planet evolution. A 10% higher or lower starting point of the stellar high-energy flux translates to a difference in the final planet radii of the order of 1% in cases where the planet envelopes do not fully evaporate, and a difference in age where full envelope evaporation occurs of the order of 10% for the other cases.

We have assumed an evaporation efficiency parameter ϵ of 0.1, which is not
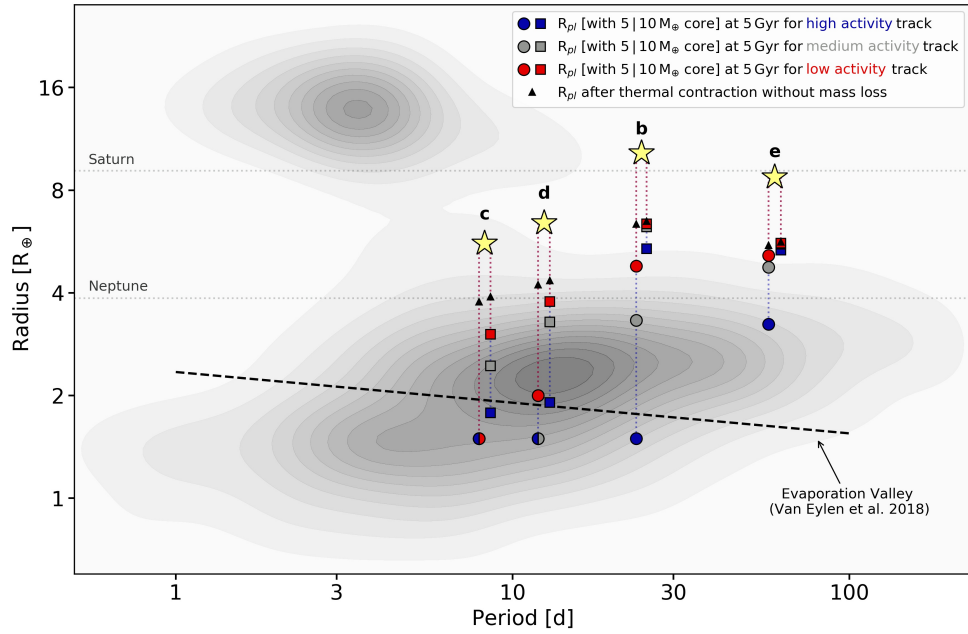
Figure 5.11: Current position of the four transiting planets around V1298 Tau in the radius-period diagram. The gold stars mark the radii and periods measured by David et al. (2019a) at a system age of ~ 23 Myr. The vertical dotted lines show possible evolutionary tracks under atmospheric photoevaporation. The dots and squares mark the planetary radii at an age of 5 Gyr resulting from our calculations for planets with a $5\,M_\oplus$ and $10\,M_\oplus$ core, respectively. The colors correspond to the stellar activity tracks assumed in the calculation, with blue colors corresponding to the high activity track, gray to the medium activity track and red to the low activity track.

unusual in comparison to the existing literature, where a wide range of values has been employed in the past. However, this also needs to be seen in the context of applicability of the energy-limited escape scenario itself. The regime of energy-limited escape has been modelled to be valid for low to moderate XUV fluxes onto the planetary atmosphere, and is consistent with observations in the solar system (Watson et al., 1981a). For high XUV fluxes, it is expected that the energy supplied by the XUV photons does no longer go mainly into lifting the planetary atmosphere out of the planet's gravitational well. Instead, the planetary atmosphere is heated to such high temperatures that it starts to cool through emission lines, which reduces the energy available for expanding the atmosphere upwards. The escape rates could then be suppressed by a factor of up to ten, compared to a ϵ factor appropriate for an energy-limited situation (Murray-Clay et al., 2009b). We currently do not take into account such deviations from the energy-limited scenario, but assume on overall time-constant efficiency parameter of $\epsilon = 0.1$ instead.

Also, currently not included in our model are hydrodynamic or magnetic effects, such as a stellar wind streaming around the planet or the potential shielding effect that a planetary magnetosphere could provide against evapora-tion. Both are expected to influence the total mass loss. The stellar wind may enhance the mass loss of exoplanets, especially if the planets have no (or only a weak) magnetic field (Cohen et al., 2015; Dong et al., 2017). However, the existence of a planetary magnetosphere may lower the evaporative mass loss, particularly from the night side of the planet (Owen & Adams, 2014). Planetary magnetic fields in the solar system display a relationship between the angular momentum of the planetary spin and their observed magnetic field strength (see Grießmeier et al. (2004) and references therein), meaning that heavy, quickly spinning planets have strong magnetic fields. If the V1298 Tau planets are heavy and not fluffy, and are spinning fast – which may be reasonable to assume since they are young –, magnetic shielding could be relevant to the mass loss.

In summary, our evaporation model is relatively simple and does not attempt to include all potentially relevant physical aspects of exoplanet evaporation, such as stellar winds, magnetic shielding, or any hydrodynamic effects. However, it is still instructive to see how even the inclusion of relatively few physical parameters, especially the stellar activity evolution and the planetary mass, can already cause a wide variety of possible future evolution tracks for the planets. In this context it is particularly important to measure masses of exoplanets around young stars, even though this is challenging, so that at least the planetary mass parameter in evaporation models can be constrained usefully.

Table 5.3: Estimates for the present-day mass-loss rates and planetary radii, as well as radii at 5 Gyr for two "fluffy" and one "high-density" planet scenarios given the three stellar activity evolutionary tracks. For the "fluffy" cases, core masses need to be explicitly assumed and we also report the planets' envelope mass fractions.

Scenario	present-day $\dot{M}$ [g s^{-1}]	present-day R_p [$R_\oplus$] (f_{env} [%])	R_p [$R_\oplus$] (envelope mass fraction f_{env} [%]) at 5 Gyr		
			high activity track	medium activity track	low activity track
Planet c [$M_{core} = 5\,M_\oplus$]	1.5×10^{13}	5.6 (7.4)	1.5 (0.0)	1.5 (0.0)	1.5 (0.0)
Planet c [$M_{core} = 10\,M_\oplus$]	5.3×10^{12}	5.6 (8.5)	1.8 (0.0)	2.4 (1.2)	3.0 (3.5)
Planet c [high-density]	1.5×10^{12}	5.6 (–)	5.2 (–)	5.5 (–)	5.5 (–)
Planet d [$M_{core} = 5\,M_\oplus$]	1.2×10^{13}	6.4 (10.7)	1.5 (0.0)	1.5 (0.0)	2.0 (0.6)
Planet d [$M_{core} = 10\,M_\oplus$]	4.4×10^{12}	6.4 (12.4)	1.9 (0.1)	3.3 (4.9)	3.8 (8.0)
Planet d [high-density]	9.7×10^{11}	6.4 (–)	6.2 (–)	6.3 (–)	6.4 (–)
Planet b [$M_{core} = 5\,M_\oplus$]	1.6×10^{13}	10.3 (33.9)	1.5 (0.0)	3.3 (5.7)	4.8 (16.2)
Planet b [$M_{core} = 10\,M_\oplus$]	4.6×10^{12}	10.3 (43.3)	5.4 (25.2)	6.2 (38.6)	6.4 (41.2)
Planet b [high-density]	6.6×10^{11}	10.3 (–)	10.2 (–)	10.2 (–)	10.2 (–)
Planet e [$M_{core} = 5\,M_\oplus$]	2.7×10^{12}	8.7 (25.7)	3.2 (5.8)	4.8 (17.4)	5.2 (21.6)
Planet e [$M_{core} = 10\,M_\oplus$]	9.0×10^{11}	8.7 (31.7)	5.3 (27.1)	5.6 (30.4)	5.6 (31.0)
Planet e [high-density]	1.5×10^{11}	8.7 (–)	8.7 (–)	8.7 (–)	8.7 (–)

5.5 Conclusions

We use X-ray observations of the young exoplanet host star V1298 Tau with Chandra and ROSAT to estimate the current high-energy irradiation the four Neptune- to Saturn-sized planets are exposed to. We find that V1298 Tau, with an age of ~ 23 Myr, is X-ray bright with a luminosity of $\log L_X \, [\mathrm{erg\, s^{-1}}] = 30.1$, and has a mean coronal temperature of approximately 9 MK. By employing a model for the stellar activity evolution together with exoplanetary mass loss, we then estimate the atmospheric evolution of the four planets. Due to the lack of measured masses, it is challenging to provide constraining predictions on the fate of these four very young planets. We therefore estimate the planetary mass and radius evolution for a "fluffy-planet scenario" and a "high-density scenario", covering a realistic/conceivable mass range. We model the four planets as fluffy planets with a 5 and 10 $M_\oplus$ rocky core underneath a thick hydrogen/helium envelope, and also as four higher-mass/density planets with masses ranging roughly between those of Neptune and Saturn ($\sim$20-70 $M_\oplus$). We show that, as expected, the low-mass planets are most affected by photoevaporative mass loss, mainly due to their weaker gravitational potential and the consequently higher mass-loss rates. Our results show that the stellar activity evolution and the age at which spin-down sets in can make a significant difference in possible life-time evaporation outcomes for the planets.

Acknowledgements

---

[7]http://www.astropy.org

5.6 Appendix

5.6.1 Planet evolution plots

Large versions of the radius and mass evolution plots for all four planets are displayed in this appendix.
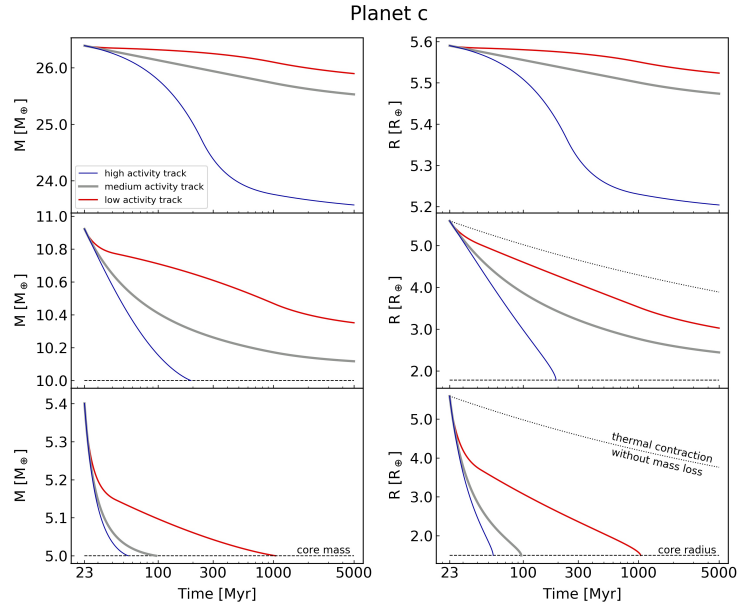
Figure 5.12: High-resolution version of Fig. 5.9.
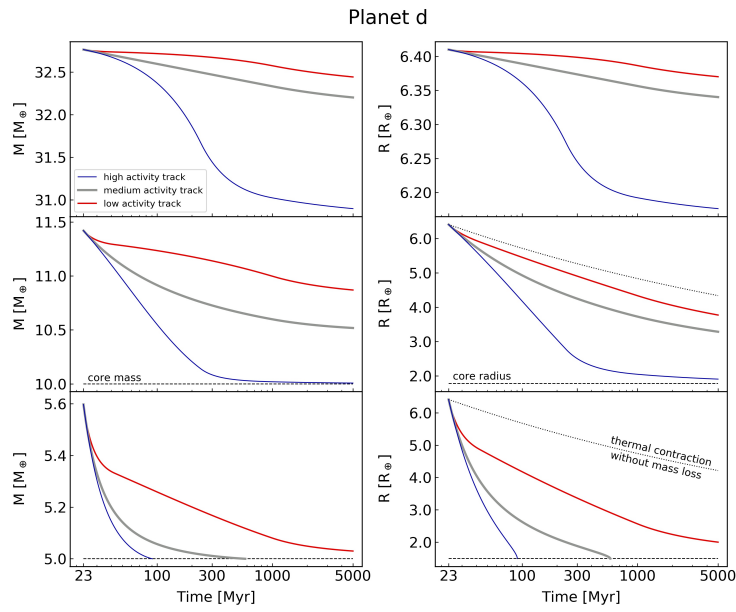
Figure 5.13: High-resolution version of Fig. 5.10.
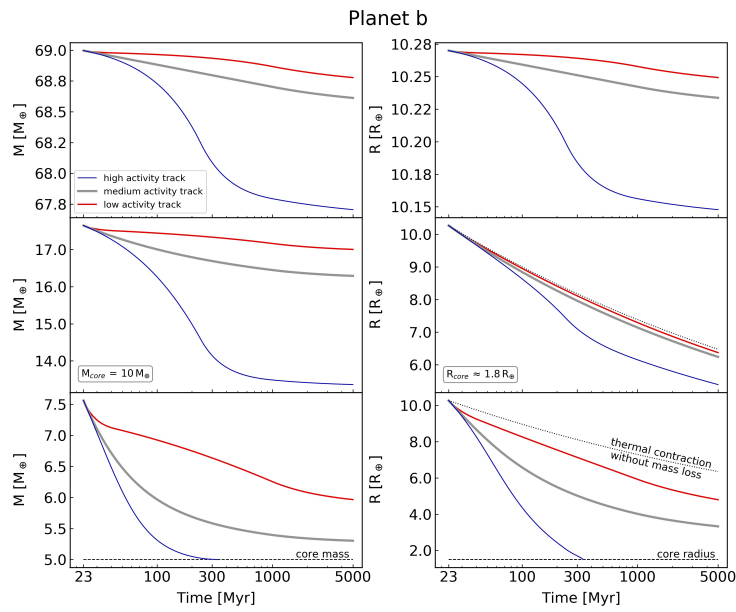
Figure 5.14: Same as Fig. 5.9, but for planet b.
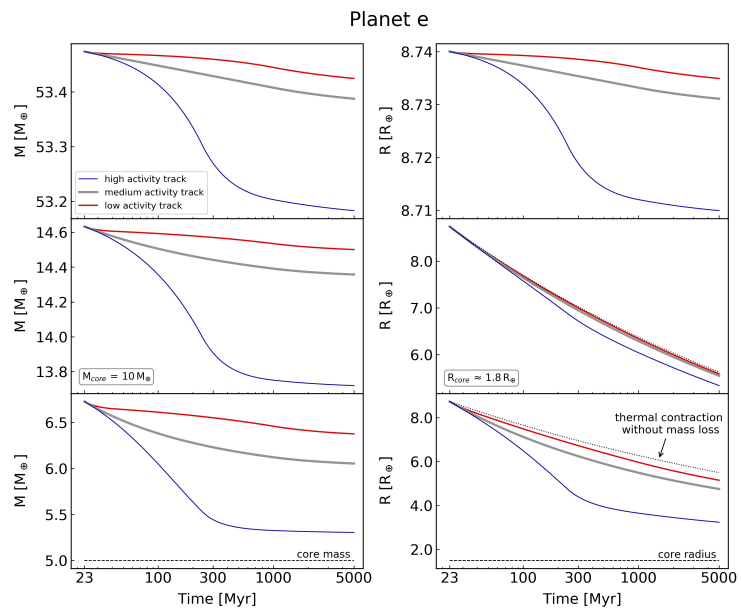
Figure 5.15: Same as Fig. 5.9, but for planet e.

6 Estimating photoevaporative mass loss of exoplanets with PLATYPOS

Ketzer, L.; Poppenhaeger, K.

Abstract

We develop PLATYPOS (PLAneTarY PhOtoevaporation Simulator), a python code to perform planetary photoevaporative mass-loss calculations for close-in planets with hydrogen-helium envelopes atop Earth-like rocky cores. With physical and model parameters as input, PLATYPOS calculates the atmospheric mass loss and with it the radius evolution of a planet over time, taking into account also the thermal cooling and subsequent radius evolution of the planet. In particular, we implement different stellar activity evolution tracks over time. Our setup allows for a prediction of whether a planet can hold on to a significant fraction of its atmosphere, or fully evaporates, leaving behind only the bare rocky core. The user supplies information about the star-planet system of interest, which includes planetary and host star parameters, as well as the star's rotational and thus activity evolution. In addition, several details for the evaporative mass-loss rate estimation can be chosen. This includes the effective absorption cross-section for high energy photons, the evaporation efficiency, and the hydrodynamic escape model.

6.1 Introduction

Thanks to the Kepler mission, it is now well established that sub-Neptune-sized planets orbiting their host star with periods less than 100 days are very abundant (e.g., Borucki et al., 2010; Winn & Fabrycky, 2015). A second striking discovery regarding these small close-in planets is the uncovered substructure in their radius distribution. Planets tend to group into two distinct populations, the so-called super-Earths and sub-Neptunes, with a significant dearth of planets with intermediate radii around $2 R_\oplus$. This had been expected from theoretical studies (Owen & Wu, 2013; Lopez et al., 2012) before being observed (Fulton et al., 2017b; Van Eylen et al., 2018b; David et al., 2021).

The gap-like feature, or bimodality in the radius distribution, is predominantly explained by atmospheric erosion of H/He atmospheres caused by the high-energy X-ray and ultraviolet (together: XUV) irradiation from the host star, a process also known as photoevaporation (e.g., Lopez et al., 2012; Owen & Wu, 2013); although also alternative scenarios involving core-driven evaporation have been suggested (Ginzburg et al., 2018; Gupta & Schlichting, 2019). The planetary properties paired with the external stellar environment, which is determined by host star properties and activity history, impact the strength of the mass loss. If a planet can hold on to a significant fraction of its primordial atmosphere, its radius will be large enough to place the planet above the radius gap. In case of a complete loss of the envelope, only the bare rocky core with a radius below the gap survives.

The age up to about a Gyr is thought to be most important for the fate of a planet because this is where the most significant mass loss is taking place (e.g., Owen & Wu, 2013). Planets still host extended atmospheres because they have not had enough time to cool and contract, and at the same time, they receive the highest XUV flux because young stars can maintain high activity levels. Due to different initial stellar rotation rates, activity levels can vary by about an order-of-magnitude for young stars with similar masses (Wright et al., 2011b; Tu et al., 2015b; Johnstone et al., 2021). The stellar activity evolution in the first several 100 Myrs thus needs to be taken into account when estimating the planetary mass and radius evolution over time (Kubyshkina & Vidotto, 2021, Ketzer et al. in prep;).

In this work, we provide a general description of the publicly available code PLATYPOS (PLAneTarY PhOtoevaporation Simulator), which was first applied to the V1298 Tau system (Poppenhaeger et al., 2021). PLATYPOS is a python code to perform planetary photoevaporative mass-loss calculations for close-in planets with Earth-like rocky cores and H/He envelopes on top.
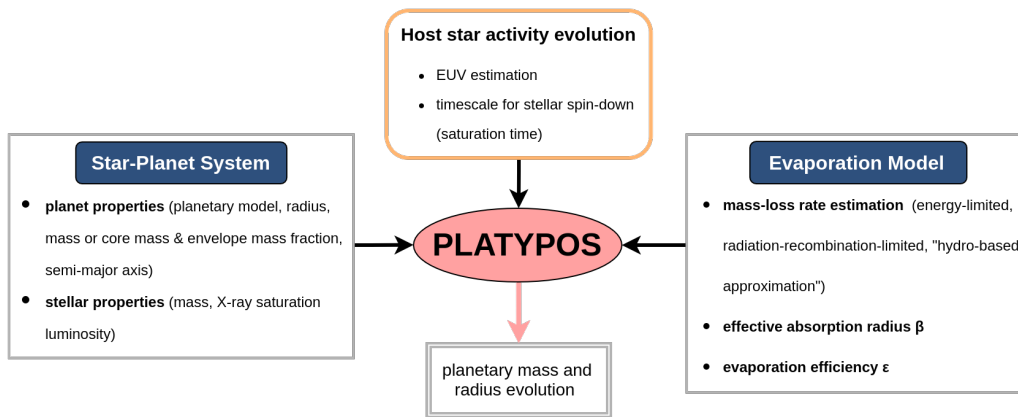
Figure 6.1: Overview of the three main building blocks of PLATYPOS and the individual parameters that need to be measured or estimated to calculate the mass and radius evolution of a planet.

We illustrate some of the capabilities of PLATYPOS in Section 6.3, using the innermost planet of the V1298 Tau system as an example.

6.2 Planetary Evolution Framework

PLATYPOS couples a planetary structure model, which includes the planet's thermal evolution, with an atmospheric photoevaporation model to investigate the mass loss and subsequent radius evolution of a planet over time (as in e.g., Lopez & Fortney, 2014a; Owen & Wu, 2017). The code can be used to investigate the mass and radius evolution of individual systems, or be applied to study how atmospheric mass loss shapes a whole population of exoplanets.

PLATYPOS also allows for an easy inclusion of the host star activity evolution in photoevaporation calculations, an important detail which has only recently been incorporated in these types of calculations by, for example, Kubyshkina et al. (2018a); Kubyshkina & Vidotto (2021).

Since photoevaporative mass loss is a complex process, which requires many ingredients, several (simplifying) assumptions need to be made – this includes the planet as well as the host star. The building blocks of PLATYPOS - the planetary models and the mass-loss description, together with additional assumptions about the host star activity evolution – are briefly presented in the following sections. An overview of the ingredients of PLATYPOS is shown in Figure 6.1.

6.2.1 Planetary models

To estimate the planetary radius at any given point in time, PLATYPOS has two planetary structure models implemented. The user can choose between the tabulated models by Lopez & Fortney (2014a) and the models by Chen & Rogers (2016), which are based on the 1-D stellar evolution code MESA (hereafter: LoFo and ChRo). Both models provide mass-radius-age relations for low-mass gaseous sub-Neptune-sized planets, taking into account the cooling and subsequent radius contraction as a planet ages. Fitting formulas for a wide grid of planetary parameters allow PLATYPOS to estimate the planetary radius for a specified core mass, envelope mass fraction, f_{env}, and bolometric incident flux at any given age over the course of the simulation. The user is cautioned that the mass-radius-age relations are only valid for a finite range of planetary parameters, which includes, but is not limited to, planetary age and envelope mass fraction. Lopez & Fortney (2014a) showed that the modeled planetary radii can be reasonably backwards extrapolated to ages of $10\,\mathrm{Myr}$ (see their Figure 2), which is the earliest starting age we recommend to the users of PLATYPOS. This age is a conservative value for the lifetime of a protoplanetary disk (e.g., Williams & Cieza, 2011): only after its dispersal, the planet is fully exposed to the stellar XUV irradiation.

Regarding the envelope mass fraction, the user can decide whether to extrapolate beyond the lower limit of 0.01%, which is reached shortly before planets lose their atmosphere completely, or to continue the calculation keeping the radius constant at the last allowed envelope mass fraction. Our tests across a grid of planets with different parameters showed, however, that in general, if a planet reaches an envelope mass fraction of $f_{env} = 0.01\%$, it cannot hold on to its atmosphere regardless of the radius estimation in the final stages. For the additional details of these models and their applicability, we refer to the original publications.

6.2.2 Mass-loss rate calculation

Several regimes of hydrodynamic escape in hydrogen-dominated atmospheres, including energy-limited, radiation-recombination limited, and photon-limited escape, have been identified in theoretical studies (e.g., Lammer et al., 2003; Murray-Clay et al., 2009a; Owen & Jackson, 2012a; Owen & Alvarez, 2016), and there is recent observational evidence of giant planets supporting these regimes (Lampón et al., 2021). The underlying physics of the escape differs in terms of the production and losses of neutral hydrogen, as well as the processes

converting the absorbed stellar radiation into work, which ultimately drives the evaporative outflow. PLATYPOS has different evaporation schemes built in, which allows for an easy comparison against each other. Photoevaporative mass loss can be estimated using an energy-limited approximation only, including the radiation-recombination limited regime, or via a hydro-based approximation.

In all cases, it is the stellar high-energy X-ray and extreme UV (EUV) radiation, which ionizes and heats the gas in the upper atmosphere. If a significant fraction of the externally supplied energy is converted into work to expand the planetary atmosphere and lift material outside the gravitational well of the planet, mass loss is said to occur in the energy-limited regime. PLATYPOS has the commonly used energy-limited hydrodynamic escape model built-in (see e.g., Owen & Jackson, 2012b; Lopez et al., 2012), which assumes that the mass-loss rates are limited by the stellar radiative energy deposition and scale linearly with the high energy incident flux ($\dot{M} \propto F_{XUV}$).

In the case of high UV fluxes, the ionization fraction and the temperature of the wind become so high that the material in the upper atmosphere reaches a state of radiation-recombination equilibrium. In this regime, a considerable fraction of the externally supplied (X)UV energy is effectively re-radiated away in the form of Hydrogen Lyman-alpha cooling radiation. This energy sink leads to the mass-loss rates having a shallower dependence on the incoming high energy flux ($\dot{M} \propto \sqrt{F_{XUV}}$), and can cause the mass loss to be very ineffective for highly irradiated planets (e.g., Murray-Clay et al., 2009a; Salz et al., 2016a). If chosen by the user, PLATYPOS evaluates both the energy-limited and the radiation/recombination-limited mass-loss rate at each time step of the calculation, and adopts the lesser of the two. This ensures that mass-loss rates are not overpredicted for highly irradiated planets, which is particularly true for young planets orbiting close to their still very active host star. For a more detailed explanation of the radiative/recombinative mass-loss rate calculation implemented in PLATYPOS, see section 2.3 in Lopez (2017).

The hydro-based approximation is based on the computation of a large grid of hydrodynamic upper atmosphere models (Kubyshkina et al., 2018a). The authors provide analytical expressions for the mass-loss rates as a function of the system parameters based on the grid results. They not only take into account the contribution from high-energy radiation, but also the planetary intrinsic thermal energy and surface gravity. Compared to pure energy-limited mass loss, these mass-loss rates can be orders of magnitudes larger for highly irradiated, low-density planets, and a few factors of 10 lower for more massive planets at larger orbital separations (Kubyshkina et al., 2018b).

Models of escaping atmospheres are extremely complex, and hydrodynamic

simulations can predict a wide range of mass-loss rates based on the detailed physics and chemistry included. For this reason, we implement all three of the aforementioned evaporation schemes to give the user the choice to compare them against each other for similarities and differences, and to get a more feasible range of possible mass-loss rates.

6.2.3 Effective absorption radius and evaporation efficiency

Observations as well as hydrodynamic simulations both show that heated and expanded planetary atmospheres can make a planet appear significantly larger when observed in X-ray or EUV compared to optical wavelengths (e.g., Poppenhaeger et al., 2013b; Salz et al., 2016a). To obtain reasonable mass-loss rate estimates, the effective XUV absorption radius, as well as the evaporation efficiency, need to be estimated for a given planet.

PLATYPOS has two methods implemented for approximating the XUV photosphere of a planet. One is the approximation by Salz et al. (2016a), which is motivated by results from detailed numerical simulations, while the other is a more theoretical calculation following the arguments presented in Murray-Clay et al. (2009a), Chen & Rogers (2016) and Lopez (2017). The size of the XUV absorption radius can change significantly for different planet properties, with the gravitational potential playing an important role. In particular, lower-mass planets can host atmospheres, which can be extended up to a few times the optical radius, making them much more susceptible to mass loss. Due to the weak observational constraints on this parameter up to now, we give the user a choice of how to estimate the effective absorption radius for XUV photons. In addition, the user can also choose to set this parameter equal to the optical radius.

In the literature, a wide range of values for the evaporation efficiency parameter, or heating efficiency, have been reported. The values range from 0.4 (Lalitha et al., 2018) down to 0.01 and even lower for Jupiter-mass planets (Salz et al., 2016a). For planets in the sub-Neptune mass regime, values between 0.1 and 0.3 are commonly used (e.g., Owen & Wu, 2013; Salz et al., 2016a). PLATYPOS currently requires the user to choose a constant heating efficiency, which is then held constant for the whole duration of the calculation.

6.2.4 Host star activity evolution

To investigate the atmospheric erosion that planets (might) undergo since their release from the protoplanetary disk, it is important to account for changes

in the XUV flux a planet receives over time. Rotational spin-down driven by angular momentum loss via the magnetized stellar wind leads to a decreased stellar activity and with it high-energy XUV over time (Güdel et al., 1997; Ribas et al., 2005b; Booth et al., 2017). This means that young planets receive XUV-irradiation levels that can be several orders of magnitude higher than for the present-day Sun, causing their atmospheres to be hotter, more expanded and susceptible to mass loss.

In addition, the activity level and high-energy emission strongly depends on the rotation rate of the star (Reiners et al., 2014). Stellar rotational evolution models and observations indicate that stars with spectral type F, G, or K start their spin-down earlier than M-dwarfs and at a wide range of ages, with stars born as fast rotators staying active much longer than stars born as slow rotators. This spread in saturation timescales seems to be more pronounced for stars with masses similar to or larger than the Sun (e.g., Tu et al., 2015b; Garraffo et al., 2018) and becomes tighter for lower mass stars (e.g., Johnstone et al., 2021; Magaudda et al., 2020). In general, evolutionary state, activity level, and spectral type all contribute to stars emitting variable amounts of X-ray and UV radiation (Chadney et al., 2015), and should be taken into account when studying the atmospheric mass loss of exoplanets. Exoplanet host stars have been investigated for their current X-ray and extreme-UV emission (Poppenhaeger et al., 2010; Monsch et al., 2019; Foster et al., 2022a); however, we point out that estimating the past activity history of any given star from present-day measurements is highly non-trivial (Kubyshkina et al., 2019a).

Currently, the user can choose between the commonly used broken power-law activity evolution with a phase of constant X-ray luminosity, followed by a power-law decay, or a two-piece broken power-law activity decay, which can be used to more realistically simulate X-ray activity tracks with a wide range of saturation or spin-down ages (see Tu et al., 2015b). An example of the approximated high, intermediate and low activity evolution tracks used in Poppenhaeger et al. (2021), together with the detailed model tracks for a fast and slow rotator by Tu et al. (2015b), are shown in Figure 6.2. The code can be easily extended to include any activity track desired by the user.

The important EUV contribution to the high-energy flux can be estimated through the empirical relations between X-ray and EUV surface fluxes by Chadney et al. (2015) or Johnstone et al. (2021), which have been shown to yield more accurate predictions for active stars and are thought to be valid even on the pre-main sequence. The user can, however, also choose the empirical scaling relation between X-ray and EUV energy bands for late-type stars
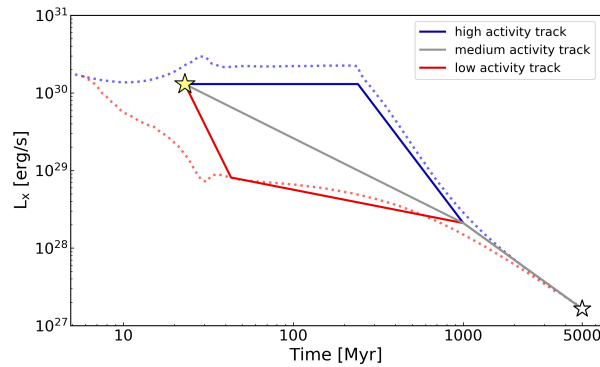
Figure 6.2: A set of example stellar activity tracks for the ~ 23 Myr-old pre-main sequence star V1298 Tau is shown. The age of the system was determined from isochrone fitting using stellar models that account for magnetic fields (David et al., 2019a), and the current X-ray level has been measured with Chandra. It is not well constrained at which age the star will spin down and decrease its activity. We therefore calculated the mass loss of the planets for a low, intermediate and high stellar activity scenario (red, grey and blue, respectively). For more details, see Section 4.2.4 in Poppenhaeger et al. (2021).

based on synthetic XUV spectra by Sanz-Forcada et al. (2011b), or the EUV luminosity estimation via Lyα (Linsky et al., 2013, 2014).

6.2.5 Details on the integration

PLATYPOS computes the momentary mass-loss rate for a given planet according to one of the mass-loss formalisms introduced in Section 6.2.2, and has estimated the effective absorption radius with one of the methods introduced in Section 6.2.3. It then uses the latest radius, envelope-mass fraction, and stellar XUV flux to calculate the mass-loss rate at the age of the simulation run. Using a fourth-order Runge-Kutta integration method, the mass lost within a given time step is calculated. If the radius change is negligible or too drastic, the time step is adjusted. PLATYPOS then calculates the updated radius with the reduced gaseous envelope based on the planetary model specified by the user (LoFo or ChRo). In the next step, the XUV flux is updated based on the specified stellar evolution track and EUV estimation method, and this cyclic procedure continues until the planetary radius has reached the core radius and no atmosphere remains, or the final age of the simulation is reached. The temporal mass and radius evolution caused by planetary cooling and atmospheric photoevaporation for the specified stellar activity track is then saved.

A big advantage of PLATYPOS is that it enables the user to easily change and compare various model assumptions, and to investigate their impacts on the strength of the mass loss and the fate of the planet of interest.

6.2.6 Code limitations

PLATYPOS does not make use of complex radiative-hydrodynamical simulations, but instead brings together parametrized models for the planetary structure, the atmospheric escape as well as the stellar activity evolution for a quick and easy-to-use estimation of planetary photoevaporative mass loss. All in all, the tool is relatively simple and does not seek to include all potentially relevant physical aspects of exoplanet evaporation. Examples of effects not considered are interactions of the stellar wind with the planetary outflow, any magnetic shielding effects due to a planet's magnetic field, or any hydrodynamic effects. In addition, the evaporation efficiency is taken to be constant for the whole duration of the calculation. This has been shown to be an oversimplification since the parameter depends on planetary mass, radius, and the amount of ionizing flux, quantities, which can vary by orders of magnitude over the lifetime of the star-planet system (see e.g., Owen & Wu, 2013). Various simulations, however, indicate that values around 0.1-0.2 are reasonable for low-mass planets in the super-Earth and sub-Neptune regime (Lopez & Fortney, 2013b; Owen & Wu, 2013; Salz et al., 2016a).

Despite these limitations, PLATYPOS makes it feasible to visualize how even the inclusion of a few physical parameters can significantly alter the predicted future mass and radius evolution of a planet. This includes the stellar activity evolution, and with it a star's X-ray saturation luminosity, spin-down behavior, and EUV emission, but also planetary parameters like core mass or initial envelope mass fraction. A third important component is the evaporation model, in particular, the mass-loss rate estimation and the effective XUV absorption radius. In the future, more observations are needed to put tighter constraints on theoretical models and their underlying assumptions.

6.3 Planet V1298 Tau c as an example

We use the innermost planet of the V1298 Tau system to illustrate how PLATYPOS can be used to explore how some of the underlying assumptions regarding the planet and the evaporation-model details impact the mass-loss predictions. In Poppenhaeger et al. (2021), we estimated the fate of the four V1298 Tau

planets using the LoFo models, energy-limited mass loss, and the EUV estimation by Sanz-Forcada et al. (2011b), and showed that the stellar activity track also plays a major role in determining whether a close-in planet can hold on to some atmosphere or will evaporate completely. More details on the role of the host star in photoevaporation population studies will be discussed in Ketzer et al. (in prep.).

We highlight here that the exact details of the planetary structure model affect how quickly a planet cools and contracts. This directly influences the amount of atmosphere needed to match the observed planetary radius at the current age of the system. For a 10 Earth-mass core, using the LoFo model, the innermost planet of V1298 Tau requires an envelope mass fraction of about 8%, while for the ChRo models this value is 14% at an age of 23 Myr. In general, a more massive atmosphere is more compact and thus less susceptible to mass loss. As a direct consequence, the ChRo planet will end up with a more massive atmosphere compared to the LoFo one for the same evaporation model and activity track (see Figure 6.3). Nonetheless, the prediction that the planet can hold on to enough atmosphere to stay above the gap is the same for both planet models under the assumption of a medium activity track and the energy-limited evaporation model. The beta and EUV estimations were calculated as described in Poppenhaeger et al. (2021).

The second observation regards the choice of the evaporation model. For the most irradiated planet in the system, the difference between the energy-limited mass loss and the inclusion of a radiation/recombination-limited regime does not change the final results significantly. We only show the calculation for the medium activity track in Figure 6.3, but the results look qualitatively similar for the low and high activity track. However, the difference in the amount of mass lost between the two evaporation models becomes larger going from a low to high activity track. This is due to the fact that for a prolonged phase of high irradiation levels, the planet is able to cool more efficiently through radiative cooling and thus lose less atmosphere compared to energy-limited mass loss only. A striking difference, however, can be seen when comparing energy-limited (or radiation/recombination-limited) mass loss to the hydro-based calculation. The predicted initial hydro mass-loss rates are more than an order of magnitude higher, which means the planet will lose its atmosphere within less than 300 Myrs (see Figure 6.3).

The EUV estimation can also have a large impact on the final results. In general, the EUV estimation based on surface fluxes by Johnstone et al. (2021) predicts fluxes a few factors lower than the EUV estimation method by Sanz-Forcada et al. (2011b). For V1298 Tau c, this means that the mass loss, in
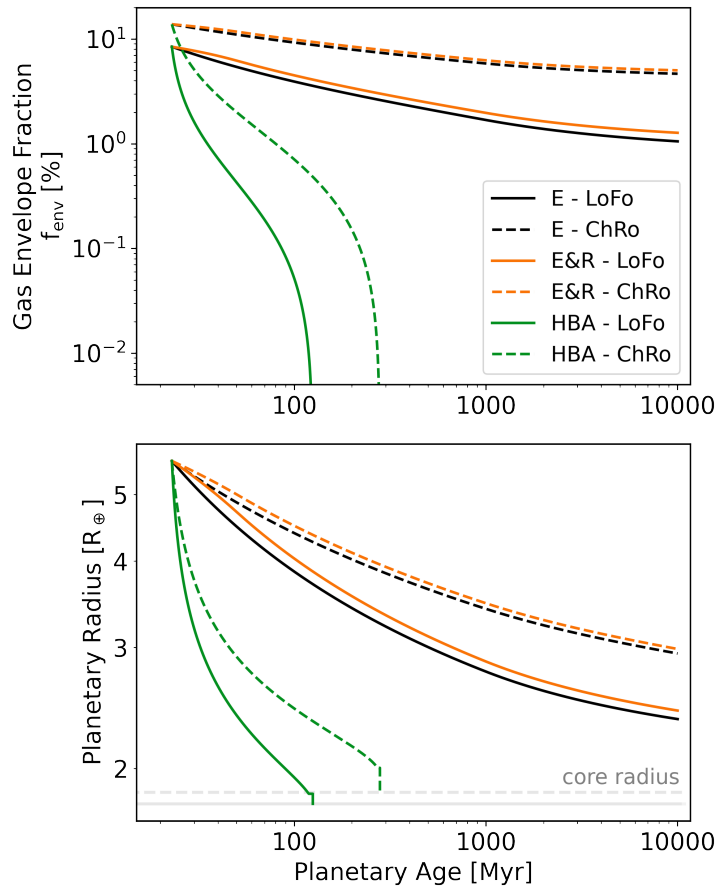
Figure 6.3: Results of our example calculation for the planet V1298 Tau c assuming a 10 Earth-mass core and the medium stellar activity track (gray) from Figure 6.2. The evolved planets all match the observed radius at 23 Myr, the starting age of the simulation. The top panel shows the evolution of the envelope mass fraction, the bottom panel the corresponding radius evolution. We show how the three different evaporation models, as well as the choice of the planetary model, impact the fate of the planet. The energy-limited approximation (E) is shown in black, the evaporation including a radiation/recombination-limited regime (E&R) in orange, and the hydro-based approximation (HBA) in green. The solid lines are for the LoFo model, while the dashed lines represent the ChRo model. The gray lines indicate the radius for a 10 Earth-mass core, as predicted by the LoFo and ChRo models. The sharp drop in radius for the green tracks arises because the planets, after having reached an envelope mass fraction of 0.01%, evaporate completely within the next, 0.01 Myr-short, time step.

particular in the early stages, is less detrimental and more atmosphere can survive. For the LoFo planet, the final fate of the planet is unchanged for all mass-loss calculations, but for the ChRo planet with the more massive initial atmosphere, the lower EUV irradiation from the "Johnstone"-estimation method leads to the planet surviving with about 1% of atmosphere even for the hydro-based mass-loss calculation (see Figure 6.4). This result stresses the importance of having a good handle on the X-ray and EUV luminosity of a star in the first Gyr or so, when the strongest mass-loss is occurring.

Ultimately, not only the details of the mass-loss rate estimation, like evaporation model, effective absorption cross-section or heating efficiency, can make a large difference in the predicted fate of a planetary atmosphere, but also the stellar evolution track, as well as the amount of X-ray and EUV emission from the host star, can change the calculation results significantly. Detailed predictions of the influence of individual parameters in the model across a wide range of stellar and planetary parameters can be complicated due to the large number of partly intertwined model parameters. More observations of escaping atmospheres are needed to put tighter constraints on mass-loss models and to decide if the mass-loss rates are indeed as high as predicted by the hydro-approximation. In addition, more detailed simulations of the interaction with the stellar wind or planetary magnetic shielding can help to determine the true strength of the mass loss in the first few 100 Myrs (see, e.g Carolan et al., 2021). We stress that among all evaporation details, the host star and its level of X-ray and EUV emission in the saturated phase, as well as the timescale for the activity decay should not be neglected in photoevaporation studies.

6.4 Summary

We present PLATYPOS, a publicly available Python code to assess the atmospheric mass loss due to XUV irradiation of planets in the super-Earth and sub-Neptune regime. The code makes it easy to estimate the future mass and radius evolution of a young planet, and to explore the impact of the evaporation model details or the stellar activity evolution on the fate of a planet.

6.5 Acknowledgments
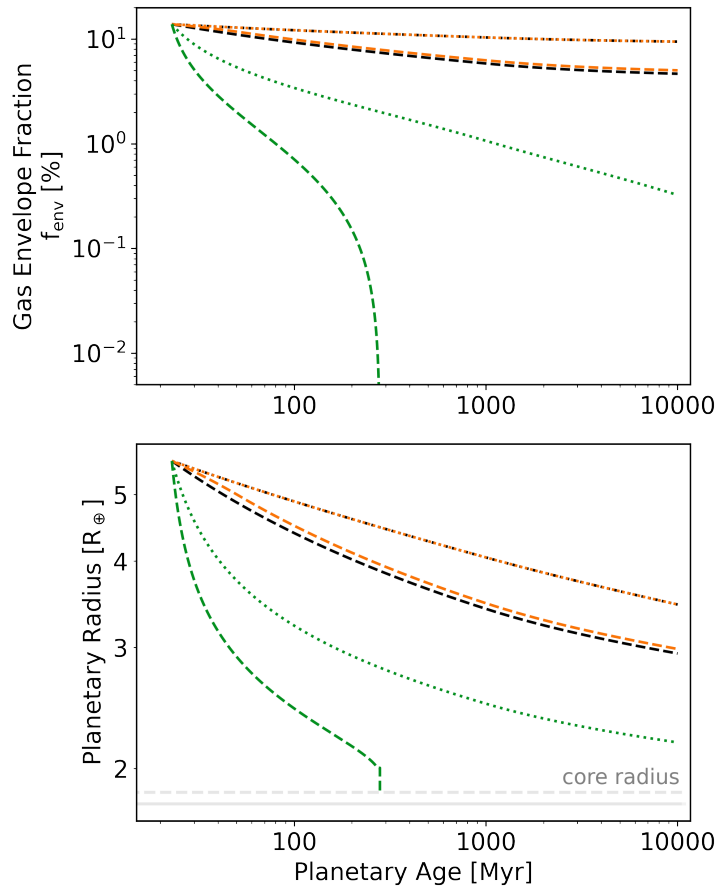
Figure 6.4: Results for the ChRo planet model and all three mass-loss rate estimation methods. The dashed lines are the same as in Figure 6.3, making use of the EUV estimation from Sanz-Forcada et al. (2011b), while the dotted lines represent the evolution for envelope mass fraction and radius for the EUV estimation by Johnstone et al. (2021), which predicts EUV fluxes that are about a factor 4 lower.

7

The influence of host star activity evolution on the population of super–Earths and mini–Neptunes

Abstract

The detected exoplanet population displays a dearth of planets with sizes of about two Earth radii, the so-called radius gap. This is interpreted as an evolutionary effect driven by a variety of possible atmospheric mass loss processes of exoplanets. For mass loss driven by an exoplanet's irradiation by stellar X-ray and extreme-UV photons, the time evolution of the stellar magnetic activity is important. It is known from observations of open stellar clusters that stars of the same age and mass do not all follow the same time evolution of activity-induced X-ray and extreme-UV luminosities. Here we explore how a realistic spread of different stellar activity tracks influences the mass loss and radius evolution of a simulated population of small exoplanets and the observable properties of the radius gap. Our results show qualitatively that different saturation time scales, i.e. the young age at which stellar high-energy emission starts to decline, and different activity decay tracks over moderate stellar ages can cause changes in the population density of planets in the gap, as well as in the observable width of the gap. We also find that while the first 100 million years of mass loss are highly important to shape the radius gap, significant evolution of the gap properties is expected to take place for at least the first 500-600 million years, i.e. the age of the Hyades cluster. Observations of exoplanet populations with defined ages will be able to shed more light on the radius gap evolution.

7.1 Introduction

One of the surprising discoveries of the Kepler mission is not only the abundance of planets below the size of Neptune (Borucki et al., 2010), but even more so the bimodal-structure of the radius distribution of these small planets. The observed population seems to be divided into two distinct groups, the so-called super-Earths and sub-Neptunes (Rogers, 2015), which are separated by a deficit in planets of around $2\,R_\oplus$. This gap-like feature or valley has been shown to have a dependence on the planetary orbital period or irradiation, supporting the interpretation that atmospheric mass loss is the main cause of the substructure in the observed exoplanet population. This had been predicted by theoretical studies (Owen & Wu, 2013; Lopez & Fortney, 2013b) before being observed (Fulton et al., 2017b; Van Eylen et al., 2018b; David et al., 2021).

The prevailing explanation for this gap-like feature is atmospheric erosion caused by the high-energy X-ray and ultraviolet (together: XUV) irradiation from the host star, also known as photoevaporation (e.g. Lopez & Fortney, 2013b; Owen & Wu, 2013, 2017); but also mass-loss driven by the internal luminosity of the cooling planetary core is able to reproduce the observed feature (e.g Ginzburg et al., 2018; Gupta & Schlichting, 2019). In both scenarios it is assumed that planets are born with rocky cores, generally having masses of a few $M_\oplus$, which are surrounded by primordial hydrogen/helium (H/He) atmospheres. Over the course of a planet's life, the strength of the atmospheric mass loss determines whether it is completely stripped of its atmosphere, leaving behind only the bare rocky core (super-Earths), or if it can hold on to some fraction of its envelope, retaining a radius which places it above the radius gap (sub-Neptunes).

In the photoevaporation scenario, the stellar environment plays a crucial role in the evolution of the planetary atmosphere over time. Stellar high-energy photons, ranging from UV to X-rays, shape a planet's atmosphere by dissociating molecules and photoionizing atoms. They alter the chemistry in the atmosphere and cause significant heating, which, in turn, can drive a hydrodynamic outflow, leading to the loss of the atmosphere over time (Watson et al., 1981b; Lammer et al., 2003; Lecavelier des Etangs et al., 2004). To properly take into account this externally-driven mass-loss process, it is necessary to understand the evolution of the host-star activity over time. Stellar activity is an umbrella term used to describe phenomena related to the presence of magnetic fields in cool stars, like the chromospheric and coronal high energy emission, or stellar flares and coronal mass ejections. As stars age, stellar rotation and the magnetic activity, which is driven by the stellar dynamo,

decrease hand in hand. The amount of XUV radiation a star produces depends on several factors like age, activity level and rotation, as well as spectral type (Preibisch & Feigelson, 2005a; Wright et al., 2011b; Jackson et al., 2012a; Reiners et al., 2014; Tu et al., 2015b; Johnstone et al., 2021).

The first few hundred million years are thought to sculpt planetary atmospheres most strongly, since this is the timescale over which stars maintain high activity levels and thus planets receive the highest XUV flux. Additionally, in the early stages of planetary evolution, planets still host extended atmospheres because they have not had enough time to cool and contract. The interplay between these factors leads to the general assumption that the most significant photoevaporative mass loss is taking place early on (e.g. Owen & Alvarez, 2016). Core-powered mass loss on the other hand is a more gradual process, sculpting planets on gigayear timescales. Recent observational studies investigating the age dependence and time evolution of the radius gap hint that the fraction of super-Earths to sub-Neptunes increases with stellar age, going from young planets less than 1-2 Gyr to older ones (Berger et al., 2020; Sandoval et al., 2021). Additionally, the radius gap appears to fill in over gigayear timescales (David et al., 2021). While this could be seen as an indication of core-powered mass loss, the results, due to the very small number of planets with ages less than a few 100 Myr, do not yet constrain the evolution at the earliest times, when photoevaporation is thought to dominate the mass loss (e.g. Owen & Wu, 2017). On top of that, the exact time evolution of the stellar X-ray and EUV output can extend the timescale where photoevaporative mass loss is important to Gyrs (King & Wheatley, 2021).

An additional complication arises from stars of similar mass experiencing a non-uniform stellar spin down. One cause may be the different initial rotation rates that stars are born with, or differences in the magnetic field complexity (Tu et al., 2015b; Garraffo et al., 2016). As a consequence, a stars' spin-down behavior varies and with it the age at which the spin-down, and thus the activity decay, sets in. If differences in the initial rotation rate are the cause, the timescale for the onset of the activity decay can range from a few Myr to a few 100 Myr, for slow and fast rotators, respectively. This leads to a spread of about an order-of-magnitude in the activity levels of young stars with similar masses, comparable to what has been observed (Wright et al., 2011b; Tu et al., 2015b; Johnstone et al., 2021). The stellar activity evolution in the first several 100 Myrs is thus another factor that needs to be taken into account when estimating the future planetary mass and radius evolution of young systems over time (e.g. Kubyshkina & Vidotto, 2021). For individual systems with mature ages of several Gyrs where the planets have retained

some fraction of their primordial atmosphere, it is already possible to put constraints on the past rotational history of the host star using the measurable present day planet properties. This approach exploits the fact that the observed properties like the planetary radius depend strongly on the mass-loss history of the planet, which is driven by the amount of high energy flux received by the planet during its lifetime; and the emitted XUV flux, in turn, is determined by the rotational evolution of the host star (Kubyshkina et al., 2019b,a; Bonfanti et al., 2021). While this approach is promising for well constrained, individual systems, the rotational histories of most exoplanet host stars known to date remain unconstrained.

In this work, we study the effect of various stellar activity tracks on the radius distribution of an observationally motivated population of exoplanets. We compare an energy- and radiation-recombination-limited model with hydro-based mass-loss rates, and highlight how sensitively photoevaporation calculations depend on the assumed X-ray saturation timescale and luminosity, as well as the estimation of the EUV contribution to the total high-energy flux. Details on the input physics of the planetary structure model and the mass-loss calculations are given in Section 7.2. A detailed description of the host star activity model, i.e. the stellar XUV evolutionary tracks used for this work, are provided in Section 7.3. In Section 7.4, we describe the input planet population and provide details on the simulation setup. We summarize our findings regarding the influence of the activity tracks on the 1D and 2D radius distribution of our sample population in Section 7.5.

7.2 Planetary mass loss

We use a coupled thermal evolution and atmospheric photoevaporation model to investigate the mass loss and subsequent radius evolution of a large population of planets (similar to e.g. Lopez & Fortney, 2013b, 2014b; Owen & Wu, 2013, 2017). We consider here the atmospheric mass loss driven by stellar XUV photons, and investigate how the inclusion of a distribution of low, medium, and high activity tracks for the host star – as opposed to assuming only one track for all stars in the population – affects the final planetary radius distribution at mature system ages. Our calculations are performed with the publicly available python code PLATYPOS[1], for which a description of the code's functionality was presented in Ketzer & Poppenhaeger (2022). In the following, we describe the relevant inputs for this work in more detail.

---

[1]https://github.com/lketzer/platypos/

7.2.1 Planetary models

PLATYPOS gives the choice to select either the planetary structure models by Lopez & Fortney (2014b) or the MESA-based models by Chen & Rogers (2016) (hereafter: LoFo14 and ChRo16). The models assume the planetary cores to be of an Earth-like mixture of silicates and iron, with the surrounding envelope composed of predominantly hydrogen and helium. Lopez & Fortney (2014b) and Chen & Rogers (2016) compute planetary radii for a large grid of planetary parameters, and provide fitting formulae to estimate the radius at a specified age, core mass, envelope mass fraction, f_{env}, and bolometric incident flux. For specific details of these models, we refer to the original publications. We use their fitted mass-radius-age relations for low-mass gaseous sub-Neptune-sized planets to estimate their radius at any given time over the course of the simulation. For this paper, we choose to use the MESA-based ChRo16 model because the resulting radius gap qualitatively best matches the observations. This comparison is based on the assumption the planet radius from the evolutionary models is equal to the optical white light transit radius. Transit radii in narrow wavelength bands can be different due to additional absorption in the thin atmosphere; however, this is outside the scope of this work. We discuss differences with the LoFo14 model and motivate our choice for the ChRo16 model in Appendix 7.8.1.

A caveat of both models is that the fitting formulae should only be used within a certain range of planetary parameters, with age and envelope mass fraction being of particular importance for our calculation. In general, the first 100 Myr of planetary evolution are influenced by the assumed initial conditions. Both the LoFo14 and ChRo16 models assume the so-called hot-start scenario, where planets form with large initial entropy and thus present enlarged radii at a young age (Marley et al., 2007; Fortney et al., 2007). Those authors note, however, that due to the short cooling timescale for the enlarged, low-mass hot-start planets, the rapid initial cooling and subsequent contraction erases any differences resulting from the choice of initial entropy by ~ 10 Myr. Lopez & Fortney (2014b) explicitly showed that the modeled planetary radii can be reasonably backwards extrapolated to ages of 10 Myr (see their Figure 2), and we therefore chose to extrapolate both models to 10 Myr as the starting age of our simulations.

Both model-fits are also only valid for planets with an atmospheric mass fraction greater than 0.01%, but planets in our sample undergo mass loss, and thus might enter a regime with an envelope less than this lower f_{env} limit. Rogers & Owen (2021) note that below an atmospheric mass fraction of 0.01%

the planetary radius becomes indistinguishable from the core radius in transit observations, making it reasonable to assume complete stripping below this limit. We performed two test simulations to assess the effect of extrapolating the models to atmospheric mass fractions below 0.01%. Once, we allow for extrapolation and continue decreasing the envelope mass until no envelope is remaining, or the simulation reaches the final age. For comparison, once a planet reaches the lower limit, we keep $f_{\rm env}$ fixed at 0.01% for the remainder of the simulation run, and continue the mass-loss calculation with a constant envelope mass. We find that in general, if a planet reaches an envelope mass fraction of $f_{\rm env} = 0.01\%$, it cannot hold on to its atmosphere regardless of the radius estimation in the final stages.

7.2.2 Mass-loss rate calculation

Several regimes of hydrodynamic escape of hydrogen-dominated atmospheres have been identified in theoretical studies (e.g. Lammer et al., 2003; Murray-Clay et al., 2009a; Owen & Jackson, 2012b; Owen & Alvarez, 2016). This includes energy-limited, radiation-recombination limited and photon-limited escape. Recent observational evidence of giant planets support the presence of these regimes (Lampón et al., 2021), which differ in terms of the underlying physics of the escaping planetary wind. Important is the consideration of how neutral hydrogen is produced and lost, but also the processes of converting the absorbed stellar radiation into work, which ultimately drives the evaporative outflow, has to be taken into account.

We built different evaporation schemes into PLATYPOS, which allows us to compare them against each other. Photoevaprative mass loss can be estimated using an energy-limited approximation only, including the radiation-recombination limited regime, or via a hydro-based approximation, which takes into account not only the contribution from high-energy radiation but also the planetary intrinsic thermal energy and surface gravity (Kubyshkina et al., 2018a). The different evaporation scenarios and their respective parameterized mass-loss rate calculations are explained below.

Energy-limited mass loss

The stellar high-energy radiation impinging on the planet photoionizes and heats the gas in the upper atmosphere. Mass loss occurs in the energy-limited regime when a (significant) fraction of the external energy supply is efficiently used to do PdV work expanding the atmosphere and lifting material out of the

planet's gravitational well, while little energy is lost to radiation and internal energy changes (Murray-Clay et al., 2009a). We adopt the commonly used energy-limited hydrodynamic escape model (see e.g. Owen & Jackson, 2012b; Lopez et al., 2012), which assumes that the mass-loss rates are limited by the stellar radiative energy deposition and scale linearly with the high energy incident flux:

$$\dot{M}_{\mathrm{Elim}} = -\epsilon \frac{(\pi R_{\mathrm{XUV}}{}^2) F_{\mathrm{XUV}}}{K G M_{\mathrm{pl}}/R_{\mathrm{pl}}} = -\epsilon \frac{3\beta^2 F_{\mathrm{XUV}}}{4 G K \rho_{\mathrm{pl}}}, \tag{7.1}$$

where ϵ is the efficiency of the atmospheric escape, M_{pl} the mass and ρ_{pl} the density of the planet, F_{XUV} the high-energy flux received by the planet, and R_{pl} and R_{XUV} the planetary radii at optical and XUV wavelengths, respectively; we use $\beta = R_{\mathrm{XUV}}/R_{\mathrm{pl}}$ as a shorthand in the following. The factor K encompasses the impact of Roche lobe overflow (Erkaev et al., 2007), and can take on values of 1 for no Roche lobe influence and < 1 for planets filling significant fractions of their Roche lobes. The values for the efficiency parameter, ϵ, reported in the literature, range from as high as 0.4 (Lalitha et al., 2018) down to 0.01 and lower for Jupiter-mass planets (Murray-Clay et al., 2009a; Salz et al., 2016a; Lampón et al., 2021). Planets in the mass regime of sub-Neptunes are predicted to have heating efficiencies between 10 and 30% (e.g Owen & Wu, 2013; Salz et al., 2016a).

Radiation/recombination-limited mass loss

At high UV fluxes, the temperature of the planetary wind and the ionization fraction become so high that the flow enters a state of radiation-recombination equilibrium. Recombination of hydrogen becomes so efficient that a considerable fraction of the absorbed UV energy is efficiently lost to the subsequent cooling radiation, particularly through the hydrogen Lyman-alpha (Ly α) line. The losses regulate the gas to a near-constant temperature of $\sim 10^4$K, which leads to a shallower dependence of the mass-loss rates on the incoming high energy flux ($\dot{M} \propto \sqrt{F_{XUV}}$) (e.g. Murray-Clay et al., 2009a; Salz et al., 2016a). Recent calculations using a hydrodynamics code for exoplanetary atmospheres and explicitly solving the photoionization equilibrium give a more detailed view on the relation between high-energy heating and radiative cooling of individual modelled exoplanets (Caldiroli et al., 2021, 2022).

Following Chen & Rogers (2016); Lopez (2017); Lopez & Rice (2018), we use a modified prescription for the mass-loss rate, which takes into account the influence of significant radiative cooling for highly irradiated planets (Murray-Clay et al., 2009a). The mass-loss rate is given by:

$$\dot{M}_{\mathrm{RRlim}} = -4\pi c_{\mathrm{s}} R_{\mathrm{s}}^2 \mu_{+,\mathrm{wind}} m_{\mathrm{H}} \left(\frac{F_{\mathrm{XUV}} G M_{\mathrm{pl}}}{h\nu_0 \alpha_{\mathrm{rec,B}} c_{\mathrm{s}}^2 R_{\mathrm{XUV}}^2} \right)^{1/2} \times \exp\left[\frac{G M_{\mathrm{pl}}}{R_{\mathrm{XUV}} c_{\mathrm{s}}^2} \left(\frac{R_{\mathrm{XUV}}}{R_{\mathrm{s}}} - 1 \right) \right]$$

(7.2)

where R_{s} is the radius of the sonic point and $c_{\mathrm{s}} = (k_{\mathrm{B}} T_{\mathrm{wind}}/\mu_{\mathrm{wind}} M_H)^{1/2}$ the isothermal sound speed of a fully ionized wind at the sonic point. For H/He envelopes, the mean molecular weight of the wind is set to $\mu_{\mathrm{wind}} = 0.62$, taking into account that most of the hydrogen is ionized. The case B radiative recombination coefficient for hydrogen at 10^4 K is $\alpha_{\mathrm{rec,B}} = 2.70 \times 10^{-13}$ cm^{3}s^{-1}, and the mean molecular weight of ions at the base of the wind is given by $\mu_{+,\mathrm{wind}} = 1.3$. The formula given above is only correct when R_{XUV} does not exceed R_{s}, which may not be true for many low-mass planets early in their evolution. In case of $R_{\mathrm{XUV}} > R_{\mathrm{s}}$ at any given point in the simulation, we impose that $R_{\mathrm{XUV}} = R_{\mathrm{s}}$. To greatly simplify the calculation, the spectral dependence of the incoming photons is neglected, and instead, following Murray-Clay et al. (2009a), we assume that the ionizing radiation has a typical photon energy of 20 eV. For a more detailed explanation on the calculations of this mass-loss rate, see Section 2.3 in Lopez (2017).

For each time step of our calculation, we evaluate both the radiation/recombination-limited and energy-limited mass-loss rate and adopt the lesser of the two. This is to ensure that the mass-loss rates for highly irradiated planets, particularly at young ages when the host star is still very active, are not overpredicted.

Hydrodynamic-based approximation

Kubyshkina et al. (2018b) argue that the energy-limited mass-loss rates can be severely underestimated for highly irradiated low-density planets or overestimated for planets with hydrostatic atmospheres. They compute a large model grid of hydrodynamic upper atmosphere models (Kubyshkina et al., 2018a) and present, based on the grid results, an analytical expression for the mass-loss rates as a function of the system parameters. This "hydro-based approximation" assumes an efficiency of $\epsilon = 0.15$, takes into account Roche-lobe effects, and self-consistently accounts for the effective absorption radius (i.e. β, which is given by the ratio of the XUV to the optical planetary radius). It is important to note that in their upper-atmosphere simulations, atmospheric escape can, in addition to being XUV-driven, also occur due to a favorable combination of planetary intrinsic thermal energy and low surface gravity. This is a major

difference to the energy- and/or radiation/recombination limited mass-loss rate calculations, where only XUV-driven escape is taken into account. Their results show that mass-loss rates for planets in a so-called "boil-off" regime are several orders of magnitude, up to 10^8, larger than compared to energy-limited mass-loss rates. For planets with higher masses and/or lower incident fluxes, on the other hand, the energy-limited mass-loss rates can be overestimated by up to a factor 50 (Kubyshkina et al., 2018b).

For this paper, we choose to calculate the mass-loss rates based on the energy-limited approximation, but with the inclusion of a radiation/recombination-limit as described in Section 7.2.2. Due to recent cautions (see Krenn et al., 2021) about energy-limited mass loss, we also perform our simulations using hydro-based mass-loss rates for comparison. The main differences and implications for our simulations are discussed in Appendix 7.8.3, where we show that hydro-based mass loss evaporates most mini-Neptunes in our simulations, leaving behind almost no planets above the gap for the initial planet population used in this work.

7.2.3 Effective absorption radius

Planetary radii can have vastly different sizes when observed at X-ray, EUV or optical wavelengths (Poppenhaeger et al., 2013a; Kulow et al., 2014; Ehrenreich et al., 2015). Optical photons can penetrate much deeper into the atmosphere, while high-energy photons are readily absorbed in higher altitudes. In addition, planetary parameters like the gravitational potential affect the height at which XUV photons are absorbed, with some lower-mass planets hosting extended atmospheres a few times the size of the optical radius (e.g. Salz et al., 2016a; Lampón et al., 2021). That planets appear significantly larger at shorter wavelengths is further supported by UV and X-ray observations of the gas giant HD 189733 b, which show an enhanced transit depth and thus indicate an enlarged XUV absorption radius (Poppenhaeger et al., 2013a).

The effective absorption radius of the high-energy radiation, R_{XUV}, is only weakly constrained by existing observations. To obtain reasonable mass-loss rate estimates, R_{XUV} (i.e β) needs to be estimated. The two available methods are the relation by Salz et al. (2016a) (from here on called "Salz-β"), as well as the relation presented in Chen & Rogers (2016) and Lopez (2017), which follows the arguments presented in Murray-Clay et al. (2009a) (we label this "Lopez-β"). The "Salz-β" calculation is motivated by results from detailed numerical simulations, while the "Lopez-β" is derived from analytical calculations. In our simulations, we choose to use the "Lopez"-β". We also introduce "Salz"-β" in

Appendix 7.8.2, and then compare and discuss the two methods. For both methods, we impose that the effective absorption radius, R_{XUV}, cannot be larger than the Roche lobe radius of the planet. If R_{XUV} exceeds the Roche lobe at any point in the simulation, we set R_{XUV} equal to the Roche lobe radius, R_{Rl}. It is given by $R_{\mathrm{Rl}} = a(M_{\mathrm{pl}}/(3M_{\mathrm{pl}} + M_*))^{1/3}$, where a denotes the semi-major axis of the planet. In general, we find that young, low mass planets which are most prone to fulfilling this criterion in their early evolution, do not stand a chance of retaining an atmosphere in our simulations.

"Lopez-β" calculation

Following Chen & Rogers (2016) and Lopez (2017), we also implement a theoretical approximation to estimate the radius of the XUV photosphere, which is based on simplifying assumptions on the structure of the atmosphere. The photoionization base of the evaporative wind is where the atmosphere becomes optically thick to XUV photons, and the difference between the XUV and optical photosphere can be estimated as follows

$$R_{\mathrm{XUV}} - R_{\mathrm{pl}} \approx H_{\mathrm{below}} \times \ln\left(\frac{P_{\mathrm{photo}}}{P_{\mathrm{XUV}}}\right), \qquad (7.3)$$

with $H_{\mathrm{below}} = (k_{\mathrm{B}}T_{\mathrm{eq}})/(\mu_{\mathrm{below}}m_{\mathrm{H}}g)$ approximating the scale height of the atmosphere between the optical and the XUV photosphere. This layer is taken to be close to isothermal at the equilibrium temperature of the visible photosphere, T_{eq}, and having a mean molecular weight of $\mu_{\mathrm{below}} = 2.5$ due to H/He being in molecular form below the photoionization base. At the visible photosphere, the pressure is set to $P_{\mathrm{photo}} \simeq 20\,\mathrm{mbar}$ (Fortney et al., 2007), while at the XUV photosphere it is approximated by $P_{\mathrm{XUV}} \approx (m_{\mathrm{H}}GM_{\mathrm{pl}})/(\sigma_{v_0}R_{\mathrm{pl}}^2)$, using $\sigma_{v_0} = 6 \times 10^{-18}(h\nu_0/13.6\mathrm{eV})^{-3}\mathrm{cm}^2$. Instead of taking the whole spectrum into account, we assume that the typical energy of an ionizing photon is $h\nu_0 = 20\,\mathrm{eV}$ ($\sim 60\,\mathrm{nm}$) (Murray-Clay et al., 2009a).

7.3 Host star activity evolution

Once the protoplanetary disk dissolves, a planet orbiting a young star becomes exposed to high energy radiation from the host star. For orbital periods less than 100 days, this is expected to drive the erosion of the planetary atmosphere. As stars age, rotational spin-down causes a decrease in magnetic activity and with it their high-energy X-ray and ultraviolet emission (e.g. Güdel et al., 1997;

Ribas et al., 2005b; Booth et al., 2017). Young stars with ages less than a Gyr emit XUV radiation that can be several orders of magnitude higher than for the present-day Sun. For planets, the XUV irradiation level thus is much higher in the early stages compared to more mature ages. As a result, their atmospheres are hotter, more expanded and therefore more susceptible to mass loss. When investigating the atmospheric erosion of planetary atmospheres, it is thus important to account for changes in the mass-loss rates induced by changes in the received XUV flux.

In this study, we take into account the observed spread in X-ray luminosities of stars in open clusters with ages below a gigayear by modelling the host star activity evolution with a range of spin-down ages (Tu et al., 2015b; Johnstone et al., 2021). By spin-down or saturation time, we mean the age until which a star emits intense XUV flux at a constant level before decreasing. This is in contrast to most previous population studies (e.g Owen & Wu, 2017; Lopez, 2017; Rogers & Owen, 2021), which assume only one track with a saturation timescale of 100 Myr for all planet hosting stars. As has been pointed out by King & Wheatley (2021), the EUV contribution to the total high energy flux received by a planet can also significantly influence the mass-loss history of a planet, in particular after the X-ray dominated saturated phase due to the shallower decay of the stellar EUV emission compared to X-rays. To estimate the stellar EUV flux for a wide range of ages and activity levels, we make use of an X-ray and EUV surface flux relation, instead of assuming X-rays and EUVs decline at the same rate (Chadney et al., 2015; Johnstone et al., 2021).

7.3.1 Stellar activity decay

Magnetic activity and rotation are closely linked via the stellar dynamo, and decrease together as stars age. Observations of young cluster stars with similar masses and ages show that there is a large spread in rotation rates before ~ 500 Myr (Jackson et al., 2012a; Tu et al., 2015b). Stars at such young ages tend to cluster either on the fast or the slow rotational branch (Barnes, 2003d). As mentioned previously, models for the stellar rotation evolution predict a relatively rapid spin-down at a wide range of ages, or saturation times, where the long-term rotational evolution is determined primarily by stellar mass and initial rotation rate (Wright et al., 2011b; Matt et al., 2015; Tu et al., 2015b; Gondoin, 2018; Johnstone et al., 2021). Magnetic field complexity has also been considered as a factor impacting the spin-down (Garraffo et al., 2018), and the underlying cause for the spin-down is still not fully explained. What has been observed is that earlier-type stars staying in the saturated regime
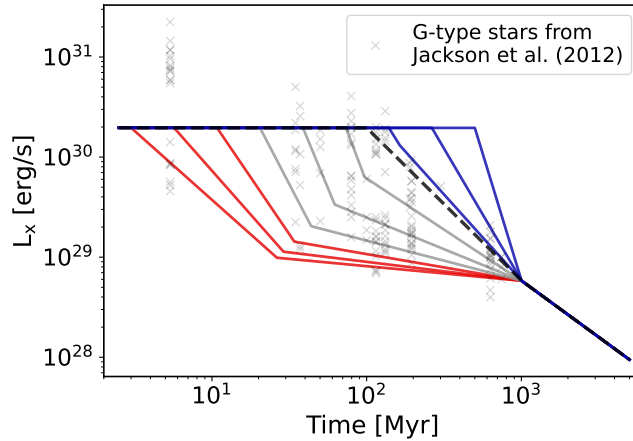
Figure 7.1: X-ray evolutionary tracks for a solar-mass star used in this work. Our tracks, which are motivated by the models from (Tu et al., 2015b; Johnstone et al., 2021), encompass the observed spread in observed X-ray luminosities for stars with ages younger than a Gyr. The X-ray measurements for G-type stars in the sample from Jackson et al. (2012a) are shown as gray X's. In red, gray and blue colors we show low, intermediate and high activity tracks. For comparison, we show the widely used "median track" with a saturation time of 100 Myr as the black dashed line.

longer than later-type stars, and that stars with similar stellar mass undergo a non-uniform spin-down. Some are able to maintain their high activity level for prolonged periods of time, while others start their spin-down and thus decrease in activity around the time the disk dissipates.

The dearth of stars with intermediate rotation periods in young open cluster (e.g Fritzewski et al., 2021b) implies that the spin-down of an individual star, once it has started, happens relatively quickly. Therefore, we assume a spread of onset ages for rotational spin-down, ranging from a few Myr to a few hundred Myr, followed by a rapid decay phase. At ages of around 1 Gyr, stars seem to converge and continue a similar rotation and X-ray luminosity evolution. This ultimately translates into a wide distribution of evolutionary tracks for the X-ray luminosity at ages younger than ~ 500 Myr (see Fig. 7.1).

Motivated by the rotational evolution model for solar-like stars $(0.9 - 1.1 \, M_\odot)$ by Tu et al. (2015b) and the updated models by Johnstone et al. (2021), we approximate the different stellar activity tracks by broken power-law models; as opposed to assuming a saturated phase followed by a single power-law decline only (see e.g. Owen & Wu, 2017; Mordasini, 2020). Each activity track

corresponds to a specific saturation time, t_{sat}, until which the star stays at a constant X-ray saturation luminosity. When the star falls out of the saturated regime, the X-ray decay can proceed with a one- or two-piece power-law until the age of 1 Gyr, where all tracks are set to converge. Tracks with a two-piece drop in X-ray luminosity are set to decay within ∼ 25 Myr. For the convergence point, we choose an X-ray luminosity that is motivated by the median value for all G-type stars in the oldest cluster in the sample by Jackson et al. (2012a). Beyond 1 Gyr, the X-ray-decrease proceeds with a power-law index which is set to −1.13, a value typical for Sun-like stars (Jackson et al., 2012a). This X-ray decay slope is also in good agreement with the activity evolution models by Johnstone et al. (2021), but shallower than the slope used in Tu et al. (2015b) (∼ −1.6), which was calibrated to match the current solar X-ray luminosity (Tu et al., 2015b). We note that the slope used for the X-ray and EUV decay in many other evaporation studies is often quite steep, with values up to −1.5 (e.g. Owen & Wu, 2017; Rogers & Owen, 2021). A power-law decline with such a steep slope implies that the total high-energy emission is dominated mostly by the saturated phase.

In Figure 7.1 we show the set of nine activity tracks for a one solar-mass star used in this work, together with a 100 Myr "median track" for comparison. The saturation timescales are evenly spaced in log-space, ranging from 3 to 500 Myr. Since we want to investigate the effect of a mixture of stellar activity tracks on the final radius distribution of a sample of exoplanets, we need to assign each track with a certain occurrence probability. Informed by the spin-down-age dependence on stellar mass from Johnstone et al. (2021) (see their Figure 10), we choose a mean saturation time of 40, 25 and 15 Myr for K, G and F stars, respectively. From 0.9-1.1 $M_\odot$ we count a star as G-type, while lower masses are taken as K, and higher masses as F spectral type. For each of the three mass bins, we construct a lognormal probability distribution for the saturation time, with 40, 25 and 15 Myr as the mean and a standard deviation of 0.45. With this in hand, we can estimate the probability that a random star, with a given mass, will evolve along one of the nine tracks. For a G-type star, 60% of stars will follow one of the gray intermediate tracks, while 30% follow one of the low activity, red tracks and 10% one of the blue high activity ones. A consequence of the mass dependence is that more K stars will follow the higher activity gray and blue tracks in Figure 7.1, while most F stars fall out of the saturation regime early on and will mainly follow the red and gray tracks.

Another important parameter of a realistic stellar activity track is the value of the X-ray luminosity, $L_{\text{X}_{\text{sat}}}$, in the saturated phase. We use the relation by Wright et al. (2011b), given by $\log(L_{\text{X}_{\text{sat}}}/L_{\text{bol}}) = 10^{-3.13}$, to estimate $L_{\text{X}_{\text{sat}}}$. This

relation is almost independent of spectral type, which means we can use it for all the K, G and F stars in our sample. To take into account that we start our calculations at very early ages when some stars are still on the pre-main sequence, we use the bolometric luminosity right when a star reaches the Zero Age Main Sequence (ZAMS) to estimate the X-ray saturation luminosity. We find that this approach gives more reasonable saturation values for stars with masses higher than the Sun, when compared to using a main-sequence mass-luminosity relation (Pecaut & Mamajek, 2013). The bolometric luminosities at the ZAMS for stars of a given mass are extracted from the pre-MS MESA models by T. Steindl (priv. comm.).

7.3.2 Estimating the stellar EUV luminosity

While X-rays ($\sim 10 - 100$ Å) can contribute to atmospheric heating, in particular for young active stars (Owen & Jackson, 2012b), it is the stellar EUV emission ($100 - 912$ Å) that provides the majority of radiation power to ionize hydrogen in planetary atmospheres (e.g. Murray-Clay et al., 2009b; Sanz-Forcada et al., 2011b; Wang & Dai, 2018b). Atmospheric mass loss ultimately depends on the combined XUV input, since both X-rays and EUVs heat the upper atmosphere and thus drive the escaping wind. While X-ray measurements are readily available with current space-based telescopes, observing the UV emission from stars other than the Sun is challenging. Between ~ 400 and 912 Å (the H ioniyation threshold) the interstellar medium absorbs all radiation, even for nearby stars. Currently, no spaced-based telescopes for the observable portion of the EUV spectrum ($\lesssim 400$ Å) are in operation, and archival data is only available for a handful of stars. This complicates the estimation of the important EUV content for planet hosting stars.

A simplification that is often made in photoevaporation studies is to assume that the EUV and X-ray irradiation of planetary atmospheres decline at the same rate (e.g. Owen & Jackson, 2012b; Owen & Wu, 2017; Mordasini, 2020; Rogers & Owen, 2021). Studies of the Sun's high energy emission over the course of the solar activity cycle have shown, however, that the EUV emission remains rather strong as X-ray surface flux decreases (Chadney et al., 2015; King et al., 2018). Chadney et al. (2015) further demonstrated that simply scaling the entire solar spectrum based on measured stellar X-ray fluxes is not appropriate for stars with spectral types and/or activity levels other than the Sun. They show that, instead, a power-law relation between EUV and X-ray *surface fluxes* provides a more effective way to estimate the unobservable stellar EUV emission. This relation prevents a significant overestimation of the stellar

EUV output for young and active stars, but also implies that the stellar EUV output falls off less steeply in time than X-rays. This is also in agreement with e.g. Ribas et al. (2005b); Claire et al. (2012); Shkolnik et al. (2014); King & Wheatley (2021) who showed that for sun-like stars, the X-ray emission decays faster than the EUV one. The use of a single relation between X-ray and EUV surface fluxes for all spectral types is further supported by Johnstone et al. (2021), who note that the relation seems to hold true also for young and active planet-hosting stars on the pre-main sequence.

As a consequence of the shallower EUV decline, the total XUV radiation received by an exoplanet at Gyr-timescales can still be high enough to cause considerable mass-loss at later times well past the saturated phase (King & Wheatley, 2021). To take this into account in our mass-loss simulations, we assume that X-ray and EUV luminosities evolve hand in hand (see Section 7.3.1), but decaying at different rates. The power-law slopes of the X-ray decline are given by our model for the stellar activity evolution, while the EUV emission is estimated via the updated surface-flux scaling relation by Johnstone et al. (2021) (short: Jo21). We use the main-sequence mass-radius relation by Eker et al. (2018) to convert the surface fluxes to luminosities, and then take the total high energy output of the star as the combined X-ray and EUV luminosity.

In Figure 7.2 we compare several EUV estimation methods for a $1\,M_\odot$ star. In addition to the X-ray and EUV surface flux relation by Chadney et al. (2015) and Johnstone et al. (2021), we show two other EUV estimation methods widely used in the literature. One is the empirical scaling relation between X-ray and EUV energy bands for late-type stars based on synthetic XUV spectra by Sanz-Forcada et al. (2011b), while the other makes use of the tight correlation between X-ray and Lyα luminosities for a sample of K to F dwarfs (Linsky et al., 2013), which in turn can be used to estimate EUV luminosities from Lyα measurements (Linsky et al., 2014) (short: Li14). In this work, we have chosen the method by Johnstone et al. (2021), Jo21, as our baseline, but the other options can be calculated with PLATYPOS as well (see Appendix 7.8.6). Figure 7.2 shows that for highly active stars the relation by Sanz-Forcada et al. (2011b) (short: SF11) predicts EUV luminosities which can be more than an order of magnitude higher than the estimates from Lyα or the surface flux relations.

7.3.3 Integrated XUV emission

Figure 7.3 shows the time-integrated XUV emission for a low, intermediate and high activity track (red, gray, blue) of a solar mass star, together with
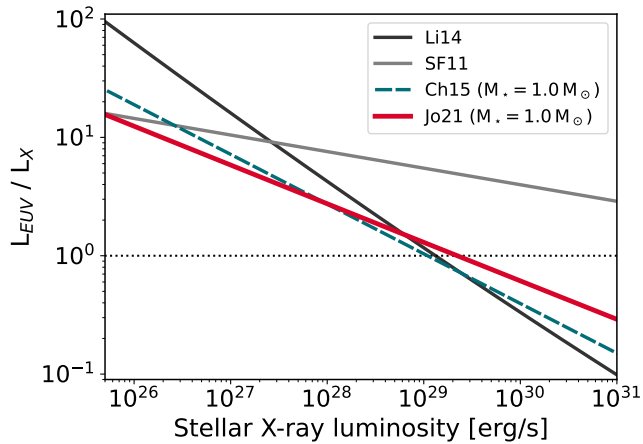
Figure 7.2: Estimates of stellar EUV emission for a range of X-ray luminosities based on four different methods. The relation by Sanz-Forcada et al. (2011b) (SF11) is shown in gray, the one by Linsky et al. (2014) (Li14) in black, and the surface-flux relations by Chadney et al. (2015) (Ch15) and Johnstone et al. (2021) (Jo21) in blue and red, respectively. The surface-flux relations have a slight mass-dependence, and we only show the $1\,M_\odot$ case.

a commonly used 100 Myr track (black). These tracks are constructed as described in Sec. 7.3.1, with the EUV content estimated according to the power law relation between X-ray surface fluxes and EUVs by Johnstone et al. (2021) (Jo21). For comparison, we also show the XUV tracks from King & Wheatley (2021) (Ki21) and Rogers & Owen (2021) (Ro21). For easier comparability, we normalize everything to the cumulative XUV emission of the 100 Myr track at 100 Myr. We show this comparison for two reasons. One is to make the reader aware of how much differences in the choice of X-ray and EUV saturation luminosity and decay slope can impact the emitted stellar XUV radiation over time, and the other is to show how different saturation timescales, i.e. a low, intermediate and high stellar activity track, reflect on the total XUV luminosity around 100 Myr and at Gyr ages.

The first thing we want to highlight is the difference in XUV saturation luminosity between our tracks with the Jo21 EUV estimation and the Ro21 tracks. Due to the lower saturation luminosity (factor 2.4 lower than ours) and the steeper XUV decline of the Ro21 track, their integrated XUV emission at 10 Gyr is comparable with the emitted radiation in the first 100 Myr of a star which follows one of our higher activity tracks. So overall, the planets in our

sample receive significantly larger integrated XUV fluxes when compared to the works by e.g. Rogers & Owen (2021) or Owen & Wu (2017). Due to the similar X-ray saturation luminosity between the Ki21 and Ro21 tracks, the Ki21 tracks give a XUV emission similar to the Ro21 tracks in the first 100 Myr, but their shallower EUV decline causes the EUV emission beyond one Gyr to still contribute significantly to the total XUV flux.

The second thing we want to point out is the difference in the time-integrated XUV emission before ~ **1Gyr** between our low, intermediate, and high activity track with the Jo21 EUV estimation. If a star drops out of the saturated regime early on, the total XUV flux received by a planet by the age of 100 Myr can be a factor 10 lower than for a planet around a star that stays saturated longer. So while the cumulative emission at 10 Gyr is comparable within a factor 4 between the low activity and reference track, a planet around a low activity star receives much less flux early on. For a plant whose mass is dominated by its core, the amount of XUV exposure early in its life can be crucial because the atmosphere is still warm and inflated and material can be most easily lifted out of the planet's gravitational well.

7.4 Evolution of the planetary sample

Our aim is to investigate how the inclusion of a stellar activity track distribution affects the planetary radius distribution at Gyr ages. Kubyshkina & Vidotto (2021) recently performed a comparative study of sub-Neptune-like planets orbiting a range of stellar masses and including different evolutionary histories. They show the impact of a slow and fast rotating star on a fixed grid of exoplanets. In contrast to their study, we construct an exoplanet population, which is motivated on the one hand by the properties of the observed super-Earth and sub-Neptune planets discovered with *Kepler*, and on the other hand by numerical simulation results from planet formation studies predicting the primordial planet composition after the dispersal of the protoplanetary disk.

We do not aim to fit the observed bimodal radius distribution, but instead, using a reasonable primordial planet population, show the relative influence of a distribution of stellar activity tracks on the final radius distribution, and the slope, width and location of the radius gap.
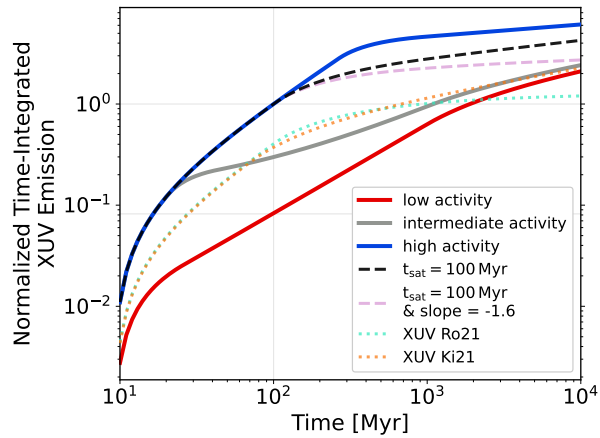
Figure 7.3: Cumulative XUV emission from 10 Myr to 10 Gyr normalized to the cumulative XUV emission of the reference track at 100 Myr (t_{sat} =100 Myr; black dashed line). A low, intermediate and high activity track for a one solar mass star are shown in red, gray and blue, respectively. The large difference in emitted XUVs below 1 Gyr is clearly visible. For comparison, we also show the cumulative XUV emission used in Rogers & Owen (2021) (Ro21) and King & Wheatley (2021) (Ki21) as green and orange dotted lines, as well a track with a saturation time of 100 Myr, but with a steeper X-ray slope of -1.6, in pink.

7.4.1 Input planet population

We construct a planet population consisting of short-period exoplanets ($P \leq$ 100 days) with Earth-like rocky cores underneath gaseous H/He envelopes. To generate a planet population with properties similar to the observed *Kepler* population, we choose an orbital period distribution which has been obtained by fitting the planets in the *Kepler* sample and correcting for transit probabilities (Owen & Wu, 2017; Ginzburg et al., 2018):

$$\frac{\mathrm{d}N}{\mathrm{d}\log P} \propto \begin{cases} P^2, & \text{if } P < 8 \text{ days} \\ \text{constant}, & \text{otherwise}. \end{cases} \tag{7.4}$$

The core masses range from 1 to 25 $M_\oplus$, and are distributed according to a broken-power law, with cores below a certain threshold mass, M_c, being described by a Rayleigh distribution, and more massive cores by an inverse square tail:

$$\frac{\mathrm{d}N}{\mathrm{d}M_c} \propto \begin{cases} M_c \exp\left(-M_c^2/(2\sigma_M^2)\right), & \text{if } M_c \geq 5\, M_\odot \\ M_c^{-2}, & \text{otherwise}. \end{cases} \tag{7.5}$$

Ginzburg et al. (2018) showed that such distribution is in good agreement with the observed high-mass tail from radial velocity measurements. Similar to Gupta & Schlichting (2019), we set the dividing mass, $M_c = 5\, M_\oplus$, and use $\sigma_M = 3\, M_\oplus$ for the Rayleigh distribution (Owen & Wu, 2017).

The planets in our population are set to orbit sun-like stars with masses similar to the ones found in the *Kepler* sample (Fulton et al., 2017b). The stellar mass distribution can be described by a Gaussian centered at 0.97 $M_\odot$ and a standard deviation of 0.14 $M_\odot$. To be able to better disentangle the influence of varying XUV saturation levels due to different stellar masses and the effect of different stellar activity tracks, we also conduct simulation runs with one solar mass host stars, only.

As stated before, we do not attempt to fit the observed bimodal radius distribution, but rather reproduce the general shape by making reasonable assumptions about the primordial planet population and assuming photoevaporation as the main mechanism shaping the envelopes of the planets over time. We assume the primary atmosphere of the planets has been accreted during their formation inside the protoplanetary disk, and consists mainly of hydrogen and helium. To estimate the post-formation envelope mass fraction, f_{env}, which is defined as the fraction between the mass of the envelope and the total mass of the planet, we rely on the results from two numerical simulations. Mordasini

(2020) (short: M20) predict that post-formation envelopes are positively correlated with core mass, but with an inverse dependence on orbital separation. For our sample, this corresponds to a median initial envelope of around 4% in mass. Gupta & Schlichting (2019) (short: Gu19) on the other hand, based on a study on accretion and mass loss during the disk dispersal phase (Ginzburg et al., 2016), report a positive dependence on core mass only. This predicts the planets in our sample to be born with more massive envelopes, with a median mass fraction of 10%. We choose the M20 study to predict the primordial envelope masses of the planets in our sample, and show a comparison to the Gu19 envelope mass fractions in Appendix 7.8.4.

By 10 Myr, a typical protoplanetary disk has dispersed (e.g. Haisch et al., 2001; Williams & Cieza, 2011; Pecaut & Mamajek, 2016; Venuti et al., 2017), and we set this as the starting age for all planets in our sample. We tested different starting ages but find that at Gyr-ages, the exact starting time does not have a significant influence on the final planetary radii. Additionally, we make the simplifying assumption that planetary orbits are circular, planets undergo negligible migration beyond the disk dissipation age, and that the change in stellar bolometric luminosity from pre- to post-MS has a negligible effect on the thermal contraction of the planets. For works covering these effects we did not include, see (e.g. Lopez & Fortney, 2014b).

To avoid having planets with nonphysical properties in the unevolved population, we follow Kubyshkina et al. (2018a) and further remove any planets with a bulk density lower than 0.03 $g\,s^{-3}$, where the Roche lobe is closer than 0.5 $R_\oplus$ from the planetary surface, and that have a Jeans escape parameter greater than 80, which indicates that the outflow not in the hydrodynamic regime (Fossati et al., 2017).

We run our simulations from 10 Myr to 10 Gyr, and in general, show the final population at one single chosen age. Since in reality, the observed population includes a distribution of star-planet system ages, we also include the option of generating an age distributed exoplanet population. Similar to Modirrousta-Galian et al. (2020), we fit a truncated Gaussian to the ages of a selected sample of observed exoplanets. We downloaded the catalog from exoplanet.eu on March 9th, 2022, and select only confirmed planets with periods ≤ 300 days, and age errors less than 50%. We obtain a mean of ~ 3.1 Gyr, standard deviation of ~ 3.8 Gyr, setting the minimum and maximum age for the fit to 10 Myr and 13.8 Gyr. We create snapshots of our simulation run at 20 different log-spaced ages from 10 Myr to 10 Gyr. From the fit to the observed ages, we estimate the probability of a planet having one of the given snapshot ages. To construct the age-distributed population, for each planet in the sample we randomly

pick one of the 20 ages based on the estimated probabilities, and obtain with it the corresponding planet parameters at the given age. Our findings show that for the chosen age distribution, where the majority of star-planet systems have ages of several Gyr, and only a small fraction ($\leq 30\%$) has ages younger than 2 Gyr or older than 7 Gyr, the 1D radius distribution is not significantly different from a single intermediate age of several Gyrs. For the sample with a single intermediate stellar activity track, less than 2% of the planets in the age-distributed sample end up either above or below the gap compared to the 5 Gyr single-age sample. We further discuss the effect of an age distribution in Section 7.6.2.

7.4.2 Chosen parameters for the simulations

For the simulation results shown in Section 7.5, we use the ChRo16 planet models for a population with a core mass distribution peaked at 3 $M_\oplus$. The primordial envelope mass fractions are estimated according to M20. Regarding the host stars, we either assume a single host star mass of 1 $M_\odot$, or a distribution of stellar masses ranging from K to G to F stars.

To estimate the mass-loss rates, we combine energy- and radiation/recombination-limited mass loss with the Lopez-β estimation (unless stated otherwise). Previous works have demonstrated that the evaporation efficiency for close-in exoplanets can vary based on planetary properties, in particular the gravitational potential, and irradiation levels (e.g. Murray-Clay et al., 2009b; Owen & Jackson, 2012b; Salz et al., 2016a). Hydrodynamic simulations predict values between $\sim 0.1 - 0.3$ for the planetary masses present in our sample. We perform all runs with a fixed constant evaporation efficiency of 10%. All simulation outcomes are shown at a single chosen age.

We focus our Results and Discussion sections on the impact of the stellar activity evolution on the predicted planetary radii at Gyr ages. The Appendix shows the impact of other simulation inputs like the planetary structure model, effective absorption radius, primordial gas envelope mass fraction, or core-mass distribution. Some limitations of our assumptions and model details are discussed in Section 7.6.3.

Besides the input planet population and the evaporation model, the strength and evolution of the host star XUV emission has to be chosen. Planetary XUV fluxes change according to the host star activity track, directly affecting the photoevaporative mass-loss rates and thus the fate of the planets. For each planet in our sample, we calculate the temporal mass and radius evolution for the nine tracks introduced in Section 7.3, and choose the Jo21 method

to estimate the important EUV contribution. A detailed description of the modeled stellar activity decay is given in Section 7.3.1, and Appendix 7.8.6 discusses the impact of the EUV estimation and the slope of the X-ray decay.

Combining all these inputs, we compute the momentary mass-loss rate at each time step from the starting age to the final age of the simulation run. For each planet, we use the latest radius, envelope-mass fraction, XUV absorption radius and stellar XUV flux to calculate the mass-loss rate at the age of the simulation run. If the XUV absorption radius exceeds a planet's Roche lobe, it is set to the Roche lobe value. We then compute the mass lost in a given time step, and adjust the time step if the radius change is too drastic ($> 0.5\%$) or too little ($< 0.02\%$). We allow for time steps to range from 0.01 to 10 Myr, and reduce or increase the time step by a factor of 10 if the radius change is too extreme. We then update the planet mass and use ChRo16 planetary models to calculate the new radius with the reduced gaseous envelope. Next, we update the XUV flux based on the specified stellar evolution track and then continue this cyclic procedure until the planetary radius has reached the core radius and no atmosphere is remaining, or the end of the simulation is reached. This allows us to trace the temporal mass and radius evolution induced by atmospheric photoevaporation and planetary cooling for a range of stellar activity tracks (see Fig. 7.1), and compare them against each other.

7.5 Results

We study the effect of an observationally-motivated distribution of stellar activity tracks (see Section 7.3) on the 1D and 2D radius distribution of a reasonable population of exoplanets. First, we describe the impact of different individual activity tracks, and then how a distribution of activity tracks impacts the radius gap.

Photoevaporation simulations are complex, multidimensional problems due to the large number of required assumptions and inputs. We try to disentangle and visualize individual influences on the radius distribution of our planetary sample in Appendix 7.8.1-7.8.6, and focus here only on the impact of different activity tracks for a single set of simulation assumptions (see Sec. 7.4.2). We do not try to reproduce a radius gap which matches the observed radius valley slope and location, but instead investigate the relative changes in the radius distribution caused by the host star activity evolution. Our simulations qualitatively reproduce the bimodal radius distribution, and show that the duration a star spends in the saturated regime shifts the location of the radius

valley. In addition, a spread in saturation times can cause the borders of the radius gap to become fuzzier.

7.5.1 Single stellar activity track vs. distribution of activity tracks

In Figure 7.4, we show several Gaussian kernel density estimates (KDEs) of the radius distribution of our planet population after ongoing evaporation around one solar mass host stars at 5 Gyr. We compare the radius distribution for three individual activity tracks to a mixture of stellar activity tracks. The simulations with a single stellar activity track are chosen to cover the extremes, from very low, to intermediate, to very high activity (red, gray and blue, respectively). Note that we do not simply scale the intermediate track up or down as e.g. in Mordasini (2020), but in our case, low, intermediate and high refers to different saturation times (see Section 7.3.1). As a reminder, in the sample with a distribution of stellar activity tracks, the bulk of G-type planets will follow an intermediate track (60%), while 30% follow one of the lower activity, and about 10% a high activity ones.

As expected, in the simulation with the highest activity track, the largest number of planets completely lose their atmosphere and become bare rocky cores. In the first few hundred Myr, when planets are still cooling and contracting, they are most susceptible to mass loss. Thus, the longer a star spends in the saturated phase, constantly emitting large amounts of XUV photons, the more detrimental the mass loss for the planet. As a consequence, more planets with small cores further out and planets with more massive cores closer in are completely stripped of their atmosphere, compared to stars with shorter saturation timescales. For the simulation run shown in Figures 7.4 and 7.6, this translates to a fraction of bare cores below the gap of 30, 35 and 51% of the entire planet sample for the low, intermediate and high activity track, and about 34% for the mixed track sample.

In the 1D radius distribution in Figure 7.4, the bimodal shape is present across the whole range of activity tracks, although the second peak is quite diminished for the highest activity track. In this case, the overall evaporation is so strong that the large number of lower mass planets in our sample with core masses below 5 $M_\oplus$ stand almost no chance of retaining an envelope by the age of 5 Gyr. The slight shift of the first peak to larger radii for the highest activity track is caused by more massive ($\sim$ 5-10 $M_\oplus$) and thus larger bare cores. The location of the gap minimum is comparable for low and intermediate
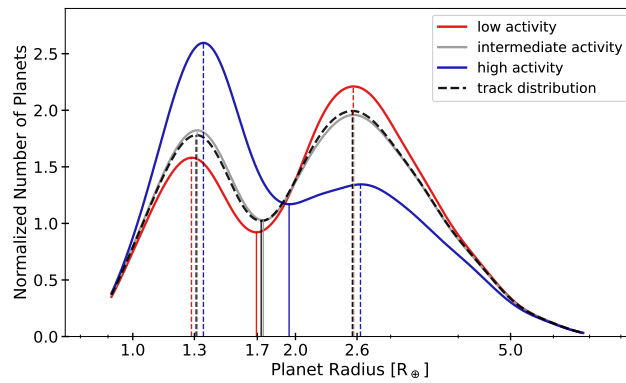
Figure 7.4: Influence of the stellar activity track on the 1D radius distribution for a single stellar mass. We compare the 1D KDEs of the radius distribution at 5 Gyr for three individual stellar activity tracks, ranging from stars which start their spin down after a few Myr and thus are considered to have very low activity (red), to stars with a saturation time around 40 Myr and thus an intermediate activity (gray), to highly active stars which remain saturated for several hundred Myr (blue). The bimodal shape is visible, but the second peak is very diminished for the high activity scenario, due to the prolonged intense XUV irradiation and thus high mass-loss rates in the first Gyr. This also causes the first peak, and in particular the radius gap minimum to shift to larger radii, because planets with more massive and thus larger bare cores get completely stripped and fall below the gap. We also show the same planet sample but with a distribution of stellar activity tracks as the black dashed line. The shape of the 1D radius distribution and the location of the gap minimum is still set by the large number of intermediate tracks in the sample, and is not significantly changed by the inclusion of a low and high activity tail.

tracks in this run, and only shifts to larger radii for the extreme high activity track. Again, this shift is caused by more massive, and thus larger bare cores populating the first radius peak and thus pushing the gap to larger radii. In the population with a distribution of stellar activity tracks, the gap minimum is not significantly affected by the inclusion of very low and very high stellar activity tracks. The shape of the radius distribution in 1D is mostly dominated by the large number of star-planet systems with intermediate activity tracks.

While we investigate here the effect of varying saturation times, or activity tracks, the result also highlights how the overall XUV exposure – for which the first several 100 Myr contribute significantly – can alter the radius distribution, in particular the location of the gap minimum and the relative height of the peaks. It is thus very important to pay attention to the estimation of the X-ray saturation luminosity and the EUV contribution. We show the impact of other simulation inputs like the planetary core mass distribution or the effective absorption radius on the radius distribution in the appendix, but our simulations suggest that the inclusion of an observationally-motivated stellar activity track distribution compared to a single intermediate track does not significantly affect the shape of the radius distribution in 1D. Other simulation parameters, like for example the EUV estimation method, the estimation of the effective absorption radius or the mass-loss rate calculation, seem to have a stronger impact on the location of the gap minimum.

7.5.2 Location and slope of the gap

2D structure of the gap in period space

We show in Figure 7.6 and 7.7 the 2D radius distribution at 5 Gyr for a single stellar mass and a distribution of stellar masses – on the left for a distribution of stellar activity tracks, and on the right for three single activity tracks ranging from low, to intermediate to high. The main features – two populations of planets separated by a less populated gap – are clearly visible in all of our simulation runs, but the number of planets below the gap increases significantly going from the low to the high activity track. The lower edge of the gap is populated by the heaviest cores that can be stripped, and thus a shift of the gap to larger radii can be observed, going from low to high activity. The slope of the gap is consistent across all individual tracks, and the inclusion of a mixture of activity tracks with only a small fraction of very extreme low or high activity tracks also does not change the slope of the gap in period or flux

space (typically, the gap slope in period space is $\mathrm{d}\log R_\mathrm{p}/\mathrm{d}\log P \approx -0.19 \pm 0.01$ for a single stellar mass and $\approx -0.16 \pm 0.01$ for a mix of stellar masses).

To quantify the slope and width of the gap in our simulations, we derived a gap fitting method suitable for those respective planet distributions. In line with previous radius-gap determinations, we assume a linear relationship between the radius gap and the planetary period or the insolation in log-log space (e.g. Van Eylen et al., 2018b; Martinez et al., 2019; Loyd et al., 2020).

We found that many of the existing gap-fitting approaches struggle either with capturing the gap properties in the case where a significant number of planets exist inside the gap – which we call here "fuzziness" of the gap, or in the case when the gap is completely empty (e.g. Van Eylen et al., 2018b; Martinez et al., 2019; Loyd et al., 2020; Petigura et al., 2022). In particular, Van Eylen et al. (2018b) fitted the gap position and slope in their data set by starting out with the usual likelihood function for fitting a straight line to a set of data. However, since the desired output is a fit to an absence of data, they inverted the likelihood function, so that the likelihood was maximized when the fitted line was placed away from the data at both edges of the gap. We note here that this approach can only work for a completely empty gap, because their inverted likelihood is ill-defined and goes towards infinity whenever the line happens to go through a data point. If there are planets located inside the gap, as is the case for several of our scenarios, it happens quite often that an MCMC sampling of the line fit parameters reaches those ill-defined points in the parameter space, making the Van Eylen et al. (2018b) fit method not applicable for the simulations which yield a fuzzy gap. Van Eylen et al. (2018b) and David et al. (2021) also used an approach based on support vector machines (SVMs) to find the line which maximizes the boarders between two distinct classes of planets in the period-radius or insolation-radius plane. Petigura et al. (2022) note that this approach struggles for a sample where the gap is not completely devoid of planets.

There are other approaches in the literature which are based on kernel density estimates (KDEs) of the planet population, for example in the period-radius plane. Martinez et al. (2019) and Petigura et al. (2022) apply a KDE to get the number density of detected planets, find the minimum density along a number of vertical lines, or 1D projections through the chosen plane, and fit a power law to the train of minima. The 'gapfit' code by Loyd et al. (2020) subtracts off a trial gap relationship and evaluates the 1D KDE of the residuals. These approaches are significantly influenced by the chosen smoothing parameter, which determines how much weight the planets near the gap edges have on the fit compared to the planets further away.

We instead try a different approach to fit the gap by defining a test strip of width w, surrounded by two comparison strips of width $w/2$ next to it (see Fig. 7.5). A test strip that captures the empirical location of the gap (in terms of slope, y-intercept and width) will produce a low number of planets inside the test strip compared to the number of planets in the comparison strips. We therefore calculate the ratio of the counted planets in the test and comparison strips for a grid of reasonable gap widths and slopes[2] and select the parameters yielding the lowest ratio as the representation of the gap. In the case of fuzzy gaps, our fit results agree very well with the gap-fitting methods which are based on KDEs (Martinez et al., 2019; Loyd et al., 2020; Petigura et al., 2022); those KDE approaches, however, do not yield width estimates. For empty gaps, we find that those methods only yield results similar to our method when decreasing the kernel bandwidth to better capture the sharp boundaries of the gap. While the slope of the gap is always in agreement, the gap fit is strongly drawn towards the cloud of planets above the gap, if the smoothing parameter is too large. We also find that the gap fits from the SVM approach are in good agreement with our orthogonal distance approach for both a non-empty, or noisy gap, as well as a well-defined empty gap. In our approach, we have extra information on whether the planets have some remaining envelope or not since our planets are simulated, and can therefore label them accordingly for SVMs – however, such information is not readily available for the observed exoplanet population. This labelling allows the SVMs to also work well on our data with a fuzzy gap. These agreements show that our test strip method captures the parameters of the gap well, while adding a gap width estimate to the toolbox.

Differences of the 2D gap in period or flux space

While the effect of a mixture of stellar activity tracks on the 1D radius distribution seems negligible (see Sec. 7.5.1), in planetary radius vs. period or planetary irradiation space, some influences on the gap are visible. For the single stellar mass run in Figure 7.8, panels (a)-(d), going from an individual intermediate track to a mix of tracks, the gap becomes slightly narrower and fuzzier in period and flux space. This arises from the fact that the planet population with a stellar activity track distribution is a superposition of the

---

[2]This method only works if the test and comparison strips actually capture the relevant parts of the planet distribution and manage to capture a decent number of planets in the strips. We therefore restricted our test grid to gap positions motivated by the 1D population, and restricted the minimum gap width to avoid combinations where zero planets were captured in the strips.
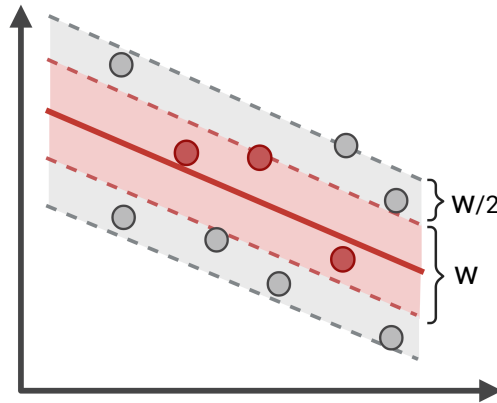
Figure 7.5: Schematic of the used fitting routine. We determine, for a given strip with, w, how many planets lie in the central strip around the empirical location of the gap, and how many lie in the two comparison strips of width $w/2$ next to it. We then minimize this ratio of planets inside and outside the strip across a grid of appropriately chosen parameters for the slope, y-intercept and width, to find the line and strip width that best fits the radius gap.

populations with a single stellar activity track. Around stars with high activity, for the same orbital separation, planets with more massive cores can be stripped compared to stars with low or intermediate activity. This causes the bare core boundary, or lower edge of the gap, in the mixed track sample to be composed mostly of bare cores around stars which stay active for prolonged periods. At 10 (50) days, the bare core mass increases from 5.4 (4.0), to 5.6 (4.1) and 6.3 (4.7) $M_\oplus$ going from low to high stellar activity, and with 5.8 (4.3) $M_\oplus$ is slightly higher for the mixed-track sample compared to the intermediate track. So while the lower edge of the gap is populated by the more massive bare cores resulting from stars with high activity, planets with slightly smaller or similar core masses around stars with low or intermediate activity tracks can hold on to envelopes of 1-2% of the total planet mass and populate the upper edge of the gap.

The fuzziness of the 2D gap induced by stellar activity tracks

For a distribution of stellar masses ranging from K to F spectral type, going from an single activity track to a mix of tracks, our simulations show that the gap becomes wider and fuzzier in period space, but stays relatively empty in
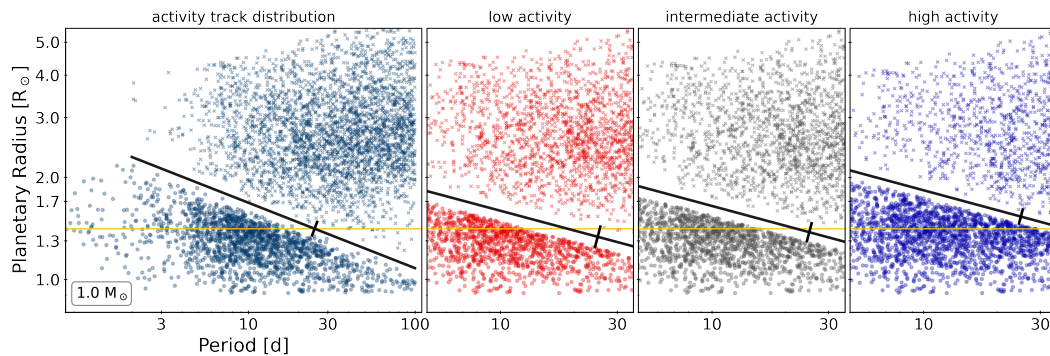
Figure 7.6: Influence of the stellar activity track on the exoplanet radius gap, for a single stellar mass. We show from left to right the same planet population at 5 Gyr for the mixed-track sample, and a single low, intermediate and high activity track. Two distinct populations separated by a band with almost no planets is visible in all panels. The orthogonal distance fit of the gap and the corresponding gap width are shown in black. The gap slope is consistent across all four samples, but going from low to high stellar activity, the gap shifts upwards due to more massive and larger cores below the gap. The fitted gap width decreases with increasing stellar activity from 0.06, 0.05, to 0.04 dex for the low, intermediate and high activity track. Higher levels of evaporation lift the bare core boundary and narrow the gap. For the mixed track sample, the width of the gapfit is even smaller, with 0.03 dex. The gap is less pronounced and fuzzier due to the superposition of planets shaped by the different stellar activity tracks. The horizontal dashed line is drawn to highlight the shift of the gap between individual tracks and the mixed-track sample.
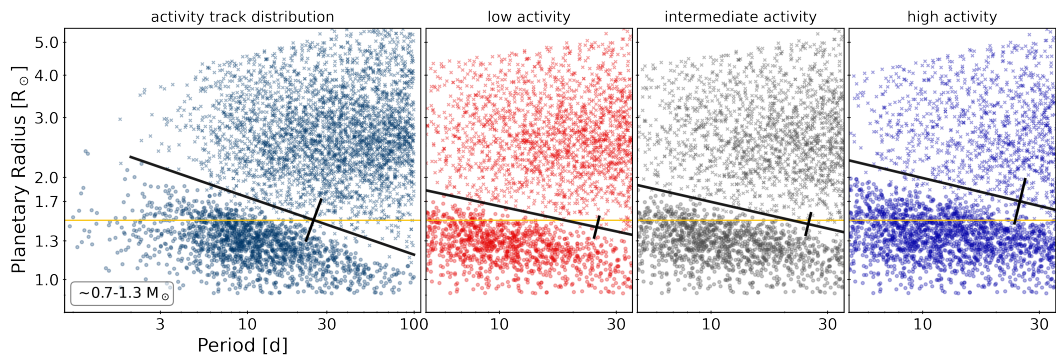
Figure 7.7: Influence of the stellar activity track on the exoplanet radius gap, for a sample with mixed stellar masses. Same as Figure 7.6, but for the planet population with a distribution of stellar masses of F, G and K spectral type. Although less pronounced, a deficit of planets separating the planets with envelope from the bare cores is still visible. For the highest activity track, the gap becomes hard to discern. Due to the extreme mass loss, very few planets remain above the gap. Here, the width of the gap is largest in the mixed-track sample on the left. The superposition of planets with various activity tracks makes the already filled-in gap in the stellar mass sample appear wider. Planets inside the gap are either bare cores or planets that can hold on to very thin envelopes of $\leq 1\%$ in total planet mass in our simulation setup.

(a)

(b)

(c)

(d)

(e)

(f)
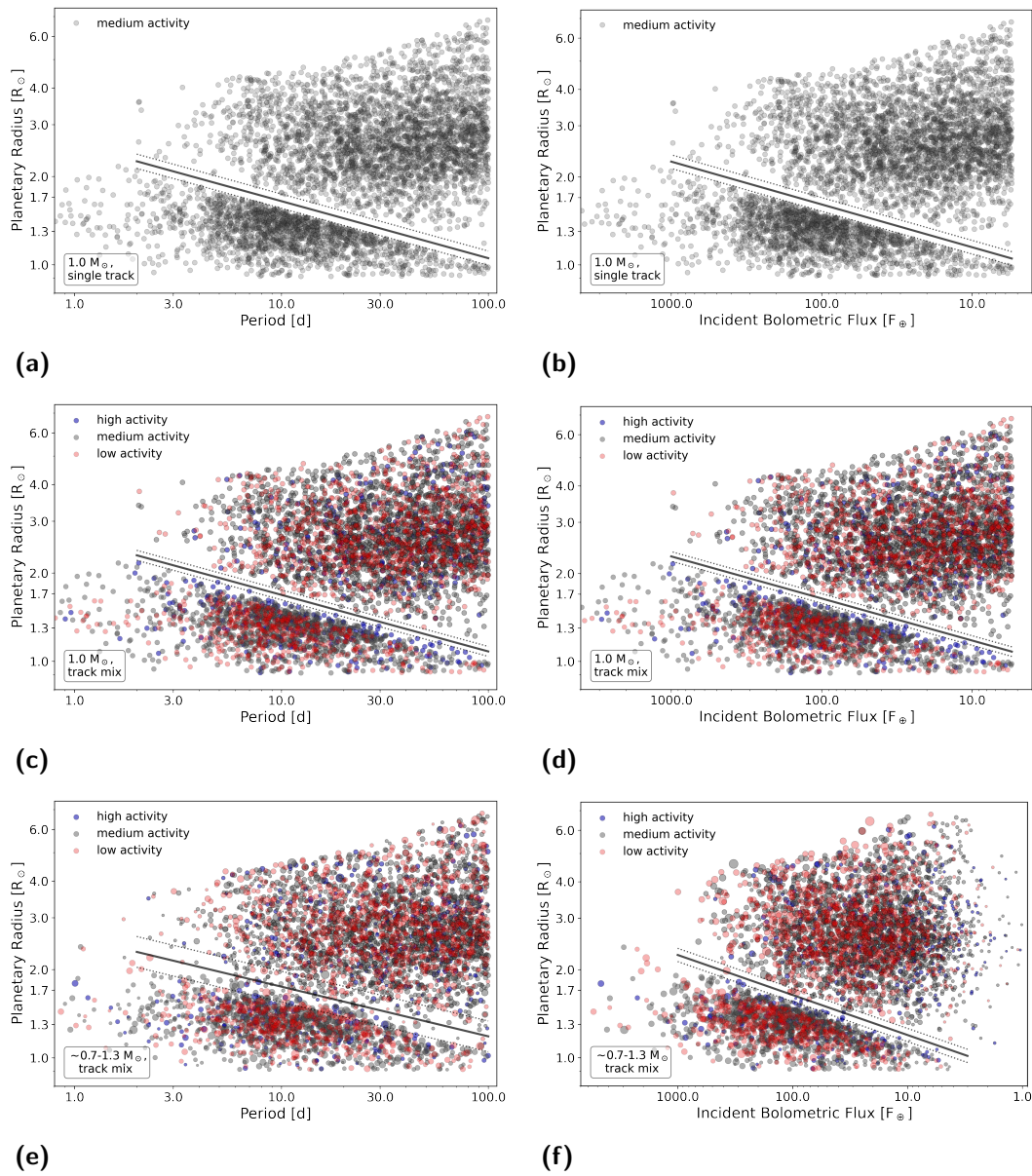
Figure 7.8: Impact of stellar activity tracks on the exoplanet radius gap, for a single stellar mass and a distribution of K, G and F stars. In the left column we show planetary radius as a function of period, and on the right as a function of incident flux in Earth units. Going from panels (a) and (b) to (c) and (d) one can see the impact of a distribution of activity tracks on the simulated exoplanet population for one solar mass host stars.

Figure 7.9: For a single stellar mass, the radius gap is still a relatively empty band, but the lower boarder is populated mainly by bare cores of planets around highly active stars. Going to a mixture of stellar masses ranging from K to F spectral types in panels (e) and (f) one can see that the gap is significantly less pronounced in period space, but stays relatively empty in flux space. In period, the lower boarder of the radius gap is mainly populated by planets around the more massive host stars in our sample, while in flux space the lower boarder is populated by planets around highly active stars. In flux space, stellar mass dependencies are reduced, which is why one can again see the impact of a distribution of stellar activity tracks on the gap edges, similar to the one solar mass case. Highly active stars emit large amounts of XUV flux longer compared to stars with low or intermediate activity, which causes planets of similar initial properties to end up as bare cores around highly active stars, and to retain thin envelopes around stars which drop out of the saturated regime earlier.

flux space. By fuzzier, we mean a gap that has a less sharp lower edge and a larger number of planets inside. This is shown in Figure 7.8, panels (e) and (f), in comparison to a single stellar mass in panels (c) and (d). In period space, the gap is not completely empty anymore, even for a single activity track. This is due to the stellar mass dependence on the saturation XUV luminosity in our simulations. Planets around K dwarfs experience lower irradiation levels in the saturated phase compared to planets around F dwarfs, which impacts the critical core mass that can be fully evaporated and shifts the features of the bimodal radius distribution to lower radii for K dwarfs, and larger radii for F dwarfs. In period space, a planet at the same orbital period thus experiences different levels of evaporation around different host star spectral types. As a result, the lower boarder of the radius gap in period space is populated by planets around the more massive host stars in our sample ($\gtrsim 1\ M_\odot$), whereas the upper boarder with planets that retain thin envelopes is composed mostly of the G and K stars in our sample. In flux space, this stellar mass difference is effectively cancelled out and the gap appears cleaner. A stratification of planets with low, intermediate and high activity host stars is visible in the bare core population, with planets around highly active stars having slightly heavier evaporated cores and thus populate the lower edge of the radius gap. Comparing panels (d) and (f) in Figure 7.8, we find that in flux space the gap appears still quite empty, but with the inclusion of an activity track distribution a few massive planetary cores around highly active stars, or planets around

low activity stars which can retain a thin envelope, fill the gap from below and above.

Regarding the planets in the vicinity of the gap, our simulations show that planets populating the lower border are stripped bare cores, or super-Earths, while planets inside and residing close to the top boarder are sub-Neptunes with thin envelopes. In the mixed stellar mass sample with the noisy gap in period space (panel (e) of Fig. 7.8), the planets inside the gap all have envelopes with less than 1% in mass. At larger radii, just outside the gap, one enters a regime of relatively stable planets with envelope mass fractions of around 1-2%. For the solar mass sample (panel (c) in Fig. 7.8), the few non-bare planets inside the gap have very thin envelopes of less than 0.1%. If we double our fitted gap width and investigate the planets inside a gap that has twice the width, the envelopes present extend to 0.5-1%. The same behavior is true for the solar-mass and mixed-mass samples when viewed in flux space (panels (d) and (f) in Fig. 7.8). The effect of stellar mass on the gap and its slope is further discussed in Section 7.6.1

7.6 Discussion

We discuss now possibilities to compare structures seen in our simulated exoplanet populations to real populations that can actually be observed. Observed exoplanet samples typically do not allow inferring the past activity history of the host star, with the possible exception of some multi-planet systems (e.g. Kubyshkina et al., 2019a,b, 2022). Therefore, observed samples will typically have a spread of stellar activity histories, whose effect we described in the results section. However, some other stellar parameters may be controlled for, namely stellar mass and stellar age.

7.6.1 Influence of stellar mass

The observed population of exoplanet host stars has a range of stellar masses. With a growing pool of known exoplanets, one can investigate the properties of the exoplanet radius gap in increasingly narrow bins of host star masses to explore the resulting relationship.

The stars in the detected Kepler exoplanet sample roughly follow a Gaussian distribution, which is peaked around one solar mass and covers an approximate mass range from 0.7 to 1.3 solar masses (Petigura et al., 2017), i.e. relatively few M dwarfs. We focus on F, G and K stars in this work, which all exhibit short

time scales of activity saturation early in their lives and then follow various decreasing activity tracks, as described in Section 7.3. M dwarfs are observed and modelled to have much longer activity saturation timescales and possibly a narrower spread in activity tracks (e.g. Magaudda et al., 2020; Johnstone et al., 2021), but those stars are not at the focus of our present work here.

The main difference in terms of the exoplanet evolution comes from the different saturation X-ray luminosities of the young-age F, G and K stars, since their saturated phase is characterized by a constant level of L_X/L_{bol}, see Section 7.3; this translates to saturated X-ray luminosities of 0.2 and 3.5 times the X-ray luminosity of a $1\,M_\odot$ star for stellar masses of $0.7\,M_\odot$ and $1.3\,M_\odot$, respectively. The XUV emission in the saturated phase crucially shapes the mass loss a planet undergoes early on, when the atmosphere might still be warm and expanded.

The result can be seen in Figure 7.10, where we show our modelled radius distribution at 5 Gyrs for the same planet population around an $0.7\,M_\odot$, $1.0\,M_\odot$ and $1.3\,M_\odot$ star, respectively. For the simulation with $0.7\,M_\odot$ host stars (light gray), only 16% of the planets lose their primordial atmosphere and as a consequence, the first peak is barely visible. For the $1.0\,M_\odot$ simulation (medium gray) the bare core number increases to 35% and the two peaks have comparable heights. For the highest host star mass of $1.3\,M_\odot$ (dark gray), 51% of planets in the sample fully evaporate, causing the second radius peak to almost disappear. The clearly different gap locations - $\sim 1.4, 1.8, 2\,R_\oplus$ for $0.7, 1.0, 1.3\,M_\odot$, respectively – are governed by the distribution of core masses for the bare core planets and the planets with remaining envelope. On both sides of the gap, the location of the peak shifts to larger planet sizes for larger stellar masses: With higher XUV fluxes and thus larger amounts of evaporation, planets with more massive cores get stripped, leaving behind more massive bare cores below the gap. At the same time, planets with remaining envelope above the gap have more massive cores compared to the lower stellar mass simulations. So while the number of planets which can hold on to some envelope decreases, the location of the second peak shifts to larger radii as well.

If we introduce a stellar mass distribution like the one of the Kepler host stars, we find only small differences of the 1D radius distribution to the purely solar-mass case, since that sample happens to be centered on solar-mass stars. However, observationally, planet populations can be split into sub-samples by stellar mass, where the gap location could be observed to change similar to the light gray/medium gray/dark gray distributions in our Figure 7.10.

In 2D, going from 0.7 to 1.3 $M_\odot$, the simulated planet populations also show a shift of the gap position upwards, as expected; this change is about 0.13 dex,
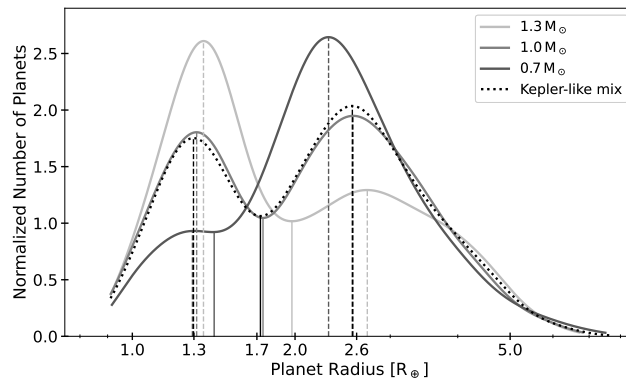
Figure 7.10: Influence of stellar mass on the radius distribution. Comparison of the 1D-KDE estimation of the same exoplanet population but assuming that all planets orbit a star with mass 0.7 (light gray), 1.0 (medium gray) or 1.3 (dark gray) $M_\odot$. The radius distribution for a Gaussian stellar mass distribution peaked around $1.0\,M_\odot$ is shown as the dotted black line for comparison. In our simulation, the amount of evaporation around a $0.7\,M_\odot$ star is not large enough to populate the first radius peak, while for the $1.3\,M_\odot$ run, the second peak almost disappears due to the high mass loss. The gap locations extend from ~ 1.4 to $2.0\,R_\oplus$, which agrees with the observed gap extent as determined by Fulton & Petigura (2018).

which corresponds to a shift from 1.4 to 1.9 $R_\oplus$ at a period of 10 days. The gap slope is consistent across individual stellar masses, but turns out to be shallower for the mixed stellar population; we find a gap slope of typically -0.19(1) in period space for samples with a single stellar mass versus a slope of -0.16(1) for the mixed sample. This is due to the fact that there is a larger number of planets below the gap in wider orbits for the F stars, which has a relatively high weight in the fit, since there are almost no bare-core planets in those orbits for the lower-mass stars. The slope of the gap in flux space is around 0.15(1) in our simulations, and in agreement for single stellar masses as well as a mixture of stellar masses.

We find that the best way to display the 2D planet population is in units of bolometric irradiation, not orbital period, consistent with e.g. Martinez et al. (2019); Berger et al. (2020). The fuzziness of the gap, i.e. how many planets populate the gap, is significant in period space, since the total accumulated XUV irradiation of a planet in a given orbit around an F, G or K star differs drastically depending on the host star, and therefore we observe an overlay of different gap positions in period space. However, in irradiation space, differences in the bolometric luminosity of the host stars are cancelled out and the difference in

gap positions only comes from different L_X/L_{bol} evolutions over time, which are much smaller than the differences in actual stellar X-ray (or XUV) luminosity. We therefore find a much emptier gap in our simulated planet populations in irradiation space, see Figure 7.8, panels (e) and (f).

The shifting of the radius gap to larger radii for larger stellar masses in the observed exoplanet population has been pointed out by several authors, including Zeng et al. (2017); Fulton & Petigura (2018); Wu (2019); Berger et al. (2020). One of the suggested reasons is a dependence of planetary mass on stellar mass, i.e. more massive host stars host more massive planets (Fulton & Petigura, 2018; Wu, 2019; Petigura et al., 2022). In our simulations, planetary and host star mass are uncorrelated, and the shift in the radius gap is a result of the different XUV saturation luminosities. In period space, the lower edge of the radius gap is populated by the more massive host stars in our sample (see Figure 7.8, panel (e)), while in flux space the stellar mass-dependence is effectively scaled out. If such host star mass stratification in the upper boarder of the bare core population would be observed in period-space but not flux-space, this could indicate that the XUV dependence on stellar mass is shifting the radius gap rather than differences in the initial planet population around F, G, K stars.

7.6.2 Influence of stellar age

The typical currently observed population of exoplanet host stars has a range of stellar ages. There is a bias towards older ages due to the easier detectability of exoplanets around quieter host stars, and the bulk of stars with exoplanets detected in the era of the *Kepler* mission has ages of around 3-7 Gyr (Batalha et al., 2010). Thanks to dedicated campaigns, the number of young planets with ages less than 1-2 Gyr is gradually rising (e.g. Newton et al., 2019b; David et al., 2019a; Plavchan et al., 2020; Mann et al., 2022). In terms of exoplanet evolution, the age at which we observe a system can be decisive in the detection or non-detection of an atmosphere, in particular if the mass loss is not restricted to the first 100 Myr.

Photoevaporation population studies usually present the evolved radius distribution at one specific final age, ranging from 3 to 10 Gyr (e.g. Owen & Wu, 2017; Lopez, 2017; Jin & Mordasini, 2018; Mordasini, 2020). In Figure 7.11, we show a population with an observationally-motivated age spread, similar to the one expected to be present in the solar neighborhood (see Sec. 7.4.1), in comparison to the same sample at a single age of 5 Gyr. In the age-distributed sample, the bulk of planetary ages is around 3-7 Gyr, with a smaller number

of younger and older planets. With the inclusion of a small fraction (20%) of young planets (10 Myr to 2 Gyr), the radius gap is not influenced significantly compared to a single age (5 Gyr). A small difference in the peak height of the first peak and the location of the second peak are nonetheless visible. In the age-distributed sample, some of the young planets (less than 1.5% of the whole sample) still retain an envelope and reside above the gap, while in the 5 Gyr sample, the same planets have completely lost their atmosphere and populate the first peak. These planets all sit close to the top border of the radius gap in the age-distributed population and have very thin atmospheres with envelope mass fractions less than 0.1-0.2%. In the age-distributed sample, the opposite is true for a handful of close-in (< 5 days) planets with ages above 5 Gyr (less than 0.5% of the whole sample). They end up as bare cores in the age-distributed sample, but retain a thin envelope in the 5 Gyr sample. In general, about 1% more planets reside above the gap in the age-distributed sample compared to the single age 5 Gyr population.

In the 2D view of the planet population, the slope and location of the radius gap are in agreement for a single stellar age sample of 5 Gyr and a solar neighborhood age composition. The width of the gap is also not significantly changed by the inclusion of an age distribution for a population which has evolved along a single intermediate activity track, and the gap remains almost as clean as in Fig. 7.8 (a). For a mixture of tracks, we observe that the combination of young age and a low to intermediate activity track leads to a slightly larger number of planets to survive just above the gap with envelope mass factions less than 0.2%. In the 5 Gyr sample, these planets will have lost their remaining atmosphere. The lower border of the gap, which is populated by bare cores, is still sharp after the inclusion of an age-spread for a single activity track, while this is no longer the case when we include a mixture of tracks. We therefore attribute the fuzziness of the lower border mostly to differences in the stellar activity history, rather than an age spread.

Currently, most exoplanets have host stars whose ages are not known to high accuracy. This may change in the future through increased numbers of exoplanet detections in open clusters, where the member stars have very similar ages. In such a manner, one could investigate the effects of stellar age on the shape of the exoplanet radius distribution and the gap itself. This has recently been performed for the first time for a small number of age bins by e.g. Berger et al. (2020); Sandoval et al. (2021); David et al. (2021).

Following these recent observational studies, we split our sample with the solar-neighborhood age distribution into two age bins; a young bin with planet ages less than 2 Gyr, and a second "old" bin with ages above. The corresponding
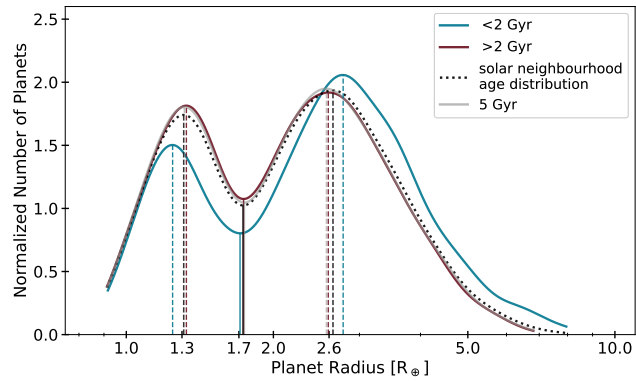
Figure 7.11: Influence of a solar-neighborhood age spread on the radius distribution for one solar mass host stars. We compare the age-distributed sample in black (dotted line) to the single-age case at 5 Gyr (gray). The KDEs are qualitatively similar, but the small number of young planets in the age-distributed sample which still maintain an envelope cause the height of the first peak to be slightly smaller. These planets still reside above the gap in the age-distributed sample, but have ended up as bare cores below the gap in the 5 Gyr sample. We also show the age-distributed planet population, split up into two age bins: planets with ages less than 2 Gyr (blue) and planets with ages above 2 Gyr (red). The gap location is basically unchanged going from the younger to the older age bin, but the gap is much more filled in at later ages. The first radius peak is at smaller radii in the young sample, while the second peak is located at larger radii. At young ages, only planets with less massive cores have been fully evaporated, and planets with envelope above the gap have had less time to cool and contract.
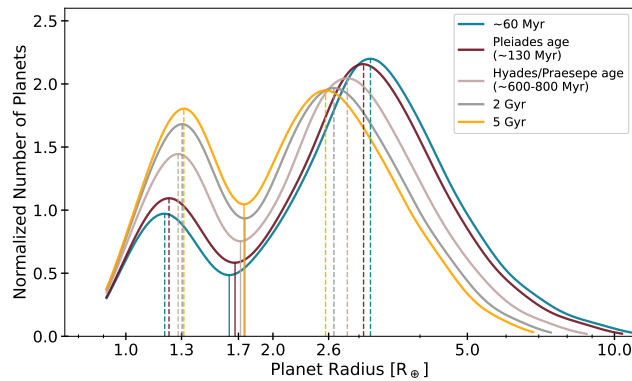
Figure 7.12: Influence of age on the radius distribution for a single intermediate activity track. The extreme XUV exposure and high mass-loss rates quickly strip the lightest, closer-in planets of their thin primordial atmospheres, giving rise to the bimodal structure early on. Over time, the first peak and gap minimum shift to larger radii due to the growing number and mass, or size, of the bare cores. The second peak drifts to smaller radii due to cooling and subsequent radius contraction. The height of the first peak increases while the second peak becomes smaller, and the gap region becomes narrower and progressively more filled.

KDEs are shown in Figure 7.11. The results, as expected, show that when observing a sample of exoplanets with ages less than $1 - 2$ Gyr, the gap should be emptier and wider in the young sample, and more filled in a sample of older host stars. This is qualitatively similar to the observational findings by David et al. (2021), who report that the radius valley appears much more filled in for planets older than $\sim 2 - 3$ Gyr.

While splitting the observed exoplanet sample into very thin age bins, similar to the ones presented in Figure 7.12, is currently not feasible, the growing number of younger exoplanets has already allowed for a separation into a few coarse age bins. In the future, with more and more planet detections in young open clusters, it might become possible to trace the radius distribution and gap evolution across narrow age bins. This will put important constraints on the strength of evaporation in the first several hundred million year. In Figure 7.12, we show our modelled radius distribution for one solar mass and a single intermediate activity track at five different ages, motivated partly by known young clusters. Early on, when planets are exposed to extreme XUV fluxes and the mass loss is detrimental for close-in, low mass planets, the first peak and the radius gap shift visibly towards larger radii. This is explained by an increasing number of more massive bare cores. Going from ages 60, 130,

~ 600 Myr, to 2 and 5 Gyr, the percentage of bare cores increases from 18, 21, 28, 33 to 35%. So while the lightest close-in planets in our sample are stripped of their envelope within less than 100 Myr – giving rise to the bimodal structure early on – there still is significant mass loss afterward. It is thus not just the first 100 Myr that play a role in sculpting the exoplanet population, but also the subsequent times up to Gyr ages. This is partly driven by the EUV contribution to the total XUV flux, with EUVs decaying less strongly than the X-rays, in agreement with the findings by King & Wheatley (2021).

After roughly 600-800 Myr, or the age of the Hyades or Praesepe, we find that while the location of the radius gap is mostly unaffected, we observe a gradual filling in of the gap up to Gyr ages. This is caused on the one hand by more massive/ larger bare cores gradually populating the lower boundary of the gap, and on the other hand by planets with core masses around 3-5 $M_\oplus$ and envelopes of $1-2\%$ slowly losing mass and drifting towards the gap on Gyr time scales, ending up with either no envelope or very thin envelopes of less than 1% in our simulation. Across all ages, the second peak shifts to smaller radii, which is driven mainly by planetary cooling and contraction, and only slightly by mass loss. As expected, and in agreement with David et al. (2021), the gap is wider at younger ages and becomes narrower at later ages.

While we attribute the shifting of the gap to larger radii and gradual filling in over time first and foremost to age (and thus, the total amount of XUV exposure), our simulations show that the inclusion of an activity track, where some planets do drop out of the saturated regime very early on, while others stay saturated for prolonged times, slows down the growth of the first peak and filling in of the radius gap up to an age of about 1 Gyr. In our one solar-mass simulation, a difference in the 1D radius distribution peak heights and gap depth/width between a single track with $t_\text{sat} \approx 40$ Myr and a distribution of activity tracks is visible up to roughly 600-800 Myr. Going from ages 60, 130, ~ 600 Myr, to roughly 2 and 5 Gyr, the percentage of bare cores increases from 15, 18, 26, 32 to 34% for an activity distribution, as opposed to 18, 21, 28, 33 to 35% for a single intermediate track. Beyond about 1-2 Gyr, differences in the 1D distribution due to activity differences have been mostly erased; peak heights and radius gap depth are then roughly in agreement (see Fig. 7.13). This behavior is due to the overall larger number of tracks with intermediate and low activity (and saturation times less than 40 Myr), than higher activity tracks in the sample with activity spread. A dropping out of the saturated regime early on alters the early phase of otherwise intense mass loss, allowing planets around such stars to hold on to their envelopes longer compared to planets around stars which stay in the saturated regime longer. However, due
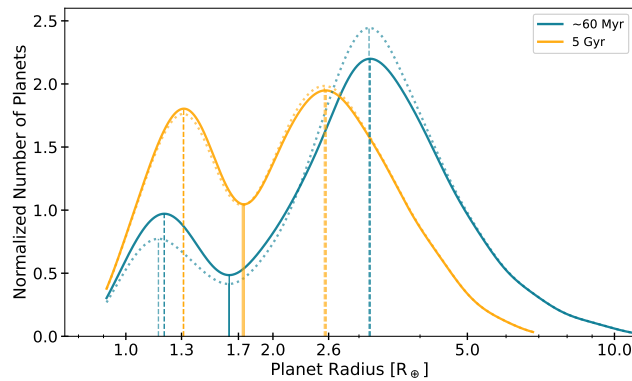
Figure 7.13: Influence of a stellar activity spread on the 1D radius distribution at young and old age. The solid lines show the population for a single intermediate track with $t_{\rm sat} \approx 40$ Myr, and the dotted lines show the same population but with a distribution of low, intermediate and high activity tracks. At young age – here we show ~ 60 Myr as an example – there are fewer bare cores in the activity-distributed sample compared to the intermediate track. At later ages – 5 Gyr shown here – differences in the 1D distribution due to activity differences have been erased. Around low to intermediate activity stars, which drop out of the saturated regime before 40 Myr, the lower mass-loss rates stall the atmospheric stripping of their planets. However, the remaining XUV irradiation is still sufficient to eventually strip their remaining envelopes by 1-2 Gyr, erasing differences in the 1D distribution due to an activity spread at Gyr ages.

to the significant EUV contribution up to Gyr ages in our simulations, as time progresses, these planets still influence enough mass loss afterward to eventually get stripped by an age of 5 Gyr. This erases major differences in the 1D distribution attributed to the spread in activity tracks. At older ages, only in 2D, e.g. the radius vs. period plane, the imprints of the activity spread remain, namely as the smoothed out, fuzzier borders of the gap – a byproduct of planets with more massive cores undergoing complete envelope loss around stars with prolonged saturation levels, and thus larger cumulative XUV exposure. In summary, we find that the inclusion of an activity spread changes mainly the sharpness of the lower border of the gap, but the gap evolution over stellar age agrees with the trends found by works studying the observed planet populations (e.g. Berger et al. 2020; David et al. 2021).

7.6.3 Caveats and model limitations

We briefly discuss some of the uncertainties introduced into our modelling from the underlying assumptions of the evaporation model and the input planet population. The main limitations of the energy-limited escape modelling, the role of magnetic fields and stellar wind interactions are given in Poppenhaeger et al. (2021) (Section 4.3). Some additional simplifying assumptions that we make here and that are explored in more realistic setups by other authors are: circular orbits and no planet migration after disk dispersal (see Attia et al. (2021) for eccentricity and migration effects on photoevaporative mass loss at later ages); lack of planetary compositional diversity (see Venturini et al. (2020) or Zeng et al. (2021) for the impact of compositional differences, like the inclusion of cosmic ices and water on the radius distribution); lack of a photon-limited escape regime (e.g. Owen & Alvarez, 2016; Lampón et al., 2021).

While we choose – if possible – observationally motivated stellar and planetary parameters for the initial exoplanet population, the exact details, like core mass distribution or post-formation envelope mass fraction, will influence the final predictions made by our simulations. Impacts of a range of simulation inputs on the evolved planet population or the radius gap have already been discussed in several works, including e.g. Modirrousta-Galian et al. (2020); Mordasini (2020); Rogers & Owen (2021); Kubyshkina & Vidotto (2021). Further uncertainties arise from the estimation of X-ray and EUV fluxes in the saturated regime and beyond, due to the partly unknown high energy spectra of stars of different spectral type and age (see e.g. King & Wheatley (2021)). The impact of the EUV estimation and the X-ray decay slope is further discussed in Appendix 7.8.6.

As we show in Appendix 7.8.3, assuming energy-limited and radiation/recombination-limited mass loss yields quite different outcomes than assuming hydro-based mass loss. The mass loss predicted by the hydro-simulations, in particular in the first 100 Myr, is orders of magnitude greater compared to the energy-limited and/or radiation/recombination-limited simulations. This results in much more severe mass loss for planets across the whole range of orbital separations and core masses. Under our simulation assumptions, which includes mostly lower-mass cores below $\sim 10\ M_\oplus$, this leads to a large number of planets which fully evaporate, leaving behind almost no significant second radius peak in most simulations with hydro-based mass-loss rates. These results suggest that for a planet population similar to the one used in this work, the predicted hydro-based mass-loss rates under the assumed XUV irradiation levels are too high to reproduce the observationally known bimodal radius

distribution. To preserve the second peak in the radius distribution, it would require significantly lower XUV fluxes or a population with a much larger number of cores above $\sim 10 M_\oplus$ for there to be enough planets surviving with an envelope.

In general, our simulations yield a bimodal radius distribution, with a negative slope of the radius gap in radius-period space, qualitatively similar to observations. The exact values of the two peaks and the gap minimum, as well as the height of the peaks, depend sensitively on the choice of the input population, and the overall strength of the mass loss, which includes the evaporation scheme and its details, as well as the host star's XUV emission and its activity evolution. The main conclusion of this study, that the radius gap boarders become fuzzier and less pronounced by the inclusion of a stellar activity track distribution, hold true for a range of tested simulation inputs.

7.7 Conclusions

We investigate the effect of a distribution of host star activity evolutionary tracks on an observationally-motivated population of exoplanets shaped by photoevaporative mass loss. In our study, the host star activity track is associated with an X-ray saturation luminosity, a timescale for which the star stays at constant XUV flux at early ages, a set of XUV decay paths afterward, as well as a method to approximate the contributing EUV radiation. The stellar activity track does have a mass dependence, with the more massive F stars being X-ray brighter, but having saturation times that are shorter than for G and K stars. Within each spectral type, stars follow a distribution of low, intermediate, and high stellar activity tracks.

Our qualitative comparison suggests that for the activity track distribution used in this work, the slope, and location of the gap is not significantly changed compared to a single activity track for all host stars in the sample. However, compared to a single activity track for all host stars, the radius gap, which is a prediction of photoevaporative mass loss, does become fuzzier and less clean for a mixture of activity tracks, i.e. the lower edge of the gap is less sharp and the number of planets with radii inside the gap is larger. The inclusion of a small number of high and low activity tracks causes the gap to be narrower, because the lower gap boarder becomes filled in with more massive bare cores around stars with prolonged activity, while the upper gap becomes populated by planets around lower activity host stars which can hold on to thin envelopes of a few percent.

A quantitative comparison of the exoplanetary radius gap with model predictions in principle can put constraints on the underlying core mass distribution, planetary composition, or the post-formation envelope mass fraction (e.g Rogers & Owen, 2021). For individual multi-planet systems, even the rotational history of the host star can be deduced (e.g. Kubyshkina et al., 2019a). While this is a promising approach, it comes with a lot of challenges due to the large number of input parameters in the mass-loss modelling. Here we have explored the influence of the previously not well studied realistic spread of stellar activity tracks. Going forward, there is also a large uncertainty in estimating the important EUV irradiation planets receive from their host stars. This calls for EUV observations of planet hosting stars from space, and more detailed observations of planetary mass loss are needed to put constraints on the strength of hydrodynamic escape or other mass-loss processes, like core powered mass loss at ages below and above $\sim$ 1Gyr. Models will benefit from decisive tests through observations, and will enable a better understanding of the fate of exoplanets over time.

Acknowledgements

7.8 Appendix

We show here the effects of different simulation inputs and assumptions on an exoplanet population that has been shaped by photoevaporation. This includes the planetary structure model, the effective absorption radius, the evaporation model and efficiency, the primordial envelope mass estimation, the core mass distribution and the EUV estimation method. This section aims to visualize and give the reader a feel for the impact of the different simulation inputs on the 1D and 2D radius distribution. To better disentangle these different effects, we only show a one solar mass population at an age of 5 Gyr. Unless

stated otherwise, we assume the energy- and radiation-recombination-limited mass-loss model, the Lopez-β, an evaporation efficiency of $10\,\%$, and only show the results for a single intermediate activity track ($t_{sat} \approx 40$ Myr). The details on the exoplanet populations can be reviewed in Section 7.4.1.

7.8.1 Planetary structure model

The exact details of the planetary structure model impact the final radius distribution. The most striking difference between the LoFo14 and the ChRo15 models is the location and width of the second peak in the 1D radius distribution. Using the LoFo models, the evolved population shows a relatively broad second peak that is located at larger radii compared to the ChRO models (see Figure 7.14). The difference arises from differing planetary radius dependencies on planetary mass, envelope mass fraction, stellar insolation and age between the models. This leads to slightly different initial radii at young age, before photoevaporation shapes the envelopes, and a different radius evolution due to cooling and contraction.

The planets under consideration in this paper ($M_{core} \leq 25\,M_\oplus$) show enhanced radii at early ages, with lower-mass planets showing the most extreme radius enhancement due to lower surface gravities, but similar internal energies compared to their more massive counterparts. As planets cool over time (with the puffy planets cooling the fastest), this radius difference for different planetary masses becomes less pronounced, resulting in a gradual flattening of the mass-radius curve. In Figure 7.15, we show the mass-radius relation for the ChRo16 and LoFo14 models at 5 Gyr. It is evident that even at more mature ages, the predicted radii can vary due to slight differences in the modeling.

The LoFo models predict, in general, larger planetary radii at any given age for the planets in our sample with masses between $\sim 3-15\,M_\oplus$, stellar insolation less than a few $100\,F_\oplus$, and envelope masses greater than $\sim 2\,\%$. As a consequence, the predicted sizes for such planets are in most cases larger than the ChRo models. This gives rise to the second radius peak in the 1D distribution being shifted to larger radii (see Fig. 7.14). The observed radius distribution of close-in exoplanets indicates that the planets above the gap peak between 2.4-2.7 $R_\oplus$ (Fulton et al., 2017b; Van Eylen et al., 2018b; Martinez et al., 2019). This is most closely matched by our ChRo simulations, which is why we only show the results using the ChRo models in the main body of the paper.

The location of the first radius peak, which is mainly set by the peak of the core mass distribution (see also Sec. 7.8.5) and amount of evaporation, is
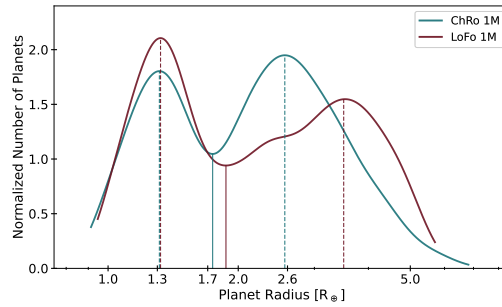
Figure 7.14: Influence of the planetary model on the 1D radius distribution for one solar mass host stars. We compare the 1D KDEs for two comparable planet populations using the ChRo (red) and the LoFo (blue) planet models. The main difference can be seen in the second peak, which is broader and at much larger radii for the LoFo models.
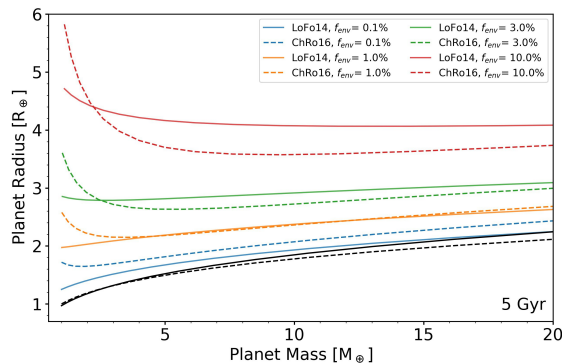
Figure 7.15: Mass-radius relation for four different envelope mass fractions (f_{env} = 0.1, 1.0, 3.0, 10.0 %) at 5 Gyr for LoFo14 (solid) and ChRo16 (dashed) planetary models. The black lines show the mass-radius relation for an Earth-like rocky core, as implemented in the LoFo14 and ChRo16 models. There are two notable differences between the models that affect the planetary mass-loss calculations. The LoFo14 models predict larger radii for planets with envelope mass fractions greater than a few percent, while the ChRo16 models predict larger radii for thin envelopes less than 1 %.

(a)   **(b)**
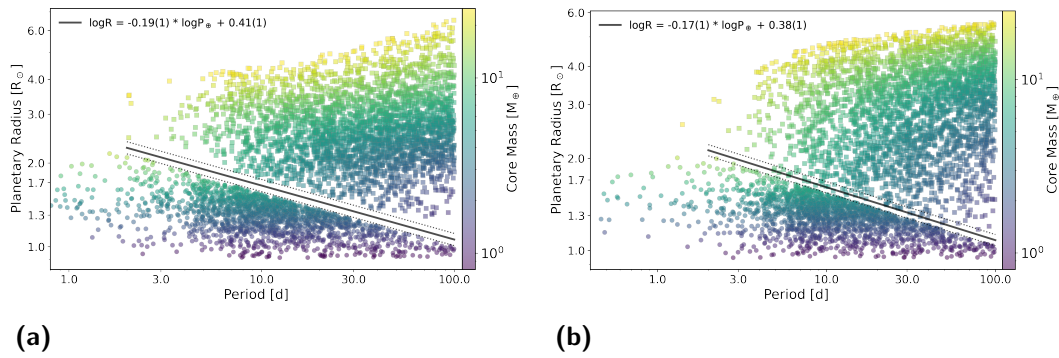
Figure 7.16: Influence of the planetary model on the 2D exoplanet radius gap for one solar mass host stars. We show the radius vs. period distribution for the ChRo and LoFo population (panel (a) and (b), respectively), together with the gap fits. For the ChRo models, a thin, empty gap with negative slope is clearly visible. The LoFo models on the other hand produce a gap region that is much more filled in compared to the ChRo population. The slope of the gap is slightly shallower for the LoFo models compared to the ChRo models ($\mathrm{d}\log R_\mathrm{p}/\mathrm{d}\log P \approx -0.17 \pm 0.01$ vs. $\approx -0.19 \pm 0.01$).

similar for both planetary models and only differs in height. This is due to the LoFo simulation ending up with slightly more low mass bare cores, causing the first peak to be more pronounced. When we compare the slope of the gap fit in Figure 7.16 panels (a) and (b), we see that the simulation run with the LoFo planets produces a gap with a shallower slope. Compared to the ChRo models under the same simulation assumptions, more LoFo planets with slightly more massive and thus larger cores at large distances from their host star end up fully stripped, influencing the slope of the gap. Additionally, it is evident that the gap is more pronounced and the gap region much emptier for the ChRo models. For the LoFo models, the gap is not as well-defined, and the fit is mostly driven by the bare core boundary. The ChRo16 models predict larger radii for low mass planets ($\lesssim 3\,M_\oplus$) and/or planets with very thin envelopes ($\lesssim 1-2\,\%$) (see Fig. 7.15), and as a consequence of this, many ChRo planets, once they reach an envelope mass small enough, still undergo sufficient mass loss to have this last bit of atmosphere removed. A comparable LoFo planet on the other hand might still be able to hold on to a very thin atmosphere ($\lesssim 1\,\%$) in our simulations, ending up with a radius "inside" the radius gap between $\sim 1.4 - 2.0\,R_\oplus$. This causes the radius gap to be more filled in for the LoFo simulation, and the gap to be more spread out in the 1D radius histogram.

7.8.2 Effective absorption radius

The effective absorption radius, or β-parameter, is another ill-constrained parameter in photoevaporation simulations, and thus relies on being estimated. In addition to the "Lopez"-β calculation introduced in 7.2.3, PLATYPOS has a second estimation method for the important XUV absorption radius built-in. We call this the "Salz"-β calculation.

Based on detailed upper planetary atmosphere simulations, Salz et al. (2016a) derived a scaling law for the planetary XUV radius as a function of planetary gravitational potential and their XUV irradiation. They find that super-Earth-sized planets with hydrogen atmospheres host extended atmospheres, which increases the effective surface area exposed to the high-energy stellar irradiation, and thus causes them to experience enhanced photoevaporative mass loss. In general, their findings indicate that the effective XUV absorption radius increases with decreasing gravitational potential, and to a lesser degree, with higher irradiation levels due to the resulting expansion of the thermosphere. We take Eq. 4 from Salz et al. (2016a) to estimate β for all planets in our sample at any point in time during the mass-loss calculation. We note that the aforementioned study only included planets with a gravitational potential of $\log_{10}(-\Phi_G) > 12.0$. Since many of the lower-mass planets in our sample fall below the lower limit of the Salz-relation, we impose a cutoff by setting β to the value predicted by the relation for the smallest and largest valid gravitational potential and XUV flux, respectively.

We show the effect of the effective absorption radius on the same planet population in Fig. 7.17. The blue and red 1D radius distributions show the evolved population having estimated β according to the Lopez- and Salz-approximation described in Sec. 7.2.3 and this section. For comparison, we also show the same run but with $\beta = 1$ (rose), which means that the effective XUV absorption radius is equal to the optical radius for any given age step in the simulation.

The most notable difference between the 1D radius distributions is the height of the two peaks. In general, a larger β, or larger effective absorption cross-section, leads to a greater amount of photoevaporation. This causes more planets in the sample to completely lose their atmosphere, decreasing the height of the second peak around 2.6 $R_\oplus$, and subsequently filling in the first peak around 1.3 $R_\oplus$. More massive evaporated cores explain the shift of the first peak and with it the gap to slightly larger radii. We tested this behavior for both the ChRo and LoFo planet models and found the behavior to be qualitatively similar.
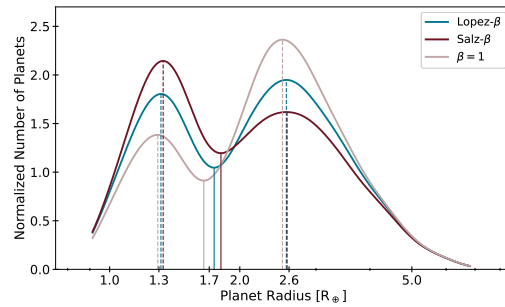
Figure 7.17: Influence of the effective absorption cross-section, β, on the 1D radius distribution for one solar mass host stars. We show the 1D KDE estimation of the same planet population, having estimated β according to the "Salz"- or "Lopez"-method (blue and red, respectively). For comparison, we also show the corresponding run where β is set to unity (rose). In this simulation, the Salz-β values are on average 25 % larger than the Lopez ones, causing more planets to fully evaporate, fill in the first "bare core"-peak, and shift the gap to slightly larger radii.

For the simulation run described here, the Salz-β ranges from ~ 1.5 to 2.8 at the start of the simulation (mean of around 2.1), and decreases to ~ 1.5 to 2.3 (mean of around 1.7) at an age of 5 Gyr. The Lopez-β covers a larger range of values at early ages, ranging from 1.1 to 4.5, but has a lower overall mean of 1.6 compared to the Salz-estimation. At 5 Gyr, the Lopez-β is predicted to range from 1.1 to 2.4, with a mean around 1.3, again lower than the Salz-β. On average, the Salz-β is about 25% larger than the Lopez-β, leading to more mass loss and more evaporated bare cores in the Salz-simulation.

Since many of the lower-mass planets in our sample fall below the lower limit of the Salz-relation, we also tested the impact of imposing a cutoff to the Salz-beta to prevent a potential overestimation for low-gravity planets. Once, we allow for the extrapolation of the relation to smaller gravitational potential values, and once we impose a cutoff to the Salz-β when a planet falls below the minimum range of applicability. In this case, β is set to the value predicted by the relation for the smallest and largest valid gravitational potential and XUV flux, respectively. For the run under consideration, at early ages, where we find the largest number of low-gravity planets due to their puffy envelopes, the cutoff leads to a slightly lower mean of 1.9, compared to the beta's estimated without the cut. This difference is too small to change the location of the gap, and the result is almost indifferent to the Salz-run without a cutoff.

When investigating differences in two dimensions, we find that the slope of all three runs is consistent within one sigma. Since the Salz-β is on average

(a)   **(b)**
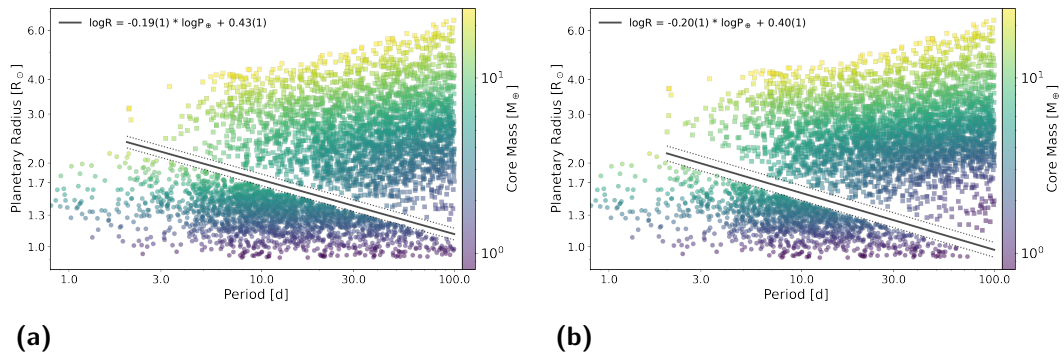
Figure 7.18: Influence of the effective absorption cross-section on the 2D exoplanet radius gap for one solar mass host stars. We show the radius vs. period distribution for the ChRo population with the Salz-β and $\beta = 1$ in panels (a) and (b), respectively, together with our fit of the gap. These plots can be compared with the Lopez-β run in panel (a) of Fig. 7.16. When β is set to unity, the gap is lower compared to both the Salz- and the Lopez-β runs. The mass-loss rates at any given age are lower, which means fewer planets end up rocky and less massive cores can be stripped. The gap appears to be a bit wider with less evaporation.

larger, more massive planets can be fully stripped, ending up below the gap. This shifts the gap slightly upwards to larger radii compared to the run with the Lopez-β. As expected, in the $\beta = 1$ run fewer planets and planets with lower core masses turn into rocky cores, causing the gap to be shifted downwards to smaller radii. The radius vs. period plots are shown in Fig. 7.16 panel (a), and Fig. 7.18 panels (a) and (b).

While the choice of β does not significantly change the properties of the gap itself, it strongly affects the number of planets propagating downwards across the gap over time and is therefore an important parameter in the atmospheric evolution of planets, as shown in Fig. 7.17.

7.8.3 Evaporation model and efficiency

The calculation of the mass-loss rates is one of the crucial assumptions in photoevaporation studies. First, we compare energy-limited mass loss (short: E) only, with a combination of energy- and radiation/recombination-limited mass loss (short: ER). At early ages, when the XUV flux is highest, the radiation/recombination-limited mass-loss rates apply to close in and/or lower-mass planets in the population, when calculated according to Sec. 7.2.2. For the planets in our simulation this, however, has no significant effect on their

final radius, as almost all planets with recombination-limited mass loss end up as bare cores. For the one-solar-mass run with the intermediate stellar activity track, less than 4% of all planets in the sample, which retain an envelope under the Lopez-beta assumption, have final radii which differ by less than 1%. For the Salz-beta the same is true for about 7% of the planets. All the planets which are affected by the recombination-limited mass-loss rates have remaining envelopes of $\lesssim 1\%$ and reside just above the gap. Only in the Salz-case a handful of planets cannot retain a thin envelope and instead end up as bare rocky cores in the case of energy-limited mass loss only. Due to the negligible difference on the planets in our sample, we chose to show the simulation runs with a combination of energy-limited and radiation/recombination-limited mass-loss rates only.

The third mass-loss rate estimation that is implemented in PLATYPOS are the hydro-based mass-loss rates (short: HBA) by Kubyshkina et al. (2018b). Planets are predicted to be particularly susceptible to mass loss at early ages due to their warm, puffy, and low-gravity atmospheres. For comparison, for the one solar mass population, the HBA mass-loss rates at 10 Myr are on average a factor 15 higher than for the simulation using the ER mass-loss rates and the Lopez- or Salz-beta. This early phase of intense mass loss leads to more planets losing their envelope completely and ending up as bare cores in the HBA run. At Gyr ages, all three mass-loss rates are comparable within a factor 2, and the Salz and HBA rates are almost identical across the planetary sample.

Figure 7.19 clearly shows that, compared to the ER simulation, in the HBA population the majority of planets fully evaporate, leaving behind almost no planets above the gap populating the second peak in 1D radius distribution. This makes the radius gap to disappear almost completely. Another consequence of the initially high HBA mass-loss rates is that more massive cores can be fully stripped compared to the ER runs. This can be seen in the first radius peak slightly shifting to larger radii due to the larger number of more massive, and thus larger cores, as well as in a shift of the radius gap above 2 $R_\oplus$. Even for a slightly larger core mass distribution as used in Sec. 7.8.5, the same conclusions for the HBA run hold true, and almost no second peak remains. This means that a planet population similar to ours, which undergoes photoevaporation on the same order as predicted by the HBA mass-loss rates using our XUV irradiation levels, cannot reproduce the observed bimodal radius distribution. The population would need to contain many more massive cores and/or envelopes for there to be enough planets able to retain an envelope to preserve the second peak in the radius distribution.

When comparing the slope of the radius gap in 2D, we find that the gap,
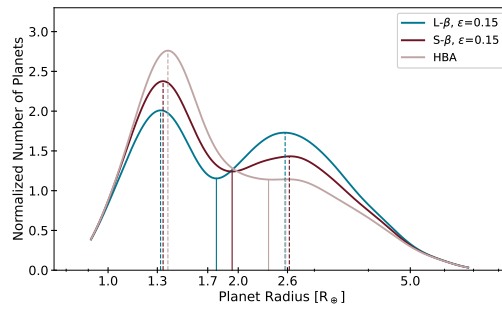
Figure 7.19: Influence of the mass-loss rate calculation on the 1D radius distribution for one solar mass host stars. We show in blue and red the 1D KDEs of the same planet population using the ER mass-loss rates with the Lopez- and Salz-beta, respectively. In rose, we plot the final distribution of planetary radii having used the hydro-based mass-loss rates. This radius distribution appears significantly different to the ER distributions. With the relatively large number of low-mass cores in our population, the majority of planets cannot retain any of its primordial envelope and end up as bare cores, leaving behind no pronounced second radius peak. An additional result of the higher HBA mass-loss rates is that more massive cores can be stripped, shifting the radius gap to larger radii. Note that for the ER runs shown here, we used an evaporation efficiency of 0.15 for better comparison with the HBA mass-loss rates.
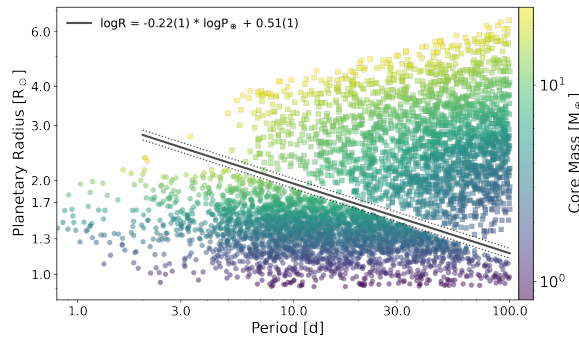
Figure 7.20: Radius vs. period distribution for the planet population, which has evolved using the hydro-based mass-loss rates. Our fit to the radius gap is shown in gray. One can easily see that, compared to the ER runs (e.g. panel (a) in Fig. 7.16 and Fig. 7.18), more massive cores end up as rocky cores below the gap, shifting the gap upwards. Compared to the ER runs, the gap is slightly steeper and narrower.

although almost non-visible in 1D, is still clearly visible in two dimensions. When comparing the HBA gap in Fig. 7.20 with the ER gap in panel (a) of Fig. 7.16 or Fig. 7.18, we see that although empty, it appears to be narrower and shifted upwards to larger radii. Interestingly, the slope of the gap is also slightly steeper for the HBA mass-loss rates, most likely because of the larger number of massive cores in close-in orbits ($\mathrm{dlog}R_\mathrm{p}/\mathrm{dlog}P \approx -0.22 \pm 0.01$ vs. $\approx -0.19 \pm 0.01$).

The evaporation efficiency is another parameter which affects the strength of the energy-limited mass-loss rates. While we make a simplification and set the efficiency parameter as a constant, its exact value will still linearly increase or decrease the mass-loss rates at any given time in the simulation. We show, in Fig. 7.21, how a small increase of the evaporation efficiency from 0.1 to 0.15 impacts the 1D distribution features. The location of the two peaks still agrees within one sigma even with a small difference in evaporation strength, but of course the height of the peaks changes, with more planets evaporating and filling in the first peak when $\epsilon = 0.15$.

When it comes to the location of the gap, more massive bare cores tend to cause a shift to larger radii. Assuming an intermediate activity track for the evolution, the shift is small for the Lopez-beta simulation, but for the Salz run, which already predicts higher mass-loss rates compared to the Lopez run, this shift in the gap minimum becomes larger, as the gap shifts from 1.8 to 1.9 $R_\oplus$. We also tested this behavior for a lower and higher stellar activity track and found that the gap shift increases going from low to high activity, or XUV flux.
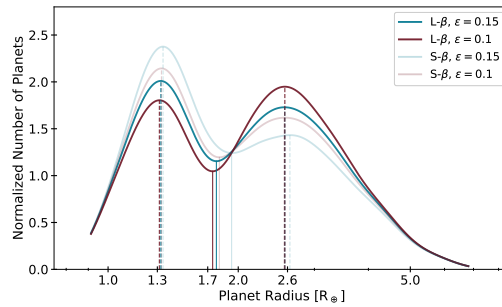
Figure 7.21: Influence of the evaporation efficiency on the 1D radius distribution for one solar mass host stars. In red and blue, we show the KDE of the evolved planet population for the Lopez-β and $\epsilon = 0.1$ and 0.15, respectively. The slightly transparent KDEs show the same for the Salz-β. A small change in the evaporation efficiency can change the peak heights, but not their location. The radius gap is almost unaffected.

In general this indicates that the larger the mass loss, as set by the evaporation model, the beta-parameter and the evaporation efficiency, the larger is the shift on the gap location in 1D. In 2D, the slope of the gap is unchanged by a small change in the evaporation efficiency.

7.8.4 Primordial gas-envelope mass

We check the impact of varying the initial envelope mass fraction of the planetary sample at the starting age of our simulation on the final radius distribution and the radius gap. We either calculate the primordial gas-envelope mass according to the simulations by Mordasini (2020) (short: M20), or based on the results by Ginzburg et al. (2016); Gupta & Schlichting (2019) (short: G19). As a reminder, the envelope masses predicted by M20 have a positive dependence on core mass and a negative dependence on orbital separation, while the G19 primordial envelopes have a dependence on core mass only. For the one-solar-mass run considered here, the M20 envelope mass fractions cover a larger range ($\sim 0.2 - 38\,\%$) but have a lower median ($4\,\%$) compared to the G19 ones, which range from ($\sim 4 - 20\,\%$) with a median of $\sim 10\,\%$. This is illustrated in Figure 7.22.

The 1D radius distributions in Figure 7.23 show that the second peak is shifted to larger radii for the G19 run. The reason for this is that, on average, the G19 primordial envelopes are more massive than the M20 ones, which makes them harder for the planets to lose under the same simulation assumptions,
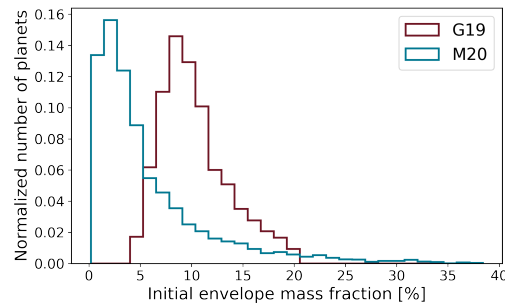
Figure 7.22: Distribution of the gas envelope mass fractions at 10 Myr, the starting age of the simulation. In blue, we show the M20 distribution, where the initial envelope mass fraction is dependent on planetary core mass and envelope mass fraction, and in red we show the G19 distribution with a dependence on core mass only. Planet with primordial atmospheres according to G19 are significantly higher in mass.

and as a result the planets end up with more massive final envelopes and thus are larger in size. In the G19 population, fewer planets are able to completely lose their envelope, which is why the first peak is less pronounced. Interestingly, the location of the gap in 1D is not significantly affected by the choice of the primordial envelope mass fraction.

In 2D, when looking at the G19 radius vs. period distribution in Fig. 7.24, one can see that the bulk of the planets above the gap, which are able to retain envelope, reside at larger radii, clustered around $\sim 3\,M_\oplus$. The region underneath until the gap is sparsely populated compared to the M20 run (see Fig. 7.16 panel (a) for comparison), but an empty gap is still clearly visible. The slope of the G19 gap is consistent with the slope of the M20 gap, but the gap is slightly shifted downwards because there are fewer, more massive bare cores in this simulation. The G19 and M20 gaps do however still overlap, telling us that the impact of the primordial envelope mass fraction only has a minor impact on the location of the gap. This conclusion is unchanged for the choice of β and/or the evaporation scheme. As a caution, the two starting populations are not exactly identical due to the imposed "physicality"-check (see Sec. 7.4). With the G19 primordial envelopes having no dependence on the distance to the host star, planets with core masses below $2\,M_\oplus$ have envelopes massive and large enough to fulfill our low-density and Roche lobe cutoff, and thus are excluded. For this reason, the G19 population has about 100 fewer
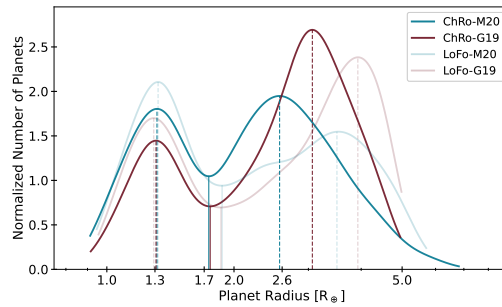
Figure 7.23: Influence of the primordial gas-envelope mass on the 1D radius distribution for one solar mass host stars. We show the KDEs for a population with primordial envelope masses calculated according to M20 (blue) and G19 (red). The transparent blue and red plots the results when using the LoFo models and are just shown for comparison. The main difference between the M20 and the G19 radius distributions is the location and height of the second peak. The majority of G19 planets has a larger primordial envelope. Under the same simulation assumptions, more planets can retain envelope in the G19 run and also more planets end up with heavier and thus larger envelopes compared to the M20 population. The location of the first peak and the gap are unchanged by the choice of primordial envelope mass estimation.

planets with core masses below $2\,M_\oplus$, which is why there are fewer planets with radii around $1\,R_\oplus$ compared to the M20 population.

7.8.5 Core-mass distribution

Previous studies have shown that the core mass distribution has a significant influence on the radius distribution in photoevaporation studies. More massive cores can hold on to their envelopes more easily, but once a more massive core does get stripped, its bare core radius will also be larger. For reference, a $3\,M_\oplus$ bare rocky core has a radius of $1.3\,R_\oplus$, whereas a $5\,M_\oplus$ core has a radius of $1.5\,R_\oplus$. This can impact the location of the first and second peak in the 1D radius distribution, and with it the gap.

To illustrate how the radius distribution is affected by the core masses of the sample, we compare the population where the core masses peak at $3\,M_\oplus$ (short: $3M_c$) with a slightly heavier population which peaks at $5\,M_\oplus$ (short: $5M_c$). As can be seen in Fig. 7.25, the $5M_c$ simulation thus has fewer planets below $\sim 3\,M_\oplus$, and more planets with intermediate masses between 5 and $20\,M_\oplus$.

In the 1D radius distribution, one can most easily identify the effect of a
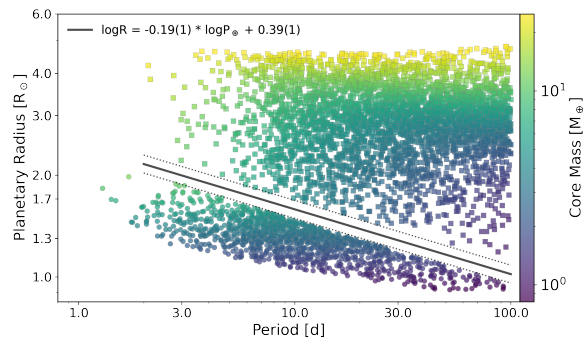
Figure 7.24: We show the radius vs. period distribution for the planet population for which the primordial envelope mass fractions were calculated according to G19. Planets which can hold on to envelopes tend to cluster around $3\,M_\oplus$, and an empty gap is clearly visible. Our fit to the gap is shown in gray. This plot can be compared with the M20 simulation in panel (a) of Fig. 7.16.
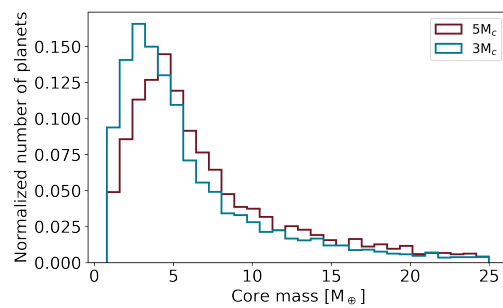
Figure 7.25: Histogram of the core mass distributions for the $3M_c$ and $5M_c$ simulation, which peak at 3 and $5\,M_\oplus$, respectively. The $5M_c$ population has fewer planets below $3\,M_\oplus$ and more planets at higher masses above $5\,M_\oplus$.
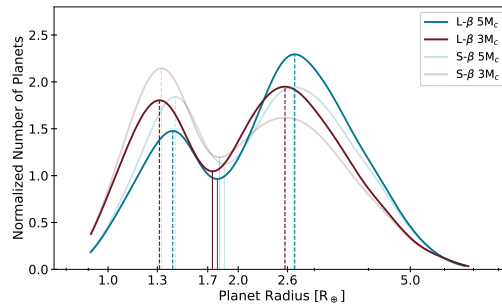
Figure 7.26: Influence of the core mass distribution on the 1D radius distribution for one solar mass host stars. The planet population with core masses peaking at $5\,M_\oplus$ is shown in blue and the population with a $3\,M_\oplus$ peak in red. For comparison, the transparent lines show the same populations but using the Salz-β. The shift of the first peak from 1.3 to $1.5\,R_\oplus$ is clearly visible, as well as a shift of the second peak to larger radii. The change in the location of the gap is almost negligible.

heavier planet sample. Figure 7.26 clearly shows that the first peak is shifted from 1.3 to $1.5\,R_\oplus$ for the $5M_c$ simulation due to the larger number of close-in, more massive, and thus larger in size cores, which end up fully stripped. In general, more massive stripped cores shift the radius gap to larger radii, but as a result of having more massive cores in the sample, the number of planets which can fully evaporate in the $5M_c$ case decrease overall. These two effects combined lead to the location of the radius gap being almost unchanged between the $3M_c$ and the $5M_c$ run. The second radius peak is also shifted to slightly larger radii because more massive planets have larger primordial envelopes to begin with and can better hold on to their envelope, reducing the total mass loss. As a result, there are more planets with larger sizes in the $5M_c$ simulation.

In 2D, there are noticeably fewer planets below the gap, but both the slope and height of the $5M_c$ gap are in good agreement with the $3M_c$ one. This shows that at least small changes in the core mass distribution, while being noticeable in 1D, have no significant impact on the radius gap in 2D.

7.8.6 Influence of EUV estimation method and X-ray power-law slope

Stellar EUV emission ionizes hydrogen and drives the mass loss of planetary atmospheres, in particular at later ages when the stellar X-ray emission has significantly died down. Understanding the decay details of both X-ray and
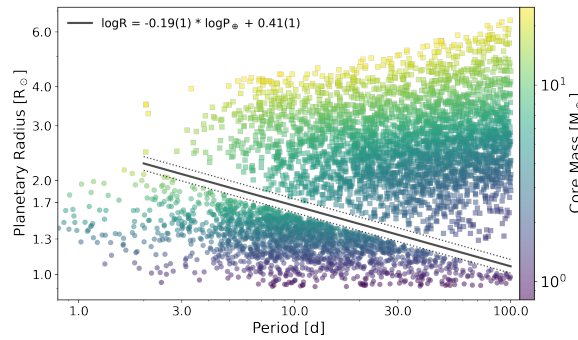
Figure 7.27: Radius vs. period distribution for the planet population with more massive cores ($5M_c$), for comparison with the $3M_c$ simulation in panel (a) of Fig. 7.16. Our fit to the gap is shown in gray.

EUV emission over time and across the whole range of stellar spectral types is crucial for accurately predicting the XUV irradiation of an exoplanet.

As described in Sections 7.3.1 and 7.3.2, we use the works by Tu et al. (2015b); Jackson et al. (2012a); Johnstone et al. (2021) for solar-mass stars to approximate our X-ray evolutionary tracks. In Poppenhaeger et al. (2021), we used the X-ray evolution model by Tu et al. (2015b) only, and estimated the EUV flux using the SF11 relation. The difference to the current work is a slightly lower X-ray luminosity around 1 Gyr, where all the activity tracks are set to converge, as well as a steeper decay beyond this age. We now show how the assumptions about the X-ray decay slope and/or the EUV estimation method impact the evolved 1D and 2D radius distribution.

Figure 7.28 presents the 1D radius distribution for different EUV estimation methods and two different power-law slopes for the X-ray decay. We show the distribution at 10 Gyr, because only at this old age, a small difference between the Jo21 (black) and Li14 (blue) EUV estimation is visible by eye. Li14 predicts EUV luminosities which are up to a factor of 10 higher than the Jo21 ones at X-ray luminosities below $\sim 10^{28}$ **erg/s**, which the stars in our sample reach roughly after one to three Gyrs. For this reason, the EUV estimation at Gyr ages, although the overall XUV fluxes are low, can still have an influence on the radius distribution, with higher EUV luminosities leading to some of the planets at the top edge of the radius gap to become fully stripped of their remaining thin atmosphere. This changes the height of the peaks slightly, but has no impact on the location of the peaks or the gap. In 2D, the location, slope and width of the gap are unchanged.

By using the SF11 method (red) for estimating the important stellar EUV
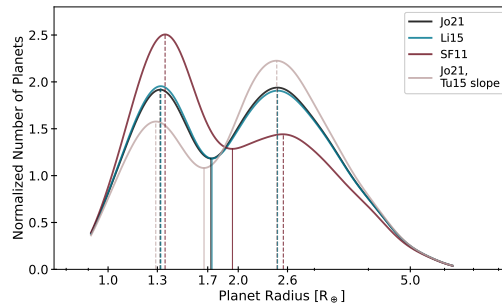
Figure 7.28: Influence of EUV estimation and power-law slope of the X-ray decay. Comparison of the 1D-KDE estimation of the same planet population which have evolved using the Jo21 (black), Li14 (blue) and SF11 (red) method to estimate the stellar EUV output. The Jo21 and Li14 simulations are almost identical, but the SF11 simulation predicts many more evaporated cores due to the high EUV fluxes at young ages. In rose, we also show the same population with EUVs calculated according to Jo21, but with a steeper power-law slope of the X-day decay of −1.58 instead of −1.13. The steepness of the slope impacts the total amount of XUV irradiation the planets receive, with a steeper slope leading to less XUV exposure and fewer evaporated cores.

output, however, the radius distribution at Gyr ages looks significantly different. Due to the EUV luminosity being about 10 times larger than the X-ray luminosity for the first few Gyr, the total XUV flux a planet receives is immense compared to all the other EUV estimation methods. This leads to almost 50% of the planets in our sample to end up as bare rocky cores, compared to around 36% for the Jo21 and Li14 simulations. Due to more planets and planets with more massive cores being completely stripped, the second peak becomes very weakly pronounced and the radius gap shifts to larger radii. In 2D, the gap slope is still consistent within one sigma, but the gap is shifted to larger radii. We observe that in our simulations, the gap becomes slightly narrower as the number of evaporated bare cores increases and the number of planets with envelopes above the gap increases. This comparison shows that the EUV estimation method, as in the case of SF11, can significantly alter the radius distribution. The results support the notion that the SF11 method overestimates the crucial EUV output and should be used with caution for young and/active stars. However, methods adopted to young and active stars like Jo21 (or Ch15) and Li14 lead to matching radius distributions which agree in peak and gap heights and locations, and preserve the second radius peak much like the one present in the observational data.

Not only the EUV estimation method can play a role, but also the steepness of the X-ray decay. In Figure 7.28 we also show the radius distribution for the same population, but having used a steeper power-law slope (-1.58 compared to -1.13) for the X-ray decay – and thus lower EUV and XUV predictions – in Figure 7.28 (rose). It is evident that with less XUV exposure, fewer planets fully evaporate. The second peak is still well populated and due to the smaller number of heavier evaporated cores, the gap minimum is located at sightly smaller radii compared to the simulation runs with a shallower power-law slope. This is just to highlight that the amount and decay shape of X-ray and EUV radiation from the host star influences the location and height of the peaks and the gap in the 1D radius distribution. When trying to model the observed radius distribution, similar to e.g. Modirrousta-Galian et al. (2020); Rogers & Owen (2021), the choice of the slope for the X-ray and EUV decay can substantially impact the conclusions of such studies.

Ultimately, the amount of XUV flux a planet receives is set by the value of the saturation X-ray luminosity, the time a star spends in the saturated phase, the steepness of the X-ray decay and the amount of EUV emission at early and later ages. A general outcome for the lowest mass planets in our sample, or planets really close to their host star, is, that the exact details do not change the fate of these planets – they will lose their atmosphere. For planets with intermediate masses and/or larger distances, the details of the XUV evolution determine if a planet gets fully stripped or can hold on to an envelope. In addition, depending on the strength of the X-ray emission in the saturated phase and the steepness of the decay, the EUV estimation method can have a bigger or smaller impact on the total amount of evaporation a planet undergoes. When the X-ray fluxes are lower, the EUV contribution to the total XUV output becomes more important. As a consequence, small differences in the EUV estimation become more pronounced. On the other hand, if the X-ray fluxes are high, small differences between, for example, the Jo21 and Li14 EUV estimation do not change the total XUV flux significantly, shrinking any differences between the two EUV calculations.

To summarize, our simulations show that the choice of the power-law slope for the X-ray decay can have a much larger impact on the final radius distribution than the EUV estimation method – when using the methods adopted for young and active stars.

8

Three young planets around the young K–dwarf K2–198: High–energy environment, evaporation history and expected future

Ketzer, L.; Poppenhaeger, K.; Baratella, M.; Ilin, E.

Abstract

Planets orbiting young stars are thought to experience atmospheric evaporation as a result of the host stars' high magnetic activity. We study the evaporation history and expected future of the three known transiting exoplanets in the young multiplanet system K2-198. Based on spectroscopic and photometric measurements, we estimate an age of the K-dwarf host star between 200 and 500 Myr, and calculate the high-energy environment of these planets using eROSITA X-ray measurements. We find that the innermost planet K2-198c has likely lost its primordial envelope within the first few tens of Myr regardless of the age at which the star drops out of the saturated X-ray regime. For the two outer planets, a range of initial envelope mass fractions is possible, depending on the not-yet-measured planetary mass and the stars' spin-down history. Regarding the future of the system, we find that the outermost planet K2-198b is stable against photoevaporation for a wide range of planetary masses, while the middle planet K2-198d is only able to retain an atmosphere for a mass range between ~7 and $18\,M_\oplus$. Lower-mass planets are too susceptible to mass loss, and a very thin present-day envelope for higher-mass planets is easily lost with the estimated mass-loss rates. Our results support the idea that all three planets started out above the radius valley in the (sub-)Neptune regime and were then transformed into their current states by atmospheric evaporation, but also stress the importance of measuring planetary masses for (young) multiplanet systems before conducting more detailed photoevaporation simulations.

8.1 Introduction

Young planetary systems ($\leq 1\,\mathrm{Gyr}$) offer snapshots of the earlier stages of planetary evolution and can give insights into how planets have formed and are evolving. The first few hundred million years are expected to be most formative, with different physical processes shaping the planetary systems and their architectures. Processes that are thought to influence the evolution of young planetary systems are the shrinking and contraction of the cooling planet itself (e.g. Baraffe et al., 2006; Mordasini et al., 2012a), orbital migration (for a review, see Baruteau et al., 2014), planet-planet scattering (for a review, see Davies et al., 2014), tidal and magnetic star-planet interaction (e.g. Poppenhaeger & Schmitt, 2011; Strugarek et al., 2017; Shkolnik & Llama, 2018; Ilic et al., 2022), as well as processes that drive the atmospheric mass loss of the primordial planetary atmosphere (e.g. Liu et al., 2015; Watson et al., 1981a; Ginzburg et al., 2018).

The use of radial velocity follow-up and transit timing variations (TTVs) in measuring mass, as demonstrated in studies by e.g. Marcy et al. (2014); Rogers (2015); Jontof-Hutter et al. (2016), has revealed that planets with radii smaller than approximately $2\,R_\oplus$ have densities that suggest a rocky composition similar to Earth, while those with larger radii have lower densities indicating the presence of gaseous envelopes. These primordial atmospheres are thought to be mostly composed of hydrogen and helium and susceptible to mass loss on lower-mass planets. Giant impacts (e.g. Liu et al., 2015; Wyatt et al., 2020) can explain some mass loss, but the two leading physical processes are photoevaporation, an externally induced mass loss mechanism where the star's high energy radiation (X-rays and extreme UVs, together XUV) heats the upper atmosphere and launches a hydrodynamic outflow (e.g. Watson et al., 1981a; Güdel, 2007; Owen & Jackson, 2012a; Lopez et al., 2012), and core-powered mass loss (e.g. Ginzburg et al., 2018; Gupta & Schlichting, 2019), which is driven by the internal luminosity given off by the cooling planetary core. Both processes are able to explain the prominent features in the observed exoplanet population: the radius gap, a deficit of planets with radii around $1.8\,R_\oplus$, separating the rocky planet population below the gap from the planets with volatile, gaseous envelopes above (Fulton et al., 2017b; Van Eylen et al., 2018b), the hot Neptunian desert at very short orbital periods (Mazeh et al., 2016; Lundkvist et al., 2016), and the eccentricity distribution of exoplanets (e.g. Correia et al., 2020). Recently, gas accretion during the gas-poor phase of disk evolution (Lee et al., 2022), and the existence of water- and ice-worlds (e.g.

Zeng et al., 2019; Venturini et al., 2020) have also been put forth as mechanisms to explain the radius dichotomy of close-in exoplanets.

The gaseous envelopes surrounding Neptunes and mini-Neptunes are prone to escaping, leading to the observation of planetary tails comprised of escaping gas detected through the hydrogen Lyman-alpha line (e.g Ehrenreich et al., 2015; Bourrier et al., 2018; Zhang et al., 2022), and more recently through helium absorption, as demonstrated in studies by e.g. Spake et al. (2018); Mansfield et al. (2018); Damasso et al. (2023). Detecting outflows in young planetary systems is particularly interesting because the strength of the mass loss can put constraints on planetary evolution models and might help to distinguish between different mass loss processes. While the discovery and subsequent characterization of young planets is challenging due to the high activity level of the host star, the number of young planets is increasing thanks to dedicated campaigns, giving insights on the role of photoevaporation in early exoplanet evolution. Interesting systems with detected outflow signatures are K2-100b, a ∼750 Myr old, highly irradiated planet right at the border of the hot Neptunian desert with notable ongoing evaporation, causing the planet to significantly decrease its size over the next few Gyr (Barragán et al., 2019a; Gaidos et al., 2020). Zhang et al. (2022, 2023) further detect atmospheric escape for four young (<1 Gyr) mini-Neptunes, predicting the loss of the remaining hydrogen-rich atmospheres for all the planets. These results indicate that for planets orbiting sun-like stars, photoevaporation is an efficient mechanism for stripping primordial gaseous atmospheres, transforming planets from mini-Neptunes above the radius gap into super-Earths below the gap.

In extremely young multiplanet systems like V1298 Tau and AU Mic (≤ 25 Myr) (Vissapragada et al., 2021; Carolan et al., 2020; Cohen et al., 2022), as well as more mature systems like TOI-560 or K2-136 (∼500-700 Myr) (Barragán et al., 2022; Fernández Fernández & Wheatley, 2022) all planets have experienced the same evolution of the high energy emission caused by the spin down and subsequent magnetic activity decay of the star. While this is not only unique to young systems, but also older ones, young multiplanet systems are of particular importance because the most extreme mass loss occurs early on. Depending on the properties of the planet and the host star, young planets can undergo drastic changes in size and mass within the first few 100 Myr. The photoevaporative mass loss of a planet can be quantified in terms of the mass-loss rate, an instantaneous quantity measuring the atmospheric mass loss at any given point in time, or the mass-loss timescale, the corresponding time-integrated quantity, and a measure of the total amount of envelope mass lost within a chosen time interval. The mass-loss timescale depends sensitively on the total

amount of XUV exposure, which is influenced by the time at which the star has dropped out of the saturated X-ray regime, and two planets of similar age could have received an accumulated XUV flux that differs by a factor of 10 between a low activity star that drops out of the saturated regime after a few Myr, versus a highly active star that stays saturated for a few 100 Myr (see e.g. Fig. 3 in Ketzer & Poppenhaeger (2023)). In multiplanet systems, we can conduct comparative mass-loss studies where the stellar contribution is controlled for. Since observable properties like the planetary radius depend strongly on the mass-loss history of the planet, well-constrained systems with planets below and above the radius gap in some cases can be used to constrain the rotational history of the host star (Kubyshkina et al., 2019a,b; Bonfanti et al., 2021). Owen & Campos Estrada (2020) also showed that systems with planets straddling the radius valley can be used to estimate the minimum mass of planets above the valley with remaining gaseous envelope. This makes multiplanet systems interesting targets for dedicated observing campaigns to measure masses as well as ongoing mass loss.

In this paper, we focus on characterizing the three-planet system K2-198, which was flagged as an interesting target for future atmospheric mass loss studies in Foster et al. (2022a). The host star, a K-dwarf, is orbited by three known transiting exoplanets discovered in the *Kepler* K2 data (Mayo et al., 2018; Hedges et al., 2019). The innermost planet c resides well below the radius gap in the regime of rocky planets, while the middle planet d, with a radius of $2.4\,R_\oplus$, sits just above the radius gap in the regime of mini-Neptunes. The outermost planet b has a Neptune-like radius, placing it well above the radius rap in the regime of planets with significant volatile envelopes (Otegi et al., 2020b) (see Table 8.1 for a summary of stellar and planetary parameters). K2-198 was detected in X-rays by eROSITA with an X-ray luminosity of 7.9×10^{28} erg s^{-1}in the 0.2-2.0 keV band (Foster et al., 2022a). Such X-ray luminosity suggests an active host star, placing the planets into an intense high-energy irradiation regime. The combination of an X-ray active host star, orbited by a close-in, likely rocky planet which has lost its primordial hydrogen-helium envelope, a planet straddling the top of the radius gap at a slightly larger orbit, and a Neptune-sized planet further out, make this system of great interest for atmospheric mass loss studies. Further observations and studies of this relatively unexplored three-planet system may provide valuable insights into the formation and evolution of close-in planets and their atmospheres.

In this work, we use photometric and spectroscopic observations to estimate the age of the K2-198 system (Sec. 8.3.4), and characterize the current high energy environment (extreme UV and X-ray; together: XUV) and irradiation

Table 8.1: Properties of the K2 198 star-planet system as provided by Mayo et al. (2018); Hedges et al. (2019).

Parameter	Value
Star:	
Spectral type	K-dwarf
$M_\star$ $[M_\odot]$	$0.799^{+0.045}_{-0.091}$
$R_\star$ $[R_\odot]$	$0.757^{+0.035}_{-0.016}$
T_{eff} [K]	$5212.9^{+49.2}_{-99.0}$
Distance [pc]	$110.56^{+0.87}_{-0.86}$
planet b:	
P [d]	$17.0428683^{+0.0000035}_{-0.0000071}$
R_P $[R_\oplus]$	$4.189^{+0.228}_{-0.098}$
Semi-major axis $(a/R_\star)$	$25.86^{+0.95}_{-0.48}$
Planet c:	
P [d]	$3.3596055^{+0.0000040}_{-0.0000021}$
R_P $[R_\oplus]$	$1.423^{+0.081}_{-0.036}$
Semi-major axis $(a/R_\star)$	$8.76^{+0.32}_{-0.16}$
planet d:	
P [d]	$7.4500177^{+0.0000026}_{-0.0000052}$
R_P $[R_\oplus]$	$2.438^{+0.130}_{-0.056}$
Semi-major axis $(a/R_\star)$	$14.90^{+0.55}_{-0.28}$

received by the three exoplanets in the system using updated eROSITA X-ray measurements. In Sec. 8.3.5, we re-estimate the current mass loss rates of the two outer planets and calculate their expected mass loss evolution over time scales of gigayears, using the code PLATYPOS[1], which is based on an energy-limited evaporation model (Ketzer & Poppenhaeger, 2022). We also explore the past of the planetary system to test the possible range of initial conditions, taking into account reasonable stellar spin-down and thus activity evolutionary tracks.

8.2 Observations and data analysis

The system was observed in X-rays by the eROSITA space telescope, as well as in the optical with TESS and K2.

---

[1]https://github.com/lketzer/platypos/

8.2.1 X-ray data

The position of the K2-198 system was observed by eROSITA (Predehl et al., 2021), an X-ray instrument onboard the Spectrum-Röntgen-Gamma spacecraft (Sunyaev et al., 2021). eROSITA is sensitive to photons in the energy band from 0.2-10 keV, and started an all-sky survey in 2019, where the whole sky is scanned every six months in great circles roughly perpendicular to the ecliptic. The position of K2-198 has been covered by five eROSITA All-Sky Surveys, called eRASS1 to eRASS5.

The X-ray luminosity of the host star K2-198 was first reported by Foster et al. (2022b) to be 7.9×10^{28} erg/s in the 0.2-2 keV energy band, based on a detection of the star in the eRASS1 survey. Since then, data from the following four eRASS surveys (eRASS2 to eRASS5) has been made available to the eROSITA-DE consortium. The survey data sets were processed by the eRSOITA-DE consortium; specifically, a single-band detection in the 0.2-2.3 keV band was run on the stacked data from all five surveys, which was used as the input catalog for a forced photometry in the individual eRASS surveys[2].

We cross-matched the resulting catalog with the position of K2-198 within a $10''$ radius, and we checked that the matched X-ray sources are likely to be of stellar nature, along the lines of Foster et al. (2022b). In this way, we found two detections and three non-detections for the five surveys available for K2-198's position. Specifically, K2-198 was detected individually in the eRASS1 and eRASS5 surveys, undetected in the individual eRASS2, 3 and 4 surveys, and detected in the stacked data from all five surveys together.

8.2.2 K2 and TESS photometry

K2-198 was observed twice with the *Kepler* space telescope during the extended *K2* mission in 2014 and 2018 (Campaign 6 and 17), and once by the transit exoplanet survey satellite (TESS) in 2021 (Sector 46). We use the Python package *lightkurve* (Lightkurve Collaboration et al., 2018) to download the pre-processed lightcurves available for K2-198, which have been corrected for instrumental systematics related to the spacecraft using different detrending methods. We visually inspect the lightcurves for periodic amplitude modulations likely caused by star spots, and derive rotation periods using the Lomb-Scargle periodogram. We select the short and long cadence lightcurve products from the K2, EVEREST, and K2SFF pipeline (Stumpe et al., 2012; Vanderburg &

---

[2]The following consortium catalog versions all_eN_SourceCat1B_221031_poscorr_mpe_photom.fits with N= 1...5 were used.

Johnson, 2014; Luger et al., 2018), as well as the 20-sec and 2-min cadence lightcurves from the TESS SPOC pipeline (Jenkins et al., 2016), normalize the lightcurves, measure the highest amplitude peak in each periodogram, and take the mean of all peak frequencies to determine the value for the rotation period of the exoplanet host star.

8.2.3 TRES spectral analysis

In order to constrain the age of K2-198, we derive the lithium (Li) and barium (Ba) abundances by synthesizing the 6708 Å and 5853 Å regions of the stellar spectrum. We refer the reader to Sect. 3.3.3 for a detailed discussion.

We downloaded the extracted TRES spectrum available on the ExoFOP website[3], with a resolution R=44000 and a SNR per resolution element of 52.9. In particular, we extracted and analyzed only order 38 (for Li) and 31 (for Ba), which contain the two spectral lines of interest. We also found an existing HIRES spectrum, which, however, is of such poor quality preventing us from a good Li or Ba detection.

We synthesized the two spectral regions using the code MOOG (Sneden, 1973) and creating the line lists with `linemake` (Placco et al., 2021), which has the most up-to-date database of experimental atomic parameters of each spectral line. For the model atmosphere, we linearly interpolated from the ATLAS9 grid of Castelli & Kurucz (2003), with solar-scaled chemical composition and new opacities (odfnew). We did not perform a complete abundance analysis, but we estimated the effective temperature (T_{eff}) using magnitudes from the 2MASS (Skrutskie et al., 2006) and *Gaia* DR3 (Gaia Collaboration et al., 2016, 2022a) catalogs with the `colte` program by Casagrande et al. (2021) (adopting the *E(B-V)* value from the TIC catalog (Paegert et al., 2021)). The T_{eff} spans values from 5190±62 in *(R_p-K)* to 5273±68 K in *(G-J)*, and a weighted mean of 5225±40 K. We estimated the surface gravity and the microturbulence following the same approach in Baratella et al. (2020), finding 4.60±0.09 dex and 0.82±0.05 km s^{-1}. For the synthesis, we adopted a *v* sin *i* values from 4 and 5 km s^{-1} making sure that the profiles of other nearby lines match the observed spectrum.

---

[3]https://exofop.ipac.caltech.edu/tess/

8.3 Results

To characterize the high-energy environment of the multiplanet system and estimate the atmospheric mass loss of the three planets, we derive the current X-ray irradiation of the planets and constrain the age of the system using photometric and spectroscopic data.

8.3.1 eROSITA X-ray luminosity

The X-ray source matched with K2-198's position in the stacked eROSITA data, and has a nominal catalog flux of $3.8 \times 10^{-14}\,\mathrm{erg\,s^{-1}\,cm^{-2}}$ in the 0.2-2.3 keV energy band, representing the average flux of the star. However, the nominal catalog fluxes were calculated assuming an underlying power law, while stellar coronae have an underlying optically thin thermal plasma spectrum. Following the analysis of Foster et al. (2022b), we therefore multiply the catalog fluxes by a conversion factor of 0.85 to derive coronal fluxes of the star in the more commonly used 0.2-2 keV energy band. In this way, we derive stellar X-ray fluxes of $3.2 \times 10^{-14}\,\mathrm{erg\,s^{-1}\,cm^{-2}}$ (0.2-2 keV) as the average flux over the five eROSITA surveys, and $5.4 \times 10^{-14}\,\mathrm{erg\,s^{-1}\,cm^{-2}}$ and $7.0 \times 10^{-14}\,\mathrm{erg\,s^{-1}\,cm^{-2}}$ (0.2-2 keV) for the two individual detections in the eRASS1 and eRASS5 surveys. The non-detections in eRASS2, 3 and 4, which happen to have a shorter exposure time at K2-198's position, amount to X-ray flux upper limits of 8.5×10^{-14}, 1.0×10^{-13}, and $1.2 \times 10^{-13}\,\mathrm{erg\,s^{-1}\,cm^{-2}}$, using the same conversion factor.[4]

In our further analysis, we use the average X-ray flux over the five surveys, which is a lower value than the one reported by Foster et al. (2022b), who only used the eRASS1 data, which apparently observed the star in a higher magnetic activity state. We note that since the number of excess counts is only on the order of 10 in surveys 1 and 5 together, a detailed spectral analysis with a fit of the coronal temperature is not feasible.

We use the *Gaia* DR3 distance of 109.6 pc to convert the measured average X-ray flux into an average X-ray luminosity of $L_X = 4.6 \times 10^{28}\ \mathrm{erg\,s^{-1}}$ ($\log L_X\,[\mathrm{erg\,s^{-1}}] = 28.7$) (Gaia Collaboration et al., 2016, 2022b).

---

[4]The eROSITA upper limits (Tubín-Arenas et al. 2023, submitted) were computed based on X-ray photometry on the eROSITA standard calibration data products (counts image, background image, and exposure time) and following the Bayesian approach described by Kraft et al. (1991). The upper limits are given as one-sided 3σ confidence intervals (99.87%) and use the photons from eROSITA's 0.2-2.3 keV energy band.

8.3.2 Stellar rotation period and flaring activity

All inspected light curves, covering a timespan from 2014 to 2021, show highly visible periodic brightness variations on the order of 2-3%, typical for a young and active star with large star spots on the stellar surface Stauffer et al. (e.g. 2016). From the Lomb-Scargle periodogram, we derive a mean rotation rate of 7.1 ± 0.1 days.

We used AltaiPony (Ilin, 2021) to inject synthetic flares into the Sector 47 TESS light curve, and quantify their recovery efficiency. Flares with energies below $\sim 10^{34}$ erg are typically not recovered, so there could be at least one flare with $\sim 10^{34}$ erg in the light curve. This gives a minimum flare rate of 15 flares per year above $\sim 10^{34}$ erg in K2-198, which is up to an order of magnitude above the flare rate of stars with $T_{\mathrm{eff}} > 5000$ K in the Pleiades (Ilin et al., 2021), and in the range of the most active Sun-like stars (Shibayama et al., 2013).

8.3.3 Lithium and barium abundance

From our analysis of the TRES spectrum, we derive a lithium (Li) abundance of $A(\mathrm{Li})_{\mathrm{LTE}} = 2.07 \pm 0.08 \pm 0.13$, where the first uncertainty is due to the fitting procedure and the second is the contribution of the atmospheric parameter uncertainties. With the NLTE corrections from Lind et al. (2009), we find a lithium abundance of $A(\mathrm{Li})_{\mathrm{NLTE}} = 2.15 \pm 0.08 \pm 0.13$. In addition, we also derive a barium (Ba) abundance ratio of $[\mathrm{Ba/H}] = +0.41 \pm 0.10 \pm 0.09$ dex over the solar values from Asplund et al. (2021). The uncertainties are computed in the same way as for Li.

8.3.4 Stellar age determination

To put the K2-198 system into context, and describe the high-energy irradiation environment of the three planets together with their past and future atmospheric evolution (see Sec. 8.3.5), we first need to constrain the stellar age of the system. We use the determined rotation period, X-ray activity level as well as independent spectroscopic age indicators to estimate an age between 200 and 500 Myr, and adopt the logarithmic mean of 316 Myr as the present age of the system.

Rotation-based age

We use the periodic brightness variations from star spots as a proxy for the stellar rotation period, and by applying gyrochronology, to estimate an age of

the system. For a K-dwarf, this well-constrained rotation period of roughly 7 days is still relatively short, indicating a young age (see e.g. Barnes (2003d)). Figure 8.1 shows a color-period diagram for stars in the Pleiades, Blanco 1, NGC 3532, Group X, Praesepe and Hyades cluster, covering an age range from approximately 100 to 800 Myr (Curtis et al., 2020a; Gillen et al., 2020; Fritzewski et al., 2021c; Messina et al., 2022; Wright et al., 2011a; Newton et al., 2016; Douglas et al., 2019)(Douglas et al., 2019; Wright et al., 2011a). By visual inspection, the K-dwarf K2-198 is located above the gyrochronological sequence of the Pleiades and Blanco 1 (~130 Myr), and well below that of the Praesepe and Hyades (~600-800 Myr). With its 7-day rotation period, the star can be placed nicely on the rotational sequence for the ~300 ± 60 Myr old clusters NGC 3532 and Group X, indicating the youth of the star-planet system. The absence of flares in the TESS light curve, as discussed in Sec. 8.3.2, is compatible with the estimated young age of K2-198.

We also make use of *stardate* (Angus et al., 2019), a Python tool, which combines isochrone fitting with gyrochronology, to infer a Bayesian age for our system. The tool employs the affine invariant ensemble sampler *emcee* (Foreman-Mackey et al., 2013). We use 50 walkers, 500,000 samples and a burn-in phase of 500, and obtain an age of $0.46^{+0.04}_{-0.13}$ Gyr, in agreement with the location on the color-period diagram.

X-ray activity

In Figure 8.2, we show the X-ray luminosity normalized by the bolometric luminosity, L_{bol}, as a function of the Rossby number for late-type stars in young open clusters of different ages. The data is taken from (Wright et al., 2011a), and the conversion from stellar rotation period, P_{rot}, to Rossby number, Ro, is done using the empirically determined convective turnover times, τ_c, by Wright et al. (2018) (their Eq. 6) and is given by $Ro = P_{\mathrm{rot}}/\tau_c$. The location of K2-198, with $L_X/L_{\mathrm{bol}} = 2.9 \times 10^{-5}$ and $Ro = 0.33$, indicates that the star is well beyond the breakpoint between the saturated regime, where L_X/L_{bol} is approximately constant, and the unsaturated regime, which stars enter during their spin-down phase as they age. A comparison with clusters of various ages points towards an age of K2-198 between ∼ 150 and 600 Myr, in agreement with the age determination from gyrochronology.

The X-ray fluxes reported in Sec. 8.3.1 indicate that the star displays some variability over the observed timescale of roughly 2 years. Given the determined average X-ray flux and the larger value of the two individual detections, we estimate a variability amplitude of around 2.2. ϵ Eridani (∼ 400 Myr), and
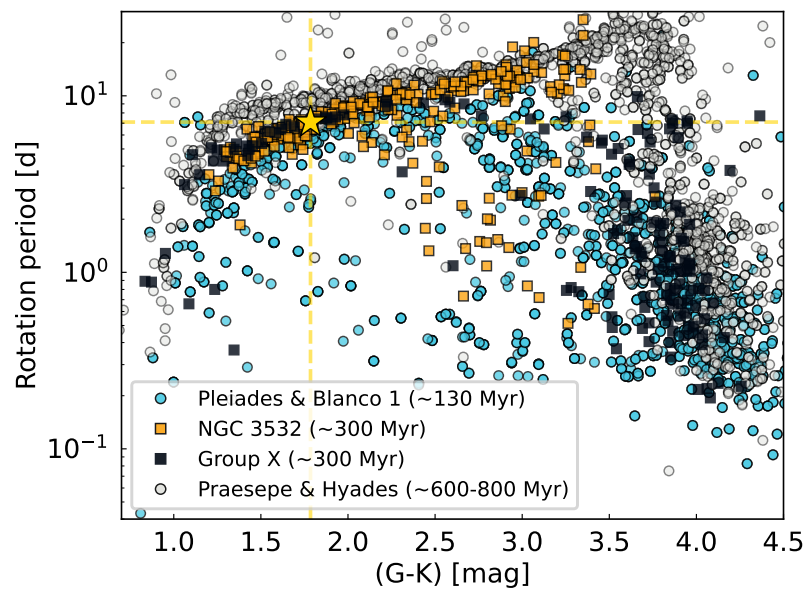
Figure 8.1: Color-period diagram showing the rotational sequences for selected clusters of different ages. The location of K2-198, which is marked with a yellow star, indicates an age older than roughly 100 Myr, but significantly younger than 600-800 Myr.
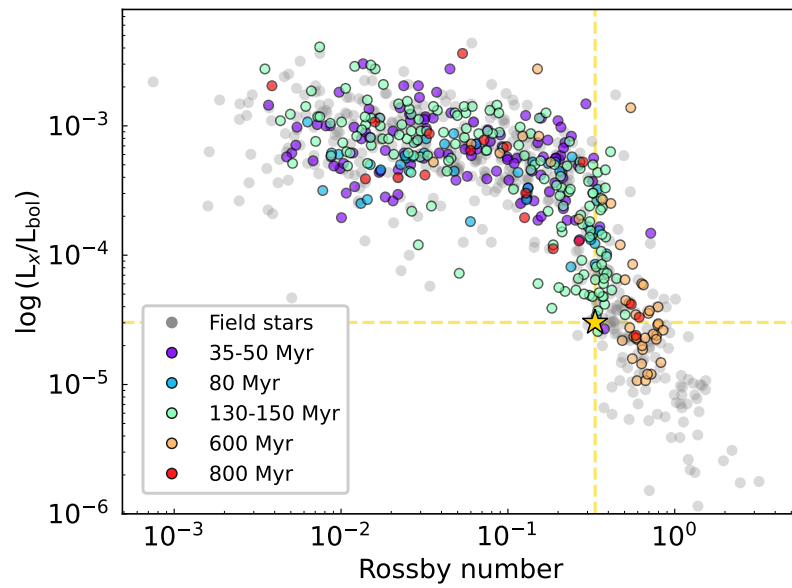
Figure 8.2: Plot of $L_X/L_{\rm bol}$ as a function of Rossby number for all stars in the sample by Wright et al. (2011a) with measured rotation periods. Field stars are marked in gray, while cluster stars with ages below ~1 Gyr are shown in five different-colored age bins. The location of K2-198, which is marked with a yellow star, indicates that the star has already dropped out of the saturated regime and concurs with an age between ~150 and 600 Myr.

ι Horologii ($\sim$ 600 Myr), the two youngest solar-like stars with detected X-ray activity cycles, exhibit not only the shortest X-ray cycles (with approximately 1.6 and 2.9 years), but also the smallest variations in X-ray luminosity (on the order of 2 throughout the cycle) among all stars with detected coronal cycles (Sanz-Forcada et al., 2019; Coffaro et al., 2020). Kepler-63, a fast rotator ($P_{\rm rot} \approx 5.4$ days) (Sanchis-Ojeda et al., 2013) with an estimated age of 200 Myr, did not display cyclic X-ray variability, suggesting that stars much younger than 400 million years might have inhibited X-ray cycles due to a significant presence of coronal magnetic regions (Coffaro et al., 2022). Although no cycle was detected, the X-ray data for Kepler-63, which covers just over a year, shows a minimum-to-maximum variation smaller than a factor 2. While the eROSITA data for K2-198 does not allow for detailed statements about cyclic variability, the data is compatible with the variability observed in other young stars.

Lithium and barium

It is well known that the photospheric abundance of Li decreases with increasing age in late-type stars. When a star is born, its Li abundance reflects the abundance of the interstellar medium from which it has formed. Then, thanks to several transport mechanisms, some of the photospheric Li is brought into deeper layers where it is exposed to temperatures larger than $\sim 2.6 \times 10^6$ K, with the consequence of easily being destroyed. Therefore, Li is depleted in the photosphere as the star evolves by a factor 30-60 after the first dredge-up, and it can be used as powerful age diagnostics (Iben, 1967; Jeffries et al., 2013; Romano et al., 2021).

In addition to Li, it has recently been demonstrated that in young stellar clusters (open clusters, moving groups and local associations), the Ba abundance increases dramatically with decreasing age, with values around [Ba/Fe]$\approx$+0.65 dex at 50 Myr (D'Orazi et al., 2009; Reddy & Lambert, 2015; Magrini et al., 2018). The same trend has been also observed in solar twins (Reddy & Lambert, 2017), where the authors, for the first time, showed an interesting correlation with activity. In Baratella et al. (2021) it was finally demonstrated how the anomalous over-abundance does not result from peculiar nucleosynthesis, but is mostly related to alterations of the spectral line formation due to the more intense stellar activity at such young ages. This behavior is valid for all young/active stars, not only in open clusters, but also in the field (see also D'Orazi et al. 2022 for a complete review on the topic). While the main process behind such alterations is not well understood yet, such chemical peculiarities can nevertheless be used to probe the youth of a star.
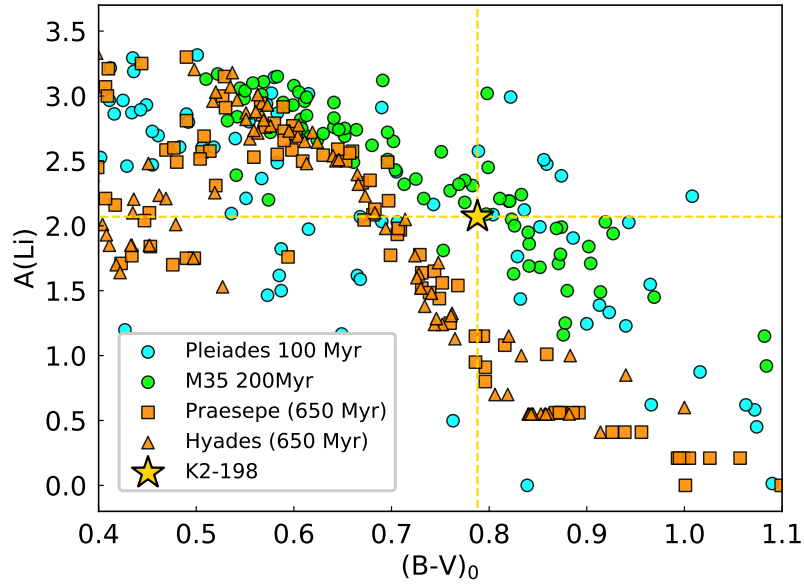
Figure 8.3: Abundance of lithium as a function of the color index $(B\text{-}V)_0$ of different young clusters. The stellar ages range from as young as 100-200 Myr (circles) to roughly 650 Myr, or the age of Praesepe and Hyades (squares and triangles). K2-198 is marked with a yellow star. For a K-dwarf, the measured lithium abundance indicates an age significantly younger than the Praesepe/Hyades.

In Figure 8.3, we plot the lithium abundance, A(Li), as a function of $(B\text{-}V)_0$ for different young stellar clusters. We show the Pleiades (~100 Myr, Bouvier et al. 2018), M35 (~200 Myr, Anthony-Twarog et al. 2018), the Hyades and Praesepe (~600-650 Myr, Cummings et al. 2017). Our target places near the Pleiades and M35 distribution, suggesting an age of ~200 Myr and definitely younger than the Hyades/Praesepe. This is also corroborated by the Ba abundance, for which we found an abundance ratio of [Ba/H]=+0.41±0.10±0.09 dex over the solar values from Asplund et al. (2021). The super-solar Ba abundance is similar to what is found at similar ages in Galactic open clusters in Baratella et al. (2021) and D'Orazi et al. (2022), suggesting an age significantly younger than 1 Gyr.

Kinematic Age Determination

Another independent way to statistically estimate stellar ages is through the empirical age-velocity dispersion relation (short: AVR) (Strömberg, 1946;

Holmberg et al., 2009), which is based on the observation that older stars have a larger velocity dispersion. As part of their Planets Across Space and Time (PAST) project, Chen et al. (2021) characterize the membership of galactic components based on stellar kinematics (i.e., astrometry and radial velocities) provided mainly by Gaia and LAMOST, and derive stellar kinematic ages, with a typical uncertainty of 10-20%, for a sample of 2000 exoplanet host stars. In their published catalog of kinematic properties, they report relative probabilities for stars belonging to different galactic components (e.g., thin/thick disk), which they show is correlated with stellar age (see their Fig. 18). The kinematic age generally increases with the relative membership probability, TD/D (thick disk over thin disk), illustrating that TD/D is indeed an indicator of age for stars in the Galactic disk. Fig. 18 in Chen et al. (2021) shows that the predicted age of K2-198 is well below 1 Gyr, highlighting the youth of the system. With a reported relative probability, TD/D, of 1.85e-02, the predicted kinematic age is ~0.84 Gyr. Kinematic methods like the AVR are ideally used for an ensemble of stars and not for individual systems, which is why we do not include this age value in our final estimate. Nevertheless, it supports the notion that K2-198 is a young star, with age <1 Gyr.

Based on the age constrained by the rotation period, X-ray activity and lithium abundance, we are confident about the youth of the system and estimate K2-198's age to lie between 200 and 500 Myr. We adopt the logarithmic mean of 316 Myr as the present age of the system, and use this as input for the atmospheric evolution and escape calculations.

8.3.5 Atmospheric evolution and escape

We estimate the current atmospheric mass loss rate of the K2-198's two outer planets, which reside above the observed radius gap and likely still host gaseous envelopes. We perform two types of calculations: in Sec. 8.3.5 we estimate the future radius evolution of the two outermost planets to test whether one of the two planets can survive above the gap; and in Sec. 8.3.5, we investigate the past of all three planets by calculating backwards in time.

All simulations are conducted with the publicly available python code PLATY-POS[5]. For a detailed description of the code and its limitations, see Ketzer & Poppenhaeger (2022) and Sec. 2 in Ketzer & Poppenhaeger (2023). The code uses the formalism of energy-limited atmospheric escape, with the inclusion of a radiation/recombination-limit, to calculate atmospheric mass loss rates of

---

[5]https://github.com/lketzer/platypos/

planets with gaseous hydrogen-helium envelopes atop rocky cores. Unless stated otherwise, we adopt a heating efficiency of 0.1, calculate the XUV absorption radius according to Lopez (2017), and the extreme ultraviolet (EUV) flux based on the updated X-ray-EUV surface flux relation by Johnstone et al. (2021). The planetary radius evolution is modelled using the mass-radius-age fitting formula by Chen & Rogers (2016), which takes into account that planets contract as they cool.

Regarding the future activity evolution of the host star, based on the estimated age range of 200-500 Myr and the measured X-ray luminosity of 4.6×10^{28} erg s^{-1}, we infer that the star has already dropped out of the saturated regime, converged onto the slow-rotator sequence and will continue its activity decay along one specific track. For our investigation of the past of the star-planet system, we take into account that stars of similar spectral type drop out of the saturated regime over a range of ages, depending on initial rotation rate and/or magnetic field complexity (Wright et al., 2011b; Matt et al., 2015; Tu et al., 2015b; Gondoin, 2018; Garraffo et al., 2018). The stellar high-energy activity tracks used in this work are motivated by the spread in X-ray luminosities of young cluster stars of similar age (see Fig.8.4) (e.g. Wright et al., 2011b), and to some extent by the rotational spin-down, and thus activity evolution models by Johnstone et al. (2021). We choose several ages, at which the star might have dropped out of the saturated regime, covering a range from low to high activity expected for K-dwarfs. The X-ray luminosity in the saturated regime is calculated according to the updated $\log(L_{X_{sat}}/L_{bol})$-fit by Johnstone et al. (2021).

Planetary mass estimates and current mass loss rate estimates

Since no planetary masses have been measured for this system, we use the observed radii and existing mass-radius relations to estimate masses for the three planets. For the innermost planet c, we assume it to be fully rocky, which, given the mass-radius relation for Earth-like rocky cores (Lopez & Fortney, 2014b; Chen & Rogers, 2016), corresponds to a bare core of $3.9\,M_\oplus$. The two outer planets d and b have radii which place them in the volatile regime according to Otegi et al. (2020b). Using their observationally-based mass-radius relation (see their Fig. 2), we estimate a realistic mass range of $3.6 - 22.0\,M_\oplus$ for planet d, and $7.7 - 25.0\,M_\oplus$ for planet c. While the 2σ envelope of the mass-radius relation by Otegi et al. (2020b) predicts a mass as high as $60\,M_\oplus$ for a planet with a radius of $4.1\,R_\oplus$, our upper mass limit for the outermost planet is set by the grid-limits behind the mass-radius-age fitting formula by

Chen & Rogers (2016). For the calculation of the planets' past in Sec. 8.3.5, we restrict ourselves to three example masses, covering the estimated mass ranges for planets d and b.

At present, the X-ray irradiation levels of the three planets are 1.7×10^4, 6.0×10^3, and 2.0×10^3 $\mathrm{erg\,s^{-1}\,cm^{-2}}$, going from the innermost planet c to the outer ones d and b. By estimating the EUV emission according to Johnstone et al. (2021), we obtain XUV fluxes of 4.1, 1.4 and 4.7×10^3 $\mathrm{erg\,s^{-1}\,cm^{-2}}$for planets c, d and b, respectively. Planet c resides below the exoplanet radius gap and is thus assumed to be an evaporated, leftover, bare rocky core. According to Fossati et al. (2017), photoevaporation of planetary atmospheres occurs when the restricted Jeans escape parameter is smaller than 80, which is true for all the planets under consideration. Thus, assuming the two outer planets, which are located above the radius gap, still host volatile envelopes, we estimate present-day mass loss rates of 2.5×10^9 to 3.7×10^{10} $\mathrm{g\,s^{-1}}$ for planet d and 4.0×10^9 to 2.0×10^{10} $\mathrm{g\,s^{-1}}$ for planet b, using the modelling assumptions and planetary masses described above.

Future of the planetary system

We evolve the two outermost planets d and b forward in time to investigate their future atmospheric mass loss and subsequent radius evolution, and to predict whether they will lose their remaining envelope and fall below the gap or not. Planet c already resides below the gap and thus is assumed to have lost its envelope by the present age (which we take to be 316 Myr in the simulation). We terminate the simulations at a final age of 5 Gyr, which is approximately solar system age and close to the median age of the observed exoplanet population (Gaidos et al., 2023), or the age at which the planet turns into a bare core.

For the inner planet d, an envelope mass fraction of $\leq 1.1\%$ is needed to match the observed radius. The fraction decreases with increasing planet mass, with only 0.02% needed to reproduce today's radius for a $22\,M_\oplus$ planet. We show the radius evolution across a range of planetary masses for the middle planet of the K2-198 system in Figure 8.5 (purple). The results indicate that there is an intermediate mass range, spanning approximately from ∼6.6 to $18\,M_\oplus$, in which planet d can hold on to some of its atmosphere and continue to reside above the gap with envelope mass fractions between 0.02% and 0.3%. Lower mass planets, which do have the largest envelope mass fractions at present age, will lose their remaining envelope by 5 Gyr. Their low gravitational potential helps boost the mass loss. Interestingly, we see a dichotomy in the planets that lose
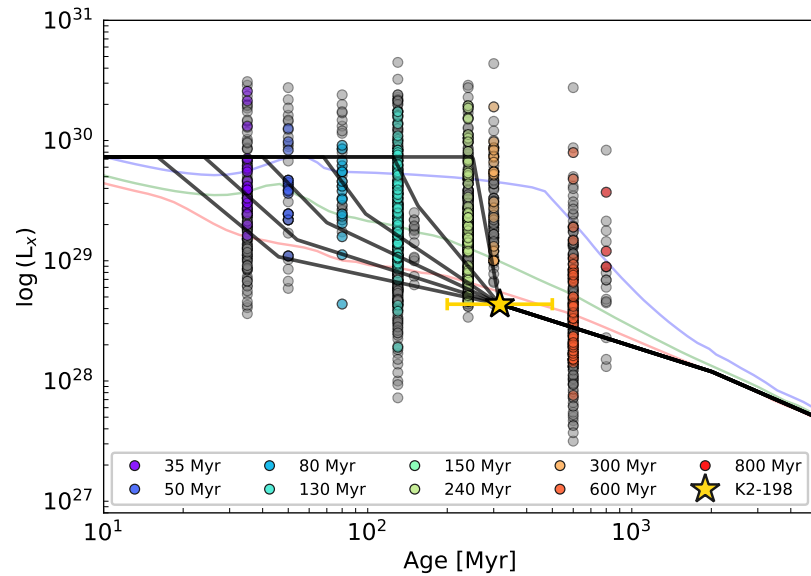
Figure 8.4: Plot of L_X as a function of stellar age for stars in open clusters below 1 Gyr (Wright et al., 2011a). We show all stellar types in gray, and color-code only the stars with stellar masses between 0.7 and 0.9 $M_\odot$ by age. The translucent red, green and blue lines show stellar spin-down models for a $\sim 0.8\,M_\odot$ star for an initially slow, intermediate and fast rotator (Johnstone et al., 2021). We plot K2-198 based on the measured eROSITA X-ray luminosity and the adopted age of 316 Myr. The errorbars mark our constrained age range of 200-500 Myr. K2-198's location indicates that the star is on the inactive side for its age and spectral type, and has already dropped out of the saturated regime, in agreement with Fig. 8.2.

their envelope for planet d. In our simulation, the most massive planets also lose their very thin envelopes. While planets with massive cores are generally much better at holding on to their atmospheres, only a very thin envelope is needed to match the observed radius because the bare core itself is already quite large. Even such massive planets cannot hold on to their thin envelopes and will turn into large bare cores by 5 Gyr.

For the outer planet c, the results show that across the whole mass range under consideration (7.7 to 24 $M_\oplus$), and envelope mass fractions in the range of 9-10%, all planets are able to retain a significant fraction of their envelope by 5 Gyr and undergo only minor radius evolution. The planets only lose between ∼0.1 and 1% of their total envelope mass, which is negligible in comparison to their large envelopes. This is visualized in red in Figure 8.5.

We also conduct all calculations at the younger estimated age of 200 Myr, and the conservative upper age limit of 500 Myr. While the mass range for planet d surviving above the gap is somewhat shifted to lower/higher masses (±0.4 $M_\oplus$ for 200/500 Myr), a slightly different age does not qualitatively change the finding of an intermediate 'survival' mass range. Planet b, which experiences less intense evaporation, is not significantly impacted by the starting age of the calculation.

Ill-constrained past of planets d and b in the absence of planetary masses

We further evolve all three planets backwards in time across a range of evolutionary tracks with different spin-down ages (tracks shown in Fig. 8.4) to investigate how these planets might have started out their lives. Our stopping age for the backwards calculation is 100 Myr, which is the age limit for which the planetary models are valid. The aim of this backwards calculation or exploration of the planets' past is not to make quantitative predictions, but rather to highlight the degeneracy induced by core mass and envelope mass fraction.

If we assume that the innermost planet c has just evaporated at the present age, our backwards calculation leads to envelope mass fractions at 100 Myr between 10% for the lowest activity track, and 20% for the highest activity track. Due to the high XUV irradiation levels and likely high mass-loss rates at even younger ages, the initial envelope mass fractions were possibly larger. Planet formation models predict initial envelope mass fractions between 0.5 and 9% (Lee & Chiang, 2015; Mordasini, 2020; Gupta & Schlichting, 2019), so the innermost planet c would have easily lost an envelope of this mass by the
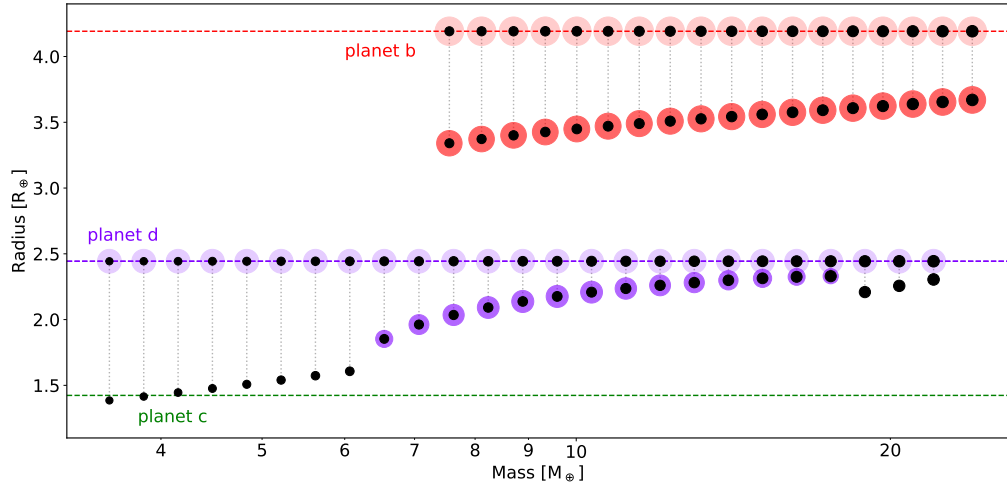
Figure 8.5: Future radii of planets b, c, d at an age of $5\,\mathrm{Gyr}$. The current radii of planets c, d and b are shown as dashed lines, together with the current and final radii for a range of planetary masses for the outer two planets d and b; the core is represented by a black circle, while the envelope is shown as a colored circle around the core. The core size increases with increasing mass. Note that the size scaling of the envelope compared to the core is arbitrary. It is chosen such that one can easily compare present and final planetary radii and immediately see, which configuration can hold on to some fraction of the envelope and remain above the gap. While the outermost planet b will retain enough envelope to remain well above the radius gap around $1.8\,R_\oplus$ for all masses considered, we find that for planet d there is an intermediate mass range between ~7 to $18\,M_\oplus$, for which planets can retain an envelope and survive above the gap. Lower mass planets will experience enough mass loss to completely lose their envelope, while higher mass planets only have very thin envelopes at present age to match the observed radius due to their larger core size, that their thin envelope is easily lost, in spite of their large mass. Planet c is assumed to be rocky at present and will not change its size significantly. The current radius of planet c matches well with the radii predicted for Earth-like rocky cores in the mass regime of 3-5 $M_\oplus$.

present age. We therefore conclude that planet c has likely been a bare core for many tens of Myr.

For planets d and b, such comparison is complicated by the fact that on top of the unknown spin-down age of the star, the planetary masses are unconstrained. If we take three core masses covering the assumed mass ranges, the backwards calculation leads to a range of possible scenarios. This is illustrated for the two outer planets d and b in Figure 8.6 (top and bottom, respectively). In the figure, a relatively clear trend is visible. Envelope mass fractions, as expected, are higher at younger ages due to the mass loss planets have experienced up to the current age. Lower-mass cores host even higher envelope mass fractions, due to the higher mass-loss rates compared to planets with slightly more massive cores. The range in envelope mass fractions for a particular core mass is the second noticeable result. This difference becomes more pronounced for lower core masses and is a consequence of the chosen stellar activity track, which can range from a low activity, i.e. a short saturation time, to a track with a long saturation time and thus most intense past mass loss. The difference that a stellar activity track makes further decreases with the overall XUV irradiation level – in the case of planet b, caused by the larger orbital distance.

For planet d, the envelope mass fraction at 100 Myr ranges from as little as 0.1-0.3% to 1-2.5% to 4-22% for a planet with an 18.9, 8.2, or 3.6 $M_\oplus$ core. For planet b, which is located further away from the host star, the envelope mass fractions range from 9.6-9.8% to 10.7-11.4% to 11-14% for a planet with an 19.0, 11.8, or 7.9 $M_\oplus$ core – the spread within each age bin coming from the different possible activity tracks. These values indicate that planet d, if the core mass is small, might have started out as a large, puffy young planet with a radius of 4-8 $R_\oplus$ or larger. For heavier core masses, the predicted radii at 100 Myr are in the sub-Neptune regime ($\sim$2.5-3 $R_\oplus$). For the outermost planet b, regardless of the core mass or spin down age, the results indicate a radius in the size regime between Uranus and Saturn at ages around 100 Myr or younger.

To give a rough idea about how these envelope mass fractions at 100 Myr compare to what is predicted by planet formation models, we provide some numbers. Lee & Chiang (2015) and Mordasini (2020) (together: LCM) predict primordial envelopes (around the time of disk dissipation, i.e. $\sim$10 Myr) on the order of 1-2% for the lowest mass core, while Gupta & Schlichting (2019) (short: GS) predict an envelope as large as 9% of the total planet mass. For the intermediate mass core, the predicted f_{init} is either around 3-4% from LCM or as high as 12% from GS. What this comparison tells us is that a low-mass planet with a primordial envelope as thin as predicted by LCM, stands no chance of surviving above the radius gap (with $f_{init} \sim 1\%$) by the current age of

the system. If planet d was a massive planet with a core close to $20\,M_\oplus$, our backwards calculations produce a 100 Myr planet with only a very thin envelope with $f_{init} \leq 0.3\%$. The formation predictions introduced above predict a planet of this core mass to accrete much higher primordial envelopes on the order of 10% (LCM) or 18% (GS), suggesting that the true core mass of planet d is smaller. For planet b, the LCM formation models predict initial envelopes of 3-4% (12%) for the $6.9\,M_\oplus$ core, 8% (15%) for the $11.8\,M_\oplus$ core, and 15-16% (18%) for the massive planet (with GS predictions given in parentheses). If we assume the planet to have hosted envelope mass fractions similar to or higher than the ones we estimate at 100 Myr, the LCM models suggest a planetary core on the heavier side for planet b.

We stress that the goal here is not to make any precise quantitative predictions about the past of the planetary system, or try to constrain e.g. the rotational evolution of the host star or core mass of the planets in the system, as has been done previously (e.g., Owen & Campos Estrada, 2020; Bonfanti et al., 2021). In principle, such comparisons between planet formation model predictions, stellar activity histories and planetary core masses could be used to put constraints on some of these parameters. However, due to all the uncertainties involved in the mass-loss modeling, which includes all the details in modelling the planetary structure itself, any magnetic field effects, the XUV absorption radius of the planet, or the evaporation efficiency at any given age and planet configuration, we refrain from constraining planetary mass or activity evolution and stress the importance of getting a better handle on the planetary masses before conducting more detailed studies.

Overall, our results do show that K2-198 d and b are consistent with a wide range of evaporation histories. We expect planet c to have started out as puffy mini-Neptunes, with planet c likely having lost its primordial atmosphere well before the current age of around 300 Myr. Planet d likely started out either as a puffy mini-Neptune or somewhere in the sub-Neptune regime, while planet b has likely not changed its radius drastically compared to its present-day size. Without measured planetary masses and a more detailed understanding of the rotational spin-down, which includes the factors that influence when a star drops out of the saturated regime, and the timescale for this first rapid spin-down, even multiplanet systems can present an ill-constrained problem in planetary formation and evolution.
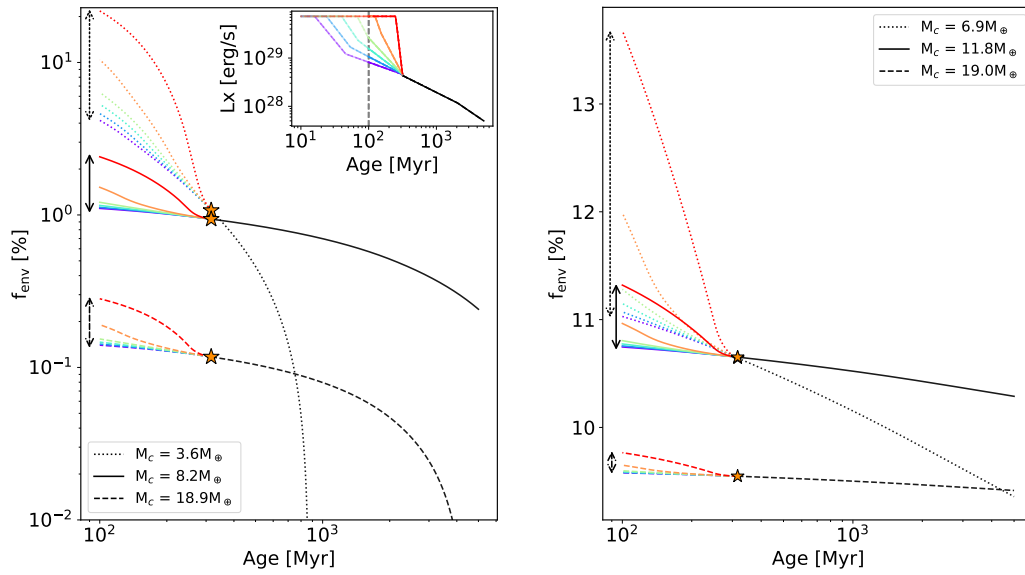
Figure 8.6: Evolution of the envelope mass fraction for planets d and b (upper and lower panel, respectively) as a function of time for three example core masses and six different past activity evolutionary tracks. The different colors represent the evolution along the corresponding activity track, as shown in the embedded L_X vs. age plot in the top right corner. This figure illustrates that without a constraint on the core mass (and to lower extent activity history of the host star), a wide range of possible f_{env} and with it radius histories for the two outer planets are possible.

8.4 Discussion

With K2-198d residing just above the radius gap and the still relatively high predicted mass loss rates, K2-198 is an interesting multiplanet system for future detailed hydrodynamic modelling and observations of atmospheric outflow signatures. Although K2-198c has likely lost its primordial envelope due to efficient and intense hydrogen escape at early ages, this planet might host a secondary atmosphere formed by outgassing volatile gases from the magma after the photoevaporation phase (Kite & Barnett, 2020; Tian & Heng, 2023).

Our findings demonstrate how photoevaporative mass loss can lead to the present-day planet parameters starting from a wide range of initial configurations. This is, for one thing, caused by the unconstrained planetary masses, and on the other because stellar spin-down is complex and not fully understood. In particular, the specific spin-down path that stars take from young to old ages may contain time stretches of rapid versus slow magnetic braking, see for example Curtis et al. (2020b); Gruner & Barnes (2020); Dungee et al. (2022). Our results stress that even for the future evolution of planets in its infant or youth stages, it is crucial to first measure planetary masses, before more constraining studies like those of the multiplanet system around the 400 Myr-old star HD 63433 (TOI-1726) (Damasso et al., 2023), V1298 Tau (Poppenhaeger et al., 2021; Suárez Mascareño et al., 2021) or K2-102 (Brinkman et al., 2023) are possible.

Our mass loss calculations suggest a dichotomy in planetary mass for planets ending up with and without a remaining primordial atmosphere. Unless the planetary mass is restricted, planets in an intermediate irradiation regime, like K2-198d, could evolve below the gap if their core mass is small enough, or large enough. In the latter case, it is not the low gravitational potential that boosts the mass loss, but instead the low mass of the planetary atmosphere, if it is indeed the large core that makes up for most of the observed planetary radius. For highly-irradiated planets like K2-198c, even for a wide range of planetary core masses such planets cannot hold on to an atmosphere, while for moderately irradiated planets further out, like K2-198b, the planet is stable against complete atmospheric mass loss for a wide range of core masses.

Measuring planetary mass loss rates across a wide range of planetary parameters, XUV environments and stellar ages will further put constraints on the atmospheric escape model and its modelling inputs, and help distinguish between different mass loss mechanisms.

Atmospheric characterization perspectives

The transiting multiplanet system K2-198, with its young age and relatively high X-ray brightness, is an interesting target for follow-up observations. Suitable options include observing the lower atmosphere layers of the planets with transmission spectra in the infrared with JWST, or trying to observe ongoing mass loss through transmission spectra in the ultraviolet hydrogen Ly-α line or the infrared metastable helium lines (He I at 10830 Å).

Regarding the characterization of lower-layer atmospheres, based on the observed radii of K2-198d and b and the estimated mass ranges, both planets most likely host volatile envelopes at the present age. We estimate a JWST transmission spectrum metric (TSM; Kempton et al. (2018)) of 13-76 for planet d and 44-138 for planet b for the mass ranges under consideration (see Sec. 8.3.5). Planet d, regardless of its estimated mass, has a TSM smaller than the recommended minimum value of 90 for small sub-Neptunes. Depending on the planetary mass, K2-198b, however, could be an interesting target for transmission spectroscopy with JWST. With its radius in the large sub-Neptune regime, the recommended TSM of 90 is exceeded if the planetary mass lies below $\sim 12\,M_\oplus$. For planet c, the estimated TSM is 18, which is above the recommended value of 10 for planets with radii smaller than $1.5\,R_\oplus$, making this planet a favorable target to search for any secondary atmosphere. The emission spectroscopy metric (ESM) for K2-198c, however, is 2.7 and thus below the recommended threshold of 7.5 for terrestrial planets for emission spectroscopy with the James Webb Space Telescope.

Regarding ongoing mass loss, observations of the He I lines are promising. It has been suggested that the metastable helium state can be efficiently populated by the stellar spectrum of K-type stars due to the relative fluxes of extreme ultraviolet radiation, which produces triplet He I in the ground state of the line, versus the near ultraviolet radiation, which ionizes it (Oklopčić, 2019). Poppenhaeger (2022) further suggest that stellar X-ray luminosity and [Fe/O] coronal abundance ratio influence the critical stellar narrow-band EUV emission. They find that young and active stars having [Fe/O] < 1 exhibit lower EUV emission in the 200-504 Å range compared to old and inactive stars with [Fe/O] > 1. K2-198 with its young age and high X-ray luminosity ($\log L_X\,[\mathrm{erg\,s^{-1}}] = 28.7$) is comparable to the high-activity K-dwarfs in the sample of Wood et al. (2018) that display [Fe/O] ratios lower than unity. This suggests that the steeper EUV-X-ray relation from Poppenhaeger (2022) should be applicable, leading to a lower EUV emission value than for stars with high [Fe/O]. Based on the scaling laws derived in Poppenhaeger (2022), we estimate

that with the current broad-band X-ray flux, planet K2-198d receives a narrow-band EUV flux on the order of 0.5 Wm^{-1}, which could translate to relatively high helium absorption scale heights on the order of 60 when compared to known systems with observed helium absorption (see their Fig. 8). For the outermost planet c, we calculate 0.2 Wm^{-1} or roughly 40 helium absorption scale heights. These estimates suggest that, especially K2-198d, although orbiting a young and active star, could be an interesting target for the search of atmospheric mass loss via the metastable helium triplet.

8.5 Conclusions

We use updated eROSITA X-Ray measurements together with photometric and spectroscopic archival data to constrain the age of the multiplanet system K2-198 to 200-500 Myr. We characterize the present-day high-energy irradiation environment of the three planets, of which the innermost planet is already below the observed exoplanet radius gap in the regime of rocky worlds, while the outer two are mini-Neptunes residing above the gap. With an X-ray luminosity of $\log L_X \, [\mathrm{erg\,s^{-1}}] = 28.7$, the star has already dropped out of the saturated X-ray regime. We use a model for the stellar activity evolution together with exoplanetary mass loss to estimate the atmospheric evolution of the two outermost planets in the mini-Neptune regime for a range of reasonable planetary masses.

Our calculations indicate that the outermost planet K2-198b will retain a gaseous envelope and survive above the gap over the next several Gyr for planetary masses between ~ 7 and $25\,M_\oplus$. Interestingly, we find that the middle planet K2-198d can only retain an envelope for an intermediate mass range of approximately 7-18 $M_\oplus$. Lower mass planets experience enough mass loss to become rocky and drop below the radius gap, while higher mass planets, which, at present, would only require a very thin envelope to match the observed radius, are easily stripped despite their larger ability to hold on to their atmospheres. K2-198c, which has likely lost its envelope early on and resides as a bare core below the radius gap, still experiences large amounts of XUV irradiation, and might be an interesting target for investigating the formation of secondary atmospheres.

Due to the lack of measured planetary masses and the unknown stellar activity history, it is challenging to provide constraining predictions to the history of the planetary system. The wide range of compatible evaporation histories for all three planets stresses the importance of getting a better handle on the

planetary masses before conducting more detailed studies. Nonetheless, the young K2-198 system is an interesting target to search for ongoing mass loss via metastable helium or possibly Lymann-α, which can be expected based on the estimated mass-loss rates, at least for the middle planet K2-198d. Depending on the prospectively measured planetary masses, K2-198d and b could also turn out to be very favorable targets for atmospheric characterization with JWST.

8.6 Acknowledgements

9   Conclusions & Outlook

The rise in the number of known exoplanets poses outstanding questions around their demographics, and the mechanisms that shape exoplanets into how we observe them today. Specifically, the inferred radius distribution and a feature known as the small-planet radius gap have drawn significant interest in the last years. The majority of planets we observe today orbit stars with ages well beyond a gigayear and their parameters have changed significantly since their formation. During the first billion years, a star emits significant amounts of X-ray and UV radiation, greatly impacting the evaporation, thermodynamics, and chemistry of the young planet's atmosphere. Young star-planet systems therefore provide a unique window into the earliest stages of planet formation and evolution and offer the possibility of observing planets before and during atmospheric mass-loss processes transform their initial parameters, making them similar to the typically much older population of known exoplanets.

This thesis revolves around the investigation of the impact of the host star activity evolution on the atmospheric mass loss of young ($\leq 1\,\mathrm{Gyr}$), close-in ($\leq 100\,\mathrm{d}$), low-mass ($\leq 20\,M_\oplus$) planets. To perform photoevaporative mass-loss calculations for close-in planets with hydrogen-helium envelopes atop rocky cores, I developed a python code called PLATYPOS (PLAneTarY PhOtoevaporation Simulator). The code is publicly available on GitHub and can be easily used to test any custom stellar activity track a user might want to input. I will first summarize the main findings of the ensemble study presented in Ch. 7, before highlighting the key findings of the individual-system studies presented in Ch. 5 and 8. I will end by giving an outlook of where the field is headed, and the future observations desirable and necessary to advance the field.

Stellar activity spread makes radius gap fuzzier and less clean

In our ensemble study, we include, for the first time in a mass-loss population study, an observationally-motivated distribution of stellar high-energy evolutionary tracks, ranging from low to high activity. Although our simulations are not full-blown hydrodynamic simulations, but simulations based on simplified analytical mass-loss approximations, the results are nonetheless instructive for the community. A question that remains under debate is whether the observed radius gap should be – if uncertainties in planetary radii are negligible – completely empty or not. Our results indicate that although the general shape and

slope of the resulting radius gap for small planets remains largely unaffected by a spread in the activity evolutions of host stars, such spread will introduce a certain scattering or fuzziness in and around the radius gap, i.e. a less clean gap. The findings show that some observed scatter in and around the boarders of the gap can be attributed to the spread in stellar activity up to about 1 Gyr and its effect on the planetary mass loss. An activity distribution – as opposed to a single activity track for all stars in the simulation – does, however, not significantly change the final radius distribution and the resulting simulated radius gap, i.e. its slope and location, of a sample of exoplanets at an age of a few gigayears. The exact details of the X-ray and EUV decay, i.e. the slope of the decay, can have a much larger impact on predictions of photoevaporation population studies, and require careful modelling, ideally supported by X-ray and UV observations of stars of different ages.

Stellar activity evolution and planetary mass are important factors for determining the fate of a young planet's atmosphere

We investigated two known, young multiplanet systems: the ~25 Myr old four-planet system V1298 Tau, and the ~300 Myr three-planet system K2-198. While the former has been known to be in its infant stages, the young age of the latter system was constrained by us for the first time, adding an interesting multiplanet system to the sample of young star–planet systems. This is a small, yet important contribution in the sense that more young systems need to be discovered or identified as such, for the systems to become well-studied and characterized – ideally with multi-wavelength follow-up observations. One motivation is to study individual systems across different ages in detail, another to study the evolution of a larger sample in a statistical sense, i.e. the demographics of planetary systems as a function of stellar age. To investigate, for example, how the small-planet radius gap (which is thought to be a feature created by atmospheric mass loss) changes as a function of time, a larger sample of systems below and around 100 Mys is needed. Studying the emergence and evolution of the radius gap in the observational data gives insights into the strength of mass loss across different ages, and when compared to simulations, might help distinguish which mass-loss processes dominate at which time.

Identifying planets of young age is the first step, which is then followed by a characterization and further investigation of the star–planet system in more detail. This includes the characterization of the system's host star. Parameters like the rotation period, X-ray luminosity, age, or information about the structure of the magnetic field can give an indication of whether

a star is a slow or fast rotator, which in turn can put constraints on the modeled activity evolution. For both V1298 Tau and K2-198, we characterize the high-energy environment the planets are embedded in by measuring the X-ray luminosity of V1298 Tau using the Chandra space telescope, and further constraining the X-ray brightness of K2-198 using the latest eROSITA values. Having a good understanding about the host star, the planet and its irradiation environment is a necessary input for any type of mass-loss simulation, and can also help to predict if ongoing mass-loss might be observable or not. For both systems, V1298 Tau and K2-198, our simulations of the future mass loss highlight the importance of measuring planetary masses – although challenging for young and active stars – because the mass loss and thus radius evolution can look significantly different depending on the mass of the planet. This is not too surprising, since low planetary gravities make a planetary atmosphere even more susceptible to evaporation. On top of planetary mass, our results show that the host star activity evolution, i.e. whether a star will spin-down early and follow a low-activity track, or stays saturated for prolonged times following a high-activity track, can also have a non-negligible impact on the fate of planetary atmospheres and their erosion. A main takeaway of our results is that when studying systems using advanced hydrodynamic mass-loss codes, it is important to capture the spread of possible activity histories of the host star when predicting the mass-loss histories of exoplanets.

The future

Observations of escaping atmospheres (or the lack of such detection), are the next step, once a young star–planet system with expected ongoing mass-loss has been identified. Exoplanet transmission spectroscopy via the 121.4 nm hydrogen Lyα line in the ultraviolet, or the 1083 nm triplet of neutral orthohelium in the infrared, has been successfully used as a probe of any extended/escaping atmosphere, even for young systems (e.g. Barragán et al., 2019a; Gaidos et al., 2020; Zhang et al., 2023; Damasso et al., 2023). More and more of these measurements put constraints on the strength of the mass loss at various ages, and help refine hydrodynamic models of the outflow.

So far, Poppenhaeger et al. (2013a) made the only detection of an exoplanetary transit in X-rays, showing that it is three times deeper than in the optical band. (King et al., 2021) observed the same planet, HD 189733b, in the near-UV and found the absorption radius to be consistent with the optical planetary radius. These results highlight that planets can appear much larger at X-ray and EUV wavelengths, a factor that needs to be taken into account in mass-loss

calculations in the form of the XUV absorption radius. The exact change of the absorption cross-section across X-ray and UV wavelengths, however, is not well understood for planets covering the observed parameter space. Measuring an X-ray transit for a young, sub-Neptune system is on the edge of feasibility with current X-ray telescopes due to the large number of transits necessary, but could give important information on how extended young planetary atmospheres are at short wavelengths. Small cube-sat missions like SEEJ (e.g. Wolk et al., 2022) or CUTE (France et al., 2023) will not only measure the high-energy flux of nearby host stars (X-rays for SEEJ, near-ultraviolet for CUTE), but also the absorption depth of X-rays and UVs in the atmospheres of hot Jupiter, Saturn, and Neptune analogs, giving insights into the physical characteristics of driven planetary winds. By studying asymmetries or absorption features in X-ray transit lightcurves, one can infer atmospheric properties, such as the presence of absorptive species or the existence of comet-like tails (Wolk et al., 2019).

Since it is not only the X-rays that drive the mass loss, but also the extreme UV portion of the stellar high-energy emission, measuring and understanding the X-ray and ultraviolet spectrum of host stars is very important. Currently, there is no space telescope in operation which can observe the EUV part of the stellar spectrum, which is why scaling relations need to be used. Star surveys like MUSCLES (e.g. Brown et al., 2023), which targets young exoplanet hosts, combine observational data from the Chandra X-ray Observatory, XMM-Newton, the Hubble Space Telescope and stellar atmosphere models to obtain continuous spectral energy distributions all the way from X-ray through infrared. A better handle on the different wavelength contributions is essential for understanding a star's effect on exoplanet atmospheric composition and evolution.

Young stars are very active and thus expose close-in planets to variable and harsh environments. By studying X-ray flares (e.g. Getman & Feigelson, 2021; Feinstein et al., 2022; Pillitteri et al., 2022), coronal mass ejections, and other stellar activities, the effects of stellar radiation and energetic particles on exoplanetary environments and the potential influence on habitability can be explored. Elaborate models of the planetary space-weather conditions, including interactions of the stellar wind with the planet and its potential magnetic field, are on the rise (e.g. Kubyshkina et al., 2022; Alvarado-Gómez et al., 2022). Modelling the response of the planetary atmosphere to high-energy events like X-ray flares, for example, can help to determine their impact on the planetary atmospheric mass loss and identify potentially observable long-term changes in the chemistry of the atmosphere induced by such flares (Louca et al., 2023).

According to the 2020 Decadal Survey in Astronomy and Astrophysics (Na-

tional Academies of Sciences, Engineering, and Medicine, 2021), the highest priority for the future of space astrophysics is the establishment of a new constellation of cutting-edge observatories. As part of one of the three highlighted key areas, "Worlds and Suns in Context", understanding the connection between stars and the worlds that orbit them is one of the main goals. This spans all the way from planet formation to evolution, of which atmospheric mass loss is one of the shaping contributors. The survey identified the need for a high-resolution X-ray observatory with spatial and spectral capabilities to investigate stellar activity across various types of stars. Modelling X-ray transmission spectra, Foster & Poppenhaeger (2022) showed that future X-ray telescopes with spatially resolved X-ray spectroscopy capabilities have the possibility of detecting X-ray absorption in outer exoplanetary atmospheres by measuring the transmission spectra of exoplanet atmospheres during transits. Such measurements, which will likely be possible with the instruments compatible with the recommendations by the decadal survey, will further enhance our understanding of the effects of X-ray irradiation on exoplanets.

To summarize, the ongoing and future advances on both the stellar and exoplanetary side show that the study of young exoplanets and their atmospheric mass loss is a rapidly evolving field that has the potential to greatly enhance our understanding of planet formation and evolution. Future X-ray missions have the capability to provide valuable insights into various aspects of exoplanets, including the use of X-ray transmission spectroscopy to study the composition and dynamics of exoplanetary atmospheres, the study of the XUV irradiation environment of close-in exoplanets and the subsequent photoevaporative mass loss, or observations of transit lightcurves at short wavelengths. Overall, future X-ray missions hold great potential for advancing our understanding of exoplanets, their atmospheres, and their interactions with their host stars.

Acknowledgments

This thesis is a culmination of the collective efforts and support from these individuals (and the many more which I haven't mentioned by name), and I am truly grateful for their presence in my life.

List of publications

The Ph.D. candidate has contributed to the following list of papers published and submitted to peer-review journals during her doctoral studies.

Refereed first and second author publications

1. Poppenhaeger, K.; **Ketzer, L.**; Mallon, M.; X–ray irradiation and evaporation of the four young planets around V1298 Tau. **MNRAS**, 500:4, December **2021**.

2. **Ketzer, L.**; Poppenhaeger, K.; Estimating photoevaporative mass loss of exoplanets with PLATYPOS. **AN**, 638:A76, June **2022**.

3. **Ketzer, L.**; Poppenhaeger, K.; The influence of host star activity evolution on the population of super–Earths and mini–Neptunes. **MNRAS**, 658:A91, February **2023**.

4. **Ketzer, L.**; Poppenhaeger, K.; Baratella, M.; Ilin, E.; Three young planets around the young K–dwarf K2–198: High–energy environment, evaporation history and expected future. **Submitted to MNRAS**. Referee report received on July 2, 2023. Revised version to be resubmitted.

Additional submitted or refereed co-authored publications

1. Keles, E.; Mallonn, M.; Kitzmann, D.; Poppenhaeger, K.; Hoeijmakers, H. Jens; Ilyin, I.; Alexoudi, X.; Carroll, T.; Alvarado-Gomez, J.; **Ketzer, L.**; et al.; The PEPSI exoplanet transit survey (PETS) I: investigating the presence of a silicate atmosphere on the super-earth 55 Cnc e. **MNRAS**, 517(3):4590–4606, December **2022**.

Bibliography

Alvarado-Gómez, J. D., Cohen, O., Drake, J. J., et al. 2022, AJ, 928, 147, doi: 10.3847/1538-4357/ac54b8

Angus, R., Morton, T. D., Foreman-Mackey, D., et al. 2019, AJ, 158, 173, doi: 10.3847/1538-3881/ab3c53

Anthony-Twarog, B. J., Deliyannis, C. P., Harmer, D., et al. 2018, AJ, 156, 37, doi: 10.3847/1538-3881/aacb1f

Arakcheev, A. S., Zhilkin, A. G., Kaigorodov, P. V., Bisikalo, D. V., & Kosovichev, A. G. 2017, Astronomy Reports, 61, 932, doi: 10.1134/S1063772917110014

Aschenbach, B. 1988, Appl. Opt., 27, 1404, doi: 10.1364/AO.27.001404

Asplund, M., Amarsi, A. M., & Grevesse, N. 2021, A&A, 653, A141, doi: 10.1051/0004-6361/202140445

Astropy Collaboration, Robitaille, T. P., Tollerud, E. J., et al. 2013, A&A, 558, A33, doi: 10.1051/0004-6361/201322068

Attia, O., Bourrier, V., Eggenberger, P., et al. 2021, A&A, 647, A40, doi: 10.1051/0004-6361/202039452

Bailer-Jones, C. A. L., Rybizki, J., Fouesneau, M., Mantelet, G., & Andrae, R. 2018, AJ, 156, 58, doi: 10.3847/1538-3881/aacb21

Baraffe, I., Alibert, Y., Chabrier, G., & Benz, W. 2006, A&A, 450, 1221, doi: 10.1051/0004-6361:20054040

Baraffe, I., Chabrier, G., & Barman, T. 2008, A&A, 482, 315, doi: 10.1051/0004-6361:20079321

Baratella, M., D'Orazi, V., Carraro, G., et al. 2020, A&A, 634, A34, doi: 10.1051/0004-6361/201937055

Baratella, M., D'Orazi, V., Sheminova, V., et al. 2021, A&A, 653, A67, doi: 10.1051/0004-6361/202141069

Barnes, S. A. 2003a, ApJ, 586, 464, doi: 10.1086/367639

—. 2003b, APJ, 586, L145, doi: 10.1086/374681

—. 2003c, Astrophysical Journal, 586, 464, doi: 10.1086/367639

—. 2003d, ApJ, 586, 464, doi: 10.1086/367639

Barragán, O., Aigrain, S., Kubyshkina, D., et al. 2019a, MNRAS, 490, 698, doi: 10.1093/mnras/stz2569

—. 2019b, MNRAS, 490, 698, doi: 10.1093/mnras/stz2569

—. 2019c, MNRAS, 490, 698, doi: 10.1093/mnras/stz2569

Barragán, O., Armstrong, D. J., Gandolfi, D., et al. 2022, MNRAS, 514, 1606, doi: 10.1093/mnras/stac638

Baruteau, C., Crida, A., Paardekooper, S. J., et al. 2014, in Protostars and Planets VI, ed. H. Beuther, R. S. Klessen, C. P. Dullemond, & T. Henning, 667–689, doi: 10.2458/azu_uapress_9780816531240-ch029

Batalha, N. M., Borucki, W. J., Koch, D. G., et al. 2010, APJ, 713, L109, doi: 10.1088/2041-8205/713/2/L109

Batalha, N. M., Rowe, J. F., Bryson, S. T., et al. 2013, ApJS, 204, 24, doi: 10.1088/0067-0049/204/2/24

Berdyugina, S. V. 2005, Living Reviews in Solar Physics, 2, 8, doi: 10.12942/lrsp-2005-8

Berger, T. A., Huber, D., Gaidos, E., & van Saders, J. L. 2018, Astrophysical Journal, 866, 99, doi: 10.3847/1538-4357/aada83

Berger, T. A., Huber, D., Gaidos, E., van Saders, J. L., & Weiss, L. M. 2020, arXiv e-prints, arXiv:2005.14671. https://arxiv.org/abs/2005.14671

Blackman, E. G., & Thomas, J. H. 2015, MNRAS, 446, L51, doi: 10.1093/mnrasl/slu163

Boese, F. G. 2000, A&AS, 141, 507, doi: 10.1051/aas:2000100

Bonfanti, A., Fossati, L., Kubyshkina, D., & Cubillos, P. E. 2021, A&A, 656, A157, doi: 10.1051/0004-6361/202142010

Booth, R. S., Poppenhaeger, K., Watson, C. A., Silva Aguirre, V., & Wolk, S. J. 2017, MNRAS, 471, 1012, doi: 10.1093/mnras/stx1630

Borucki, W. J., Koch, D., Basri, G., et al. 2010, Science, 327, 977, doi: 10.1126/science.1185402

Bourrier, V., Lecavelier des Etangs, A., Ehrenreich, D., et al. 2018, A&A, 620, A147, doi: 10.1051/0004-6361/201833675

Bouvier, J. 2007, in Star-Disk Interaction in Young Stars, ed. J. Bouvier & I. Appenzeller, Vol. 243, 231–240, doi: 10.1017/S1743921307009593

Bouvier, J., Matt, S. P., Mohanty, S., et al. 2014, in Protostars and Planets VI, ed. H. Beuther, R. S. Klessen, C. P. Dullemond, & T. Henning, 433–450, doi: 10.2458/azu_uapress_9780816531240-ch019

Bouvier, J., Barrado, D., Moraux, E., et al. 2018, A&A, 613, A63, doi: 10.1051/0004-6361/201731881

Brinkman, C. L., Cadman, J., Weiss, L., et al. 2023, AJ, 165, 74, doi: 10.3847/1538-3881/aca64d

Brown, A., Schneider, P. C., France, K., et al. 2023, AJ, 165, 195, doi: 10.3847/1538-3881/acc38a

Brun, A. S., & Browning, M. K. 2017, Living Reviews in Solar Physics, 14, 4, doi: 10.1007/s41116-017-0007-8

Burnight, T. R. 1949, Phys. Rev, 76, 19

Caldiroli, A., Haardt, F., Gallo, E., et al. 2021, A&A, 655, A30, doi: 10.1051/0004-6361/202141497

—. 2022, A&A, 663, A122, doi: 10.1051/0004-6361/202142763

Carolan, S., Vidotto, A. A., Plavchan, P., Villarreal D'Angelo, C., & Hazra, G. 2020, MNRAS, 498, L53, doi: 10.1093/mnrasl/slaa127

Carolan, S., Vidotto, A. A., Villarreal D'Angelo, C., & Hazra, G. 2021, MNRAS, 500, 3382, doi: 10.1093/mnras/staa3431

Casagrande, L., Lin, J., Rains, A. D., et al. 2021, MNRAS, 507, 2684, doi: 10.1093/mnras/stab2304

Cash, W. 1979, ApJ, 228, 939, doi: 10.1086/156922

Castelli, F., & Kurucz, R. L. 2003, in Modelling of Stellar Atmospheres, ed. N. Piskunov, W. W. Weiss, & D. F. Gray, Vol. 210, A20, doi: 10.48550/arXiv.astro-ph/0405087

Catling, D. C., & Zahnle, K. J. 2009, Scientific American, 300, 36, doi: 10.1038/scientificamerican0509-36

Chadney, J. M., Galand, M., Unruh, Y. C., Koskinen, T. T., & Sanz-Forcada, J. 2015, Icarus, 250, 357, doi: 10.1016/j.icarus.2014.12.012

Chamberlain, J. W., & Hunten, D. M. 1987, Theory of planetary atmospheres. An introduction to their physics andchemistry., Vol. 36

Chassefière, E. 1997, Icarus, 126, 229, doi: 10.1006/icar.1997.5677

Chen, D.-C., Xie, J.-W., Zhou, J.-L., et al. 2021, ApJ, 909, 115, doi: 10.3847/1538-4357/abd5be

Chen, H., & Rogers, L. A. 2016, Astrophysical Journal, 831, 180, doi: 10.3847/0004-637X/831/2/180

Chen, J., & Kipping, D. 2017a, ApJ, 834, 17, doi: 10.3847/1538-4357/834/1/17

—. 2017b, ApJ, 834, 17, doi: 10.3847/1538-4357/834/1/17

Chiang, E., & Laughlin, G. 2013, MNRAS, 431, 3444, doi: 10.1093/mnras/stt424

Claire, M. W., Sheets, J., Cohen, M., et al. 2012, ApJ, 757, 95, doi: 10.1088/0004-637X/757/1/95

Coffaro, M., Stelzer, B., & Orlando, S. 2022, A&A, 661, A79, doi: 10.1051/0004-6361/202142298

Coffaro, M., Stelzer, B., Orlando, S., et al. 2020, A&A, 636, A49, doi: 10.1051/0004-6361/201936479

Cohen, O., Alvarado-Gómez, J. D., Drake, J. J., et al. 2022, ApJ, 934, 189, doi: 10.3847/1538-4357/ac78e4

Cohen, O., Ma, Y., Drake, J. J., et al. 2015, ApJ, 806, 41, doi: 10.1088/0004-637X/806/1/41

Correia, A. C. M., Bourrier, V., & Delisle, J. B. 2020, A&A, 635, A37, doi: 10.1051/0004-6361/201936967

Covas, E., Moss, D., & Tavakol, R. 2005, A&A, 429, 657, doi: 10.1051/0004-6361:20041741

Cranmer, S. R., & Woolsey, L. N. 2015, ApJ, 812, 71, doi: 10.1088/0004-637X/812/1/71

Cumming, A., Butler, R. P., Marcy, G. W., et al. 2008, PASP, 120, 531, doi: 10.1086/588487

Cummings, J. D., Deliyannis, C. P., Maderak, R. M., & Steinhauer, A. 2017, AJ, 153, 128, doi: 10.3847/1538-3881/aa5b86

Curtis, J. L., Agüeros, M. A., Matt, S. P., et al. 2020a, ApJ, 904, 140, doi: 10.3847/1538-4357/abbf58

—. 2020b, ApJ, 904, 140, doi: 10.3847/1538-4357/abbf58

Damasso, M., Locci, D., Benatti, S., et al. 2023, A&A, 672, A126, doi: 10.1051/0004-6361/202245391

Davenport, J. R. A., Covey, K. R., Clarke, R. W., et al. 2019, ApJ, 871, 241, doi: 10.3847/1538-4357/aafb76

David, T. J., Petigura, E. A., Luger, R., et al. 2019a, APJ, 885, L12, doi: 10.3847/2041-8213/ab4c99

David, T. J., Hillenbrand, L. A., Petigura, E. A., et al. 2016, Nature, 534, 658, doi: 10.1038/nature18293

David, T. J., Cody, A. M., Hedges, C. L., et al. 2019b, AJ, 158, 79, doi: 10.3847/1538-3881/ab290f

David, T. J., Contardo, G., Sandoval, A., et al. 2021, AJ, 161, 265, doi: 10.3847/1538-3881/abf439

Davies, M. B., Adams, F. C., Armitage, P., et al. 2014, in Protostars and Planets VI, ed. H. Beuther, R. S. Klessen, C. P. Dullemond, & T. Henning, 787–808, doi: 10.2458/azu_uapress_9780816531240-ch034

Donati, J. F., & Landstreet, J. D. 2009, ARA&A, 47, 333, doi: 10.1146/annurev-astro-082708-101833

Donati, J. F., Mengel, M., Carter, B. D., et al. 2000, MNRAS, 316, 699, doi: 10.1046/j.1365-8711.2000.03570.x

Dong, C., Lingam, M., Ma, Y., & Cohen, O. 2017, APJ, 837, L26, doi: 10.3847/2041-8213/aa6438

D'Orazi, V., Baratella, M., Lugaro, M., Magrini, L., & Pignatari, M. 2022, Universe, 8, 110, doi: 10.3390/universe8020110

D'Orazi, V., Magrini, L., Randich, S., et al. 2009, APJ, 693, L31, doi: 10.1088/0004-637X/693/1/L31

Douglas, S. T., Curtis, J. L., Agüeros, M. A., et al. 2019, ApJ, 879, 100, doi: 10.3847/1538-4357/ab2468

Dressing, C. D., & Charbonneau, D. 2013, ApJ, 767, 95, doi: 10.1088/0004-637X/767/1/95

—. 2015, ApJ, 807, 45, doi: 10.1088/0004-637X/807/1/45

Dungee, R., van Saders, J., Gaidos, E., et al. 2022, ApJ, 938, 118, doi: 10.3847/1538-4357/ac90be

Ehrenreich, D., Bourrier, V., Wheatley, P. J., et al. 2015, Nature, 522, 459, doi: 10.1038/nature14501

Eker, Z., Bakış, V., Bilir, S., et al. 2018, MNRAS, 479, 5491, doi: 10.1093/mnras/sty1834

Engvold, O., Vial, J.-C., & Skumanich, A. 2019, The Sun as a Guide to Stellar Physics, doi: 10.1016/C2017-0-01365-4

Erdélyi, R., & Ballai, I. 2007, Astronomische Nachrichten, 328, 726, doi: 10.1002/asna.200710803

Erkaev, N. V., Kulikov, Y. N., Lammer, H., et al. 2007, A&A, 472, 329, doi: 10.1051/0004-6361:20066929

Feinstein, A. D., France, K., Youngblood, A., et al. 2022, AJ, 164, 110, doi: 10.3847/1538-3881/ac8107

Fernández Fernández, J., & Wheatley, P. J. 2022, Astronomische Nachrichten, 343, e10076, doi: 10.1002/asna.20210076

Foreman-Mackey, D., Hogg, D. W., Lang, D., & Goodman, J. 2013, PASP, 125, 306, doi: 10.1086/670067

Fortney, J. J., Marley, M. S., & Barnes, J. W. 2007, Astrophysical Journal, 659, 1661, doi: 10.1086/512120

Fossati, L., Erkaev, N. V., Lammer, H., et al. 2017, A&A, 598, A90, doi: 10.1051/0004-6361/201629716

Foster, A. R., Ji, L., Smith, R. K., & Brickhouse, N. S. 2012, ApJ, 756, 128, doi: 10.1088/0004-637X/756/2/128

Foster, G., & Poppenhaeger, K. 2022, Astronomische Nachrichten, 343, e20007, doi: 10.1002/asna.20220007

Foster, G., Poppenhaeger, K., Ilic, N., & Schwope, A. 2022a, A&A, 661, A23, doi: 10.1051/0004-6361/202141097

—. 2022b, A&A, 661, A23, doi: 10.1051/0004-6361/202141097

France, K., Fleming, B., Egan, A., et al. 2023, AJ, 165, 63, doi: 10.3847/1538-3881/aca8a2

Freund, S., Czesla, S., Robrade, J., Schneider, P. C., & Schmitt, J. H. M. M. 2022, A&A, 664, A105, doi: 10.1051/0004-6361/202142573

Fritzewski, D. J., Barnes, S. A., James, D. J., Järvinen, S. P., & Strassmeier, K. G. 2021a, A&A, 656, A103, doi: 10.1051/0004-6361/202140896

Fritzewski, D. J., Barnes, S. A., James, D. J., & Strassmeier, K. G. 2020, A&A, 641, A51, doi: 10.1051/0004-6361/201936860

—. 2021b, A&A, 652, A60, doi: 10.1051/0004-6361/202140894

—. 2021c, A&A, 652, A60, doi: 10.1051/0004-6361/202140894

Fulton, B. J., & Petigura, E. A. 2018, AJ, 156, 264, doi: 10.3847/1538-3881/aae828

Fulton, B. J., Petigura, E. A., Howard, A. W., et al. 2017a, Astronomical Journal, 154, 109, doi: 10.3847/1538-3881/aa80eb

—. 2017b, AJ, 154, 109, doi: 10.3847/1538-3881/aa80eb

Gaia Collaboration, Prusti, T., de Bruijne, J. H. J., et al. 2016, A&A, 595, A1, doi: 10.1051/0004-6361/201629272

Gaia Collaboration, Brown, A. G. A., Vallenari, A., et al. 2018, A&A, 616, A1, doi: 10.1051/0004-6361/201833051

Gaia Collaboration, Vallenari, A., Brown, A. G. A., et al. 2022a, arXiv e-prints, arXiv:2208.00211, doi: 10.48550/arXiv.2208.00211

—. 2022b, arXiv e-prints, arXiv:2208.00211, doi: 10.48550/arXiv.2208.00211

Gaidos, E., Claytor, Z., Dungee, R., Ali, A., & Feiden, G. A. 2023, MNRAS, 520, 5283, doi: 10.1093/mnras/stad343

Gaidos, E., Mann, A. W., Rizzuto, A., et al. 2017, MNRAS, 464, 850, doi: 10.1093/mnras/stw2345

Gaidos, E., Hirano, T., Mann, A. W., et al. 2020, MNRAS, 495, 650, doi: 10.1093/mnras/staa918

García Muñoz, A. 2007, Planet. Space Sci., 55, 1426, doi: 10.1016/j.pss.2007.03.007

García Muñoz, A. 2007, Planet. Space Sci., 55, 1426, doi: 10.1016/j.pss.2007.03.007

Garraffo, C., Drake, J. J., & Cohen, O. 2015, APJ, 807, L6, doi: 10.1088/2041-8205/807/1/L6

—. 2016, A&A, 595, A110, doi: 10.1051/0004-6361/201628367

Garraffo, C., Drake, J. J., Dotter, A., et al. 2018, Astrophysical Journal, 862, 90, doi: 10.3847/1538-4357/aace5d

Gaudi, B. S., Meyer, M., & Christiansen, J. 2021, in ExoFrontiers; Big Questions in Exoplanetary Science, ed. N. Madhusudhan, 2–1, doi: 10.1088/2514-3433/abfa8fch2

Getman, K. V., & Feigelson, E. D. 2021, ApJ, 916, 32, doi: 10.3847/1538-4357/ac00be

Gillen, E., Briegal, J. T., Hodgkin, S. T., et al. 2020, MNRAS, 492, 1008, doi: 10.1093/mnras/stz3251

Ginzburg, S., Schlichting, H. E., & Sari, R. 2016, ApJ, 825, 29, doi: 10.3847/0004-637X/825/1/29

Ginzburg, S., Schlichting, H. E., & Sari, R. 2018, MNRAS, 476, 759–765, doi: 10.1093/mnras/sty290

Gondoin, P. 2018, A&A, 616, A154, doi: 10.1051/0004-6361/201731541

Grevesse, N., & Sauval, A. J. 1998, Space Sci. Rev., 85, 161, doi: 10.1023/A:1005161325181

Grießmeier, J., Stadelmann, A., Penz, T., et al. 2004, A&A, 425, 753, doi: 10.1051/0004-6361:20035684

Griest, K., & Safizadeh, N. 1998, ApJ, 500, 37, doi: 10.1086/305729

Gruner, D., & Barnes, S. A. 2020, A&A, 644, A16, doi: 10.1051/0004-6361/202038984

Güdel, M. 2004, A&A Rev., 12, 71, doi: 10.1007/s00159-004-0023-2

—. 2007, Living Reviews in Solar Physics, 4, 3, doi: 10.12942/lrsp-2007-3

Güdel, M., Guinan, E. F., & Skinner, S. L. 1997, ApJ, 483, 947, doi: 10.1086/304264

Gupta, A., & Schlichting, H. E. 2019, MNRAS, 487, 24–33, doi: 10.1093/mnras/stz1230

Hadden, S., & Lithwick, Y. 2017, AJ, 154, 5, doi: 10.3847/1538-3881/aa71ef

Haisch, Karl E., J., Lada, E. A., & Lada, C. J. 2001, AJ, 121, 2065, doi: 10.1086/319951

Hansen, B. M. S., & Murray, N. 2012, ApJ, 751, 158, doi: 10.1088/0004-637X/751/2/158

Harbach, L. M., Moschou, S. P., Garraffo, C., et al. 2021, AJ, 913, 130, doi: 10.3847/1538-4357/abf63a

Hardegree-Ullman, K. K., Zink, J. K., Christiansen, J. L., et al. 2020, Astrophysical Journal, Supplement, 247, 28, doi: 10.3847/1538-4365/ab7230

Harris, C. R., Millman, K. J., van der Walt, S. J., et al. 2020, Nature, 585, 357, doi: 10.1038/s41586-020-2649-2

Hartmann, L., Hewett, R., Stahler, S., & Mathieu, R. D. 1986, ApJ, 309, 275, doi: 10.1086/164599

Hazra, G., Vidotto, A. A., Carolan, S., Villarreal D'Angelo, C., & Manchester, W. 2022, MNRAS, 509, 5858, doi: 10.1093/mnras/stab3271

Hedges, C., Saunders, N., Barentsen, G., et al. 2019, APJ, 880, L5, doi: 10.3847/2041-8213/ab2a74

Holmberg, J., Nordström, B., & Andersen, J. 2009, A&A, 501, 941, doi: 10.1051/0004-6361/200811191

Howe, A. R., & Burrows, A. 2015, Astrophysical Journal, 808, 150, doi: 10.1088/0004-637X/808/2/150

Howell, S. B., Sobeck, C., Haas, M., et al. 2014, Publications of the ASP, 126, 398, doi: 10.1086/676406

Hunter, J. D. 2007, Computing in science & engineering, 9, 90

Iben, Icko, J. 1967, ApJ, 147, 624, doi: 10.1086/149040

Ida, S., & Lin, D. N. C. 2010, ApJ, 719, 810, doi: 10.1088/0004-637X/719/1/810

Ikoma, M., & Hori, Y. 2012, ApJ, 753, 66, doi: 10.1088/0004-637X/753/1/66

Ikoma, M., Nakazawa, K., & Emori, H. 2000, ApJ, 537, 1013, doi: 10.1086/309050

Ilic, N., Poppenhaeger, K., & Hosseini, S. M. 2022, MNRAS, 513, 4380, doi: 10.1093/mnras/stac861

Ilin, E. 2021, Journal of Open Source Software, 6, 2845, doi: 10.21105/joss.02845

Ilin, E., Schmidt, S. J., Poppenhäger, K., et al. 2021, A&A, 645, A42, doi: 10.1051/0004-6361/202039198

Jackson, A. P., Davis, T. A., & Wheatley, P. J. 2012a, MNRAS, 422, 2024, doi: 10.1111/j.1365-2966.2012.20657.x

—. 2012b, MNRAS, 422, 2024, doi: 10.1111/j.1365-2966.2012.20657.x

Jardine, M., & Unruh, Y. C. 1999, A&A, 346, 883

Jeans, J. 1925, The Dynamical Theory of Gases (University Press). https://books.google.de/books?id=UOZwxAEACAAJ

Jeffries, R. D., Evans, P. A., Pye, J. P., & Briggs, K. R. 2006, MNRAS, 367, 781, doi: 10.1111/j.1365-2966.2005.09988.x

Jeffries, R. D., Naylor, T., Mayne, N. J., Bell, C. P. M., & Littlefair, S. P. 2013, MNRAS, 434, 2438, doi: 10.1093/mnras/stt1180

Jenkins, J. M., Twicken, J. D., McCauliff, S., et al. 2016, in Society of Photo-Optical Instrumentation Engineers (SPIE) Conference Series, Vol. 9913, Software and Cyberinfrastructure for Astronomy IV, ed. G. Chiozzi & J. C. Guzman, 99133E, doi: 10.1117/12.2233418

Jin, S., & Mordasini, C. 2018, ApJ, 853, 163, doi: 10.3847/1538-4357/aa9f1e

Jin, S., Mordasini, C., Parmentier, V., et al. 2014, Astrophysical Journal, 795, 65, doi: 10.1088/0004-637X/795/1/65

Johnstone, C. P., Bartel, M., & Güdel, M. 2021, A&A, 649, A96, doi: 10.1051/0004-6361/202038407

Johnstone, C. P., Güdel, M., Brott, I., & Lüftinger, T. 2015a, A&A, 577, A28, doi: 10.1051/0004-6361/201425301

Johnstone, C. P., Güdel, M., Stökl, A., et al. 2015b, APJ, 815, L12, doi: 10.1088/2041-8205/815/1/L12

Jontof-Hutter, D., Ford, E. B., Rowe, J. F., et al. 2016, ApJ, 820, 39, doi: 10.3847/0004-637X/820/1/39

Kasting, J. F., & Pollack, J. B. 1983, Icarus, 53, 479, doi: 10.1016/0019-1035(83)90212-9

Kempton, E. M. R., Bean, J. L., Louie, D. R., et al. 2018, PASP, 130, 114401, doi: 10.1088/1538-3873/aadf6f

Ketzer, L., & Poppenhaeger, K. 2022, Astronomische Nachrichten, 343, e10105, doi: 10.1002/asna.20210105

—. 2023, MNRAS, 518, 1683, doi: 10.1093/mnras/stac2643

King, G. W., & Wheatley, P. J. 2021, MNRAS, 501, L28, doi: 10.1093/mnrasl/slaa186

King, G. W., Wheatley, P. J., Salz, M., et al. 2018, MNRAS, 478, 1193, doi: 10.1093/mnras/sty1110

King, G. W., Corrales, L., Wheatley, P. J., et al. 2021, MNRAS, 506, 2453, doi: 10.1093/mnras/stab1863

Kiraga, M., & Stepien, K. 2007, Acta Astron., 57, 149, doi: 10.48550/arXiv.0707.2577

Kite, E. S., & Barnett, M. N. 2020, Proceedings of the National Academy of Science, 117, 18264, doi: 10.1073/pnas.2006177117

Koskinen, T. T., Aylward, A. D., & Miller, S. 2007a, Nature, 450, 845, doi: 10.1038/nature06378

Koskinen, T. T., Aylward, A. D., Smith, C. G. A., & Miller, S. 2007b, ApJ, 661, 515, doi: 10.1086/513594

Kraft, R. P., Burrows, D. N., & Nousek, J. A. 1991, ApJ, 374, 344, doi: 10.1086/170124

Krenn, A. F., Fossati, L., Kubyshkina, D., & Lammer, H. 2021, A&A, 650, A94, doi: 10.1051/0004-6361/202140437

Kubyshkina, D., & Vidotto, A. A. 2021, MNRAS, doi: 10.1093/mnras/stab897

Kubyshkina, D., Vidotto, A. A., Villarreal D'Angelo, C., et al. 2022, MNRAS, 510, 3039, doi: 10.1093/mnras/stab3620

Kubyshkina, D., Fossati, L., Erkaev, N. V., et al. 2018a, A&A, 619, A151, doi: 10.1051/0004-6361/201833737

—. 2018b, APJ, 866, L18, doi: 10.3847/2041-8213/aae586

Kubyshkina, D., Cubillos, P. E., Fossati, L., et al. 2019a, Astrophysical Journal, 879, 26, doi: 10.3847/1538-4357/ab1e42

Kubyshkina, D., Fossati, L., Mustill, A. J., et al. 2019b, A&A, 632, A65, doi: 10.1051/0004-6361/201936581

Kulow, J. R., France, K., Linsky, J., & Loyd, R. O. P. 2014, ApJ, 786, 132, doi: 10.1088/0004-637X/786/2/132

Kumar, S., Hunten, D. M., & Pollack, J. B. 1983, Icarus, 55, 369, doi: 10.1016/0019-1035(83)90109-4

Lagrange, A. M., Bonnefoy, M., Chauvin, G., et al. 2010, Science, 329, 57, doi: 10.1126/science.1187187

Lalitha, S., Schmitt, J. H. M. M., & Dash, S. 2018, MNRAS, 477, 808, doi: 10.1093/mnras/sty732

Lammer, H. 2013, Origin and Evolution of Planetary Atmospheres, doi: 10.1007/978-3-642-32087-3

Lammer, H., & Bauer, S. J. 1991, J. Geophys. Res., 96, 1819, doi: 10.1029/90JA01676

Lammer, H., Kasting, J. F., Chassefière, E., et al. 2008, Space Sci. Rev., 139, 399, doi: 10.1007/s11214-008-9413-5

Lammer, H., Selsis, F., Ribas, I., et al. 2003, Astrophysical Journal, Letters, 598, L121, doi: 10.1086/380815

Lampón, M., López-Puertas, M., Czesla, S., et al. 2021, A&A, 648, L7, doi: 10.1051/0004-6361/202140423

Landstreet, J. D. 1992, A&A Rev., 4, 35, doi: 10.1007/BF00873569

Lecavelier Des Etangs, A. 2007, A&A, 461, 1185, doi: 10.1051/0004-6361:20065014

Lecavelier des Etangs, A., Vidal-Madjar, A., McConnell, J. C., & Hébrard, G. 2004, A&A, 418, L1, doi: 10.1051/0004-6361:20040106

Lee, E. J., & Chiang, E. 2015, ApJ, 811, 41, doi: 10.1088/0004-637X/811/1/41

Lee, E. J., Karalis, A., & Thorngren, D. P. 2022, ApJ, 941, 186, doi: 10.3847/1538-4357/ac9c66

Lightkurve Collaboration, Cardoso, J. V. d. M., Hedges, C., et al. 2018, Lightkurve: Kepler and TESS time series analysis in Python, Astrophysics Source Code Library. http://ascl.net/1812.013

Lind, K., Asplund, M., & Barklem, P. S. 2009, A&A, 503, 541, doi: 10.1051/0004-6361/200912221

Linsky, J. L., Fontenla, J., & France, K. 2014, ApJ, 780, 61, doi: 10.1088/0004-637X/780/1/61

Linsky, J. L., France, K., & Ayres, T. 2013, ApJ, 766, 69, doi: 10.1088/0004-637X/766/2/69

Liu, S.-F., Hori, Y., Lin, D. N. C., & Asphaug, E. 2015, ApJ, 812, 164, doi: 10.1088/0004-637X/812/2/164

Livingston, J. H., Dai, F., Hirano, T., et al. 2018, AJ, 155, 115, doi: 10.3847/1538-3881/aaa841

Lopez, E. D. 2017, MNRAS, 472, 245, doi: 10.1093/mnras/stx1558

Lopez, E. D., & Fortney, J. J. 2013a, Astrophysical Journal, 776, 2, doi: 10.1088/0004-637X/776/1/2

—. 2013b, ApJ, 776, 2, doi: 10.1088/0004-637X/776/1/2

—. 2014a, Astrophysical Journal, 792, 1, doi: 10.1088/0004-637X/792/1/1

—. 2014b, ApJ, 792, 1, doi: 10.1088/0004-637X/792/1/1

Lopez, E. D., Fortney, J. J., & Miller, N. 2012, ApJ, 761, 59, doi: 10.1088/0004-637X/761/1/59

Lopez, E. D., & Rice, K. 2018, MNRAS, 479, 5303, doi: 10.1093/mnras/sty1707

Louca, A. J., Miguel, Y., Tsai, S.-M., et al. 2023, MNRAS, 521, 3333, doi: 10.1093/mnras/stac1220

Loyd, R. O. P., Shkolnik, E. L., Schneider, A. C., et al. 2020, ApJ, 890, 23, doi: 10.3847/1538-4357/ab6605

Luger, R., Agol, E., Kruse, E., et al. 2018, EVEREST: Tools for de-trending stellar photometry, Astrophysics Source Code Library, record ascl:1807.029. http://ascl.net/1807.029

Lundkvist, M. S., Kjeldsen, H., Albrecht, S., et al. 2016, Nature Communications, 7, 11201, doi: 10.1038/ncomms11201

Magaudda, E., Stelzer, B., Covey, K. R., et al. 2020, A&A, 638, A20, doi: 10.1051/0004-6361/201937408

Magrini, L., Spina, L., Randich, S., et al. 2018, A&A, 617, A106, doi: 10.1051/0004-6361/201832841

Mallonn, M., Nascimbeni, V., Weingrill, J., et al. 2015, A&A, 583, A138, doi: 10.1051/0004-6361/201425395

Mamajek, E. E., & Hillenbrand, L. A. 2008, ApJ, 687, 1264, doi: 10.1086/591785

Mann, A. W., Newton, E. R., Rizzuto, A. C., et al. 2016, AJ, 152, 61, doi: 10.3847/0004-6256/152/3/61

Mann, A. W., Gaidos, E., Vanderburg, A., et al. 2017, AJ, 153, 64, doi: 10.1088/1361-6528/aa5276

Mann, A. W., Wood, M. L., Schmidt, S. P., et al. 2022, AJ, 163, 156, doi: 10.3847/1538-3881/ac511d

Mansfield, M., Bean, J. L., Oklopčić, A., et al. 2018, APJ, 868, L34, doi: 10.3847/2041-8213/aaf166

Marcy, G. W., Isaacson, H., Howard, A. W., et al. 2014, ApJS, 210, 20, doi: 10.1088/0067-0049/210/2/20

Marley, M. S., Fortney, J., Seager, S., & Barman, T. 2007, in Protostars and Planets V, ed. B. Reipurth, D. Jewitt, & K. Keil, 733, doi: 10.48550/arXiv.astro-ph/0602468

Martinez, C. F., Cunha, K., Ghezzi, L., & Smith, V. V. 2019, ApJ, 875, 29, doi: 10.3847/1538-4357/ab0d93

Matt, S. P., Brun, A. S., Baraffe, I., Bouvier, J., & Chabrier, G. 2015, APJ, 799, L23, doi: 10.1088/2041-8205/799/2/L23

Mayo, A. W., Vanderburg, A., Latham, D. W., et al. 2018, AJ, 155, 136, doi: 10.3847/1538-3881/aaadff

Mayor, M., & Queloz, D. 1995, Nature, 378, 355, doi: 10.1038/378355a0

Mazeh, T., Holczer, T., & Faigler, S. 2016, A&A, 589, A75, doi: 10.1051/0004-6361/201528065

McKinney, W., et al. 2010, in Proceedings of the 9th Python in Science Conference, Vol. 445, Austin, TX, 51–56

Melosh, H. J., & Vickery, A. M. 1989, Nature, 338, 487, doi: 10.1038/338487a0

Messina, S., Nardiello, D., Desidera, S., et al. 2022, A&A, 657, L3, doi: 10.1051/0004-6361/202142276

Mestel, L. 1999, Stellar magnetism

Modirrousta-Galian, D., Locci, D., & Micela, G. 2020, ApJ, 891, 158, doi: 10.3847/1538-4357/ab7379

Monsch, K., Ercolano, B., Picogna, G., Preibisch, T., & Rau, M. M. 2019, MNRAS, 483, 3448, doi: 10.1093/mnras/sty3346

Mordasini, C. 2020, A&A, 638, A52, doi: 10.1051/0004-6361/201935541

Mordasini, C., Alibert, Y., Georgy, C., et al. 2012a, A&A, 547, A112, doi: 10.1051/0004-6361/201118464

—. 2012b, A&A, 547, A112, doi: 10.1051/0004-6361/201118464

Mullally, F., Coughlin, J. L., Thompson, S. E., et al. 2015, ApJS, 217, 31, doi: 10.1088/0067-0049/217/2/31

Murray-Clay, R. A., Chiang, E. I., & Murray, N. 2009a, ApJ, 693, 23, doi: 10.1088/0004-637X/693/1/23

—. 2009b, ApJ, 693, 23, doi: 10.1088/0004-637X/693/1/23

National Academies of Sciences, Engineering, and Medicine. 2021, Pathways to Discovery in A&A for the 2020s, doi: 10.17226/26141

Newton, E. R., Irwin, J., Charbonneau, D., et al. 2016, ApJ, 821, 93, doi: 10.3847/0004-637X/821/2/93

Newton, E. R., Mann, A. W., Tofflemire, B. M., et al. 2019a, APJ, 880, L17, doi: 10.3847/2041-8213/ab2988

—. 2019b, Astrophysical Journal, Letters, 880, L17, doi: 10.3847/2041-8213/ab2988

Noyes, R. W., Weiss, N. O., & Vaughan, A. H. 1984, ApJ, 287, 769, doi: 10.1086/162735

Obermeier, C., Henning, T., Schlieder, J. E., et al. 2016, AJ, 152, 223, doi: 10.3847/1538-3881/152/6/223

Oh, S., Price-Whelan, A. M., Hogg, D. W., Morton, T. D., & Spergel, D. N. 2017, AJ, 153, 257, doi: 10.3847/1538-3881/aa6ffd

Oklopčić, A. 2019, ApJ, 881, 133, doi: 10.3847/1538-4357/ab2f7f

Öpik, E. J. 1963, Geophysical Journal, 7, 490, doi: 10.1111/j.1365-246X.1963.tb07091.x

Osterbrock, D. E. 1961, ApJ, 134, 347, doi: 10.1086/147165

Otegi, J. F., Bouchy, F., & Helled, R. 2020a, A&A, 634, A43, doi: 10.1051/0004-6361/201936482

—. 2020b, A&A, 634, A43, doi: 10.1051/0004-6361/201936482

Owen, J. E. 2019, Annual Review of Earth and Planetary Sciences, 47, 67, doi: 10.1146/annurev-earth-053018-060246

Owen, J. E., & Adams, F. C. 2014, MNRAS, 444, 3761, doi: 10.1093/mnras/stu1684

Owen, J. E., & Alvarez, M. A. 2016, ApJ, 816, 34, doi: 10.3847/0004-637X/816/1/34

Owen, J. E., & Campos Estrada, B. 2020, MNRAS, 491, 5287, doi: 10.1093/mnras/stz3435

Owen, J. E., & Jackson, A. P. 2012a, MNRAS, 425, 2931, doi: 10.1111/j.1365-2966.2012.21481.x

—. 2012b, MNRAS, 425, 2931, doi: 10.1111/j.1365-2966.2012.21481.x

Owen, J. E., & Lai, D. 2018, MNRAS, 479, 5012, doi: 10.1093/mnras/sty1760

Owen, J. E., & Wu, Y. 2013, Astrophysical Journal, 775, 105, doi: 10.1088/0004-637X/775/2/105

—. 2017, Astrophysical Journal, 847, 29, doi: 10.3847/1538-4357/aa890a

Paegert, M., Stassun, K. G., Collins, K. A., et al. 2021, arXiv e-prints, arXiv:2108.04778, doi: 10.48550/arXiv.2108.04778

Pallavicini, R., Golub, L., Rosner, R., et al. 1981, ApJ, 248, 279, doi: 10.1086/159152

Parker, E. N. 1955, ApJ, 122, 293, doi: 10.1086/146087

—. 1958, ApJ, 128, 664, doi: 10.1086/146579

—. 1988, ApJ, 330, 474, doi: 10.1086/166485

Patten, B. M., & Simon, T. 1996, ApJS, 106, 489, doi: 10.1086/192346

Pecaut, M. J., & Mamajek, E. E. 2013, ApJS, 208, 9, doi: 10.1088/0067-0049/208/1/9

—. 2016, MNRAS, 461, 794, doi: 10.1093/mnras/stw1300

Penz, T., Micela, G., & Lammer, H. 2008, A&A, 477, 309, doi: 10.1051/0004-6361:20078364

Pepper, J., Gillen, E., Parviainen, H., et al. 2017, AJ, 153, 177, doi: 10.3847/1538-3881/aa62ab

Perryman, M. 2018, The Exoplanet Handbook, 2nd edn. (Cambridge University Press), doi: 10.1017/9781108304160

Petigura, E. A., Howard, A. W., Marcy, G. W., et al. 2017, AJ, 154, 107, doi: 10.3847/1538-3881/aa80de

Petigura, E. A., Rogers, J. G., Isaacson, H., et al. 2022, AJ, 163, 179, doi: 10.3847/1538-3881/ac51e3

Pillitteri, I., Argiroffi, C., Maggio, A., et al. 2022, A&A, 666, A198, doi: 10.1051/0004-6361/202244268

Pizzolato, N., Maggio, A., Micela, G., Sciortino, S., & Ventura, P. 2003, A&A, 397, 147, doi: 10.1051/0004-6361:20021560

Placco, V. M., Sneden, C., Roederer, I. U., et al. 2021, Research Notes of the American Astronomical Society, 5, 92, doi: 10.3847/2515-5172/abf651

Plavchan, P., Barclay, T., Gagné, J., et al. 2020, Nature, 582, 497, doi: 10.1038/s41586-020-2400-z

Poppenhaeger, K. 2022, MNRAS, 512, 1751, doi: 10.1093/mnras/stac507

Poppenhaeger, K., Ketzer, L., & Mallonn, M. 2021, MNRAS, 500, 4560, doi: 10.1093/mnras/staa1462

Poppenhaeger, K., Robrade, J., & Schmitt, J. H. M. M. 2010, A&A, 515, A98+, doi: 10.1051/0004-6361/201014245

Poppenhaeger, K., & Schmitt, J. H. M. M. 2011, Astronomische Nachrichten, 332, 1052, doi: 10.1002/asna.201111615

Poppenhaeger, K., Schmitt, J. H. M. M., & Wolk, S. J. 2013a, Astrophysical Journal, 773, 62, doi: 10.1088/0004-637X/773/1/62

—. 2013b, ApJ, 773, 62, doi: 10.1088/0004-637X/773/1/62

Predehl, P., Andritschke, R., Arefiev, V., et al. 2021, A&A, 647, A1, doi: 10.1051/0004-6361/202039313

Preibisch, T., & Feigelson, E. D. 2005a, ApJS, 160, 390, doi: 10.1086/432094

—. 2005b, ApJS, 160, 390, doi: 10.1086/432094

Price-Whelan, A. M., Sipőcz, B. M., Günther, H. M., et al. 2018, AJ, 156, 123, doi: 10.3847/1538-3881/aabc4f

Rafikov, R. R. 2006, ApJ, 648, 666, doi: 10.1086/505695

Randich, S., Schmitt, J. H. M. M., Prosser, C. F., & Stauffer, J. R. 1996, A&A, 305, 785

Rebull, L. M., Wolff, S. C., & Strom, S. E. 2004, AJ, 127, 1029, doi: 10.1086/380931

Rebull, L. M., Stauffer, J. R., Bouvier, J., et al. 2016, AJ, 152, 113, doi: 10.3847/0004-6256/152/5/113

Reddy, A. B. S., & Lambert, D. L. 2015, MNRAS, 454, 1976, doi: 10.1093/mnras/stv1876

—. 2017, ApJ, 845, 151, doi: 10.3847/1538-4357/aa81d6

Reiners, A., Schüssler, M., & Passegger, V. M. 2014, ApJ, 794, 144, doi: 10.1088/0004-637X/794/2/144

Ribas, I., Guinan, E. F., Güdel, M., & Audard, M. 2005a, Astrophysical Journal, 622, 680, doi: 10.1086/427977

—. 2005b, ApJ, 622, 680, doi: 10.1086/427977

Ricker, G. R., Winn, J. N., Vanderspek, R., et al. 2015, Journal of Astronomical Telescopes, Instruments, and Systems, 1, 014003, doi: 10.1117/1.JATIS.1.1.014003

Rizzuto, A. C., Vanderburg, A., Mann, A. W., et al. 2018, AJ, 156, 195, doi: 10.3847/1538-3881/aadf37

Rogers, J. G., & Owen, J. E. 2021, MNRAS, 503, 1526, doi: 10.1093/mnras/stab529

Rogers, L. A. 2015, ApJ, 801, 41, doi: 10.1088/0004-637X/801/1/41

Romano, D., Magrini, L., Randich, S., et al. 2021, A&A, 653, A72, doi: 10.1051/0004-6361/202141340

Salz, M., Schneider, P. C., Czesla, S., & Schmitt, J. H. M. M. 2016a, A&A, 585, L2, doi: 10.1051/0004-6361/201527042

—. 2016b, A&A, 585, L2, doi: 10.1051/0004-6361/201527042

Sanchis-Ojeda, R., Winn, J. N., Marcy, G. W., et al. 2013, ApJ, 775, 54, doi: 10.1088/0004-637X/775/1/54

Sandoval, A., Contardo, G., & David, T. J. 2021, ApJ, 911, 117, doi: 10.3847/1538-4357/abea9e

Sanz-Forcada, J., Micela, G., Ribas, I., et al. 2011a, A&A, 532, A6, doi: 10.1051/0004-6361/201116594

—. 2011b, A&A, 532, A6+, doi: 10.1051/0004-6361/201116594

Sanz-Forcada, J., Ribas, I., Micela, G., et al. 2010a, A&A, 511, L8, doi: 10.1051/0004-6361/200913670

—. 2010b, A&A, 511, L8, doi: 10.1051/0004-6361/200913670

Sanz-Forcada, J., Stelzer, B., Coffaro, M., Raetz, S., & Alvarado-Gómez, J. D. 2019, A&A, 631, A45, doi: 10.1051/0004-6361/201935703

Schatzman, E. 1962, Annales d'Astrophysique, 25, 18

Schmitt, J. H. M. M., Fleming, T. A., & Giampapa, M. S. 1995, ApJ, 450, 392, doi: 10.1086/176149

Schrijver, C. J., & Zwaan, C. 2000, Solar and Stellar Magnetic Activity

See, V., Matt, S. P., Folsom, C. P., et al. 2019, ApJ, 876, 118, doi: 10.3847/1538-4357/ab1096

Shibayama, T., Maehara, H., Notsu, S., et al. 2013, ApJS, 209, 5, doi: 10.1088/0067-0049/209/1/5

Shkolnik, E. L., & Llama, J. 2018, in Handbook of Exoplanets, ed. H. J. Deeg & J. A. Belmonte, 20, doi: 10.1007/978-3-319-55333-7_20

Shkolnik, E. L., Rolph, K. A., Peacock, S., & Barman, T. S. 2014, APJ, 796, L20, doi: 10.1088/2041-8205/796/1/L20

Skrutskie, M. F., Cutri, R. M., Stiening, R., et al. 2006, AJ, 131, 1163, doi: 10.1086/498708

Skumanich, A. 1972, ApJ, 171, 565, doi: 10.1086/151310

Sneden, C. A. 1973, PhD thesis, University of Texas, Austin

Snellen, I. A. G., & Brown, A. G. A. 2018a, Nature Astronomy, 2, 883, doi: 10.1038/s41550-018-0561-6

—. 2018b, Nature Astronomy, 2, 883, doi: 10.1038/s41550-018-0561-6

Soderblom, D. R., Stauffer, J. R., MacGregor, K. B., & Jones, B. F. 1993, ApJ, 409, 624, doi: 10.1086/172694

Solanki, S. K. 2003, A&A Rev., 11, 153, doi: 10.1007/s00159-003-0018-4

Southworth, J., Maxted, P. F. L., & Smalley, B. 2004, MNRAS, 351, 1277, doi: 10.1111/j.1365-2966.2004.07871.x

Sozzetti, A. 2010, Highlights of Astronomy, 15, 716, doi: 10.1017/S1743921310011142

Spake, J. J., Sing, D. K., Evans, T. M., et al. 2018, Nature, 557, 68, doi: 10.1038/s41586-018-0067-5

Stauffer, J., Cody, A. M., Rebull, L., et al. 2016, AJ, 151, 60, doi: 10.3847/0004-6256/151/3/60

Stauffer, J. R., Caillault, J. P., Gagne, M., Prosser, C. F., & Hartmann, L. W. 1994, ApJS, 91, 625, doi: 10.1086/191951

Steenbeck, M., & Krause, F. 1969, Astronomische Nachrichten, 291, 271

Strassmeier, K. G., Granzer, T., Weber, M., et al. 2004, Astronomische Nachrichten, 325, 527, doi: 10.1002/asna.200410273

Strömberg, G. 1946, ApJ, 104, 12, doi: 10.1086/144830

Strugarek, A., Bolmont, E., Mathis, S., et al. 2017, APJ, 847, L16, doi: 10.3847/2041-8213/aa8d70

Stumpe, M. C., Smith, J. C., Van Cleve, J. E., et al. 2012, PASP, 124, 985, doi: 10.1086/667698

Suárez Mascareño, A., Damasso, M., Lodieu, N., et al. 2021, Nature Astronomy, 6, 232, doi: 10.1038/s41550-021-01533-7

Sunyaev, R., Arefiev, V., Babyshkin, V., et al. 2021, A&A, 656, A132, doi: 10.1051/0004-6361/202141179

Terada, N., Kulikov, Y. N., Lammer, H., et al. 2009, Astrobiology, 9, 55, doi: 10.1089/ast.2008.0250

Testa, P. 2009, in Chandra's First Decade of Discovery, ed. S. Wolk, A. Fruscione, & D. Swartz, 5

Tian, F. 2015, Annual Review of Earth and Planetary Sciences, 43, 459, doi: 10.1146/annurev-earth-060313-054834

Tian, F., Chassefière, E., Leblanc, F., & Brain, D. 2013, in Comparative Climatology of Terrestrial Planets, ed. S. J. Mackwell, A. A. Simon-Miller, J. W. Harder, & M. A. Bullock, 567–582, doi: 10.2458/azu_uapress_9780816530595-ch023

Tian, F., Toon, O. B., Pavlov, A. A., & De Sterck, H. 2005, ApJ, 621, 1049, doi: 10.1086/427204

Tian, M., & Heng, K. 2023, arXiv e-prints, arXiv:2301.10217, doi: 10.48550/arXiv.2301.10217

Trümper, J. 1982, Advances in Space Research, 2, 241, doi: 10.1016/0273-1177(82)90070-9

Tu, L., Johnstone, C. P., Güdel, M., & Lammer, H. 2015a, A&A, 577, L3, doi: 10.1051/0004-6361/201526146

—. 2015b, A&A, 577, L3, doi: 10.1051/0004-6361/201526146

van Ballegooijen, A. A., Asgari-Targhi, M., Cranmer, S. R., & DeLuca, E. E. 2011, AJ, 736, 3, doi: 10.1088/0004-637X/736/1/3

Van Eylen, V., Agentoft, C., Lundkvist, M. S., et al. 2018a, MNRAS, 479, 4786, doi: 10.1093/mnras/sty1783

—. 2018b, MNRAS, 479, 4786, doi: 10.1093/mnras/sty1783

Vanderburg, A., & Johnson, J. A. 2014, PASP, 126, 948, doi: 10.1086/678764

Venturini, J., Guilera, O. M., Ronco, M. P., & Mordasini, C. 2020, A&A, 644, A174, doi: 10.1051/0004-6361/202039140

Venuti, L., Bouvier, J., Cody, A. M., et al. 2017, A&A, 599, A23, doi: 10.1051/0004-6361/201629537

Vidal-Madjar, A., Lecavelier des Etangs, A., Désert, J. M., et al. 2003, Nature, 422, 143, doi: 10.1038/nature01448

Vilhu, O. 1984, A&A, 133, 117

Virtanen, P., Gommers, R., Oliphant, T. E., et al. 2020, Nature Methods, 17, 261, doi: 10.1038/s41592-019-0686-2

Vissapragada, S., Stefánsson, G., Greklek-McKeon, M., et al. 2021, AJ, 162, 222, doi: 10.3847/1538-3881/ac1bb0

Voges, W., Aschenbach, B., Boller, T., et al. 1999, A&A, 349, 389. https://arxiv.org/abs/astro-ph/9909315

Wang, L., & Dai, F. 2018a, ApJ, 860, 175, doi: 10.3847/1538-4357/aac1c0

—. 2018b, ApJ, 860, 175, doi: 10.3847/1538-4357/aac1c0

Watson, A. J., Donahue, T. M., & Walker, J. C. G. 1981a, Icarus, 48, 150, doi: 10.1016/0019-1035(81)90101-9

—. 1981b, Icarus, 48, 150, doi: 10.1016/0019-1035(81)90101-9

Weber, E. J., & Davis, Leverett, J. 1967, ApJ, 148, 217, doi: 10.1086/149138

Weber, M., Granzer, T., & Strassmeier, K. G. 2012, Society of Photo-Optical Instrumentation Engineers (SPIE) Conference Series, Vol. 8451, The STELLA robotic observatory on Tenerife, 84510K, doi: 10.1117/12.926525

Weisskopf, M. C., Tananbaum, H. D., Van Speybroeck, L. P., & O'Dell, S. L. 2000, in Society of Photo-Optical Instrumentation Engineers (SPIE) Conference Series, ed. J. E. Trümper & B. Aschenbach, Vol. 4012, 2–16

Williams, J. P., & Cieza, L. A. 2011, ARA&A, 49, 67, doi: 10.1146/annurev-astro-081710-102548

Winn, J. N., & Fabrycky, D. C. 2015, ARA&A, 53, 409, doi: 10.1146/annurev-astro-082214-122246

Wolk, S., Hong, J., Romaine, S., et al. 2022, in AAS/High Energy Astrophysics Division, Vol. 54, AAS/High Energy Astrophysics Division, 110.65

Wolk, S. J., Drake, J. J., Branduardi-Raymont, G., et al. 2019, arXiv e-prints, arXiv:1904.04320, doi: 10.48550/arXiv.1904.04320

Wood, B. E., Laming, J. M., Warren, H. P., & Poppenhaeger, K. 2018, ApJ, 862, 66, doi: 10.3847/1538-4357/aaccf6

Wright, N. J., Drake, J. J., Mamajek, E. E., & Henry, G. W. 2011a, ApJ, 743, 48, doi: 10.1088/0004-637X/743/1/48

—. 2011b, ApJ, 743, 48, doi: 10.1088/0004-637X/743/1/48

Wright, N. J., Newton, E. R., Williams, P. K. G., Drake, J. J., & Yadav, R. K. 2018, MNRAS, 479, 2351, doi: 10.1093/mnras/sty1670

Wu, Y. 2019, ApJ, 874, 91, doi: 10.3847/1538-4357/ab06f8

Wyatt, M. C., Kral, Q., & Sinclair, C. A. 2020, MNRAS, 491, 782, doi: 10.1093/mnras/stz3052

Yelle, R. V. 2004, Icarus, 170, 167, doi: 10.1016/j.icarus.2004.02.008

Zeng, L., Jacobsen, S. B., & Sasselov, D. D. 2017, Research Notes of the American Astronomical Society, 1, 32, doi: 10.3847/2515-5172/aa9ed9

Zeng, L., Jacobsen, S. B., Sasselov, D. D., et al. 2019, Proceedings of the National Academy of Science, 116, 9723, doi: 10.1073/pnas.1812905116

Zeng, L., Jacobsen, S. B., Hyung, E., et al. 2021, ApJ, 923, 247, doi: 10.3847/1538-4357/ac3137

Zhang, M., Knutson, H. A., Dai, F., et al. 2023, AJ, 165, 62, doi: 10.3847/1538-3881/aca75b

Zhang, M., Knutson, H. A., Wang, L., et al. 2022, AJ, 163, 68, doi: 10.3847/1538-3881/ac3f3b

Zhuleku, J., Warnecke, J., & Peter, H. 2020, A&A, 640, A119, doi: 10.1051/0004-6361/202038022